PERFORMANCE EVALUATION OF LUBRICATED POLYMER GEARS

A thesis

submitted in partial fulfillment of the requirements

for the degree of

DOCTOR OF PHILOSOPHY

by

Sarita Bharti

(156103032)

Department of Mechanical Engineering

Indian Institute of Technology Guwahati

Guwahati, Assam – 781039, India

July 2023

Certificate

It is certified that the work contained in the thesis entitled "**Performance Evaluation of Lubricated Polymer Gears**" submitted by Ms. Sarita Bharti to the Indian Institute of Technology Guwahati for the degree of Doctor of Philosophy has been carried out under my supervision in the Department of Mechanical Engineering, Indian Institute of Technology Guwahati. This work has not been submitted elsewhere for the award of any other degree or diploma.

Dr. S. Senthilvelan
Professor
Department of Mechanical Engineering,
Indian Institute of Technology Guwahati,
Guwahati-781039, India

Acknowledgment

First and foremost, I would like to express my sincere gratitude and respect to my research supervisor **Prof. S. Senthilvelan**, I am thankful for all his contribution towards making my Ph.D. experience productive. I have been motivated by his patience, goodwill, and constant encouragement, and with Prof. Senthilvelan's ideology of viewing every challenge should be viewed as a chance to adopt an unwavering outlook on life. He remained deeply involved in my thesis work from scratch till completion. He provided me with relevant books, original ideas, and thorough guidance that were immensely helpful in the successful completion of my Ph.D. thesis.

I would like to express my gratitude to the doctoral committee member, **Prof. S. Kanagaraj**, **Prof. Sukhomay Pal**, and **Dr. Venkatesh R. Prasanna**, for their valuable comments, suggestion, and encouragement during the period of my research work.

My sincere gratefulness to the **Faculty** of **Mechanical Engineering**, **IIT Guwahati,** for offering me an opportunity to pursue doctoral research. I would like to acknowledge **Mr. B. R. Singh** of Oka Basu's Metal Technologies Pvt. Ltd., **Mr. K. Kaarthic** of Sakthi Drives Specialists in Gears and Gearboxes, **Mr. Joshy** of Just Preci Comps, **Mr. Prashant** of Perfect Gears Pvt. Ltd., **Mr. Shreedhar Kumar** of PSG TIFAC CORE**,** and **Mr. Uttam Basar** for their assistance.

I would like to thank **Mr. N. K. Das**, **Mr. Dhaneshwar Khaklary**, **Mr. Mrinal Sarma, Mr. Jiten Basumatary, Mr. Dilip**, **Mr. Upen Gohain**, **Mr. Minesh Ch. Medhi, Mr. Nidul Saikya, Mr. Saiffuddin Ahmed** and **Mr. Pranjol Paul,** Central Workshop staff members, and Mechanical Engineering department staff members for their contribution and help throughout my research work. I offer my thanks to all the Security Staff of IIT Guwahati. I wish to also acknowledge Central Instrument Facility IIT Guwahati for supporting various characterizations.

I wish to convey my thanks to my seniors **Dr. M. Kodeeswaran**, **Dr. A. Johnney Martens**, and **Dr. Kishor Kumar Gajrani,** for their helpful advice at various stages. It has been a great pleasure to work with my friend, research, and lab colleagues, **Dr. Karthik Pandian**, **Mayur Jadhav, Mr. Shaidul Islam, Mr. Ganesh Kumar** and **Dr. Soundhar A**. I thank all of them for helping me directly and indirectly to complete my work. I would also like to thank my colleagues **Mr. Vaibhav**, **Mr. Raaghdeep, Dr. Bikas**, **Mr. Vivekanand**, **Mr. Rishabh, Mr. Amritava Sarkar,** and **Dr. Dinesh**.

I have been fortunate to be surrounded by some amazing friends, **Dr. Deepshikha, Mr. Kishore Kumar**, **Mr. Arunjyoti, Ms. Tako Nama, Dr. Ila,** and **Mr. Nitish**. Thank you all for your help, encouragement, and indispensable emotional support in completing my work.

I would like to express my deep gratitude to my parents, sisters, brother, and husband for their affection, patience, and support toward my research work.

Sarita Bharti

Abstract

Injection molded polymer gears are being widely utilized as they offer several advantages, such as lightweight, good damping capacity, easy production, low manufacturing cost, and good mechanical properties for low and moderate-load applications. Many works have been earlier attempted to improve mechanical properties by incorporating fiber reinforcement. In this work, an attempt has been made to investigate the potential of using oil lubrication for performance improvement. In addition, the present study also aims to check the feasibility selective laser sintering (SLS) process and elastomeric material (thordon SXL) for gearing application. The sliding contact performance of these materials was also investigated using pin on disc configuration. The surface durability of the test gear was investigated using a house-developed gear rig at various loading conditions and a constant rotational speed under dry and lubricated conditions by observing the thermal response of gear teeth, lubricant temperature, periodically monitoring gear teeth surface, and failure morphology.

Oil lubricant between the gear teeth provided smooth contact and reduced frictional heating by dissipating the generated heat effectively. Under the dry condition, different failure modes of pitting and thermal softening, along with tooth cracking near the pitch region were observed based on loading conditions in injection molded test gear. Test gears under lubrication conditions showed only scuffing but did not exhibit any cracks in the pitch region or other regions owing to improved heat dissipation characteristics. To understand the adhesion effect and influence of lubrication, dissimilar material gear pair (steel-injection molded polyamide) and similar material gear pair (injection molded polyamide -injection molded polyamide) were evaluated. Due to low thermal conductivity and viscoelastic characteristics, frictional heating and hysteretic heating cause inferior life of polymer-polymer gear pair than steel-polymer at all the considered loading conditions.

Flat build configuration processed SLS gear exhibited enhanced surface contact performance at the lower load due to its brittleness and reduced ductility. However, under lubricated conditions, the lubricant diffused into the porous subsurface, which resulted in the reduction of material shear strength and inferior gear life. Due to its improved thermal stability, the lubricated SLS gear exhibited superior performance at a higher load compared to the dry condition. Thordon gear exhibited only tooth root cracks due to bending fatigue under dry as well as lubricated conditions. In contrast, the injection molded and selective laser sintered gear

exhibited wear thermal failure, scuffing, and pitting based on loading as well as environmental conditions.

Keywords: Gear, injection molding, selective laser sintering, thordon, lubrication, sliding contact

Contents

List of Figures

List of Tables

Abbreviations

ABS	Acrylonitrile Butadiene Styrene
AGMA	American Gear Manufacturing Association
AISI	American Iron and Steel Institute
ASTM	American Society for Testing and Materials
CT	Computed Tomography
CAD	Computer Aided Design
DIN	Deutsches Institut für Normung e. V.
EAP	End of Active Profile
ESC	Environmental Stress Cracking
FESEM	Filed Emission Electron Microscope
FDM	Fused Deposition Modeling
HDT	Heat Deflection Temperature
HPSTC	Highest Point of Single Tooth Contact
IR	Infrared
IM	Injection Molding
LPSTC	Lowest Point of Single Tooth Contact
OM	Optical Microscopy
PEEK	Poly Ether Ether Ketone
PA	Polyamide
PEGT	Polyethylene Terephthalate
PEW	Polyethylene Wax
PLA	Polylactic Acid
POM	Polyoxymethylene
PPS	Polyphenylene Sulfide
PP	Polypropylene
PS	Polystyrene
PTFE	Polytetrafluoroethylene
SLS	Selective Laser Sintering
SAE	Society of Automotive Engineers

STL	Standard Triangle Language
SAP	Start of Active Profile

Notations

L_{min}	Minimum contact length
ρ_1 and ρ_2	Profile radii of curvature of the driver and driven at the pitch point
ρ_n	Normal relative radius of curvature for spur gear
ρ_r	Transverse relative radius of curvature and
$\rho_{1(i)}$ and $\rho_{2(i)}$	Transverse radius of curvature driver and driven
$(F_t)_{nom}$	Normal tangential load
$b_{H(i)}$	Semi-width of the rectangular contact band
$v_{r1(i)}$ and $v_{r2(i)}$	Tangential velocity of driver and driven
μ_m	Constant coefficient of friction
β_w	Operating helix angle (in degree)
$C_P \dots C_T$	Distance along the of action
E_r	Reduced modulus of elasticity
s_b	Allowable bending stress
F_t	Actual tangential load
a_w	Operating center distance
b	Face width
F_a	Total involute profile
Fb	Total lead profile
ffa	Profile form deviation
ffb	Lead form deviation
FHa	Involute slope deviation
FHb	Lead slope deviation
h	Bending moment arm
Y	Lewis form factor
m	Module
t	Critical section thickness
ω_2	Angular velocity of driven

R_{avgx}	Average surface roughness of the driver and driven gear
K_D	Combined derating factor
$\theta_{B_{(i)}}$	Contact temperature
ρ_{M1} and ρ_{M2}	Densilty of driver and driven
g_1	Dimensionless viscosity parameter
$\xi_P, \dots \dots \dots \xi_T$	Driven roll angle at point P…… T
$\xi_{(i)}$	Driver roll angles along the line of action
n_1	Driver speed
$\bar{U}$	Entraining velocity
$\theta_{fl_{(i)}}$	Flash temperature
u	Gear ratio
P	Gear transmitted power
T_g	Glass transition temperature
X_r	Load sharing factor for smooth meshing
s_c	Maximum contact stress at pitch point
$\theta_{fl\,max}$	Maximum flash temperature
α_{wn}	Normal operating pressure loading
w_n	Normal unit load at pitch point
v_t	Operating pitch line velocity
r_{a1} and r_{a2}	Outer radii of driver and driven
K_o, K_m and K_v	Overload factor, load distribution factor and the dynamic factor.
r_{w2}	Pitch circle diameter
α	Pressure-viscosity coefficient
c_{M1} and c_{M2}	Specific heat capacity of driver and driven
K_{M1} and K_{M2}	Thermal conductivity of driver and driven
B_{M1} and B_{M2}	Thermal contact coefficient of driver and driven
θ_M	Tooth temperature
T_t	Torque at pitch point of the driven gear
p_{bt}	Transverse base pitch
η_0	Viscosity at ambient temperature and pressure
g_3	Dimensionless elasticity parameter
$\bar{h}$	Dimensionless minimum film thickness parameter

R_{at}	Equivalent surface roughness
g_4	Dimensionless system character parameter
h	Actual film thickness
λ	Specific film thickness or minimum film thickness

Chapter 1

Introduction

1.1 Fundamentals of gear

Gear is a machine element that transmits motion and power between rotating shafts by engaging a tooth projection progressively. Figure 1.1 depicts some of the basic gear nomenclatures.

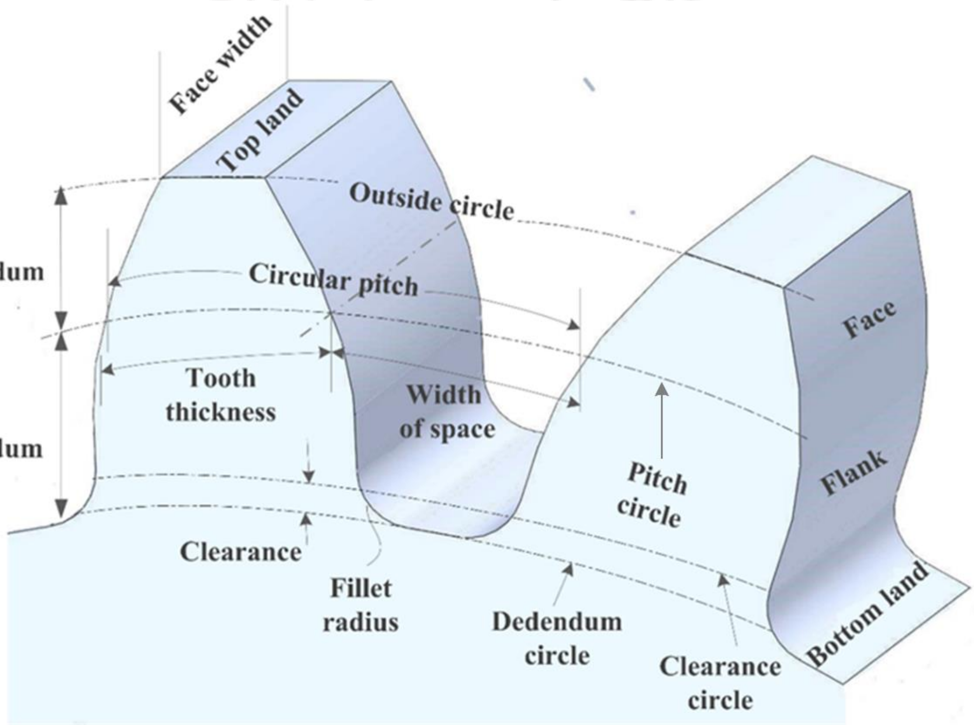

Figure 1.1 Gear nomenclatures

Root circle/dedendum circle is the circle that binds the roots or bottom of the gear teeth.

Pitch circle is the circumference of an imaginary cylinder that, if rolled without slipping, would produce the same motion as the actual gear.

Outside/tip/addendum circle is a circle that binds together the outer edges of the gear teeth.

Clearance is the term used to define the radial distance from the top of one gear to the bottom of another when two gears mesh together. The circle that passes from the top of the tooth while in the meshed condition is termed a clearance circle.

Top land is the surface of the top of the tooth.

Bottom land is the surface of the bottom of the tooth between the adjacent fillets.

Fillet is the curved portion of the tooth flank at the root circle.

Face is the tooth surface between the pitch circle and the top land.

Flank is the tooth surface between the pitch circle and the bottom land including fillet.

The radial distance from the top land to the pitch circle of the gear tooth is termed an addendum.

The radial distance from the bottom to the pitch circle of the gear tooth is termed a dedendum.

Clearance is the radial difference between the addendum and the dedendum of a tooth.

Face width is the width of the gear tooth measured parallel to its axis.

Tooth thickness is the width of the tooth measured along the pitch circle.

1.2 Gear tooth bending stress

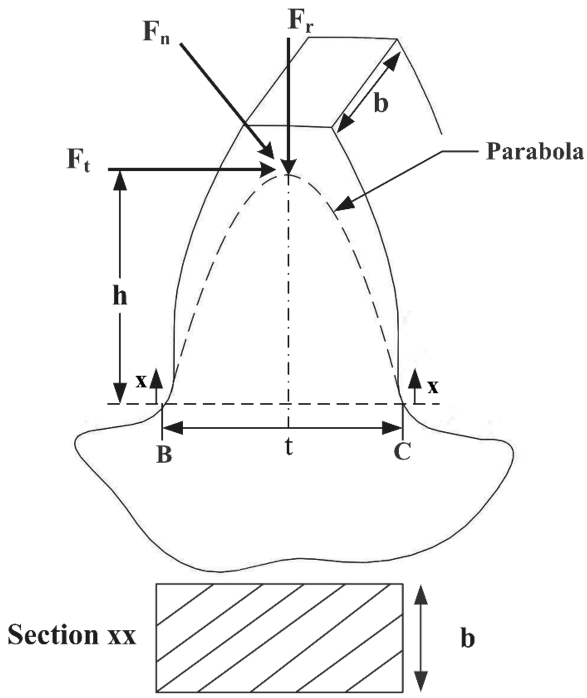

Figure 1.2 Gear tooth as parabolic beam

Principally, the gear tooth is a cantilever beam. At the base of the beam, tensile stress is on the loaded side, while compressive stress is on the opposite side acting (Radzevich (2012)). When a gear tooth breaks, it typically fails by developing a crack at the base of the tooth on the side that is under tensile stress. A gear tooth's resistance to breakage is often referred to as its beam strength or flexural strength.

Figure 1.2 shows the gear tooth and represents the typical loads (radial component (F_r), tangential component (F_t) and normal component (F_n) acting on the gear tooth. The critical section thickness and bending moment arm are t and h, respectively. The gear tooth cross-section changes from its free to fixed end (Bhandari (2017)). The parabola is created within the tooth, revealing a uniform strength beam. The parabola at section xx is tangent to the tooth profile and characterizes the gear tooth's lowest strength section. The tangential force component (F_t) is responsible for the bending moment about the gear tooth base. The maximum bending stress (allowable bending stress) corresponds to the F_t, at which the tooth can transmit without failure, and the relation between the allowable stress and F_t is represented by the Lewis equation

$$F_t = mbs_bY \tag{1.1}$$

where, s_b allowable bending stress, m is the gear module, b is the tooth face width, and Y is the Lewis form factor.

1.3 Gear tooth contact stress

Figure 1.3 shows two parallel cylindrical gear in contact with the external force. When two bodies (spherical or cylindrical) roll, or roll-slide against each, under sufficient pressure, the point or line contact changes to area contact, which results in a complex stress pattern (elliptical) generation on the contact area (Hertz (1896)).

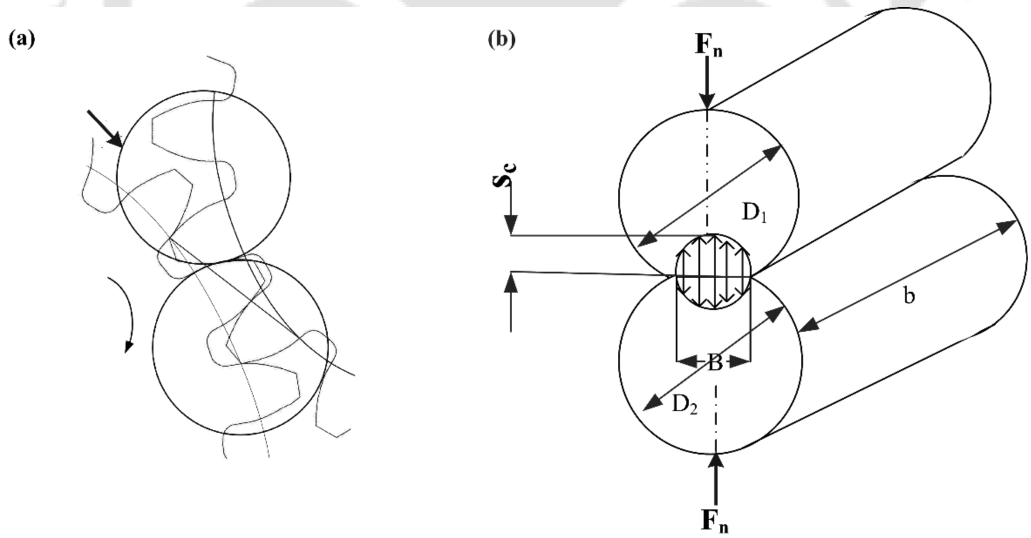

Figure 1.3 Schematic representation of (a) Equivalent cylinders from the pair of gear the tooth in mating position at pitch point and (b) Two parallel cylinders under loading condition

The area is a narrow rectangle of width (B) and length (b). The maximum contact pressure (s_c) is expressed by

$$s_c = \frac{4F_n}{\pi Bb} \tag{1.2}$$

$$B = \sqrt{\frac{8F_n(1-\nu_1^2)/E_1 + (1-\nu_2^2)/E_2}{1/D_1 + 1/D_2}} \quad (1.3)$$

where D_1, and D_2 are the equivalent diameters of gear tooth at the pitch points, ν_1, and ν_2 are Poisson's ratio materials, E_1, and E_2 are the elastic moduli of materials and F_n is the normal load.

Maximum compressive shear stress is generated at the center of the contact band surface. The subsurface cracks generate beneath the contact surface and initiate from the point of maximum shear stress, and propagate towards the surface. This subsurface shear stress is responsible for contact fatigue failure. Figure 1.4 shows the typical representation of the variation of shear stress against shear depth.

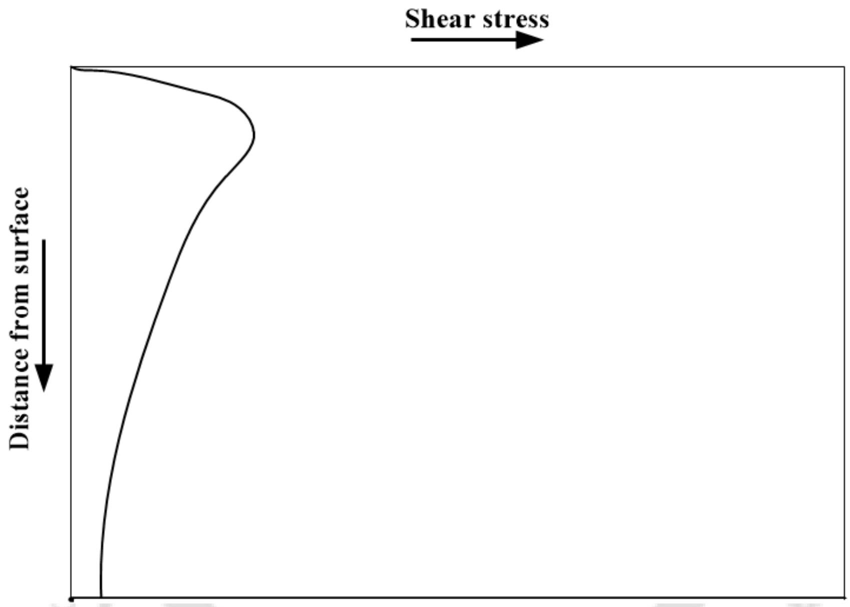

Figure 1.4 Schematic view of shear stress variation vs. shear depth.

1.4 Critical locations of gear tooth

Figure 1.5 (a) shows the schematic view of a gear tooth with various locations marked on it. Between points Q–S, the gear tooth exhibited the single tooth contact region (only one tooth pair in contacts), and between points P–Q and S–T gear exhibited the double tooth contact region (two tooth pairs in contacts). Point P represents the start of the active profile, the lowest point on the gear tooth where contact with the mating gear tooth tip can occur. Point Q is the lowest point of single tooth contact (LPSTC), the point on the smallest diameter at the single tooth contact region of spur gear while meshing with mating gear where the contact stress is calculated at an applied load. Point R is the pitch point. Point S indicates the highest point of single tooth contact (HPSTC), the point on the largest diameter at the single tooth contact region of spur gear while meshing with mating gear where the bending stress is calculated at an applied load. Finally, point T is the end of the acting profile, the highest point on the gear tooth where contact with the mating gear tooth ends. Figure 1.5 (b) shows the typical load sharing on the gear tooth.

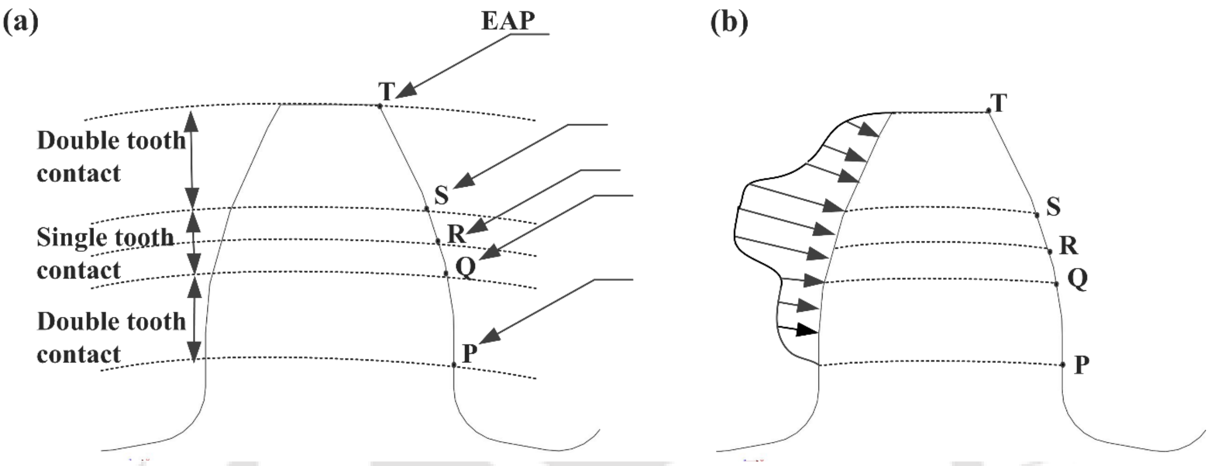

Figure 1.5 (a) Shows the gear tooth with various locations and (b) Typical load sharing on the gear tooth (Muraro *et al.* (2012))

1.5 Fundamentals of polymer

Molecules/monomers arrange into a repeating unit at a suitable temperature and pressure to form macromolecules known as a polymer (Figure 1.6 (a)). The monomer repeating unit may be the same or different, and the sides of monomers have an active bond that reacts and combines, forming a covalent bond or two-or three-dimensional chain-like structures. Repeating units linked together end to end to form a single chain known as a linear polymer (Figure 1.6 (b)) and flexible nature (Balasubramanian (2012)). Examples are polyamide, polyethylene, polystyrene etc. The adjacent linear chains are connected to each other in different positions by covalent bonds resulting in the formation of crosslinked polymer (Figure 1.6 (d)). Most rubber elastic materials belong to this category of polymer.

The polymer material can be categorized based on its response to rising temperatures. The thermoplastic material can be heated and cooled many times, and the process is reversible: they soften when heat is applied and harden when they cool. Branched polymer with flexible chains, as well as linear polymer, belongs to the thermoplastic. Thermoset polymer has three-dimensional networks (Figure 1.6 (e). This type of polymer on heat applications first becomes soft, then hardened upon heating, and afterward, it cannot be softened again by applying heat.

During heat treatment, covalent crosslinked between adjacent molecular chains resist vibration and rotational movement of chains at higher temperatures. As a result, the material does not soften again on heating and cannot be reused.

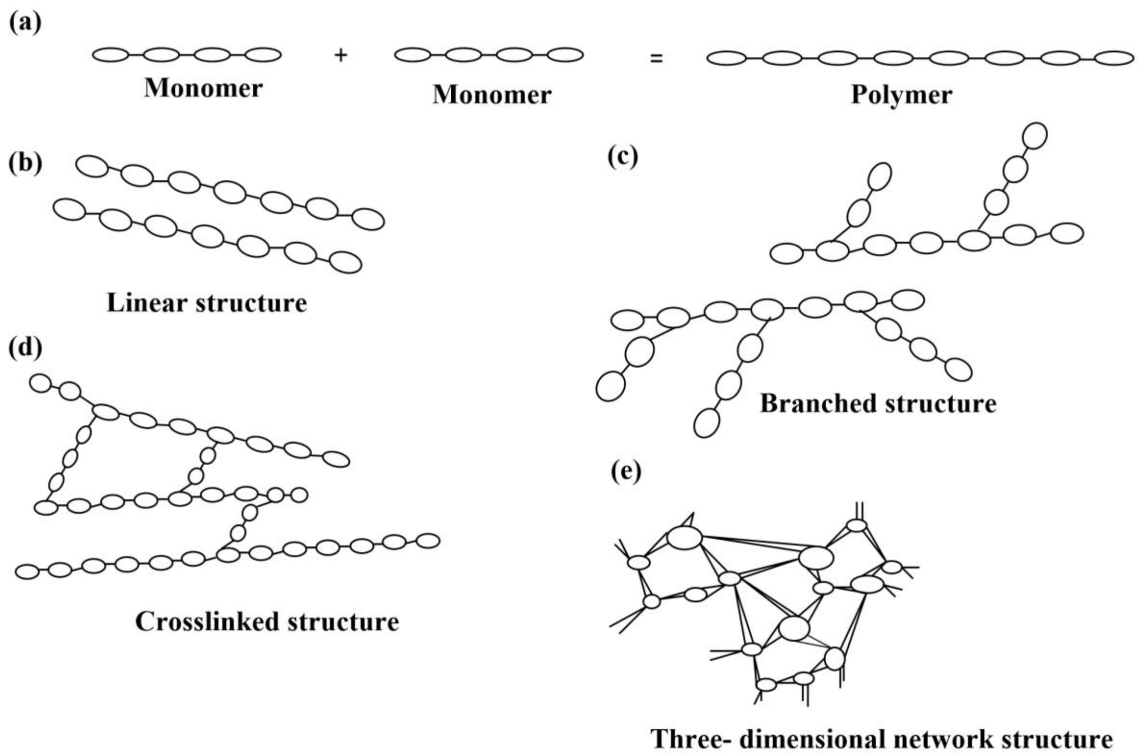

Figure 1.6 (a) Polymer; and various polymer structures (b) Linear molecular structure, (c) Branched molecular structure, (d) Crosslinked molecular structure, and (e) Network molecular structure (Balasubramanian (2012))

Examples of thermosets include phenolics, epoxies, bakelite, etc. Polymer is exhibited as a stiff solid material at low temperatures (below the glass transition temperature (T_g)) under sufficiently deformed and initiates viscoelastic deformation conditions. At temperatures ranging near the T_g, the polymer exhibits a rubbery phase. Above the T_g and melting temperatures, the polymer is viscous and liquid-like in nature in the case of an uncrosslinked polymer, whereas rubbery and stiff viscoelastic in the case of weakly crosslinked and highly crosslinked polymer, respectively. Thermoplastic-based polymer materials are mostly preferred for industry and engineering purposes. Engineering plastics often have the following characteristics – impact strength, heat resistance, and getting molded to great precision. Polyamide, polypropylene, polyvinyl chloride, low-density polyethylene, high-density polyethylene, and polystyrene are significant families of engineering thermoplastics that have been utilized for load-bearing applications.

Elastomers are made of long hydrocarbon loose chain polymers crosslinked molecules to form network structures with high deformability capacity, tensile strength, poisson ratio, flexibility, and low modulus of elasticity, can stretch repeatedly and will return to their approximate original length (Hutchings and Shipway (2017), Rangappa *et al.* (2022)), Hakami *et al.* (2022)). Elastomer material can undergo strain under stressed conditions without substantial deformation and exhibits both elastic and viscous behaviors (Felhös *et al.* (2008), Wu *et al.* (2016)). The long-chain polymers portion of elastomer is highly twisted and coiled under no loading condition, which may alter their configurations owing to its high mobility under externally applied stress. Upon release of external forces, it rapidly reverts its original unstressed state with essentially no residual or nonrecoverable strain influence of crosslinked molecules.

1.6 Injection molding

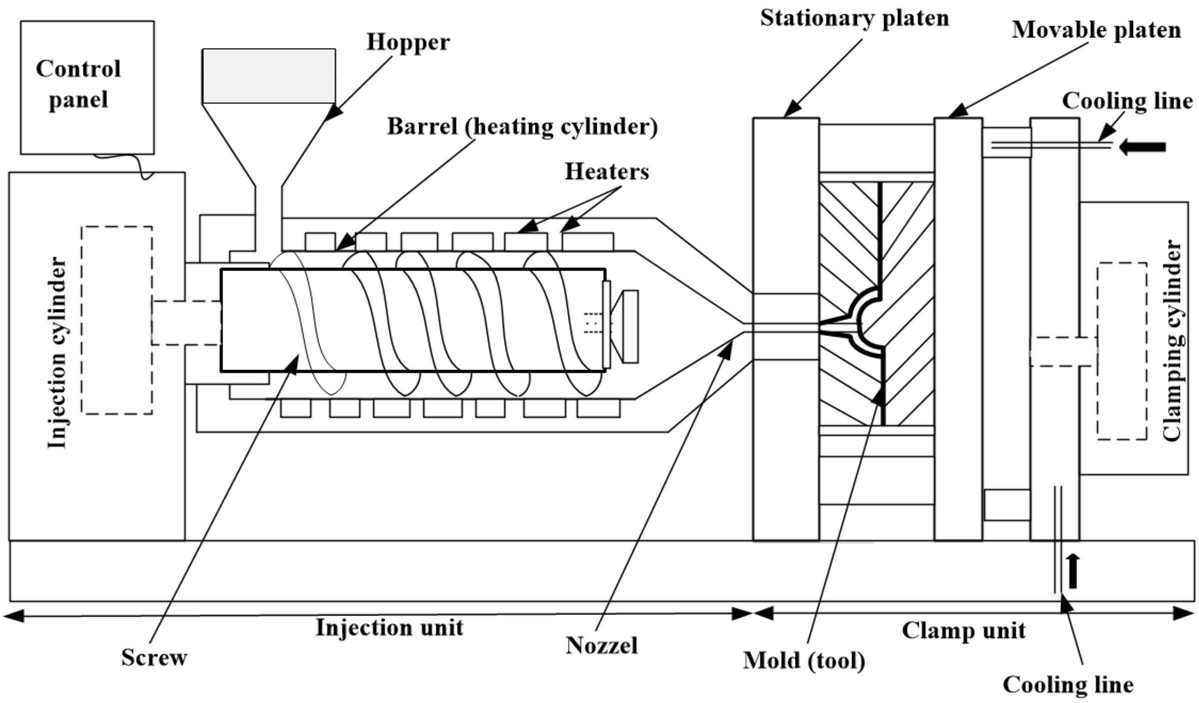

Figure 1.7 Schematic view of the injection molding process

Injection molding is the most widely used method for fabricating thermoplastic components. The schematic view of a typical injection molding configuration is illustrated in Figure 1.7. The injection molding system consists of two units; the injection unit and the clamping unit. Melting plastic pellets and injecting molten material into the mold are the two primary purposes of the injection unit. The purpose of the clamping unit is to open and close the die and eject the formed parts. The raw plastic pellets are stored and supplied to the heating cylinder with the help of a hopper. The screw is a helical-shaped rod that is part of the barrel; raw pellets move forward from the hopper to a different heating region in the barrel with the help of the screw. In addition, it mixes and homogenizes the molten plastic and generates heating friction to raise the temperature of the plastic (Bryce (1996)). A tube-shaped nozzle completes the injection unit set up at the injection barrel's face. Prior to the molten plastic material being injected, the tool, which is mainly made of stationary platen half (cavity) and movable platen (core), closes and is held under high pressure (clamp pressure) and is ready for injecting the plastic. The molten plastic gets injected by the screw. The gate present inside the tool aids in controlling the flow of molten plastic. As the tool cavity is almost full of molten material, a phase of holding (typically a few sec) begins. Then part begins to form its final solidified shape. After the holding phase, the screw is pulled back to its position, releasing pressure and allowing the part to cool by circulating oil or water. After the process of holding and cooling, the part is almost formed and is ejected by the mold.

1.7 Selective laser sintering

Selective laser sintering (SLS) is one additive manufacturing method that includes a high-powered CO_2 laser as a heating source to sinter/fuse powdered materials layer by layer. Prior to printing, the parts are created with different CAD tools, and the models are sent to a 3D printer in a numerical format (STL). The thin layer of cross-sections of a 3D model is heated on the surface of a powder bed using a laser scanning technique just above or below the melting point to produce a final 3D solid part. As each cross-section is scanned and fused, the bed is taken down by one layer of thickness, and fresh material is supplied through the top. The roller then moves across the bed to spread powder for the following layer. This process is repeated till the production of the part is finished. Sintering takes place by forming a micromelt layer at the surface of the powder particles under a liquid state; the powder particles reduce their viscosity and form a concave radial bridge (as necking) among particles as a result of the material's response to reduced surface energy. For the efficacy of the laser to raise the temperature of selective regions to reach the melting point, the unit preheats the bulk powder present in the bed till below the melting point. During sintering, parts being built are always surrounded by unsintered powder. As a result, no additional support structures are required to manufacture overhanging designed parts. It requires very short-term laser exposure to be sintered, which makes SLS printing faster than other additive manufacturing. Figure 1.8 depicts the schematic view of the SLS process.

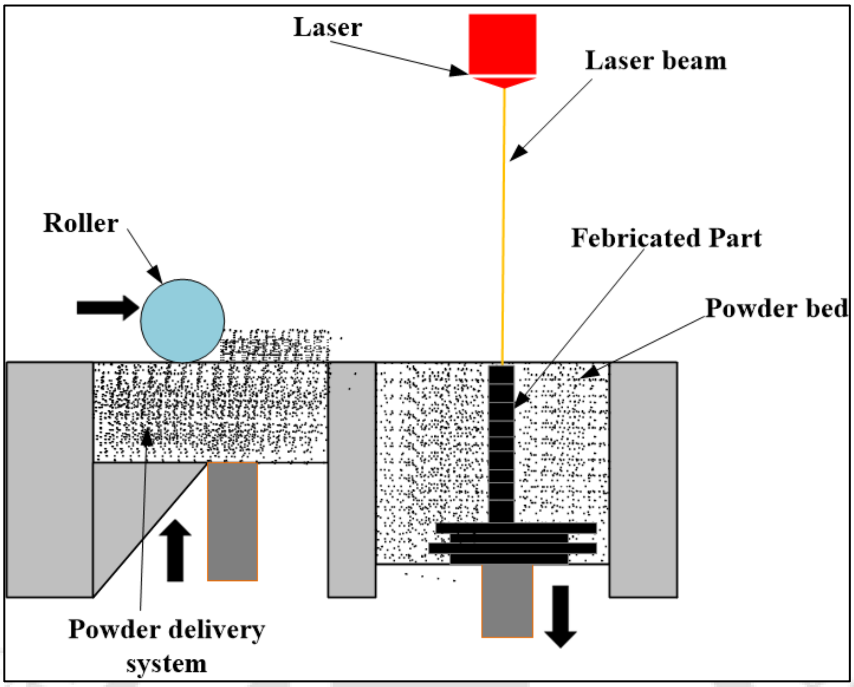

Figure 1.8 Schematic view of selective laser sintering

1.8 Mechanical behavior of plastics

Modulus: The slope of the initial linear position of the stress-strain curve is the modulus of elasticity or Young's modulus of the material, and it quantifies the stiffness/or rigidity of the material. With an increase in temperature, the elasticity modulus as well as crystallinity decreases of thermoplastic material.

Yield strength: The maximum stress at which a noticeable increase in elongation takes place without increasing the load is known as the yield strength of the material.

Tensile strength: The ratio of maximum load material experienced to the original cross-section area under the uniaxial loading condition called tensile strength or ultimate tensile strength of the material. Typically, the ultimate tensile strength of various plastics under compression is around double the tensile strength. Polymers lose strength as the temperature increases. The temperature impacts are typically more significant if they are comparable to the effects of a change in strain rate. The material gets more brittle in reaction to increased strain rate; it becomes ductile in response to higher temperatures (Rosato *et al.* (2005)). Increasing the strain rate will require higher temperatures to make a transition from a glassy to a rubbery state. The tensile strength does not significantly change until a certain temperature is reached. At this point, it fails instantly. However, the material's yield strength gradually decreases as its temperature increases (Budyans and Nisbett (2016)).

Hardness: The resistance of the material to penetration/or permanent deformation is the hardness of the material.

Creep: The time-dependent extension of material at applied constant stress (which can be tensile, compressive, or flexural) is termed a creep. The rate of creep in any material depends on the imposed stress, time, and temperature. Figure 1.9 shows the behavior of creep in the material under tensile creep testing. The strain as a function of time for a period under constant stress conditions is divided into three typical regions, primary, secondary, and tertiary creep regions. At the time (t_0) the material is suddenly loaded at constant stress and occurs rapid and high elongation (ε_0), but decreasing strain rate (due to strain hardening) with time comes under the primary creep region. In the secondary creep region, the creep rate alters little with time or is essentially steady. Once a sufficient period (primary and secondary) sustained by the material endures the strain condition, finally the tertiary creep region is characterized by a rapidly increasing strain rate (owing to necking, internal void formation diffusion (Dieter and Bacon (1976)) until failure is termed as creep failure.

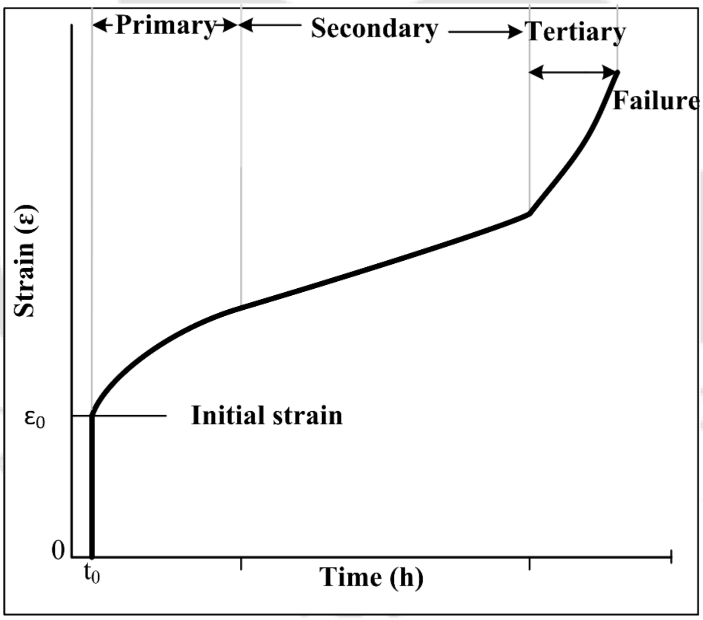

Figure 1.9 Creep curve

Stress relaxation: Stress relaxation is another time-dependent phenomenon, a decrease of stress under constant strain or deflection and fixed temperature. An increase in temperature and stress level can lead to a decreased stress relaxation rate in the material (Bedaiwi and Abdalkadum (2018)). The stress relaxation rate of thermoplastic material increases with temperature for long-term viscoelastic deformation, but thermoset plastics are unaffected up to somewhat high temperatures (Rosato *et al.* (2005)).

Hysteresis: Figure 1.10 represents the schematic stress-strain view of viscoelastic material that is elastically deformed. Viscoelastic material does not follow the same loading-unloading path after load removal though it is deformed elastically as some molecules in the material to get permanently deformed and absorb the energy. The path O-A is indicated by the upwards direction of the arrow while deforming elastically. The energy required for deformed material is high. The path indicated by the arrow downwards represents the unloading of the material. To unload the material, the energy required is less than the deforming conditions, and the amount of energy loss results in increased material temperature. Under loading, the viscous component effect, the material does not follow the same loading and unloading path. Viscoelasticity is a characteristic property of thermoplastic polymers. Under cyclic loading conditions, hysteretic heating in thermoplastic material leads to the deterioration of mechanical properties and may significantly increase the material's temperature; the viscous component of viscoelastic materials exert hysteretic heating and more energy loss under loading conditions than would be expected.

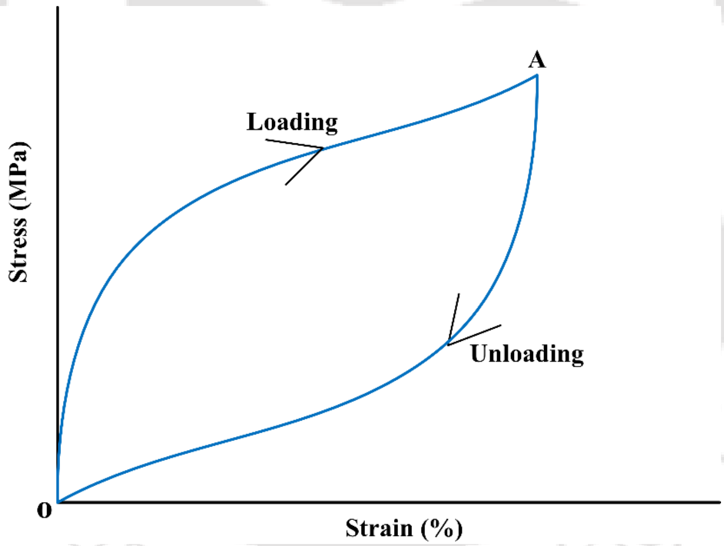

Figure 1.10 Schematic view of the hysteresis heating loop of viscoelastic polymer material.

Heat deflection temperature: Heat deflection temperature (HDT) quantifies the resistance of a material against distortion at elevated temperatures under loading conditions. According to the standard ASTM D648, material loaded to either 0.455 MPa or 1.82 MPa under 3-point bending stress and oil-controlled temperature environment, temperature increases 2 K/min until the maximum material defection is 0.25 mm (Figure 1.11).

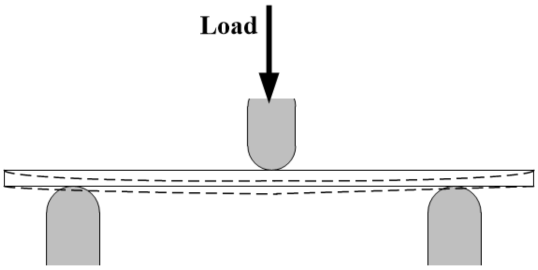

Figure 1.11 Representation of heat temperature deflection measurement

1.9 Friction and wear

When two solids are in motion with each other or against each other, the resistance encountered/ force that forms between them is friction. An adhesion force is created at the bearing area contact, and a deformation force to plough the asperities of the hard surface through the soft surface evolves into frictional force. Friction is responsible for dissipating energy to maintain motion in transmission applications.

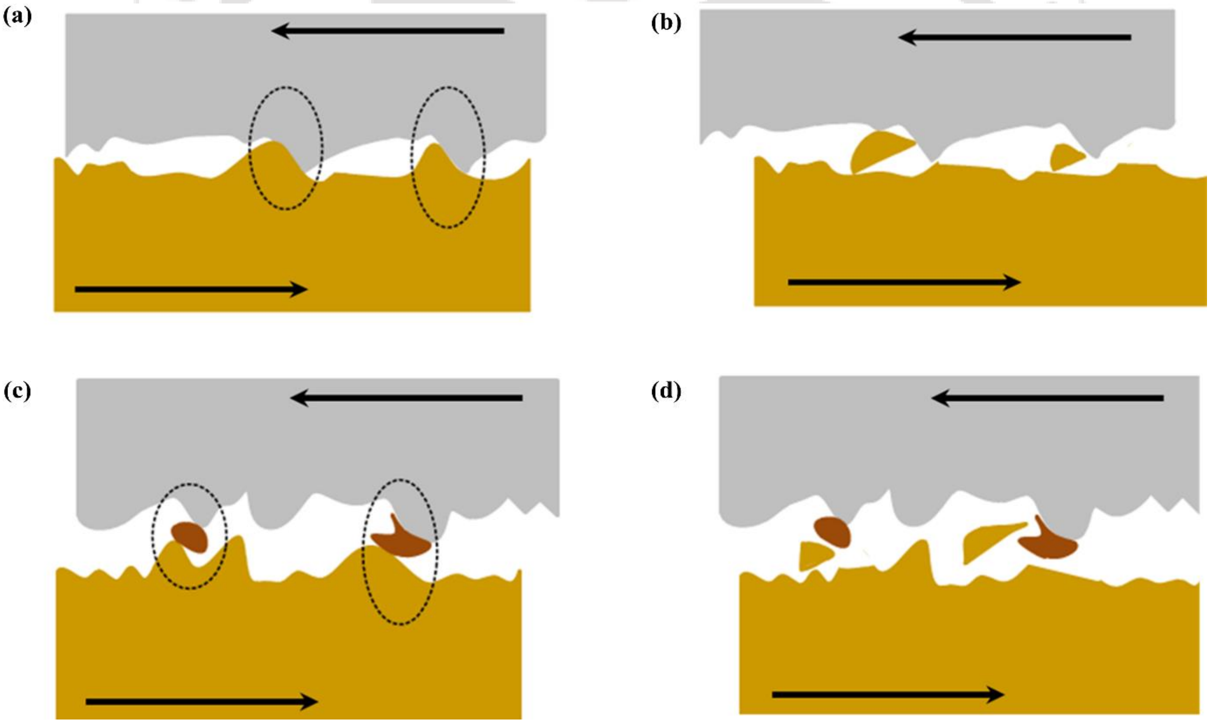

Figure 1.12 Schematic view of abrasion wear (a, b) Two body abrasion and (c, d) Three body abrasion

When the surface moves against each other, progressive loss of substance from operating wear occurs on surfaces, and wear is a slow but continuous process of removal of material. The presence of hard particles or protuberances on the counter surface results in breakage/removal or displacement of material from the other surface, while in contact (sliding and rolling) are responsible for abrasive wear. Hard asperity on the counter surface leads to two-body abrasion (Figure 1.12 (a, b)), while free-moving (sliding and rolling) foreign hard particles between the surfaces in contact lead to three-body abrasion (Figure 1.12 (c, d)).

The adhesive wear takes place on the surface of the relatively moving bodies each other while sufficiently high-pressure present between contacting asperities induced local plastic deformation and adhesion (Figure 1.13 (a, b)).

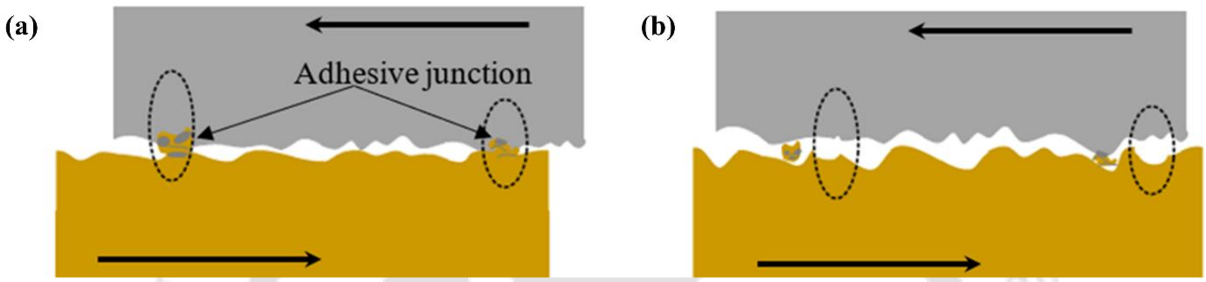

Figure 1.13 Schematic view of adhesive wear

1.10 Lubrication

Lubrication introduces between the contact surfaces lowers heat generation, wear, and resistance to movement (preventing the collision of asperities) by forming a film between contact surfaces. Under external (liquid) lubricating conditions, the lubricating layer/film forms between the interfaces based on operating conditions load, speed, surface properties, elastic deflection, and lubricant characteristics. The process of lubrication is important for machine element interfaces because it regulates friction caused during interactions. Figure 1.14 shows the regimes of lubrication.

Full film lubrication is most common for contact applications wherein excess lubricant separates moving parts entirely; as a result, the wear rate will be very low. Elasto-hydrodynamic lubrication is commonly used for elastic-contact pairs such as ball bearings and gear. Heavy load generates an elastically deforming pressure area which is called the Hertzian contact region, lubricant gets squeezed, and viscosity increases and serves as a solid anti-friction film particular region. The boundary film regime is formed when monomolecular or multimolecular lubricant films and asperities of solid elements dominate at the contact interface. It is basically due to the supply of insufficient lubricants between the contacts, which lacks in filling asperity valleys present on the surface.

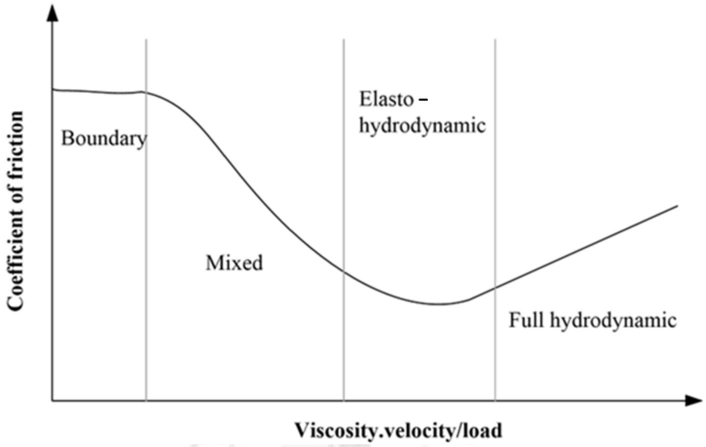

Figure 1.14 Regimes of lubrication

Tribology of polymers: In the case of polymers, weak bonding forces make adhesion, leading to friction. Van der Walls and hydrogen bonds are common in most polymers. Polymers containing the chemical group are connected with hydrogen bonds by electronegative atoms at close range; in the presence of temperature under contact, the polymer molecules move towards the solid surface and align a particular orientation, forming the interatomic bond as an adhesion junction (Sinha and Briscoe (2009)). Polar polymers (polyamide) exhibit high adhesion than non-polar polymers (polyethylene) (Hutchings and Shipway (2017)). When polymer slide against hard metal surfaces, polymer debris is generated, which creates a transfer film avoiding polymer-metal contact.

Effect of temperature on friction: Temperature exposure/heating causes polymer chains and/or bonds to loosen. When the temperature approaches melting, material adhesion and ductility increase due to thermal diffusion and creep, which further results in higher friction. Viscoelastic polymers are more susceptible to frictional heating. However, shear stress decreases when the material melts, resulting in lower friction dominated by the viscous forces in the liquid layer. Material deformation on the actual contact sites and the formation and rupture of adhesive bonds caused the temperature generation at the friction point.

Environmental stress cracking: A chemical agent degrades a plastic resin under stress, and this phenomenon is called environmental stress cracking (ESC). ESC generally causes crazing, cracking etc., in plastic components. ESC generally occurs in amorphous polymers and semi-crystalline polymers like polyethylene, polypropylene, polyamide, and polybutylene. Amorphous polymers or glass polymers have loose structures and hence get disentangled quicker as fluids penetrate easily inside the polymer structure.

1.11 Background and motivation

Polymer gears are being used in many light and medium-duty load applications, including textile, robotics, and food processing, to transmit power and motion. However, the major limitations of polymer gears over metal gears are a lower load-carrying capability and higher wear loss. Several attempts have been made to enhance the load-carrying capability and friction resistance of polymer gears by fiber reinforcement. However, fiber reinforcement increases material inhomogeneity, which in turn affects the shrinkage and micro-geometry of the polymer gear. Most of these applications only involve dry conditions. By utilizing polymer-based materials under the wet lubricant condition, load-carrying capacity can be improved. Very limited research has been carried out on the polymer gears under external lubricant, and hence there is a need to understand the effect of external lubricant on the polymer gear performance. In general, polymer gears in the application are being driven by metallic gear, and there is a need to understand the effect of mating gear material on polymer gear performance.

Bearing materials are generally manufactured through injection molding, and their friction and wear performances have been well understood. In recent years, additive manufacturing is an emerging manufacturing method being considered by many applications due to technical and economic reasons. The injection molding process freezes the material from the outer to the inner surface, forming a soft and ductile skin layer compared to the core material. The selective laser sintered (SLS) manufacturing process can replace the injection process for manufacturing low-volume products with customized design features owing to its shorter manufacturing lead time. The selective laser sintering process is slower than injection molding, forming a hard and brittle surface layer. No attempts have been made to understand the effect of different manufacturing methods (selective laser sintered) on the performance of gearing applications.

To improve bearing performance, the thordon class of materials is also being used under lubricated conditions. This class of materials is a type of elastomeric material developed through the casting process. Elastomeric materials are widely used in bearing applications because of their excellent corrosion resistance, better damping capacity, and tribological properties. Elastomeric materials are extensively being used as bearing material in marine applications; however, no attempts have been made to utilize this class of material for gear applications.

1.12 Objectives

The main aim of the thesis is to understand polymer gears comprehensively, including the effect of lubrication, mating gear material, and manufacturing method.

This objective is being attempted with the following sub-objectives.

- To understand the performance of injection molded polymer gear under dry and oil-lubricated conditions.
- To understand the effect of mating gear material on the injection molded polymer gear at dry and oil-lubricated conditions.
- To understand the effect of the manufacturing method on the polymer gear performance.
- To investigate the feasibility of utilizing bearing material that is currently being used in marine applications for gear application.

1.13 Thesis structure

Chapter 1 provides a brief introduction to gear, polymer, injection molding, selective laser sintering, elastomeric material, and factors that motivate the current research and research objectives are outlined.

Chapter 2 extensively reviews the literature related to the performance of polymer-steel gears under dry and lubricated conditions, – gear pair performance, the sliding contact performance of polymer materials, mechanical and tribological performance of 3D printed materials, the performance of elastomeric materials for bearing are discussed.

Chapter 3 describes descriptions of gear, manufacturing, metrology, the developed gear test rig, methodology, and sliding contact performance evaluation methodology.

Chapter 4 discusses the performance of injection molded polymer gear under dry and oil-lubricated conditions. A detailed discussion on the test gears' life, surface temperature, various failure modes, and failure morphology are discussed.

Chapter 5 discusses the effect of mating gear material on the injection molded polymer gear performance. Frictional, hysteresis heating and adhesion between the contact polymer-polymer gear pair results in failures are discussed. In addition, the lubrication effect on the gear pair performance is also discussed. The gear's life, various failure modes, and failure morphology wear debris are discussed.

Chapter 6 discusses the effect of the selective laser-sintered manufacturing method on polyamide gear performance. Also includes the sliding contact study of different manufacturing methods (IM and SLS) gear materials. The gear tooth surface temperature, various failure modes, failure morphology, and wear debris are discussed.

Chapter 7 deals with the investigation of thordon bearing for gearing applications. Failure modes, contact fatigue performance and wear behavior are discussed. The sliding contact performance of thordon material under dry and lubricated conditions also was evaluated.

Chapter 8 summarizes the research outcomes and the scope for further extension of the work.

Chapter 2

Literature review

2.1 Introduction

This chapter reviews existing literature being reported in the following domains:

- Metal-polymer gear under dry conditions,
- Metal-polymer gear under lubricated conditions,
- Polymer-polymer gear under dry conditions,
- Polymer-polymer gear under lubricated conditions,
- Sliding contact of injection molded /or machined polymer materials,
- Additive manufacturing: Mechanical performance
- Additive manufacturing: Bearing and gear applications
- Elastomeric materials for bearing applications.

The chapter summarizes the various gear pairs' performances, types of failures, reasons for failure, tribological performance based on different contact pairs and based on manufacturing techniques, and factors that encourage and help to design the research and research gaps to be addressed at the end of the present chapter.

2.2 Performance of metal-polymer gear pair under dry conditions

The polymer gear's major limitations over metallic gears are inferior load-bearing capacity and heat accumulation. Researchers have carried out extensive investigations on the design and application of thermoplastic gears, for which frictional and hysteresis heating leads to rapid wear and thermal failure. The viscoelastic characteristics of the polymeric gear contribute to the hysteresis heating and frictional heating caused by the combination of rolling and sliding in the gear tooth meshing. Thus, measurement of the polymer-based test gear temperature during testing is essential for condition monitoring of the test gear.

Tsukamoto (1979) reported the crack initiation in the middle of the gear face width while testing hobbed polyamide gear in pair with metal gear. This behavior is due to the heat dissipation from the sides of the gear tooth compared to the middle of the tooth. The measured metal gear temperature was higher than the polyamide since the thermal conductivity of the metal gear was higher. Tsukamoto (1981) investigated the various module polyamide gear in pair with a steel gear. The heat generated resulted in material flow and formed surface damage on the pitch region. Abrasion on the polymer gear tooth surface was found to depend on the load and sliding velocity. Calabrese *et al.* (1995) substituted polymer gear for metal gear in the diesel engine and correlated it with noise generation. Glass and carbon-reinforcement improved the gear life compared to unreinforced gear (Senthilvelan and Gnanamoorthy (2004)). Reinforced gear exhibited less temperature generation due to improved thermal resistance. The failure surface observed under the microscope revealed that the reinforcement prevented severe thermal damage compared to unreinforced gear.

The performance improvement by making a hole and inserting a steel pin in the gear tooth near the base region was attempted by Kim (2006) to lower the heat accumulation in the polymer gear. It was reported that the polyamide gear tooth temperature was reduced by this proposed method which resulted in a decrement in wear rate and an increment in service life. However, for acetal gear, the proposed method causes plastic deformation, and tooth stiffness results in increased wear due to the brittle characteristics of acetal. The gear operational speed affected the frequency of gear tooth loading, Senthilvelan and Gnanamoorthy (2007). The effect of speed on the polyamide 6 gear was found to be insignificant at the low load. However, at higher loads, speed significantly affects the gear lives. As the load and speed increased, the generated heat at the contact point deteriorated the polymer strength. Only at the low load and all the considered speeds the gear exhibited wear and cracking, but at the higher load levels, the gear exhibited plastic deformation. Research has revealed that the efficiency of polyamide 66 was found to be load-dependent (Senthilvelan and Gnanamoorthy (2009)). During operation, the gear tooth stiffness decreased due to the increase in gear temperature, which resulted in the degradation of the tooth surface and reduction of gear efficiency.

Duzcukoglu (2009a) investigated the effect of gear tooth modification on gear performance. Heat accumulation in gear while subjected to high load and cycles is susceptible to thermal failure and diminishes gear life. The gear modified by altering the ratio (force/face width) improved the heat dissipation and performance. Another research by Imrek (2009) studied the performance of the modifying polyamide 6 gear. The gear was modified by increasing the gear's face width, which resulted in lower temperature generation (10–15 K); consequently, wear also reduced and prevented failure at the pitch region.

Kirupasankar *et al.* (2012) studied the transmission efficiency of polyamide 6 and clay-reinforced polyamide composite spur gears against steel using a power absorption test. The investigation concluded that adding clay particles improved the stiffness and suppressed the visco-elastic nature of polyamide, resulting in higher transmission efficiency compared to polyamide gear. Mertens and Senthilvelan (2016) investigated the operational behavior of polypropylene gear against steel gear. Raised heat generation due to contact stress and deflection resulted in the various damage modes at the different locations at various considered loads. This includes abrasive marks on the tooth surface (face and flank region), sliding marks on the pitch, and plastic flow on the pitch region. Another study on polypropylene gear by Mertens and Senthilvelan (2018) reported that the gear generated substantial noise while operating at higher loading conditions due to higher temperature generation. The failure morphology of the gear confirmed the thermal deformation.

Kodeeswaran *et al.* (2016) investigated the polyamide and steel gear performance under unidirectional and bi-directional loading conditions. The IR camera results reveal that the heat generation was higher under bi-directional loading. The crack propagation in the root region was almost straight and manifested ductile mode failure. Another study by Kodeeswaran *et al.* (2019) reported that higher frequency testing led to the developed overlapped fractured surface on the polyamide gear. Yakut and Duzcukoglu (2014) examined pair of glass-reinforced polyamide-steel gears operating at different speeds and correlated the gear damage to operating speeds. At higher speeds, the gear exhibited a higher temperature, whereas, at a low speed, no damage was observed. The metal gear helps to dissipate the heat from the polyamide gear tooth surface and exhibits stable temperature at all considered speeds.

2.3 Performance of metal-polymer gear pair under lubricated conditions

The use of external lubrication reduces friction, minimizes the generation of frictional heat, and dissipates the heat generated. Lubrication has been extensively used in metal gear pairs to reduce noise, friction, and wear, and sufficient research has been published. However, little research has been published on the case of polymer gear lubrication (oil and water). Oil lubrication improved the hobbed polyamide gear performance (Tsukamoto (1979)). Crippa and Davoli (1995) investigated the polyamide and polyamide composite gear fatigue behavior under different environmental conditions. Lubricated polyamide 6 gears exhibited improved life compared to dry conditions. The steel-glass reinforced polyamide gear pair under oil splash lubrication exhibited severe wear on the polymer composite gear and abrasion on the steel gear surface. The study revealed that steel and glass-reinforced polyamide gear pairs are not preferred. Under higher life cycles, the glass-reinforced-molybdenum-sulfide (MoS_2) composite gear exhibited more wear than carbon composite gear.

Hobbed Delrin and Delrin 500 gear's fatigue performance was examined by Yousef *et al.* (1973) in the presence of grease and oil lubricants. The polymer gear was loaded through the polymer-coated anvil. Gear temperature was measured at two locations: near the pitch and below the root regions. The measured temperature near the pitch was significantly higher than the root temperature. Sliding velocity, as well as contact pressure, were responsible for pitch region heating, whereas viscoelastic straining, as well as the heat transferred from the contact surface, were responsible for root temperature. Lu *et al.* (2019) evaluated polyetheretherketone (PEEK) gear under jet lubrication system. Under light load and dry conditions, the gear exhibited thermal failure due to heat accumulation, causing material degradation (visible in blackish color) and cracking between pitch and root regions. Under lubricated (at light and moderate) conditions, in the initial run periods, the small pit was generated at the tip region owing to a high slide-to-roll ratio. As the test duration progressed, the pit nucleated toward the pitch region. At the end of life, the generated pit causes fracture on the pitch region. In contrast, the gear failed by inadequate root bending strength under high loads, but no thermal damage was observed.

Illenberger and Stahl (2019) investigated steel-PEEK gear pair under jet lubrication at various loading conditions. The progressive growth of pitting on the tooth surface was found to be at higher loading conditions. Under the lower loading condition, the surface damage was degressive on the tooth surface. Yu *et al.* (2020) investigated the durability of steel-PEEK gear pair under oil jet lubricated conditions at various loading conditions. Lubricated gear exhibited significantly less wear under moderate loading; the pitting caused tooth fracture. Illenberger and Stahl (2021) investigated the behavior of PEEK and PEEK composite gear in pair with steel gear under jet lubrication. For temperature measurement, the thermal sensor was inserted below the tooth surface. Results concluded that the maximum temperature rise is less than 6 K. Wear, pitting in composite gear spread over the tooth contact surface, whereas pitting dominates only on the flank region of PEEK gear. Moreover, reinforcement improved the root capacity but deteriorated gear contact performance.

2.4 Performance of polymer-polymer gear pair under dry conditions

Various investigations have been carried out on polymer-polymer gear pairs under dry conditions. Yelle and Burns (1981) estimated the contact ratio of various gear pairs; acetal-acetal showed 60 %, whereas steel-acetal gear showed 75 %. The wear pattern was significantly different in the driver and driven gear for the acetal-acetal gear pair. The tooth on the loading side formed an S-shaped with valleys on the pitch region in the driver gear, whereas the driven tooth formed a complementary S-shaped with ridges at the pitch due to differences in frictional forces (Breeds *et al.* (1993)). The gear wear was significantly dependent on loading, and the load was found to be restricted by the maximum allowable temperature for gear material. Hooke *et al.* (1993) examined the wear performance of the acetal-acetal gear pair and predicted the flash temperature of the polymer gear pair. The predicted flash temperature correlated with gear tooth wear. Mao (2007) also predicted the flash temperature for polymer-polymer gear pair.

A study reported continuous wear measurement near the pitch of the gear region at various loading conditions (Mao *et al.* (2009)). The polyoxymethylene (POM)–POM gear pair exhibited high wear and lower life compared to other gear pairs (polyamide-polyamide, polyamide–POM, and POM–polyamide). POM–POM combination exhibited different wear behavior while running; run-in, linear, and final rapid wear under medium loading conditions. In the initial two conditions (run-in and linear wear), wear was very little. After experiencing gross wear, the surface deformation eventually caused thermal damage. Polyacetal gears exhibited different failure modes based on the loading conditions, whereas polyamide gears exhibited tooth fracture for all the considered loads. Polyamide gear exhibited damage at the pitch and root cracking. The wear in polyacetal gear was significantly low when it was used as the driver. However, when polyamide was used as a driver, the wear in polyacetal gear was high.

Letzelter *et al.* (2010) measured the polyamide gear temperature (polyamide-polyamide gear mesh) at different locations using infrared (IR) camera. Friction and hysteresis contribute to the local thermal softening of polyamide 66 gears. Glass-reinforced polyamide composite gear pair at various speeds was investigated by Yakut and Düzcükoglu (2014). Heat accumulations near the pitch region was observed at all the considered testing conditions. Tooth cracking was observed at the higher speed condition. Machined acetal gear pair performance under constant loading and step loading was evaluated by Mao *et al.* (2015). Instead of taking several weeks and large numbers of gear for endurance testing, the step loading technique offers the advantage of allowing the tests to be finished in hours by utilizing few gear pairs. Initially, the wear in the acetal gear was little, but at the end-of-life, severe deformation and thermal bending were observed. Micrographs of the addendum region of the driving gear tooth revealed adhesive as dominant wear. Frictional heating and sliding velocity are responsible for the wear.

Pogacnik and Tavcar (2015) investigated acetal, polyamide, and polyamide composite gears under different combinations. During testing, the load was applied in accelerated mode (step loads). The pair of polyamide-polyamide exhibited a higher temperature and less life than the POM–POM and POM–polyamide composite gear pairs. Moreover, the gear pair's failure modes are fairly different in some cases at the same loading conditions. The overloading and high heat generation led to thermal failure in gear (polyamide–polyamide). The microscope images confirmed that the wear was the failure in the POM–POM pair. At lower loading, polyamide Glass composite pairs exhibited a lower temperature due to improved heat dissipation. However, at high loading, the effect of reinforcement was not observed, and its service life decreased. Hu and Mao (2017) studied the effect of misalignments in the acetal-acetal gear pairs. Axial misalignment results in deterioration of the tooth surface, and wear debris was observed to be scattered over the dedendum region of the driver's tooth and the driven tooth addendum surface. It was mainly due to the reduction in the overall tooth contact and edge loading. Yaw and Pitch misalignments lead to scoop wear marks and superimposed palisade marks near the pitch and root regions, respectively. Moreover, aligned and misaligned gear pairs generate an almost similar type of wear debris.

2.5 Performance of polymer-polymer gear pair under lubricated conditions

Marshek and Chan (1981) evaluated the acetal worm meshed with polyamide under mineral oil and ethylene glycol environments. Under ethylene glycol, the bulk temperature gear was found to be less than the mineral oil lubrication condition. However, the ethylene glycol lubricant softened and had a corrosive effect on the gear material, causing significant wear. Eventually, all of the gear teeth were shattered which resulted in the slurry form of lubricant. Under oil splash lubrication, both carbon-reinforced polyamide 6 composite gear pairs and glass-MoS_2 polyamide 6 composite gear pairs after ten million cycles exhibited moderate wear. Both gear pairs under grease-lubricated conditions exhibited severe wear (Crippa and Davoli (1995)). Dearn *et al.* (2013) examined the influence of different pressure angles (20° and 30°) on PEEK spur gears under SAE 15W50 lubricant conditions. The results revealed that the 30°

PEEK gear not exhibited pitting even at the higher load, whereas the 20° gear exhibited pitting on the tooth contact surface. The research concluded that the high-pressure angle steel gear is generally not preferred due to less contact ratio and excessive noise; however, PEEK gear exhibited noiseless and superior performance under high load and lubricant environments.

Yu *et al.* (2021) investigated the formaldehyde gear pair performance using micro-topography and tooth profile deviation measurement. The surface topography revealed the formation of the hump in the driver gear on the pitch region. In contrast, a gully formed on the pitch region of the driven wheel. The profile deviation examination confirmed that as the cycles progressed, the hump and gully moved towards the root of the driver and tip of the driven gear, respectively. At the higher load, driver gear tooth breakage and wear on the driven wheel were observed. Collected wear debris was in the form of long strips due to sliding-plowing-cutting action. Entrapped wear debris in the initial stage of operation caused the hump formation on the gear tooth. However, only scratches were found on the tooth surface when the lubricated gears operated at various loads. The tooth profile analysis revealed no significant deviation. Lubrication prevented direct contact between the contact pair and reduced heat generated and improved wear resistance.

Grease lubrication enhanced POM-POM gear pair transmission (Walton *et al.* (2002)). In addition, the dependency of load and speed on efficiency was effectively eliminated with the use of grease lubrication. Another research reported the efficiency and temperature of acetal-acetal gear pair under grease-lubricated and dry conditions at different speeds (Koide *et al.* (2017)). The efficiency and temperature of the acetal-acetal gear pair under grease lubrication and dry conditions were examined at different speeds. Grease lubrication improved the transmission performance (approx. 3–2%) and reduced tooth temperature (approx. 75-70%). Under the dry condition, the frictional heat was found to be dominant, whereas, under grease lubrication, hysteretic heating was dominant to raise the gear temperature. Irrespective of applied loads, the polymer gear, in mesh with a steel gear, showed improved fatigue life and reduced the maximum tooth temperature.

2.6 Sliding contact performance of polymer materials

Several studies have been carried out to understand the frictional and wear performance of polymer against polymer under dry and lubricated conditions. Most of the polymer specimens are injection molded, and very few are machined. Erhard (1983) investigated the tribological performance of various polymeric materials against polymeric material (POM-polystyrene

(PS), POM-POM, POM-PA, PA–polytetrafluoroethylene (PTFE), PA-PA, PA-POM). This work established that the adhesion component of resistance in the contact interface significantly influences the frictional behavior of polymer materials. Another study by Czichos (1983) also reported adhesive as the predominant mechanism when sliding several polymers, polytetrafluoroethylene (PTFE), polypropylene (PP), POM, and polyamide 66, against various polymers acrylonitrile styrene, polystyrene, polymethyl methacrylate. However, abrasive was the predominant mechanism when polymer materials slid against steel. Higher friction was observed under smooth-smooth surface contacts than rough-rough surface contacts due to increased contact area reported by Eiss and Mcann (1993) while investigating the tribological behavior of acrylonitrile butadiene styrene (ABS) material pair using a pin-on-disc configuration.

At slow speed, PEEK material exhibited almost the same friction coefficient under dry as well as water-lubricated conditions against steel; however, polyphenylenesulfide (PPS) material exhibited less friction under lubricated conditions (Yamamoto and Takashima (2002)). Under dry conditions, the polymeric material's transfer layer on the counter metal surface has been observed. However, under water-lubricated conditions, the transfer layer was found to be significantly less. Furthermore, the PEEK-PEEK and PPS-PPS material pair exhibited higher friction under both dry as well as water-lubricated conditions compared to PEEK-steel and PPS-steel contacts at the low-speed condition. Jia *et al.* (2007) investigated the tribological performance of different polymers using a pin-on-disc configuration under dry and liquid paraffin lubricant conditions. The lubricant improved the tribological performance of PTFE and PPS compared to dry conditions. Worn-out surfaces observed under SEM revealed scratch marks on the PTFE specimen and plastic deformation and smooth surface on the PPS specimen. The sliding contact performance of polyamide against polyamide composite and PPS composite was evaluated by Unal and Findik (2008) at various loads and a sliding speed. The friction coefficient of polyamide decreased with an increase in load and then increased again in both conditions when slid against either PPS composite or polyamide composite. However, when polyamide-polyamide composite contacts were used, the variation in friction was not as large as when polyamide-PPS composite contacts were used.

The effect of loads on the sliding contact performance of injection molded polyamide 6 under dry and lubricated conditions against steel was investigated by Srinath and Gnanamoorthy (2007). The friction coefficient under the lubricated condition was higher at the lower load, whereas, at the higher load, the friction was lower compared to the dry condition. The wear rate was found to increase as the load increased under both testing conditions (dry and lubricated). Surface plasticization by water lubricant exhibited increased wear and reduced friction of polyamide. Sanes *et al.* (2007) evaluated the influence of temperature on the sliding contact of PA 6 with steel (AISI 52100 and AISI 316 L) in the presence of an ionic liquid (IL) lubricant. Friction coefficients of 0.11, 0.05, and 0.28 were obtained at -238, 298, and 340 K temperatures against AISI 52100. This behavior can be attributed to the high thermal stability of the IL and to the high polarity of the IL molecules, which become adsorbed into layers on the steel surface. Experiments were performed against AISI 316 L at temperatures -238, 298, and 340 K, with corresponding friction coefficients of 0.14, 0.04, and 0.08 due to the absence of tribocorrosion.

Another study considered water as a lubricant and investigated the tribological performance of injection-molded polyamide–steel contact (Meng *et al.* (2009)). It is reported that the friction reduced in the presence of water lubrication; however, wear resistance was found to be poor. Under dry conditions, rough and plough marks on the worn surface were mainly due to adhesion. However, the lubricated surface exhibited exfoliating and crack features primarily due to a reduction of strength and hardness. In this research, oil was considered lubricant, and the tribological performance of nitrogen-implanted polyamide was investigated. Implanted polyamide was able to lead to the retention of oil on the surface, which lowered friction (Kalacska 2012)). Kim *et al.* (2012) investigated the sliding contact performance of polyamide 12 composites, and the wear resistance of the material was found to be influenced by the load. In reinforced polyamide, the fiber alignment direction had less influence on the tribological performance, but the amount of fiber content and the loading had a significant influence. In a study by Sułek *et al.* (2013), the influence of water and 1% aqueous solutions of alkyl polyglucosides (APG C_8–C_{10} and APG C_{12}–C_{14}) on the tribological behavior of PA were investigated. Results from these tests showed that the friction coefficient value was 0.08 in the presence of water, whereas 0.05 was in the presence of solution. Wear was also observed lesser in the presence of solutions compared to water. The wettability angle was less for the solution than for water which could be the reason for less friction and wear.

2.7 Additive manufacturing: Mechanical characteristics

In recent years, due to technical and economical advantages, additive manufacturing processes can replace many conventional polymer processes including injection molding and extrusion. Several works have been carried out to understand the effect of the manufacturing process viz injection molding (IM) and selective laser sintering (SLS) over the mechanical and fatigue properties. Blattmeier *et al.* (2012) investigated the fracture toughness of SLS and IM specimens. Higher fatigue life and lower deformation rate were exhibited by the SLS-processed specimens compared to IM specimens. Additionally, the SLS specimens exhibited significant resistance to crack formation and propagation, whereas the injection-molded specimens failed owing to severe deformation. Athreya *et al.* (2011) reported that the impact strength of SLS-processed polyamide was lower than extrusion-IM-processed polyamide. The crystallinity, as well as some spherulite structure of the SLS material, could be the reason for this inferior impact strength.

Dupin *et al.* (2012) investigated the mechanical performance of IM and SLS materials using a 3-point bending configuration. It is reported that the flexural modulus of SLS material was found to be more compared to IM material because of the high crystal weight portion. The aging characteristics of the IM and SLS material stored in different environments (dry, 50% humidity, and fully immersed) for various durations were investigated by tensile testing (Goodridge *et al.* (2010)). Van Hooreweder *et al.* (2013) correlated the thermal and hysteresis behavior on the damage mechanism of the SLS and IM specimen while subjected to tension-compression fatigue loading.

Zhu *et al.* (2015) evaluated the mechanical performance of SLS polypropylene and presented a comparison with IM polypropylene. The SLS-processed material exhibited a less dense surface than IM. SLS material exhibits higher strength and storage modulus than IM material owing to the higher crystallinity of the SLS specimen. The SLS material exhibited higher crystallinity due to the slow cooling process in SLS compared to the injection-molded process. This enhanced crystallinity is responsible for the improved strength and modulus of the specimens. Wu *et al.* (2018) investigated the performance of SLS-fabricated polyamide and compared it with compression-molded polyamide. However, the SLS material exhibited poor mechanical performance compared with compression molding but acceptable performance. The presence of high laser energy caused chain scission of macromolecules. Athreya *et al.* (2011) reported that the impact strength of SLS-processed polyamide was lesser than extrusion-IM-processed polyamide. However tensile as well as flexural strength of SLS polyamide was higher than extrusion-IM polyamide. The crystallinity, as well as some spherulites structure found in the SLS could be the reason for the lower impact strength of SLS material. Telenko and Seepersad (2012) investigated the energy consumption while manufacturing the polyamide specimen during IM and SLS process. It is reported that energy could be saved by using the SLS method for small-scale manufacturing.

SLS polyamide specimens were manufactured using different machine configurations (Stichel *et al.* (2017)). Optical Microscopy (OM), Differential Scanning Calorimeter, and X-ray computed tomography (CT) techniques were utilized to characterize SLS polyamide microstructure details. It was reported that the mechanical performance of SLS material was affected significantly based on machine configurations. SLS material exhibited quite brittle in the printing direction. OM and CT microscopies confirmed the presence of different percentages of porosity, partially molten particles aligned on the layers. Unfused particle cores created in SLS-processed material lead to composite-like structures, resulting in deviations in mechanical characteristics (Zarringhalam *et al.* (2006)). The material processed at a high energy source reduced the unfused core volume and improved the mechanical performance compared to a low energy source processed specimen. If the cooling rate is slow, SLS can result in producing stronger polyethylene parts (Bai *et al.* (2016)). In the SLS process, a slight bed temperature difference (3 K) results in agglomeration and substantial cracking, whereas at a sufficient temperature, the powder spreads properly and prevents crack formation in poly (butylene terephthalate) material (Arai *et al.* (2017)).

The fatigue performance of polyamide 12 processed material was investigated by Amel *et al.* (2016). Under the tension-tension mode, the brittle mode was exhibited by the fractured specimen. However, under the tension-compression loading condition, the ductile mode was exhibited by the fractured surface. In another study, the effect of thermal conditions on the fatigue performance of SLS process polyamide was evaluated (Salazar *et al.* (2014)). To understand the failure mechanism, the SEM characterization technique was adopted. Specimens exposed to room temperature (296 K) and below room temperature (233 K) failed due to the crazing followed by ligaments tear. More dimple areas formed across the fractured surface owing to greater elongation by crazing at room temperature. SLS polyamide subjected to tension-compression high cycle fatigue at different frequency levels reveals ductile or brittle mode failure. At the high-frequency level, since the generated temperature exceeds the glass transition temperature, material stiffness was significantly reduced, and the mode of failure was ductile mode. However, when the material is loaded at the low-frequency level, the generated temperature does not reach the glass transition temperature, and cracks originate from unfused particles of the specimen, resulting in brittle mode failure (Van Hooreweder and Kruth (2014)). The tensile and fatigue performance of SLS polyamide was evaluated (Van

Hooreweder *et al.* (2010)), and the specimen temperature was also monitored during the fatigue testing. The measured temperature showed an increase in trend at the higher load until failure, whereas at the lower loading, the variation in temperature was approximately ±1.2 K. At higher load conditions, material rigidity was reduced, which resulted in localized peak stress at deflect/impurities sites that subsequently led to cracking and eventual failure. Ajoku *et al.* (2006) investigated the flexural, tensile, and compression performance of SLS polyamide. The flat-built configuration specimen reveals superior tensile, compressive strength, and modulus due to the strong bonding between the powders than other configurations.

2.8 Additive manufacturing: Bearing and gear applications

Few researchers have evaluated the frictional and wear performance of polymeric materials which are fabricated with different additive manufacturing methods. Bai *et al.* (2015) examined the effect of the surface orientations (top/side) on the tribological performance of polyamide. The top surface indicates the parallel to the powered bed, and the side surface indicates the perpendicular to the powder bed. The side surface exhibited a lower frictional coefficient than the top surface. Palma *et al.* (2019) attempted to evaluate the macroscale frictional behavior of Multi Jet Fusion processed polyamide with reciprocating testing configuration. The friction coefficient of the horizontally built polyamide exhibited similar performance in all the sliding directions. On the other hand, the friction of vertically built polyamide increased when the sliding direction varied from 0° to 90°.

The reciprocating sliding contact performance of Fused deposition modeling (FDM) processed polylactic acid pin and plate contact was investigated by Zhang *et al.* (2020). The plate was fixed in two ways: the built direction of the plate fixed along the sliding direction, and the built direction of the plate fixed perpendicular to the sliding direction. No significant difference in friction coefficient was found in both conditions. In both conditions, the measured temperature was found to be increasing with sliding time. All tribological characteristics (friction, wear, and temperature) increased with increasing load. Amirruddin *et al.* (2022) found that the higher layer thickness results in lower friction force in the FDM-processed polylactic acid (PLA) and acrylonitrile butadiene styrene (ABS). The ABS material's wear resistance was higher than the PLA. During testing, heat generated by friction did not affect the hardness of ABS material till 379 K, but PLA material hardness was affected even at 330 K.

Few research investigations have been carried out on the fatigue performance of additively manufactured gears under dry conditions. Zhang *et al.* (2020) investigated the FDM-processed different variants of polyamide gear pairs under dry conditions and compared them with injection-molded polyamide 66. It was reported that the worn gear tooth surface of the FDM-processed polyamide 618 surfaces not exhibited any peel-off; however, another variant polyamide gear surface exhibited peel-off, which indicates weak bonding between layers. Polyamide 618 gear exhibited superior performance than injection molded gear. The performance of PLA, ABS, and PA66 gears was processed by the fused filament fabrication method and studied by Dennig *et al.* 2021. Gear surface damage was not influenced by the gears' printing quality and geometrical accuracy, but the material's friction behavior was responsible for the surface damage. The frictional heat reduced the strength of ABS gear, which can only operate under low-loading conditions. However, polyamide gear exhibited higher life compared to ABS gear, whereas PLA gear was not found to be suitable for gear applications. In polyamide and ABS, the damage was found to be root breakage, whereas PLA gear failed by material melting. Harsha *et al.* (2021) evaluated the wear performance of FDM-processed three polymers' gears (ABS, PLA, and polyamide) against steel gear at various speeds. Among all the tested gears, the polyamide gear exhibited lower wear. All the tested gear exhibited tooth damage, but breakage across the hub region was also observed in PLA gear. Tunalioglu and Agca (2022) investigated the PLA, ABS, and polyethylene terephthalate (PETG) spur gear manufactured by the FDM method. The PFTG gear exhibited better performance due to higher ductility and toughness than ABS and PLA.

2.9 Performance of elastomeric materials for bearing application

Elastomeric materials in bearing applications have been in use, particularly, thordon grade materials are extensively used in marine applications. This class of materials possesses good sliding wear resistance, high pressure-velocity limit, dimensional stability, chemical resistance, ease to machine, and better shock absorbance capacity (Thordon elastomeric bearings engineering manual version: 2022.1). Thordon COMPAC, ThorPlas, Thordon XL, and Thordon SXL are commercially available grades of elastomeric-bearing materials that are frequently used. Thordon SXL is preferred because of its low frictional coefficient, smooth service, excellent load distribution, and dry start-up capacity (World pumps (2006)). Substantial investigations have been done on thordon materials to study frictional and wear performance under dry and lubricated conditions. thordon XL and LgSn80 bearing materials were evaluated for tribological performance under dry and oil-lubricated (SAE 140 and SAE 30) environments using a block-on-ring configuration (Fernandez *et al.* (1996)). At the heavier load, the thordon XL material exhibited a sharp increase in wear due to a reduction of shear strength caused by higher heat generation. Both the considered materials exhibited better resistance under SAE 140 lubricating oil than SAE 30.

The tribological characteristics of the ThorPlas material in contact with a stainless-steel shaft were studied by Ren and Feng (2011). Under lubricated conditions, the friction coefficient was higher and increased with the slide time. The friction coefficient was low and stable with slide time under dry conditions, and wear measurement revealed the adhesive behavior. ThorPlas can be employed with oil lubrication in Kaplan turbine blade bearing applications. ThorpPlas can also be utilized in pumps for high-speed and low-pressure purposes. Berglund and Shi (2017) investigated the tribological performance of ThorPlas material using a reciprocating configuration. Under water lubrication, ThorPlas material exhibited higher wear and friction compared to dry conditions due to the transfer of carbon content from ThorPlas material to the counterface. The investigation by Rodiouchkina *et al.* (2018) revealed the effect of sliding velocities and loads on ThorPlas material. The material exhibited lesser friction at lower velocity for all the considered loads. The wear rate coefficient was also less at the lower velocity. The transferred polytetrafluoroethylene over the counterface acted as a lubricant layer and reduced friction at the high load. The tribological performance of polyurethane–polyethylene wax (PEW) based material at various water temperatures and loading conditions was investigated and compared with polyurethane and thordon material by Huang *et al.* (2021). The transfer layer formed due to the melting of PWE between the contact results in a smooth worn surface than thordon material. The effect of speed, load, and inlet coolant velocity on the heat generation of the thordon XL bearing system was studied by Zhang *et al.* (2021).

2.10 Summary

Good amount of research work has been carried out on polymer gear under dry conditions, and extensive work has been published, including efficiency, failure, failure modes, flash temperature calculation, the effect of speeds, and life. Detailed investigation of the failure morphology, including failure locations on the tooth surface and prediction of tooth contact temperature for metal-polymer gear pairs under lubrication have not been conducted. Very limited investigations on polymeric gear under oil-lubricated conditions have been reported. Hence, it is necessary to conduct a comprehensive investigation of polymeric materials under external (oil) as well as to examine the effect of mating gear material.

Sufficient investigation on mechanical and fatigue performance was carried out on selective laser-sintered materials, but they are at specimen level. Only one work has been carried out to understand the tribological performance of selective laser sintering materials, and very few have examined FDM-processed materials under dry conditions. None of the work examined the effect of different manufacturing methods on the sliding contact performance under dry and lubricated conditions. Very few studies on FDM-processed gear fatigue performance were investigated. However, except for Zhang *et al.* (2020), no comparative investigation has been done on polymer gear fatigue performance with different manufacturing methods. However, the durability of laser-sintered polymer gears has not been investigated yet.

Extensive research has been done on the tribology of elastomeric materials for bearing application. Furthermore, many thermoplastic materials have been studied for gearing applications. However, investigations on the elastomeric (thordon) material for gearing applications have not been attempted so far.

Chapter 3

Materials and methodology

3.1 Introduction

The evaluation of surface durability performance includes investigation of the thermal performance, failure morphology, tribological performance, and life curve. In the case of polymer gears, loading causes frictional and hysteretic heating, which considerably increases the gear temperature and wear. Improvement in polymer gear durability performance using oil lubrication was observed (Crippa and Davoli (1995)). A significant reduction in friction coefficient was observed in polymer contact applications (Jia *et al.* (2007)). External lubrication was considered for gear application. Hence, the effect of the lubrication on the gear application in detail is also analyzed. Injection molding is identified as the most economical process suitable for manufacturing thermoplastic gear on a large scale. Polyamide's good mechanical properties, strength, and damping characteristics make it to be used in many engineering and gear applications. Additive manufacturing has the potential to manufacture complex geometry. As mentioned earlier, most of the plastic components are fabricated using the injection molding process. But recent research has drawn interest in the area of selective laser sintering methods in many industries and research organizations for developing and designing products for compatibility with different engineering/functional applications. Recent research on SLS exhibited improved mechanical strength, stiffness, and complex structure. Various engineering materials, including polymer, elastomer, etc., have been extensively performing very well in different contact applications such as rolling, sliding, and a combination of both rolling-sliding. This chapter covers following

- Gear geometry and parameter
- Gear manufacturing
    - Injection molded gear
    - Selective laser sintered gear
    - Hobbed gear
- Gear Metrology
- In-house developed power absorption gear test rig
- Gear testing methodology

- Sliding contact performance: Specimen
- Sliding contact performance: Methodology
- Environmental stress cracking: Specimen and methodology

3.2 Gear parameters and geometry

Table 3.1 and Figure 3.1 present gear parameters and geometry.

Table 3.1 Gear parameters

Parameters	**Mating gear** (Driver)	**Test gear** (Driven)
Pressure angle (°)	20	
Module (mm)	3	
Number of teeth	18	
Pitch circle radius (mm)	27	
Root fillet radius (mm)	1.14	
Outer circle radius (mm)	30	
Face width (mm)	8	4
Materials	Hobbed steel/Injection molded polyamide66	Injection molded polyamide 66/Selective laser sintered polyamide 12/ Hobbed thordon SXL

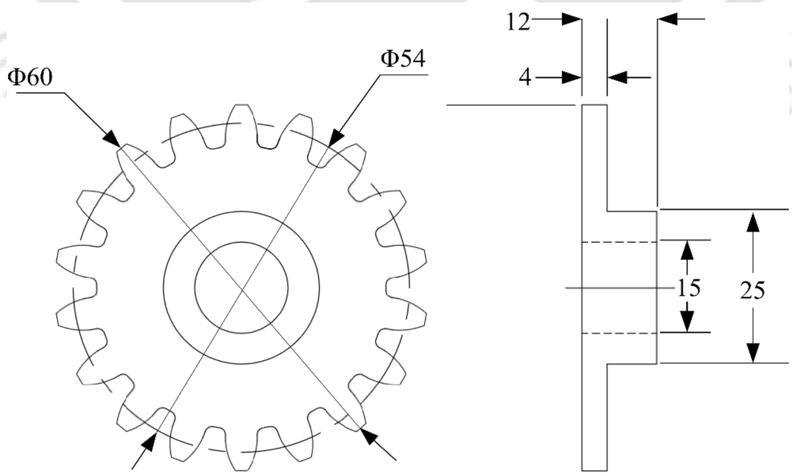

Figure 3.1 Gear geometry

3.3 Gear manufacturing

This work considered injection molding, selective laser sintering, and hobbing manufacturing processes for manufacturing test gears.

3.3.1 Injection molding

Polyamide 66 was considered as a material for injection molded gears. Injection molding of the driver and test gear was carried out using an injection molding machine (DGP Windsor, ST50) at Just Preci Comps, Thiruvananthapuram (Figure 3.2). Plastics absorb moisture from the atmosphere, and the quantity of moisture that plastics collect from the atmosphere varies depending on the type of plastic (Tsukamoto (1995)). It was essential to remove the moisture that the pellets had been holding. In order to prepare the pellets for injection molding, pellets were preheated at 353 K for 4 hours and desiccated. The injection pressure was maintained at 7 MP throughout the molding process, and the barrel's four heating zones deviation were kept about 558, 563, 568, and 573 K respectively. The injection molded driver and test gear are shown in Figure 3.3 (a) and (b).

Figure 3.2 Injection molding machine

A stylus-type perthometer (Mitutoyo Surftest SJ-140) was used to measure the test gear roughness depicted in Figure 3.4 (a). The gear surface and measured plot are shown in Figure 3.4 (b) and (c). The gear average roughness was found to be 0.90 µm.

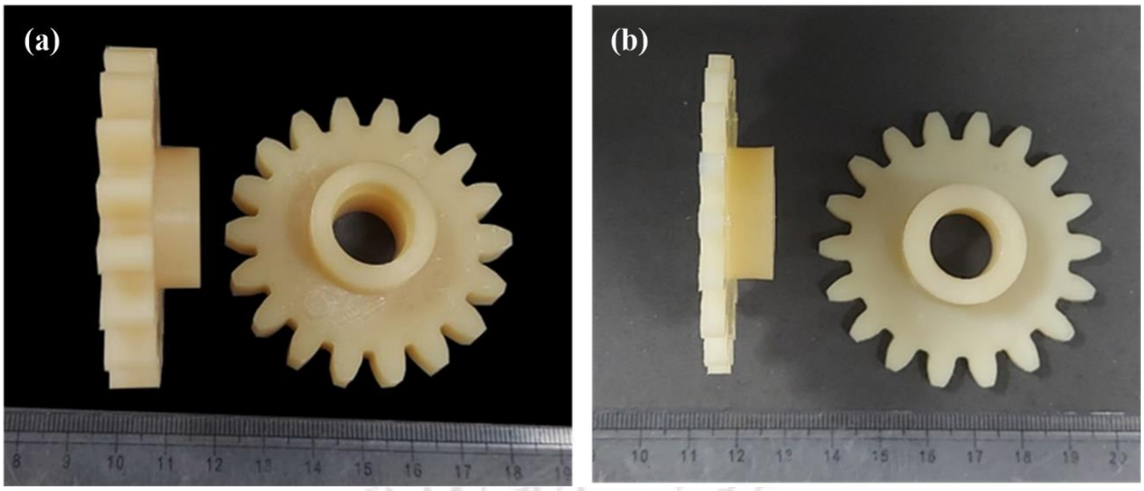

Figure 3.3 (a) Driver gear and (b) Test gear

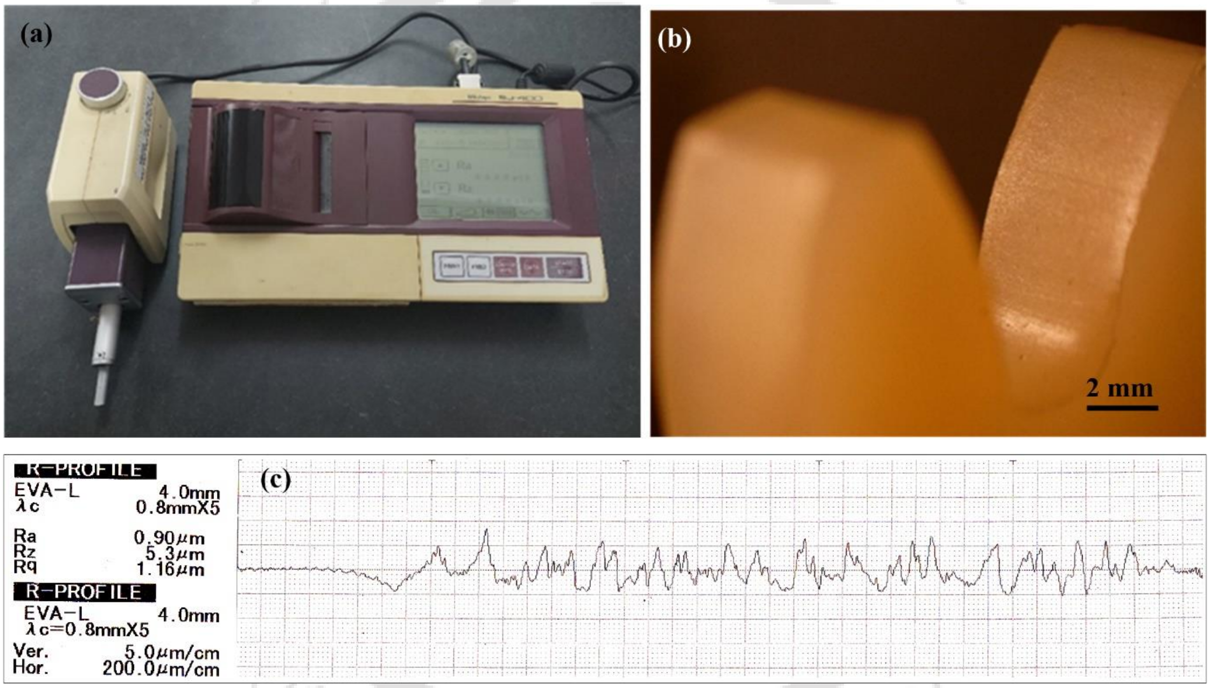

Figure 3.4 (a) Stylus-type perthometer (b) Injection molded gear tooth surface and (c) Injection molded test gear roughness plot

3.3.2 Selective laser sintered gear

Polyamide 12 was chosen as the gear material for selective laser sintering. It has been reported that polyamide-based polymer material holds 95% of the selective laser sintering market; polyamide 12 is the most commonly used polymer (Kruth *et al.* (2008)). The wide processing temperature window is the main factor behind polyamide 12's widespread use. A processing temperature window that affects the crystallization rate that can lead to shrinking and distortion. Having a broad temperature window lowers deviation in end parts by facilitating slow crystallization (Goodridge *et al.* (2012)). Sinterstation 2500 + was used to fabricate the selective laser-sintered polyamide spur gear at PSG TIFAC-CORE,Coimbatore (Figure 3.5 (a)).

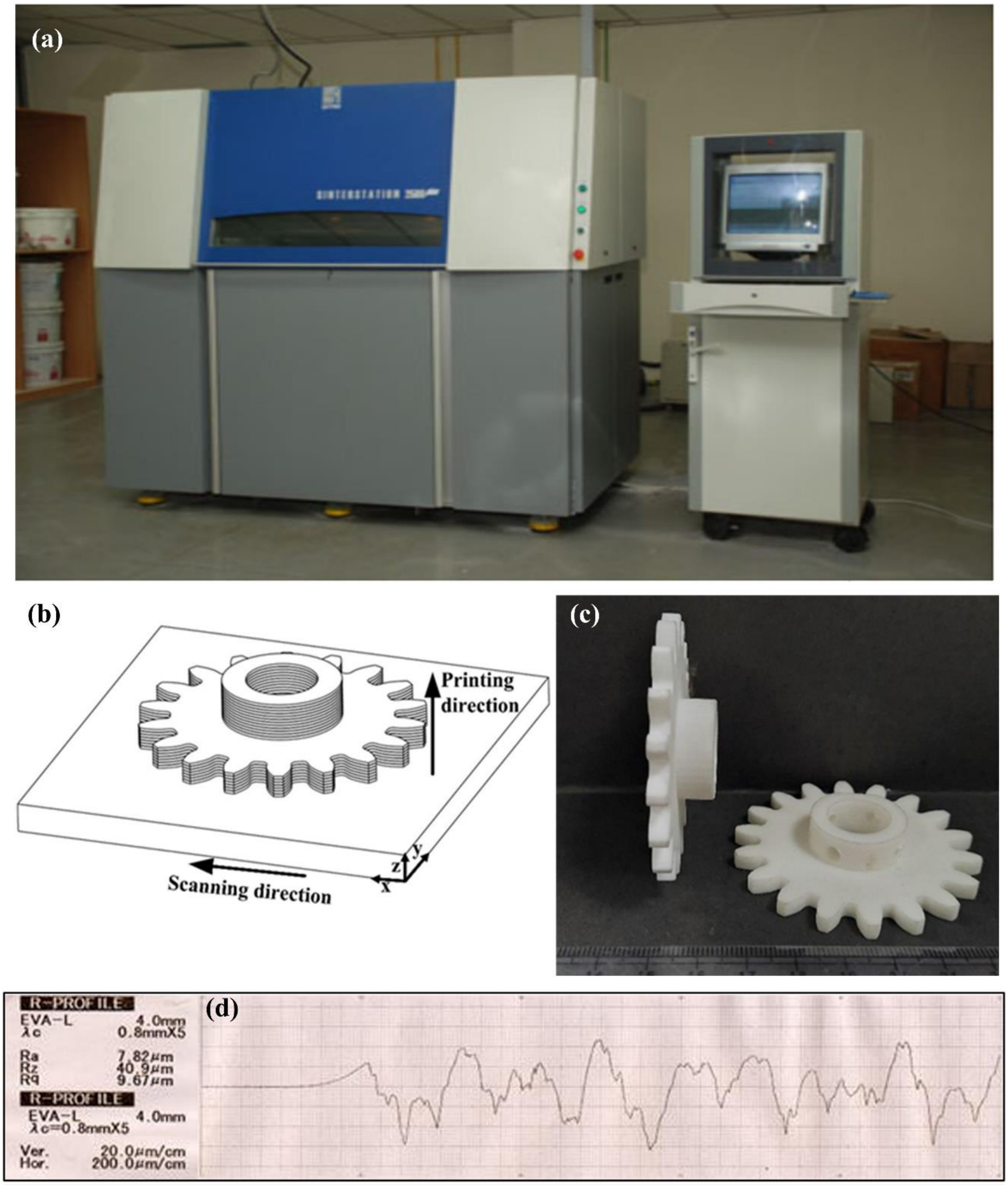

Figure 3.5 (a) Sinterstation 2500+ selective laser sintering machine (PSG TIFAC-CORE, Coimbatore) (b) Flat built configuration surface, (c) Selective laser sintered gear and (d) Selective laser sintered gear roughness plot

During the gear fabrication, the bed temperature, scanning speed, and laser power were fixed at 405 K, 5 m/s, and 12.5 W, respectively. Additionally, the beam diameter and powder layer thickness were set to 0.45 and 0.10 mm, respectively. For the process of sintering, specifications recommended by manufacturer were applied. Sintering was performed according to ISO/ASTM 52921 and followed the coordinate system direction axes of x, y, and z outlined in ISO/ASTM 52921. Accordingly, the x-axis and the build platform's front edge should be parallel. The z-axis must be perpendicular to the build surface because it follows the surface normal. Gear sintering follows a scan direction along the x-axis, and layer building follows a build direction along the z-axis. The gear was built in a flat configuration, with the gear body resting on a built platform and layers deposited along the face width, and the schematic illustration of SLS gear on the built platform is depicted in Figure 3.5 (b). Figure 3.5 (c) shows the images of SLS gear. The SLS gear tooth roughness was measured by moving the stylus probe perpendicularly to the layer orientation and found to be 7.82 µm (Figure 3.5 **(**d)**).** In the additive manufacturing process, due to the staircase effect roughness was found to be higher than the injection molded gear.

3.3.3 Hobbed gear

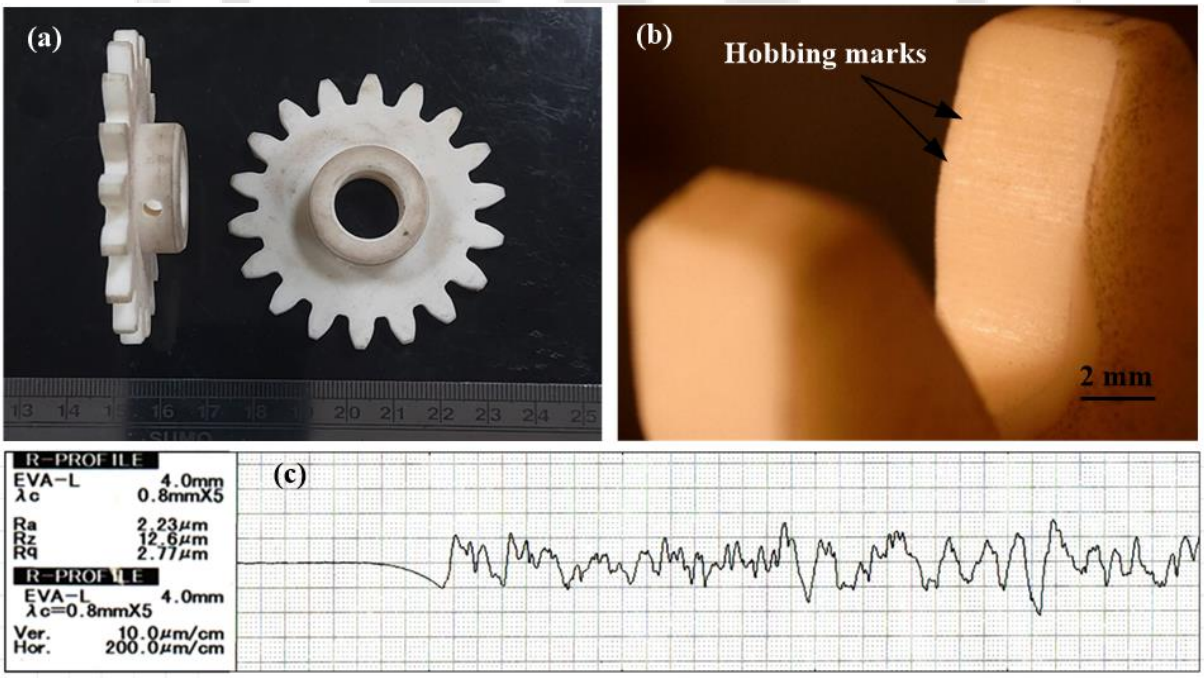

Figure 3.6 (a) Hobbed thordon gear (b) Gear indicating hobbing marks and (c) Thordon gear roughness plot

Thordon SXL material was received in cast rod form dimension of ϕ 70 mm from Thordon Bearing Inc., Canada. The thordon rod was hobbed into the spur gear and considered as test gear. The hobbing was carried out at Sakthi Drives Specialists in Gears and Gearboxes. The hobbed thordon test gear and surface measured plot are shown in Figure 3.6 (a-c). Figure 3.6

(b) revealed the machining marks on the test gear tooth surface formed owing to hobbing process resulting in the roughness being higher than the injection molded gear. The gear average roughness was found to be 2.23 µm (Figure 3.6 (c).

3.4 Gear Metrology

Gears were examined using a gear measuring system (Mahr GMX 275 C) with the support of Perfect Gears Pvt Ltd, Chennai to determine the effect of various manufacturing techniques on the gear tooth profiles and gear tooth metrological accuracy. Gear tooth profile and lead deviations were measured on both flank surfaces of three evenly spaced teeth. On the right side, the average deviation between the two teeth has been taken into consideration. Deviations were measured using DIN 3962 (1978). The deviations along the tooth profile from tip to root were measured as total involute profile (Fa) deviation, involute slope deviation (FHa), and form deviation (ffa). In contrast, the geometric deviations of total lead deviation (Fb), lead slope deviation (FHb), and lead form deviation (ffb) were measured along the face width normal to the tooth profile.

Figure 3. 7 Mahr GMX 275C (Perfect gears, Chennai)

Figures 3.8, 3.9, and 3.10 show the involute profile and lead profile deviation of injection-molded gear, selective laser sintered gear, and hobbed thordon gear. Figures 3.8, 3.9, and 3.10 indicate the involute profile and lead deviation of three teeth (teeth 1, 7, and 13) on the left and right flank surfaces. The involute profile and lead deviations are shown in a single plot for three teeth (tooth numbers 1, 7, and 13). It was observed that no appreciable profile deviations between the left and right flanks or among teeth. Hence, on the right side, the average deviation between the two teeth has been taken into further discussion. The total involute profile deviation (Fa) for injection molded polyamide, selective laser sintered, and thordon are 104.95 μm (DIN 12), 31.35 μm (DIN 10), and 77.4 μm (DIN 12). The profile slop deviations (FHa) are -112.15 μm (DIN >>12), 31.15 μm (DIN 11), and -74.5 μm (DIN >12) for injection molded

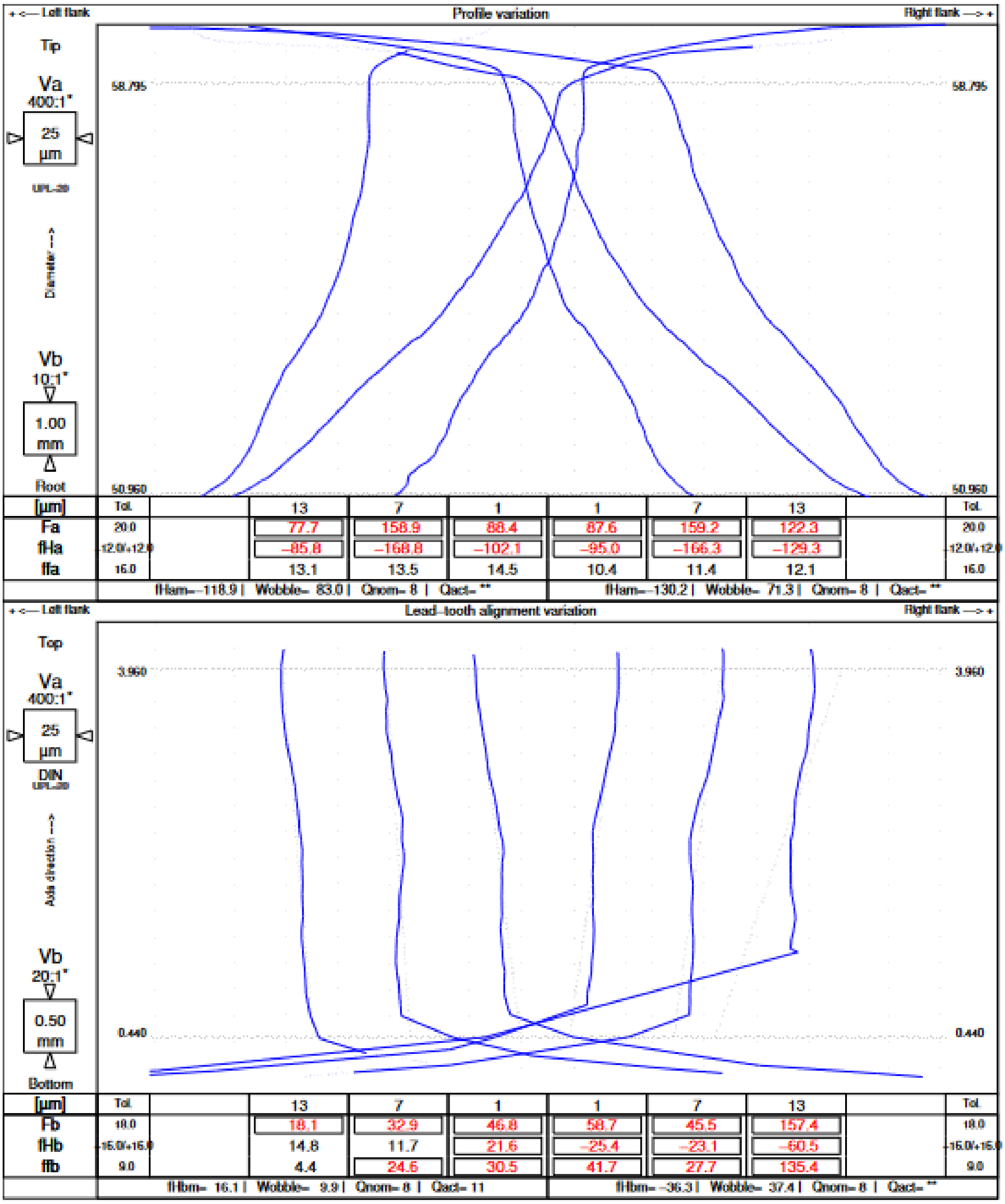

Figure 3.8 Involute profile deviation and lead deviation plot for injection molded polyamide gear

gear, selective laser sintered gear and hobbed thordon gear. The selective laser sintered gear exhibited less involute profile deviation than the injection molded and machine thordon gear. The slow cooling rate in selective laser sintering reduces the shrinkage in the gear tooth involute profile and helps to achieve a near a perfect profile. Van Hoorewedere *et al.* (2013) reported that the cooling time for injection molding and selective laser-sintered processed parts were 30 s and 12 h, respectively. During selective laser sintering, preheating and postheating

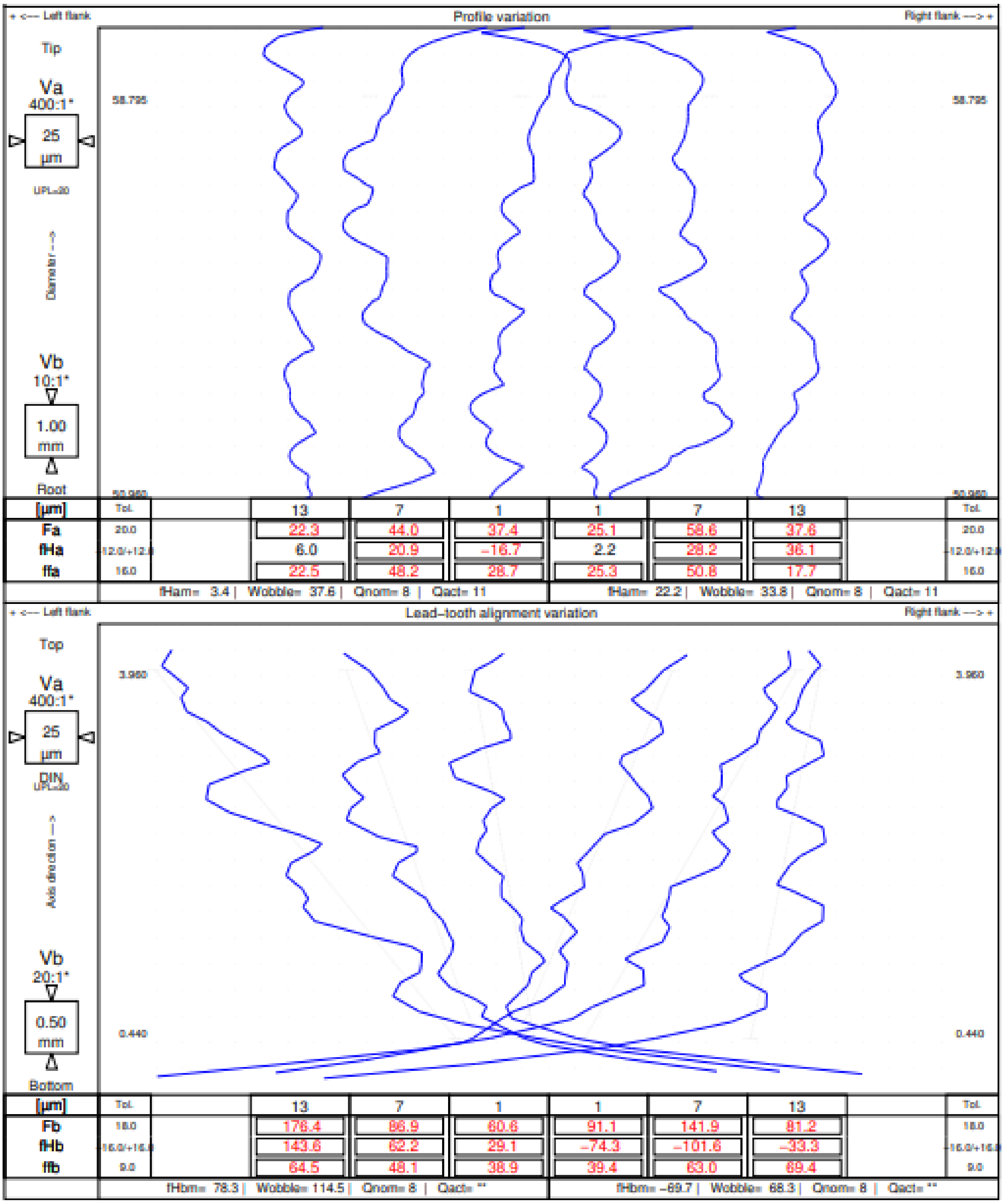

Figure 3.9 Involute profile deviation and lead deviation plot for selective laser sintered gear

of powders avoid the shrinkage in parts reported by Kruth *et al.* (2008). Machined gear also exhibited a better profile (Fa and FHa) due to the absence of the shrinkage effect. The involute form deviation (ffa) confirmed qualities 11.75 µm (DIN 8), 21.5 µm (DIN 9), and 16.65 µm (DIN 9) for injection molded polyamide, selective laser sintered polyamide and machine thordon, respectively. Due to the smooth surface, the involute profile form deviation is less in injection-molded gears than in selective laser-sintered and machined gears. Layer orientation and machined marks on the gear tooth surface deteriorate the surface smoothness causing an increase in the involute form deviation.

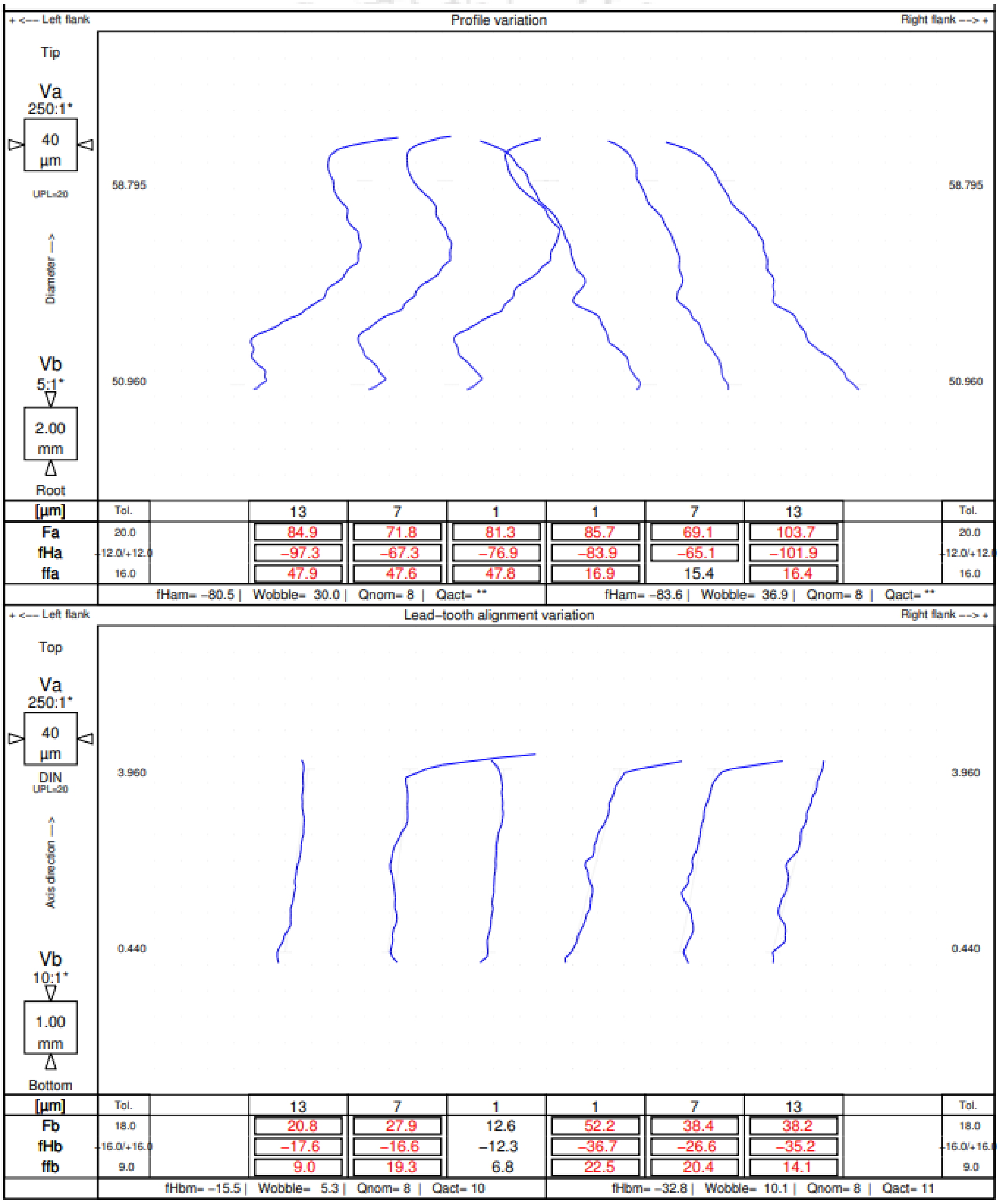

Figure 3.10 Involute profile deviation and lead deviation plot of thordon machined gear

The total lead deviation (Fb) for injection molded polyamide, selective laser sintered polyamide, and machined thordon are 52.1 µm (DIN 11), 86.15 µm (DIN 12), and 38.3 µm (DIN 10), respectively. The lead slope deviation (FHb) is -24.25 µm (DIN 9), -87.95 µm (DIN 12), and -35.95 µm (DIN 10) for injection molded polyamide, selective laser sintered polyamide, and machined thordon, respectively. Similarly, lead form deviations (ffb) are 34.7 µm (DIN 11), 66.2 µm (DIN >12), and 21.45 µm (DIN 10). The selective laser sintered gear showed a higher lead deviation than injection molded polyamide and machined thordon. As mentioned earlier, the layers were deposited along the face width of the gear tooth. Since the layer deposition does not coincide with the lead direction, an appreciable difference in measured quality was found. The machining marks in the thordon gear tooth along the direction of the face width of the gear result in better quality than selective laser gear.

3.5 In-house developed power absorption gear test rig

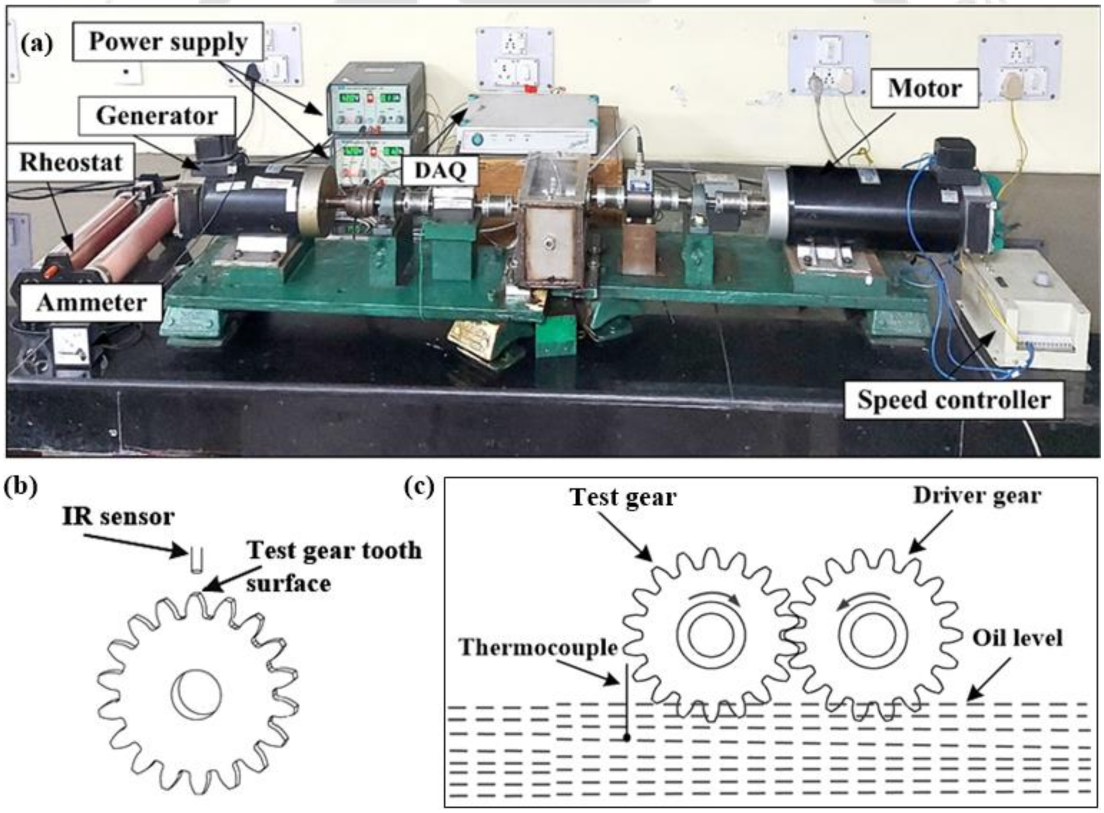

Figure 3.11 (a) Test rig developed in-house (b) Schematic illustration of IR sensor position from test (polymer) gear tooth surface and (c) Schematic illustration of the gear mesh and thermocouple position

The polymer test gear was evaluated on an in-house developed power absorption rig, as depicted in Figure 3.11 (a). The driver stainless steel (AISI 316) gear was connected to the permanent magnet direct current (PMDC) of the 3-HP motor, which can rotate at a maximum speed of 1500 rpm. The polymer test (driven) gear was loaded through a rheostat which was connected to a PMDC 1HP generator. The driver steel gear was meshed with the driven test gear for easy heat dissipation. Steel has higher thermal conductivity than polyamide. It is possible to dissipate the generated heat in the steel-polyamide gear pair contact region to some extent by using steel gears. The setup also consisted of two torque sensors (HBM T20WN accuracy; ±0.2 %) that measure input and output torque. A non-contact infrared (IR) temperature sensor (Raytek, MIDI10LT, accuracy; ±1 °C) was fixed 5 mm from the polymer gear tooth surface to measure its temperature. A data acquisition system (HBM Spider 8) was employed to record data generated by the sensors at a rate of 10 Hz. Figure 3.11 (b) depicts the IR sensor location from the test gear tooth surface. A stainless-steel reservoir was employed to store and supply lubricating oil to the test gear via splash lubrication. Shafts (driving and driven) were supported by bearings installed on each side of the reservoir. A transparent acrylic cover was placed on the top of the reservoir to prevent lubricant splashing outside and to make it possible to observe the gears during running. An arrangement has been made on the acrylic cover to hold the temperature sensor and allow for thermocouple insertion. The thermocouple was fixed at 15 mm below the oil level to avoid the effect of the environment. Figure 3.11 (c) schematic illustration of splash lubrication configuration. Figure 3.12 shows the close-up view of the gear mesh, torque sensor, data acquisition, and rheostat.

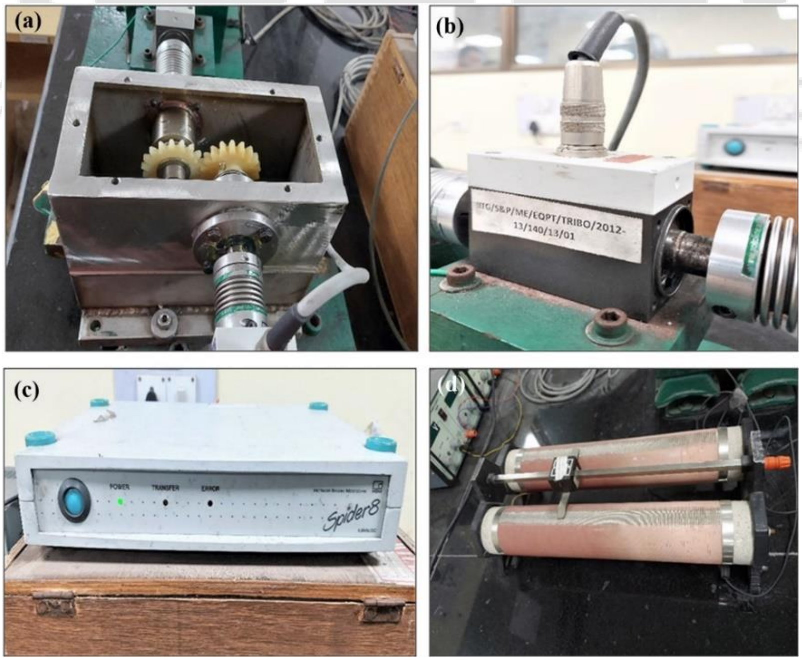

Figure 3.12 Closed-up view of gear mesh, (b) Torque sensor, (c) Data acquisition, and (d) Rheostat

3.6 Gear test methodology

The gear tests were performed at applied torques 1.8, 2.5, 3.5, 4, 4.5 Nm and a rotational speed of 800 rpm. The torque and speed were gradually introduced to the required value. Based on the developed test rig stability at various considered loads, this particular speed of 800 rpm was fixed. Very low rotational speed required a longer test duration and similarly higher rotational speed would significantly reduce the thermal stability of test gear. The test was performed under dry and lubricated conditions. Standard automotive gear oil, SAE 75W85 (Vis @ 373 K, 11.99 cSt; viscosity index, 135; flash point, 507 K), was used as the lubricant. The test gears were immersed to a maximum depth of 5 mm in the lubricant for lubricated testing conditions. The net surface temperature of the gear tooth was measured using an infrared sensor under dry conditions, and the temperature of the lubricant was measured using a J-type thermocouple. The photograph of the infrared sensor used is depicted in Figure 3.13. The test gears were preheated and postheated at 353 K for 2 hours to avoid the moisture effect under a hot air oven (Optics Technology). The photograph of the hot air used is depicted in Figure 3.14. The initial and final weights of the test gears were measured by a digital electronic weighing balance (Sartorius, BS A224S-CW, accuracy: 0.0001 g) to quantify wear. The gear tooth was periodically detected under a digital microscope (Celestron, Digital Microscope Pro) at various stages of testing until failure. The photograph of the digital microscope used is depicted in Figure 3.15. The base tangent length (across three teeth) at three locations of the test gear was measured using a gear tooth flange micrometer (Mitutoyo, IP65, accuracy: 1µm) at different stages of testing for the wear performance investigation. The photograph of the used flange micrometer is depicted in Figure 3.16. After the test, the gears that had been lubricated were washed in an ultrasonic bath with distilled water. Subsequently, the gears were dried (353K) and examined under a Field Emission Scanning Electron Microscope (FESEM) for detailed failure analysis.

Figure 3.13 IR temperature sensor (Rytek, MI)

Figure 3.14 Hot air oven (Optics Technology)

Figure 3.15 Digital microscope (Celestron, Digital Microscope Pro.)

Figure 3.16 Gear tooth flange micrometer (Mitutoyo, IP65)

3.7 Sliding contact performance: Specimen

During gear meshing, the line of contact in a spur gear is parallel to the axis of rotation. Gear teeth make their initial contact in the form of a line that extends across the tooth face, and contact occurs on lines or points (Bhushan (2013)). Basically, gear motion involves rolling and sliding. In contrast to gear tooth surface interaction, this sliding contact configuration does not have a similar effect. It is possible to evaluate the net surface temperature of the gear, weight loss, and tooth thickness reduction during durability testing. These factors are somewhat related to the friction effect when gears are tested for durability. The direct measurement of friction during gear durability evaluation could not be measured due to complex motion involvement. Hence, the effect of different materials on friction and wear and lubrication sliding contact performance was evaluated.

Injection-moulded (IM) polyamide 66, selective laser sintered (SLS) polyamide 12 (dura form), and the thordon SXL pin specimens were considered for sliding contact performance. The dimensions of the pin specimen were ϕ10 mm × 30 mm. During the injection molding process, barrel temperatures of about 558, 563, 568, and 573 K in the heating zones and an injection pressure of 7 MPa were used for pin specimen fabrication. In the selective laser sintering process, the bed temperature, scanning speed, and laser power were fixed at 405 K, 5 m/s, and 12.5 W, respectively. The beam diameter and powder layer thickness were set to 0.45 and 0.10 mm, respectively. The selective laser sintered pin specimen was fabricated in the flat-built configuration form. The thordon pin specimen was extracted from the thordon cast rod (ϕ 70 mm) using the turning process. Figure 3.17 shows the fabricated pin specimens for sliding contact testing.

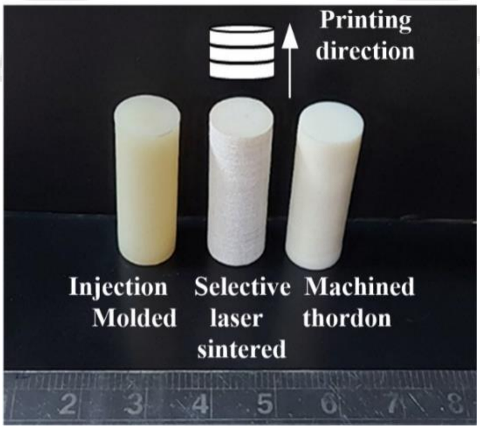

Figure 3.17 Pin specimens for sliding contact testing

3.8 Sliding contact performance: Methodology

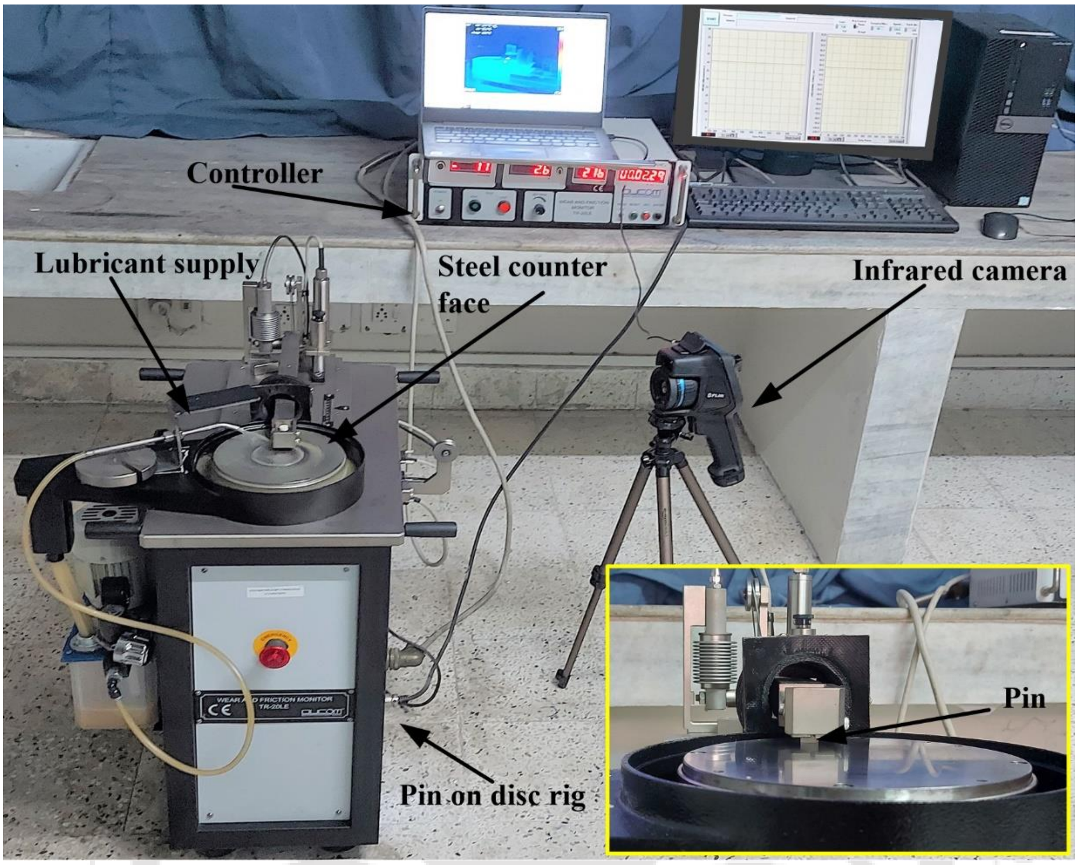

Figure 3.18 Overall configuration of sliding contact performance test

The sliding contact performance of pin specimens was evaluated according to the ASTM G99 standard using a pin-on-disc configuration (TR 20LE), as shown in Figure 3.18. Prior to testing, abrasive paper of different grit sizes (1000, 1200, 1500, and 2000) was used to prepare the pin end surface. The hardness of the specimen was measured according to ASTM D2240, using Shore D (Figure 3.19). Surface roughness was measured with a stylus perthometer (Mitutoyo Surftest SJ-401). A steel disc EN 31 was used as a countersurface to rotate against the loaded polymer pin specimen. In order to remove moisture, the specimens were dried for 2 hours before and after testing at 353 K. Testing specimens were weighed before and after testing using a weighing balance (Sartorius, BS A224S–CW: accuracy 0.0001 g) to analyze wear. Tests were performed at a 60 N applied normal load and a 1.13 m/s sliding speed under both dry and lubricated conditions. In the pin on disc configuration, only sliding can be simulated, whereas gears are subjected to sliding and rolling. Hence, the objective of the sliding performance test was not to correlate with the gear performance but to evaluate the gear material under dry and lubricated conditions. The tangential and normal loads acting on the gear tooth pitch point are 66 and 70 N, respectively, for the 1.8 Nm. The gear sliding velocity is 1.13 m/sec, corresponding to the gear rotational speed of 800 rpm. This normal load of 60 N and 1.13 sliding speed were considered in the sliding performance for measurable wear quantity for the considered test duration. The lubricant, SAE 75W85 gear oil, is supplied at 8 ml/s. Specimens' surface temperatures were measured with an infrared camera (FLIR–E95), Figure 3.20 (a). The tests were repeated three times for each material. A stereomicroscope (Nikon, SMZ25) and FESEM were used to analyze the specimen's worn-out surface morphologies. Figure 3.20 (b) shows the photograph of the stereomicroscope.

Figure 3.19 Shore D durometer

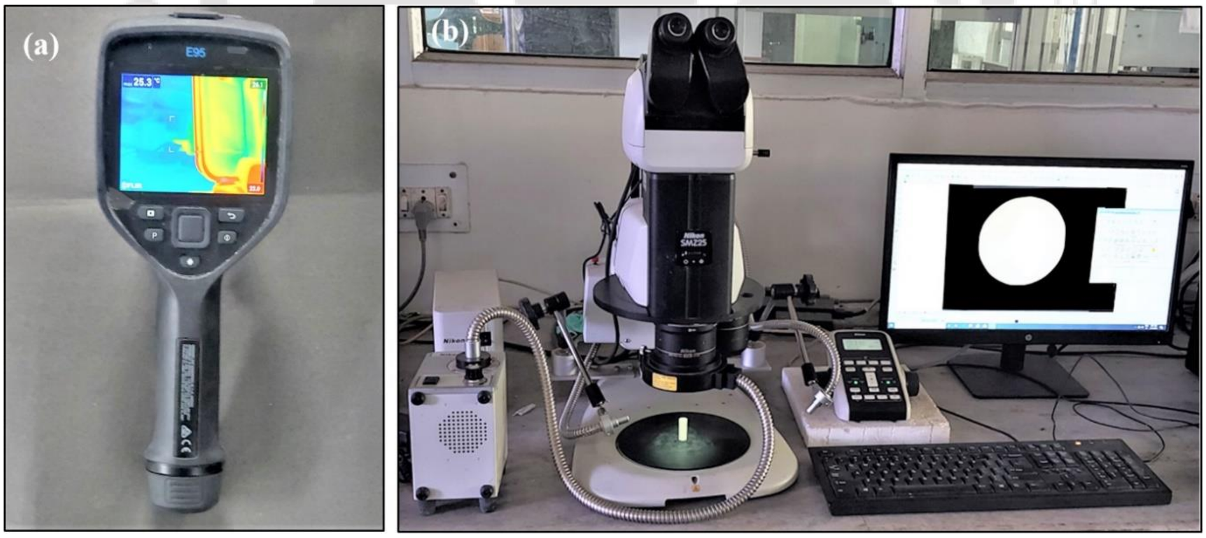

Figure 3.20 (a) Non-contact infrared camera (FLIR-E95) and (b) Stereomicroscope (Nikon, SMZ25)

3.9 Environmental stress cracking evaluation: Specimen and methodology

The photograph of the environmental stress cracking (ESC) specimen and the geometry of the ESC specimen are shown in Figure 3.21.

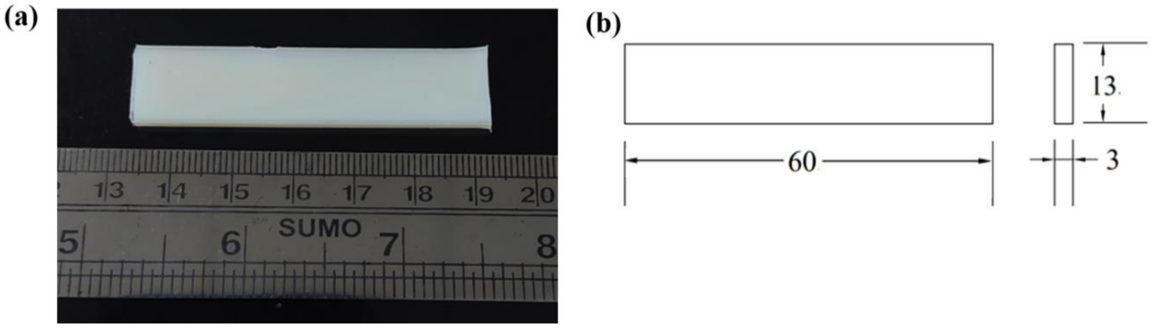

Figure 3.21 ESC specimen and (b) Geometry

Many engineering parts made of polymer or plastic are in contact with oil, grease, chemicals, etc., in stressful external environments in the automobile sector, food processing industry, and medical area. Certain plastic materials may be impacted. By applying a chemical coating or immersing the specimen in a chemical agent under constant deflection or constant stress conditions tests can be used to assess a material's chemical resistance (Rosato *et al.* (2005)). Wyzgoski and Jacques (1977) investigated stress cracking susceptibility of polycarbonate, polymethyl methacrylate, and cellulose acetate butyrate in the exposure of gasoline components at a range of strain 0.3–2.3 % under bending loading conditions. High crystalline polypropylene specimen in the exposure of scent oil at an elevated temperature was evaluated using creep testing by Wee *et al.* (2015).

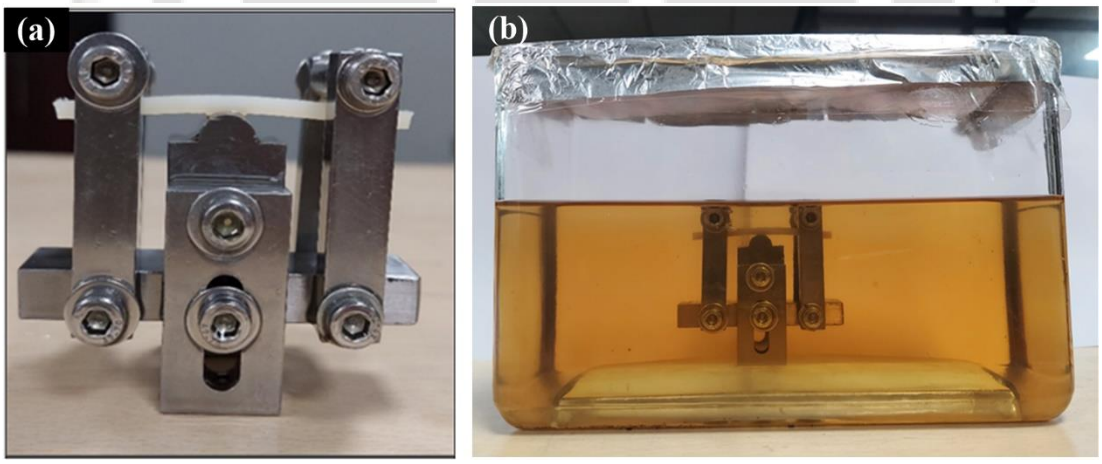

Figure 3.22 (a) Stained specimen and (b) Detailed view of ESC configuration

Environmental stress cracking (ESC) of injection molded, selective laser sintered, and machined thordon specimens was evaluated using as per standard ASTM D-3929-03. Initially, the specimen was fabricated according to ASTM-D638 type I with the injection molding and selective laser sintering process. An injection pressure of 7 MPa and barrel temperatures of about 558, 563, 568, and 573 K in the heating zones were used during the molding process. In the selective laser sintering process, the bed temperature, scanning speed, and laser power were fixed at 405 K, 5 m/s, and 12.5 W, respectively, and the beam diameter and powder layer thickness were set to 0.45 and 0.10 mm, respectively. The strip dimension 60 mm×13mm×3mm was extracted from ϕ 70 mm received thordon cast rod by milling process due to constrained thordon material availability. Injection molded and selective laser sintered processed tensile specimens (ASTM-D638 type I) were reduced its length to 60 mm.

All the fabricated specimens' roughness was measured using a stylus-type perthometer (Mitutoyo Surftest SJ-140). Specimens were also observed under an optical microscope (Carl Zeiss: Axiotech-100HD). Before testing, the prepared specimens were preheated at 353 K for 2 hours and placed in a desiccator, and specimen weight was measured. The rectangular specimens (60 mm×13mm×3mm) with a span length of 40 mm were strained at a particular strain of 1.2 % at the midpoint of specimens using a 3-point bending configuration (Figure 3.22 (a)) and immersed in oil (SAE 75W85) reservoir for 7 days at room temperature as depicted in Figure 3.22 (b). The top of the oil reservoir was sealed with aluminum foil to prevent contamination. After 7 days, the specimen was removed from the setup and wiped with tissue paper. The weight of the specimen was measured and observed under the microscope.

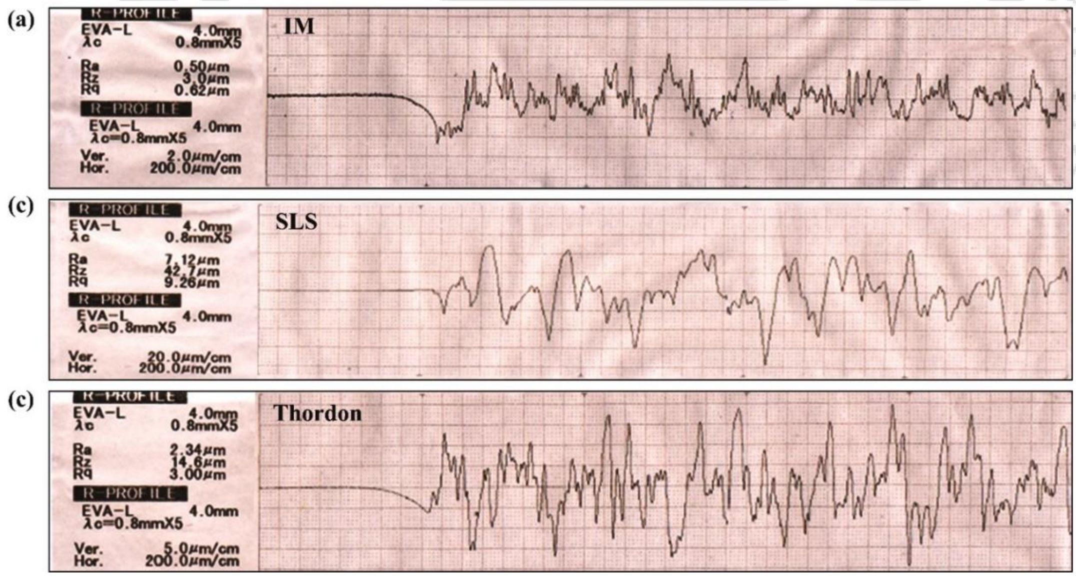

Figure 3.23 ESC specimen roughness

The measured average roughness was found to be 0.5, 7.12, and 2.34 μm for injection molded (IM), selective laser sintered (SLS), and machined thordon specimens, respectively, as depicted in Figure 3.23

3.10. Summary

The material and manufacturing of both gear and specimens were highlighted in this chapter. Details of gear test rigs and the procedures followed for the evaluation of gear under dry and lubricated conditions, including testing operational parameters, temperature measurement, wear, and the failure characterization methods were discussed in detail. The material characterization method details including sliding contact performance and environmental stress cracking evaluation and testing conditions were discussed in detail.

Chapter 4

Effect of lubricant on the surface durability performance of the steel-polyamide gear pair

4.1 Introduction

In metal-metal gear pairs, lubrication is being used to reduce friction, vibration, and noise, enhancing the gear's life and performance. Lubrication reduces friction, wear, and temperature for contact applications and improves the gear transmission efficiency performance. Polymer material have limited wide-scale applications due to thermal-sensitive mechanical properties, mostly under dry conditions. This chapter attempt to utilize oil lubrication to prevent frictional heating and improve the performance of polymer gears. The performance evaluations of an injection-molded polyamide 66 gear were carried out using a power absorption test rig. The present work aims to study the various failure modes of polymer gear (pitting, local softening, subsurface crack, abnormal wear/plastic deformation, degradation, ripples, and scuffing) under dry and lubricated conditions and predict the contact temperature of polymer gear under lubricated condition.

4.2 Methodology

The in-house developed power absorption gear test setup described in chapter 3 was used to investigate the injection molded polyamide gears' performance. The driving gear, made of stainless steel (AISI 316), was connected to a direct current 3-HP motor that could be rotated at a maximum speed of 1,500 rpm. A direct current 1-HP generator was loaded through a rheostat and was connected to the injection molded polyamide (test) gear. The test gear meshed with the driving steel gear. Injection molded test gears were subjected to a range of torques (1.8–4.5 Nm) and a rotational speed of 800 rpm under dry and lubricated conditions. Standard automotive gear oil (SAE 75W85) was used as the lubricant. The test was stopped when pitch region cracks or thermal failure was observed on gear teeth under dry conditions, and scuffing features were observed under lubricated conditions. The overall experimental test facility is already shown in Figure 3.11, and the close-up of the metal-polymer gear pair is shown in Figure 4.1. The polyamide specimen (ASTM D638 type I) was preheated at 353 K for 2 hours to remove the moisture. The tensile test of polyamide material was conducted using the universal testing machine (BISS: MEDIAN 250 KN) at a strain rate of 1 mm/min. The Youngs modulus is found to be 1.071 GPa.

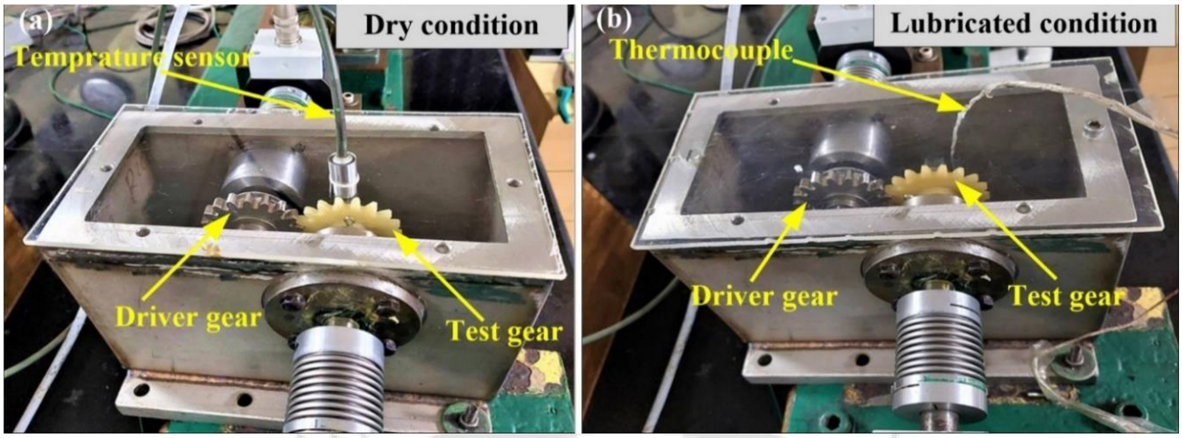

Figure 4.1 Close up view of steel-polymer gear pair

4.3 Thermal condition monitoring of the test gear

The measured surface temperatures of the gear tooth at various loads under dry conditions are shown in Figure 4.2. Frictional heating and material hysteresis are responsible for generating heat when the polymer-based gears are subjected to load, which significantly affects the gear performance. Hence, measuring the test gear temperature of polymer gears at the time of performing the test is essential. Koffi *et al.* (1985) have confirmed that frictional heating is the most dominant mechanism of heat generation for the considered test condition. The measured surface temperature of the gear is the net temperature after dissipation to the surrounding environment. For all load conditions, the test gear exhibited a gradual increase in temperature at the beginning and then stabilized. The surface temperature of the test gear tooth increased with an increase in load owing to its higher contact stress. With loads of 1.8, 3.5, 4, and 4.5 Nm (corresponding contact stress 39.6, 55.2, 58.8, and 62.6 MPa), the maximum temperature occurred after 1×10^5, 0.64×10^5, 0.54×10^5 and 0.4×10^5 cycles, respectively, and then maintained a steady temperature. The test gear exhibited a steady temperature range of 360–406 K with a load range of 1.8−4.5 Nm. According to Düzcükoğlu (2009a), and Düzcükoğlu (2009b), the stable temperature while running the polyamide 66 gear at 8.5 Nm (59.2 MPa) and polyamide 6 gear at 6.1 Nm (34.2 MPa) against a steel gear was 346 K and 351 K, respectively. A similar temperature range (338 K) was observed while testing polyamide 66 at a load of 1.5 Nm (72.9 MPa), Senthilvelan and Gnanamoorthy (2006).

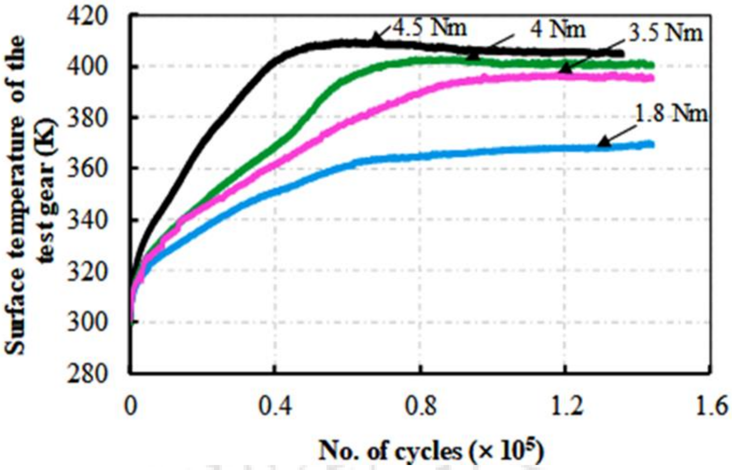

Figure 4.2 Surface temperature of gear tooth against no. of cycles run under dry conditions

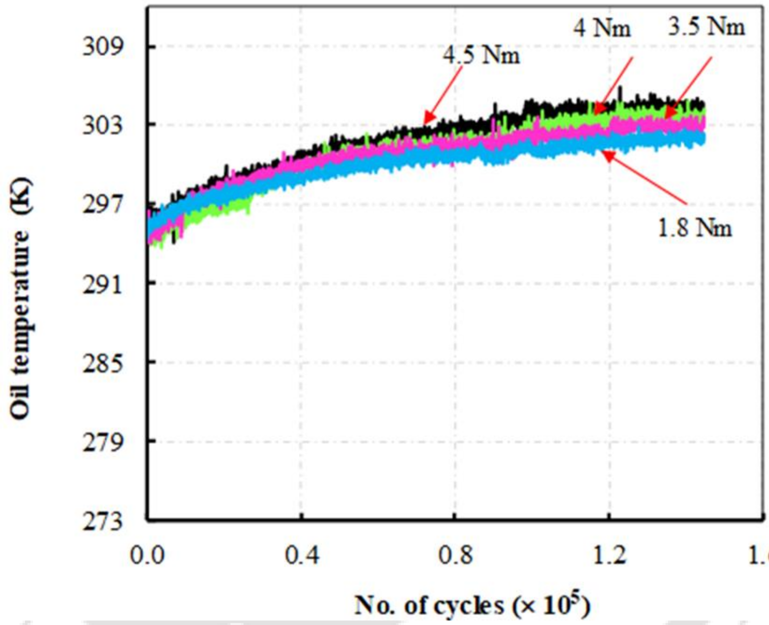

Figure 4.3 Measured lubricant temperature at various loads

Under lubricated gear conditions, the lubricant temperature was measured using a J-type thermocouple instead of an IR temperature sensor because the latter cannot be used as lubricant splashes owing to gear rotation. The measured lubricant temperature under different load conditions is shown in Figure 4.3. The maximum temperature enhancement of the lubricant is observed as 10 K. Although the temperature increase is very small, it confirms the effective dissipation of generated heat. This behavior is due to the substantial volume (1.5 L) and the splashing action of the oil lubricant.

4.4 Wear performance of test gear under dry and lubricated conditions

Figure 4.4 shows the reduction in gear tooth thickness across three teeth at 1.8 and 3.5 Nm loads. At 1.8 Nm load condition, up to 1.4×10^5 cycles duration, the test gear wear rate is found to be higher in dry conditions compared to the lubricated gear conditions. Beyond this time, the wear rate is almost the same for both dry and lubricated gear conditions. A similar trend is observed at the 3.5 Nm loading condition, i.e., initially, the gears under dry conditions exhibited a higher wear rate that later became almost the same as that under lubricated gear conditions. This behavior is due to the running-in wear of the test gear under dry conditions. At the beginning of the test, the presence of initial asperities on the gear contact tooth surfaces results in the abrasion of the surface, due to which the initial wear rate is increased under dry conditions. However, this initial wear rate is prevented by the presence of the lubricant layer in the lubricated condition. Test gear under lubricated gear conditions exhibited longer life for the same amount of wear compared to dry conditions.

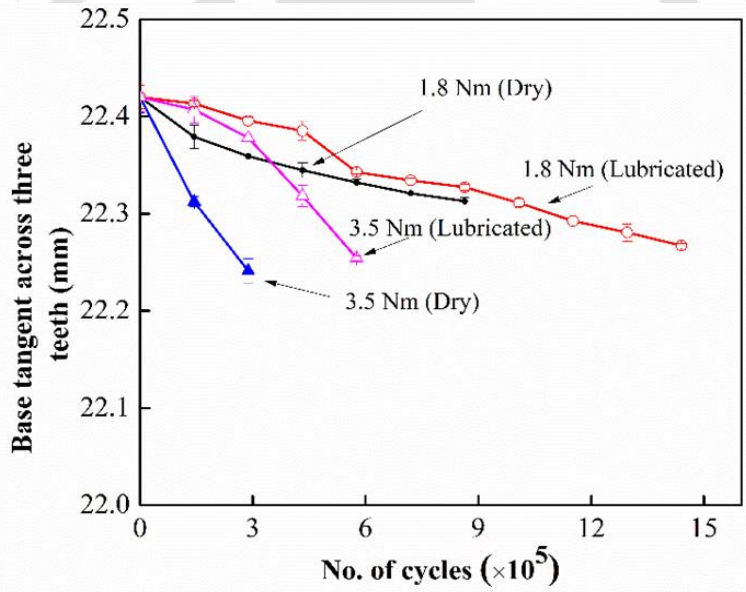

Figure 4.4 Variation of gear tooth thickness with no. of cycles run

To understand the wear performances of all the teeth in the test gear, the initial and final weight losses are considered. Figure 4.5 shows the weight loss of test gears at both loads under dry and lubricated conditions. With an increase in load, the test gear showed higher wear under both conditions (dry and lubricated). At the 1.8 Nm load condition, the presence of lubricant reduced the amount of wear by 56%, whereas at the 3.5 Nm load condition, the effect of the lubricant reduced wear by 59%. The tests were allowed to progress until the formation of cracks or excessive wear in the flank region.

For both loads (1.8 and 3.5 Nm), the gears under dry conditions exhibited subsurface cracks near the pitch region, whereas the gears under lubricated conditions showed excessive wear in the flank region.

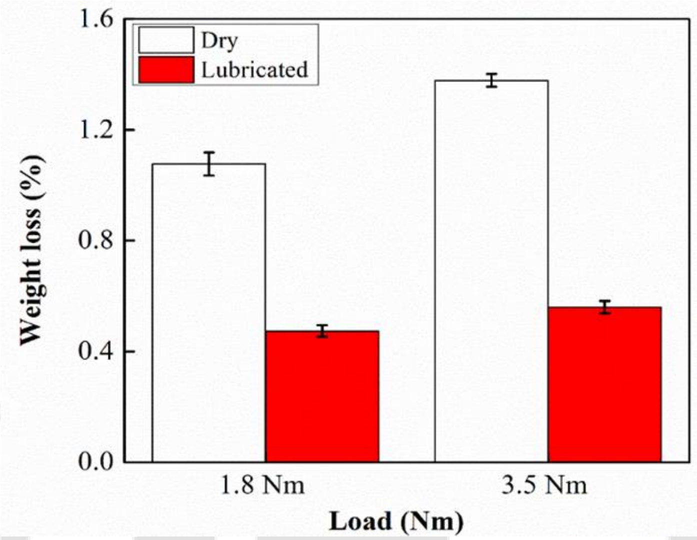

Figure 4.5 Reduction in weight of the test gear at loads of 1.8 Nm and 3.5 Nm under different conditions

4.5 Fatigue performance of test gear

The fatigue life performance of the test gears under dry and lubricated conditions subjected to various test loads 1.8 Nm–4.5 Nm (corresponding contact stress 39.6 MPa–62.6 MPa) are summarized in Figure 4.6. The induced gear tooth contact stress (s_c) was computed using the Hertzian theory by assuming an elliptic stress distribution for the considered loads and is calculated from the following equation (AGMA 908-B89 (1989)).

$$s_c = 2w_n/\pi b_H \tag{4.1}$$

where w_n is the normal unit load (in N/mm) at the pitch point and b_H is the semi-width Hertzian contact band (in mm) at the pitch point.

$$w_n = F_{wn}/L_{min} \tag{4.2}$$

where F_{wn} is the normal operating load (in N) and L_{min} is the minimum contact length (in mm)

$$F_{w_n} = F_t/Cos\alpha_{wn}Cos\beta_w \tag{4.3}$$

where F_t is the actual tangential load (in N), α_{wn} is the normal operating pressure loading (in degrees), and β_w is the operating helix angle (in degrees).

$$F_t = (F_t)_{nom} K_D \tag{4.4}$$

where $(F_t)_{nom}$ is normal tangential load (in N), and K_D is a combined derating factor.

$$(F_t)_{nom} = 1000P/v_t \tag{4.5}$$

where P is the gear's transmitted power (in kW) and v_t is the operating pitch line velocity (m/sec).

$$P = T_t \omega_2 / 1000 \tag{4.6}$$

where T_t is the torque (Nm) and ω_2 is the angular velocity (rad/sec) at the pitch point of the test gear

Angular velocity of driving (steel) gear, ω_1:

$$\omega_1 = \frac{\pi n_1}{30} \tag{4.7}$$

where n_1 is the speed of the driving gear (in rpm),

Angular velocity of driven (test gear) gear, ω_2:

$$\omega_2 = \omega_1 / u \tag{4.8}$$

where, u is the gear ratio and u = 1, Hence the angular velocity of both the driving and driven gears is the same.

Operating pitch line velocity, v_t:

$$v_t = \omega_1 r_{w1} / 1000 \tag{4.9}$$

Combined derating factor:

$$K_D = K_o K_m K_v \tag{4.10}$$

assuming K_o, K_m, and $K_v = 1$

where K_o is overload factor, K_m is load distribution factor and K_v is the dynamic factor.

The Hertzian contact band (the semi-width of the rectangular contact band (b_H) is calculated by

$$b_H = \left(8\, X_\Gamma w_n \rho_n / \pi\, E_r\right)^{0.5} \tag{4.11}$$

where E_r is the reduced modulus of elasticity (in N/mm^2), w_n is the normal unite load at the pitch point, and ρ_n is the normal relative radius of curvature (in mm) at the pitch point.

Poisson ratio of the driving (steel) and driven gear (polymer) is assumed as 0.3 and 0.41, respectively (Kodeeswaran *et al.* (2019)). The elastic modulus of the driving (steel) gear (polymer) is assumed as 200 GPa (Kodeeswaran *et al.* (2019)), and the test gear (driven) is 1.071 GPa.

The performance of the test gear is significantly affected by the loads under both dry and lubricant conditions. No thermal failure is observed when the 1.8 Nm (39.5 MPa) load is applied under dry conditions. Tooth wear, pitting, and pitch subsurface crack were observed when the 1.8 Nm (39.5 MPa) load is applied, whereas abnormal wear/plastic deformation, local softening, and pitch crack are observed for the 3.5 Nm–4.5 Nm loads (55.2 MPa−62.6 MPa). At higher loads, a higher generated temperature lowered the gear material stiffness and strength, which in turn contributed to thermos-plastic deformation and melting. Polymeric materials tend to lose 5–10% of their tensile strength for every 10 K change in temperature, as reported by Terashima *et al.* (1986).

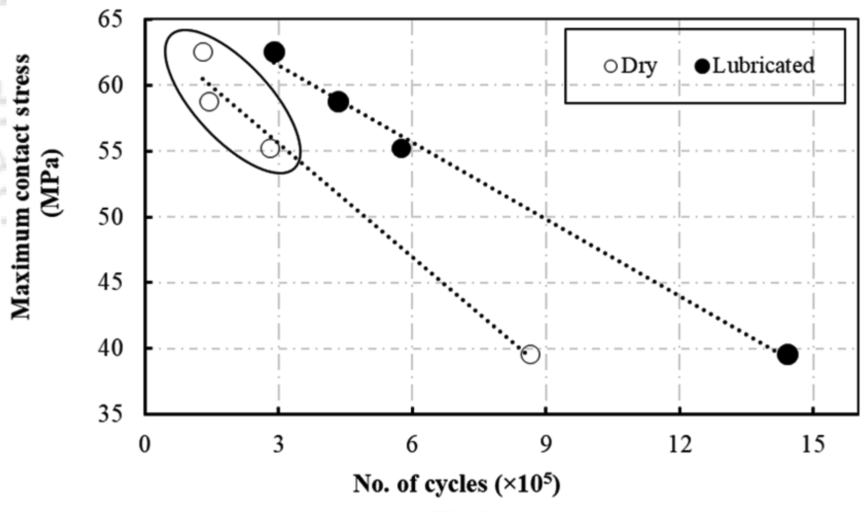

Figure 4.6 Test gear life under dry and lubricated conditions.

Under lubricated gear conditions, the failure shows only scuffing at all the considered loads 1.8–4.5 Nm (39.5−62.6 MPa). The lubricant film present between the mating surfaces of the test gear dissipates the generated heat effectively. Thus, the test gear under lubricated gear conditions shows a more superior performance than that under dry conditions for the considered load range. The percent error in the life of the test gear when the 4.5 Nm (62.6 MPa) load was applied is ±10% under dry conditions.

4.6 Wear and damage morphology of test gear under dry condition

Figure 4.7 (a–e) shows periodic observations of the gear tooth surface as it is subjected to a 1.8 Nm load under dry conditions. In the initial stage (1.4 $\times 10^5$ cycles), only wear is observed below the pitch line as depicted in Figure 4.7 (a). With an increase in the number of cycles, the formation of macro pits near the pitch region is observed. These pits are in the shape of a fan, and while they are relatively shallow, they have a large in area, as shown in Figure 4.7 (c) and

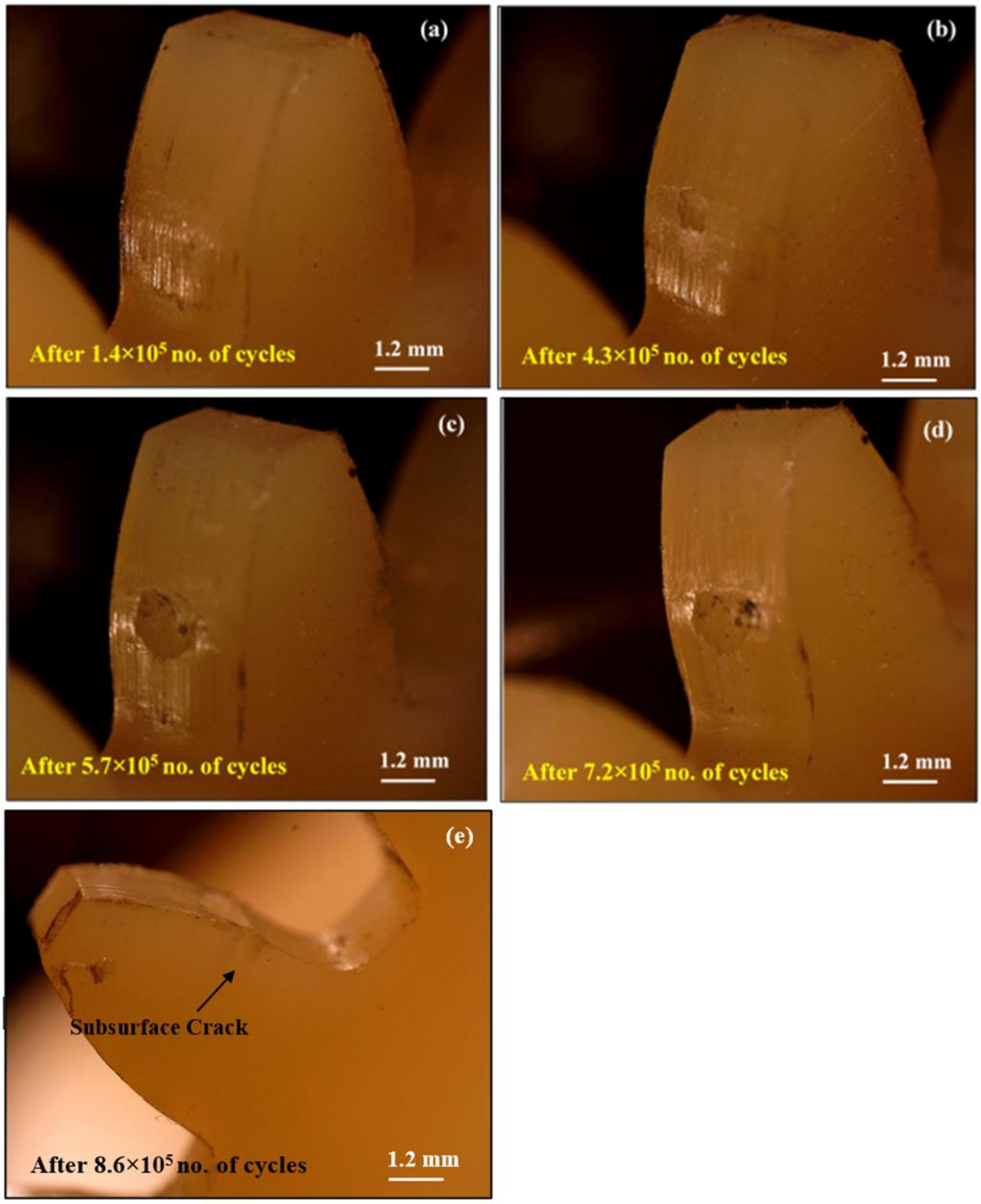

Figure 4.7 (a–e) Digital microscope image of the test gear tooth at a load of 1.8 Nm under dry conditions for 8.6×10^5 cycles.

(d). The formation of pits due to fatigue cracks originates at the subsurface of the tooth owing to the subsurface shear stress as reported in standard AGMA standard 1010- E95-*Appearance of Gear Teeth Terminology of Wear and Failure* (1995). Pitch line pitting is severe enough to form subsurface cracks near the front face of the pitch region, as illustrated in Figure 4.7 (e).

A schematic representation of failure on the test gear tooth surface is depicted in Figure 4.8 (a). To have a comprehensive analysis of the test gear wear mechanism, the worn-out surface of the test gears was observed under FESEM; the FESEM images are shown in Figure 4.8 (b–g). Plastic flow in the direction normal to the sliding direction is formed at the middle of the gear tooth face (Figure 4.8 (b)). Hoskins *et al.* (2014) evaluated the wear performance of a PEEK disc using a twin-disc test rig at various loads and slip ratios and observed similar local damage failure due to the combination of a high temperature and contact pressure on the disc. The surface near the pitch region shows macro pits that originate from the subsurface cracks (Figure 4.8 (c)). A close-up view of this region reveals the ridges form owing to the plastic flow (Figure 4.8 (d)). Multiple subsurface cracks are observed on the pitch region of the front face (Figure 4.8 (e)) and near the face edge (Figure 4.8 (f)), owing to the contact fatigue load. The formation of larger pits near the pitch region contributes to the lack of contact and excessive load on the face region. In the lower flank region, only mild sliding marks are observed at this load (Figure 4.8 (g)).

At higher load conditions (3.5 Nm), the test gear experiences a higher temperature, which accelerates subsurface crack formation owing to a reduction in gear material strength. A schematic view of the test gear tooth surface subjected at a 3.5 Nm load after $2.8{\times}10^5$ cycles is depicted in Figure 4.9 (a). The test gear shows excessive abnormal wear/plastic deformation near the root region, as indicated in Figure 4.9 (b). The tooth stiffness difference between the polymer and steel gears contributes to the rotational lag between the gear pair. At high load conditions, due to high load-induced deflections, pre-mature and extended contacts occur in the mesh cycle due to the rotational lag. Due to extended contact, the root region of the polymer gear is subjected to the scrapping action of the steel gear tooth tip region. This type of failure occurs due to tip geometry as well as higher loading condition. Terashima *et al.* (1986) observed this kind of feature while evaluating the performance of a polymer 6 gear and termed it as ‘abnormal wear’.

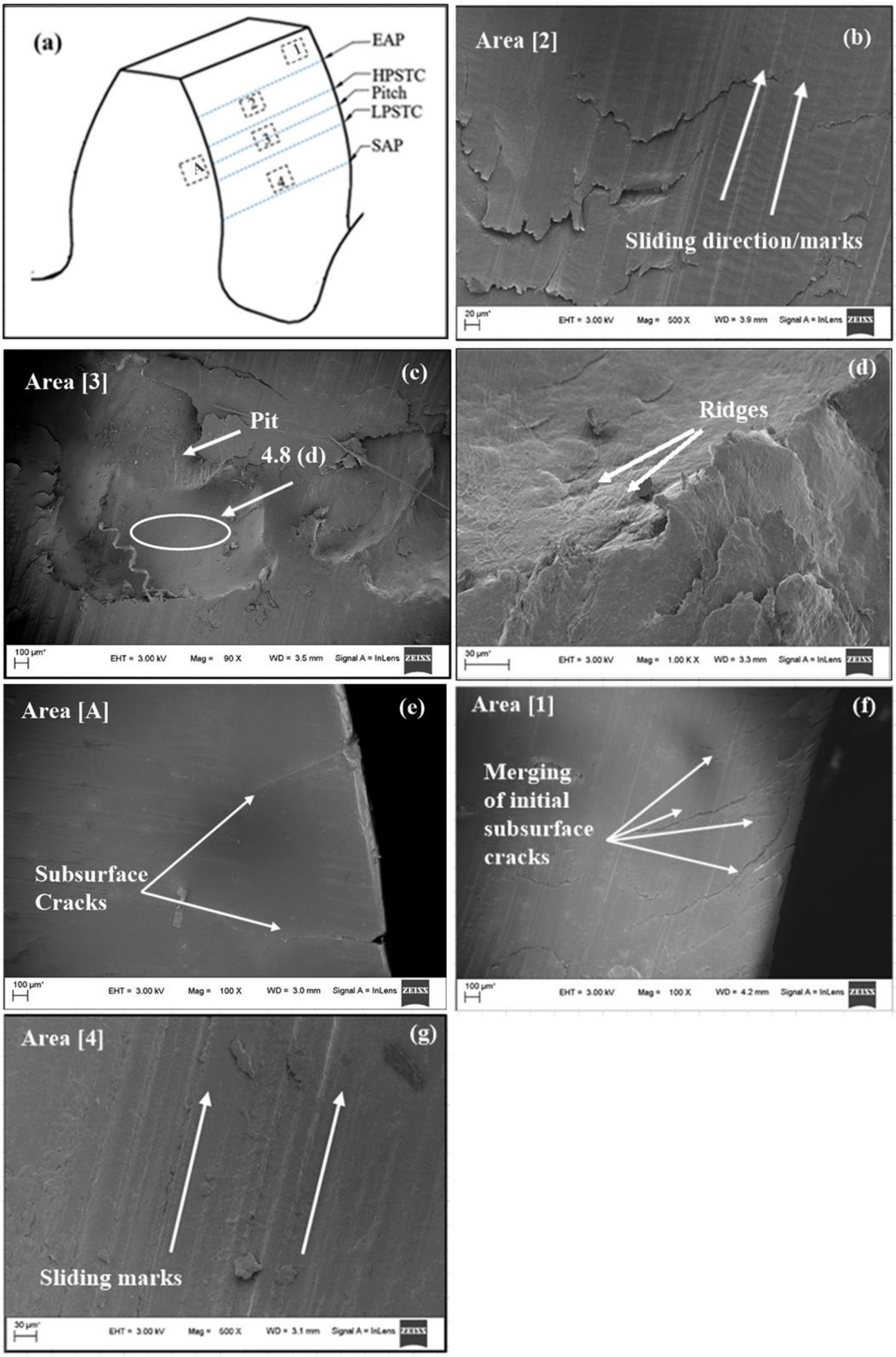

Figure 4.8 (a) Schematic view of gear tooth surface and (b-g) FESEM morphology of failure test gear tooth surface subjected to 1.8 Nm, 8.6×10^5 cycles

Local softening along with substantial sliding marks are observed on the pitch region owing to single tooth load sharing and change in the direction of sliding in this region (Figure 4.9 (b)). A close-up of this region did not reveal the pits observed, unlike at a lower load (Figure 4.7 (c)); instead, only a molten material layer is observed (Figure 4.9 (c)). Imrek (2009) observed a similar feature while investigating polyamide 6 gears. He reported that the pitch region was very sensitive to polyamide 6 gears owing to severe melting and breakage of the gear tooth. Duzcukoglu (2009b) also observed softening near the pitch region. It is worth noting that at this period (2.8×10^5 cycles), there is neither crack formation nor pitting when the gears are subjected to the 1.8 Nm load. The formation of pits is only observed after 4.3×10^5 cycles. Subsurface cracks initiated at the tooth pitch region merged together and formed larger cracks (Figure 4.9 (d)). A close-up of this region shows the merging of subsurface cracks and the formation of debris (Figure 4.9 (e)). The subsurface cracks in the direction normal to the sliding direction are formed at the center of the gear tooth face at this load (Figure 4.9 (f)). However, at lower loads (1.8 Nm), only plastic flow is observed. A similar failure morphology is observed by Chen *et al.* (2000) while evaluating the contact fatigue performance of PA 66 material. The test gear shows similar multiple subsurface cracks near the face edge at this load (Figure 4.9 (g)). In the lower flank region, severe sliding marks are observed (Figure 4.9 (h)) at this load.

Test gears subjected to a load of 4 Nm exhibited a failure morphology similar to that of test gears subjected to a load of 3.5 Nm; however, the failure is more severe in nature. Figure 4.10 (b) shows a schematic view of the test gear tooth surface. Abnormal wear/plastic deformation on the root region is observed (Figure 4.10 (a)). Local softening with the accumulated sliding material near the pitch region is also (Figure 4.10 (c)). Figure 4.10 (e) and (f)) show the culmination of subsurface cracks near the front face of the pitch region and multiple subsurface cracks near the face region.

Test gears subjected to a load of 4.5 Nm exhibited severe thermal damage and excessive wear failure. At this load, the gear tooth experiences a high temperature (Figure 4.2) at a short interval of cycles (0.4×10^5). As this temperature is well above the glass-transition temperature, significant material degradation occurs, as indicated in Figure 4.11 (a). A schematic view of the gear tooth surface is shown in Figure 4.11 (b). At this load, the test gear shows similar plastic flow in the direction normal to the sliding direction in the middle of the gear tooth face (Figure 4.11 (c)).

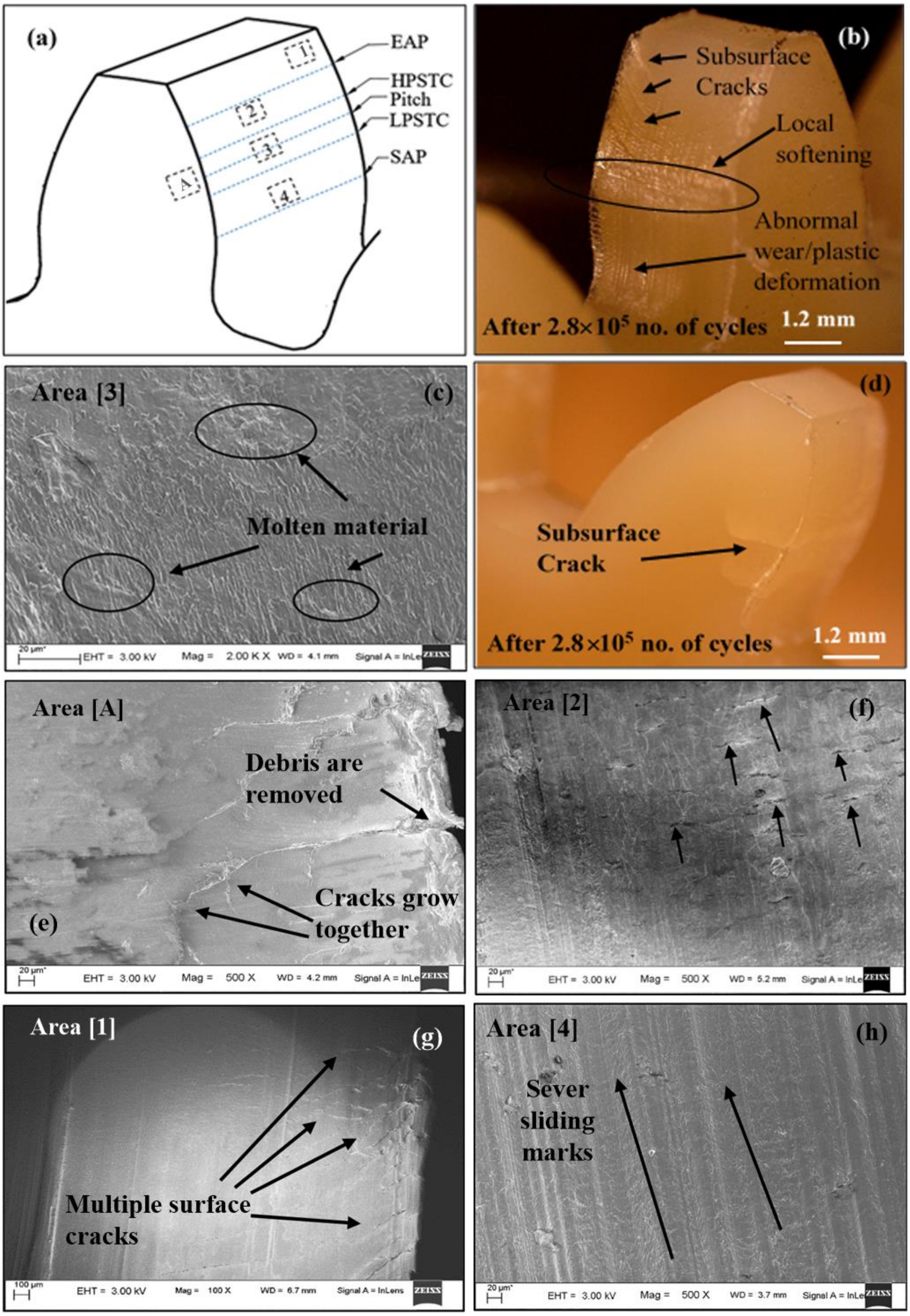

Figure 4.9 (a) Schematic view, (b, d) Digital microscope image, and (c, e, f, g, h) FESEM morphology of failure test gear tooth at a load of 3.5 Nm after completion of 2.8×10^5 no. of cycles

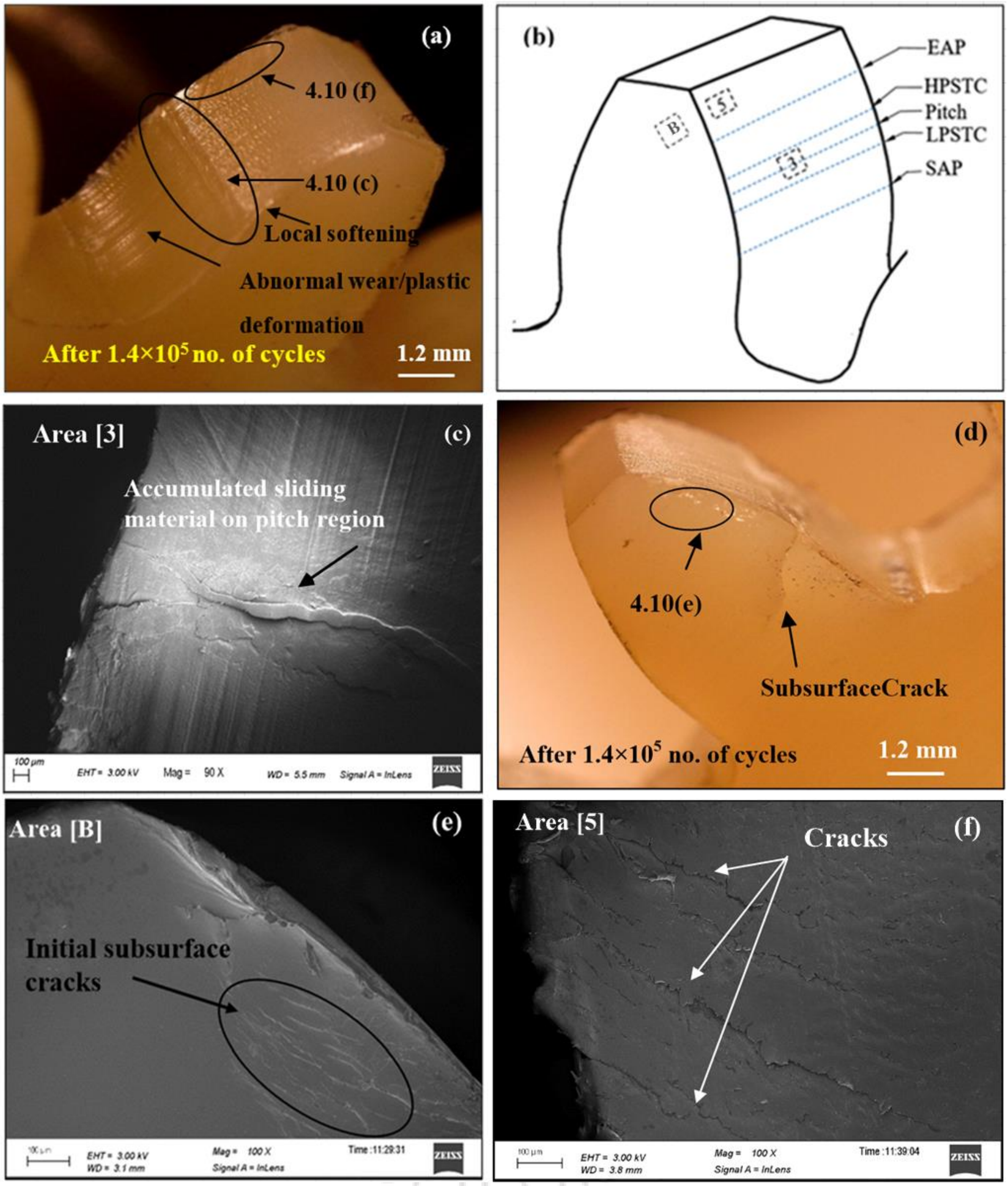

Figure 4.10 (a, d) Digital microscope images, (b) Schematic view, and (c, e, f) FESEM morphology of test gear at a loading of 4 Nm after completion of $1.4{\times}10^5$ cycles

This damage is severe and occurred over a larger area compared to the 1.8 Nm load condition (Figure 4.8 (b)). The pitch region damage is depicted in Figure 4.11 (d). Abnormal wear/plastic deformation at the root region is severe, and substantial plastic deformation is observed (Figure 4.11 (e)) at this load. A magnified view of the flank region is depicted in Figure 4.11 (f).

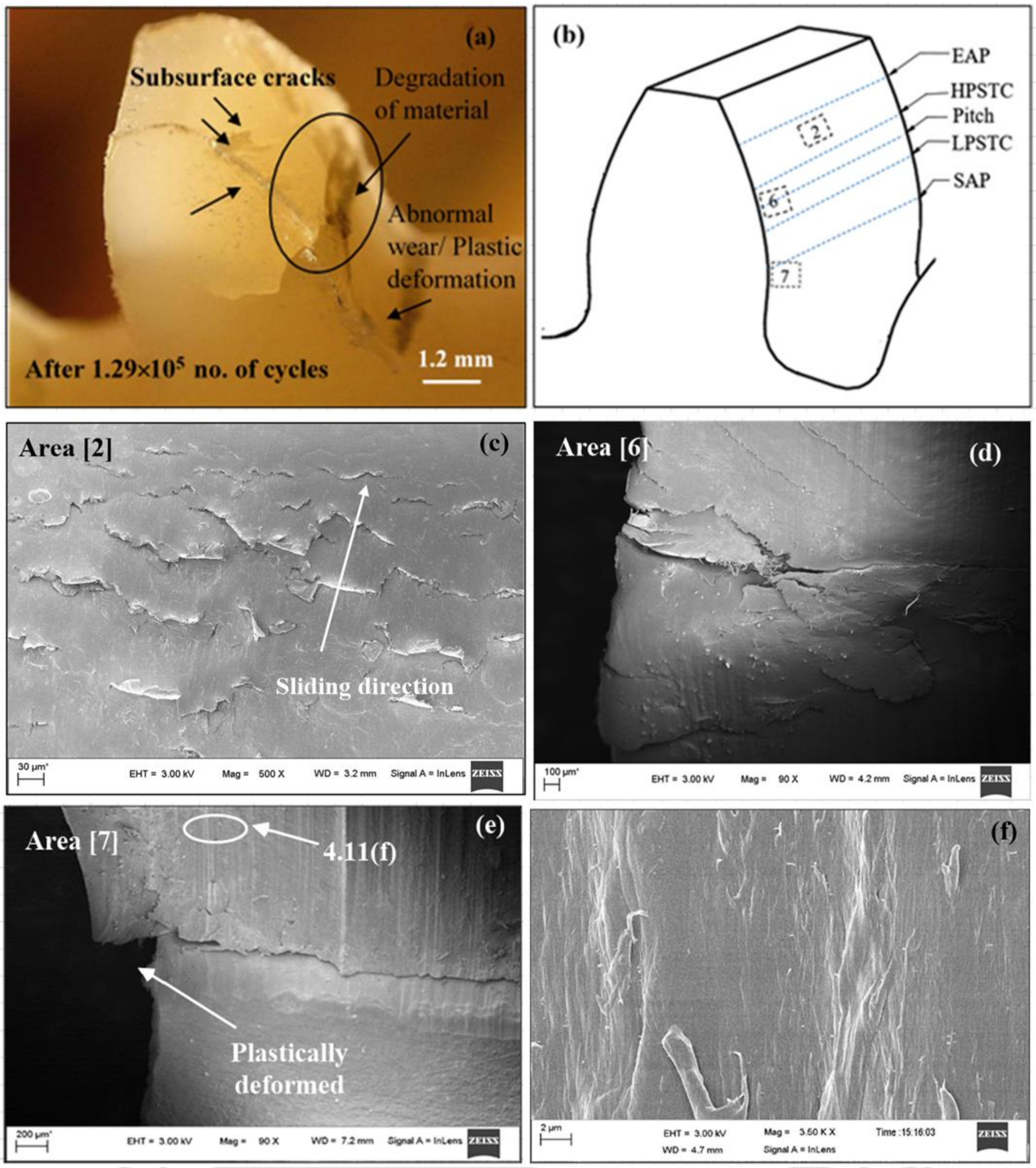

Figure 4.11 **(**a) Digital microscope image, (b) Schematic view, and (c, d, e, f) FESEM morphology, showing the failure of the gear tooth at a 4.5 Nm load under the dry condition.

4.7 Test gear performance under the lubricated condition

4.7.1 Gear tooth contact temperature and film thickness along the line of action under lubricated gear conditions

Failure of the test gear under dry conditions is predominantly dependent on the gear parameters and applied load. When the test gears are subjected to load under lubricant conditions, the lubrication characteristics also play a major role in addition to the gear parameters and the load condition. Various parameters, including relative velocity, load sharing factor, flash temperature, contact temperature, and film thickness were computed as reported in AGMA

Standard AGMA-925-A03-*Effect of Lubrication on Gear Surface Distress* (2003). For the calculation of the flash temperature of the test gear pair along the line of action at given loads under lubricated gear conditions, various parameters were computed and are shown below.

Figure 4.12 (a) and (b) show a gear pair of the involute profile with the lowest point of single tooth contact (LPSTC) and the highest point of single tooth pair contact (HPSTC) of the driven gear. The position of contact points on the line of action in the transverse plane is shown in Figure 4.12 (c). The line of action (distance in mm) in the transverse plane, C_i is measured from the interference point of the driven gear (test polymer gear) along the line of action.

$$\text{where } i = P, Q, R, S, T$$

The distance between base circles along the line of action, C_U, is computed from the operating center distance ((a_w) in mm) and transverse operating pressure angle ((α_{wt}) in degrees) by

$$C_U \ = a_w \ sin\alpha_{wt} \tag{4.12}$$

Point P locates the start of the active profile (SAP) where the tip of the driving gear tooth touches the flank of the driven gear. This point is also indicated in Figure 4.12 (c). The distance C_P is computed from the outer (r_{a1}) and base radii (r_{b1}) of the driving gear (in mm) and C_U, as follows:

$$C_P = [C_U - (r_{a1}^2 \ - \ r_{b1}^2)^{0.5}] \tag{4.13}$$

Point R locates the operating pitch point and distance C_R is computed from the C_U and gear ratio (u) value. The gear ratio is the ratio of the number of teeth of the driven gear to those of the driving gear.

$$C_R \ = \frac{C_U}{u+1} \tag{4.14}$$

HPSTC is located by S and distance C_S computed from C_P and transverse base pitch ((p_{bt}) in mm):

$$C_S = \ C_P + \ p_{bt} \tag{4.15}$$

The meshing cycles end at T or the end of the active profile (EAP), where the tip of the driven gear tooth last makes contact with the mating driving gear tooth. The distance C_T is computed by using the outer (r_{a2}) and base radii (r_{b2}) of the driven gear (in mm):

$$C_T \ = \ (r_{a2}^2 \ - \ r_{b2}^2)^{0.5} \tag{4.16}$$

LPSTC is located by Q, and distance C_Q is computed by using C_T and p_{bt}:

$$C_Q = C_T - p_{bt} \tag{4.17}$$

Z is the active length of the line of action and is computed using the C_P and C_T values.

$$Z = C_T - C_P \tag{4.18}$$

Figure 4.13 shows the transverse radii of curvature $\rho_{1_{(i)}}$ and $\rho_{2_{(i)}}$ of the gear tooth profile at a general contact point defined by the roll angle (ξ_i) along the line of action from point P to T. The roll angles along the line of action ((ξ) in radians) are given by

$$\xi_i = C_i / r_{b2} \tag{4.19}$$

Profile radii of curvature, ((ρ) in mm**)**

The transverse radius of curvature of the driven gear, ((ρ_2) in mm) is given by

$$\rho_{2_{(i)}} = r_{b2}\xi_{(i)} \tag{4.20}$$

where $\xi_P \leq \xi_{(i)} \leq \xi_U$

The transverse radius of curvature of the driving gear((ρ_1) in mm) is

$$\rho_{1_{(i)}} = C_U - \rho_{2_{(i)}} \tag{4.21}$$

The transverse relative radius of curvature, (ρ_r) = Normal relative radius of curvature, (ρ_n) for the spur gear is

$$\rho_{n_{(i)}} = \rho_{1_{(i)}} \rho_{2_{(i)}} / \rho_{2_{(i)}} + \rho_{1_{(i)}} \tag{4.22}$$

Figure 4.14 (a) Normal relative radius of curvature of gear pair along the line action.

The sliding velocity,(($v_{s_{(i)}}$) in m/sec), is given by

$$v_{s_{(i)}} = \left| v_{r1_{(j)}} - v_{r2_{(j)}} \right| \tag{4.23}$$

The variation in the sliding velocity along the line of action is depicted in Figure 4.14 (b).

The load-sharing factor for smooth meshing (X_r), is

$$X_{r_{(i)}} = \xi_{(i)} - \xi_P / \xi_Q - \xi_P \qquad \text{for } \xi_P \leq \xi_{(i)} \leq \xi_Q \tag{4.24}$$

$X_{r(i)} = 1$ for $\xi_Q \leq \xi_{(i)} \leq \xi_s$ (4.25)

$X_{r(i)} = \xi_T - \xi_{(i)} / \xi_T - \xi_S$ for $\xi_s \leq \xi_{(i)} \leq \xi_T$ (4.26)

The load-sharing factor with contact points along the line of action is depicted in Figure 4.14 (c).

Figure 4.15 shows a Hertzian contact band that has formed between two parallel cylinders in contact. The Hertzian contact band (the semi-width of the rectangular contact band (b_H) is given by

$$b_{H(i)} = \left[8X_{r(i)} w_n \rho_{n(i)} / \pi E_r\right]^{0.5} \quad (4.27)$$

where w_n is the normal unit load (in N/mm) at the pitch point and E_r is the reduced modulus of elasticity.

A constant coefficient of friction, ((μ_m) in µm), along the line of action has been assumed by AGMA 217.01 (1965) and Kelley (1953).

$$\mu_{m(i)} = \mu_{mconst} = 0.06 \times C_{R_{avg_x}} \quad (4.28)$$

$$1 \leq C_{R_{avg_x}} = 1.13 / (1.13 - R_{avg_x}) \leq 3.0 \quad (4.29)$$

where R_{avg_x} is the average surface roughness (in µm) of the driving and driven gears for a cutoff length. The surface roughness constant R_{avg_x}, is limited to a maximum value of 3.0.

The measured driver and test gear roughness is 1.87 µm and 0.90 µm for a cutoff length of 4.00 mm. The R_{avg_x} value of the driving and the driven gears is 1.3.

Thermal contact coefficient (B_M)

$$B_{M1} = (K_{M1} \times \rho_{M1} \times c_{M1})^{0.5} \quad (4.30)$$

$$B_{M2} = (K_{M2} \times \rho_{M2} \times c_{M2})^{0.5} \quad (4.31)$$

where B_{M1} is the thermal contact coefficient of the driving material, N/(mms$^{0.5}$ K), B_{M2} is the thermal contact coefficient of the driven material (N/(mms$^{0.5}$ K),

For the driving gear (SS-316), the gear material density (ρ_{M1}) is 8031 kg/m^3, specific heat capacity (c_{M1}) is 457 J/kg K (Bansal (2007)), and thermal conductivity (K_{M1}) is 16.3 W/mK (Padhy and Reddy (2006)). For the driven gear (PA 66), the gear material, density (ρ_{M2}) is

1140 kg/m^3, thermal conductivity (K_{M2}) is 0.28 W/mK (Kodeeswaran (2019)), and specific heat capacity (c_{M2}) is 1670 J/kg K.

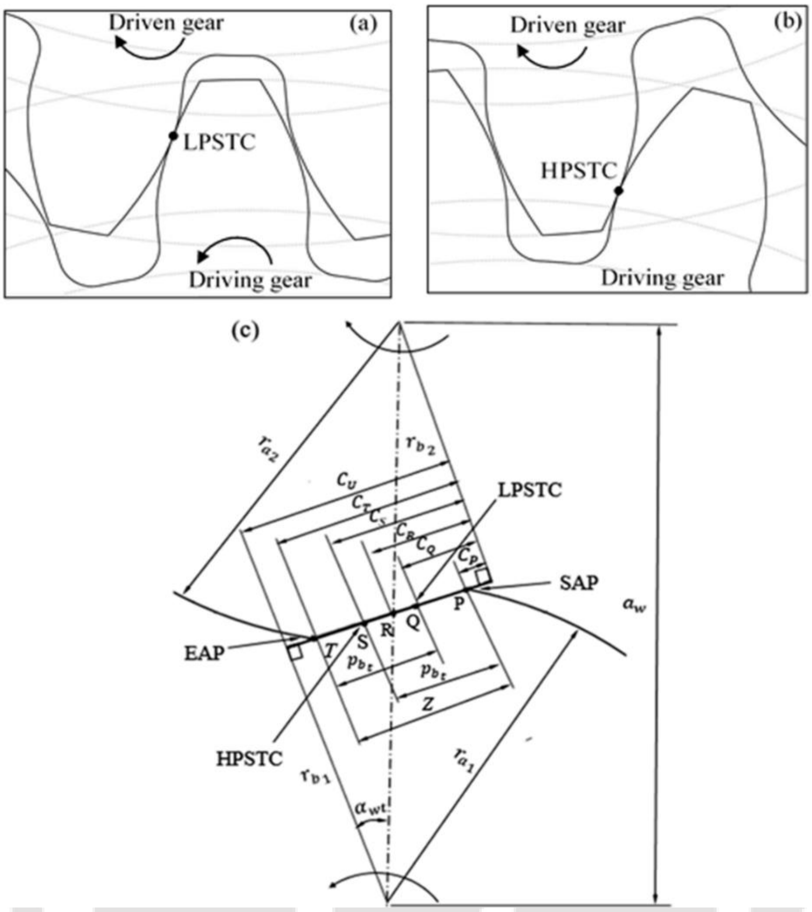

Figure 4.12 (a, b) Schematic images of LPSTC and HPSTC points of the mating gear pair; (c) Distance along the line of action of the mating gear pair

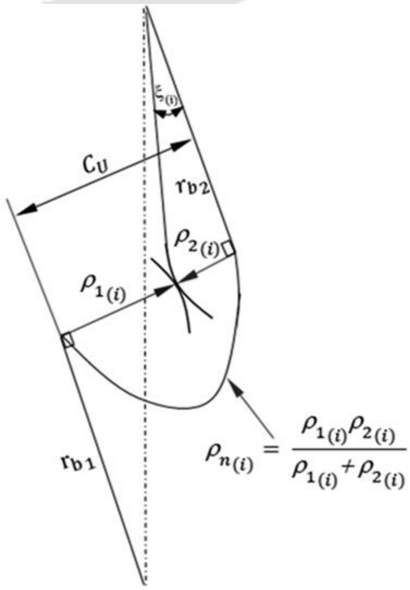

Figure 4.13 Normal relative radius of curvature for the gear pair

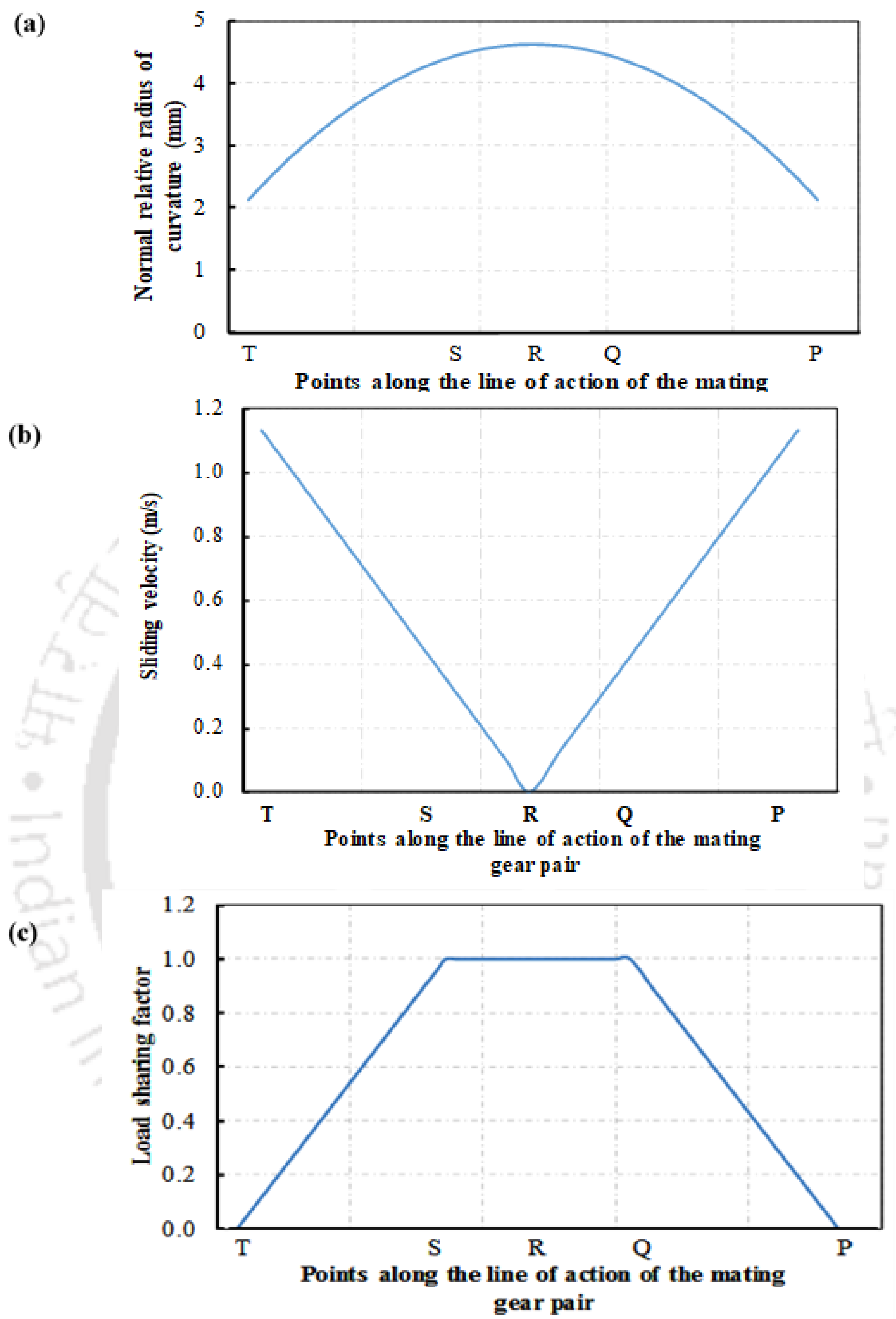

Figure 4.14 (a) Normal relative radius of curvature of gear pair along the line action, (b) Variation in the sliding velocity along the line of action, and (c) Load sharing factor along the line of action of the mating gear pair.

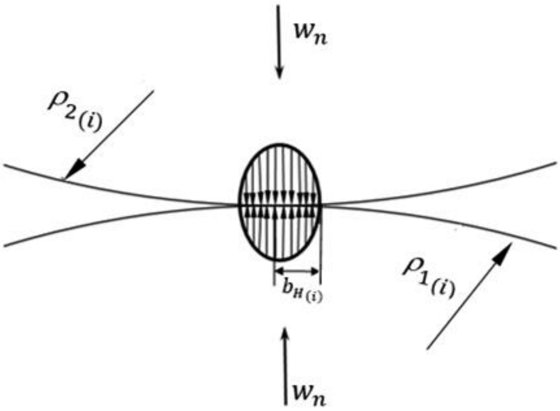

Figure 4.15 Schematic of the Hertzian contact

4.7.1.1 Flash temperature

The local and instantaneous intensification of temperature due to the frictional heating at the gear meshing zone on the gear teeth is called flash temperature. The empirical formula proposed by Blok (1937), as reported in AGMA Standard 925–A03, for the flash temperature computation is a combination of the coefficient of friction, gear geometry, gear material, and gear lubrication system.

$$\theta_{fl_{(i)}} = \frac{31.62K\mu_{m_{(i)}}X_{\Gamma_{(i)}}w_n}{\left(b_{H_{(i)}}\right)^{0.5}} \times \frac{\left|v_{r2_{(i)}} - v_{r1_{(i)}}\right|}{B_{M2}\ \left(v_{r2_{(i)}}\right)^{0.5} + B_{M1}\ \left(v_{r1_{(i)}}\right)^{0.5}} \tag{4.32}$$

where K is 0.80, a numeric value that is valid for a semi-elliptic Hertzian distribution of frictional heat over the instantaneous width, 2 b_H, of the rectangular contact band.

The gear tooth contact temperature (θ_B) at any point on the line of action is given by

$$\theta_{B_{(i)}} = \theta_M + \theta_{fl_{(i)}} \tag{4.33}$$

where θ_M is tooth temperature and $\theta_{fl_{(i)}}$ is the flash temperature.

Scuffing can occur on the flank region of the gear tooth between Q (LPSTC) and P (SAP) owing to the intense frictional heat generated by a combination of high sliding velocity and high contact stress, which in turn is associated with a lack of or a deterioration in the condition of lubrication. This behavior is due to the presence of a high flash temperature and higher sliding velocity in this region (as indicated in Figure 4.16). For scuffing, the maximum value of the flash temperature ($\theta_{fl\,max}$) along the line of action is most important. To better understand the wear of the test gear under this condition, the following section describes this critical location (where the temperature is maximum), film thickness, and maximum flash temperature in detail.

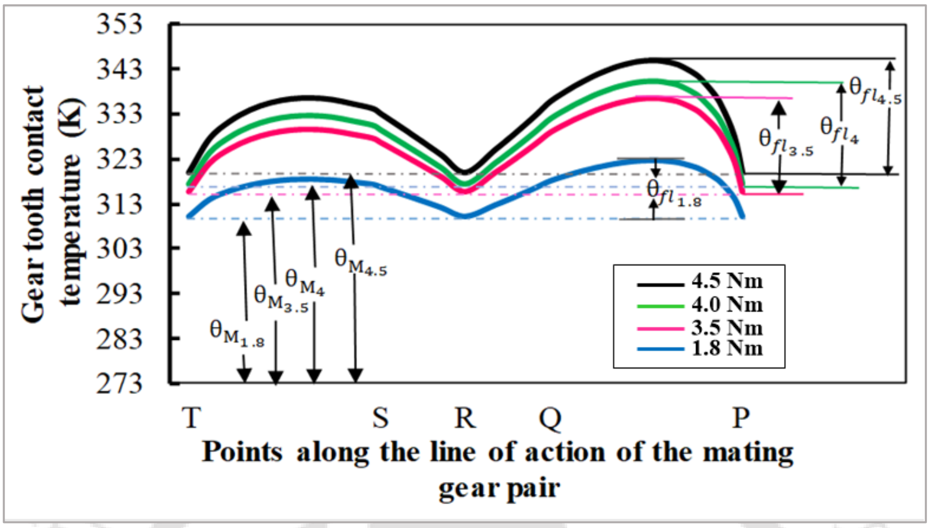

Figure 4.16 Computed gear tooth contact temperature along the line of action at various loads under lubricated conditions.

The contact temperature was calculated for the range of loads (1.8−4.5 Nm) and at a speed of 800 rpm using the model proposed by Blok and plotted in Figure 4.16. This plot indicates the gear tooth contact temperature corresponding to the tooth profile position from SAP and EAP (or P and T). By adding flash temperatures to the tooth temperatures, it is observed that the contact temperature of the test polymer gear reached a maximum in the flank and face regions compared to the pitch region. After reaching its peak point, the temperature started to decrease due to a dominant load-sharing factor in this region, as shown in Figure 4.14 (c). The main reason for the higher flash temperature in the flank region is the higher value of the sliding velocity $\left|v_{r1(i)} - v_{r2(i)}\right|$and lower value of the product of the tangential velocity and thermal contact coefficient$\left(B_{M1}\left(v_{r1(i)}\right)^{0.5} + B_{M2}\left(v_{r2(i)}\right)^{0.5}\right)$. The maximum contact temperature between SAP−LPSTC, or P−Q, is observed along the line of action. The maximum contact temperature in the flank region is 1.3−2.9 % higher than that in the face region of the test gear for the considered load. Lemanski (1965) also reported a maximum temperature between SAP−LPSTC while running a spur gear under Mil-L−7808 synthetic oil. Owing to the zero-sliding velocity at the pitch point, the resulting flash temperature becomes zero, and the corresponding maximum temperature would be due to the tooth temperature only. At SAP and EAP, the flash temperature is zero, as the load-sharing factor is assumed to be zero at this point, as shown in Figure 4.14 (c). When the load increases (1.8–4.5 Nm), the contact temperature also increases (322–345K).

4.7.1.2 Lubricant film thickness

Elastohydrodynamic lubrication (EHL) theory helps to the study of lubricant film between elastically deformable mating surfaces (bearings, gears, rubber seals, and human joints). For gear pairs under lubrication, it is essential to measure the film thickness between the contact points. The viscosity of lubricant does not vary considerably as the change in pressure is minimal in the case of polymer gear pair due to its low elastic modulus. For determining the lubrication regime, dimensionless parameters related to viscosity, elasticity, and system character are required. In this study, for the computation of film thickness, the procedure reported by Dearn *et al.* (2013) adopted

Dimensionless viscosity parameter

$$g_1 = \left(\frac{\alpha^2 {w_n}^3}{\eta_0 \overline{U} {\rho_n}^2}\right)^{1/2} \tag{4.34}$$

where α is pressure viscosity coefficient (mm^2/N) and $\overline{U}$ is the entraining velocity (mm/s).

Entraining velocity,

$$\overline{U} = \omega r_{w1}\, sin\alpha_{wn} \tag{4.35}$$

Dimensionless elasticity parameter

$$g_3 = \left(\frac{{w_n}^2}{\eta_0 \overline{U} E_r \rho_n}\right)^{1/2} \tag{4.36}$$

Dimensionless system character parameter

$$g_4 = \left(\frac{\alpha^4 {E_r}^3 \eta_0 \overline{U}}{\rho_n}\right)^{1/4} \tag{4.37}$$

(Transitional region (TR region) (0.1 < g_4< 2.2) applicable for polymer lubricated with mineral oil.

Actual film thickness

$$h = \frac{\bar{h}\eta_0 U R}{w_n} \tag{4.38}$$

Dimensionless minimum film thickness parameter

$$\bar{h} = 0.853 g_1 \, g_3^{-0.664} + 3.41 g_3^{0.77} \qquad 1 < g_3 < 100 \tag{4.39}$$

Specific film thickness or minimum film thickness

$$\lambda = \frac{h}{R_{at}} \tag{4.40}$$

where R_{at} is the equivalent surface roughness (μm)

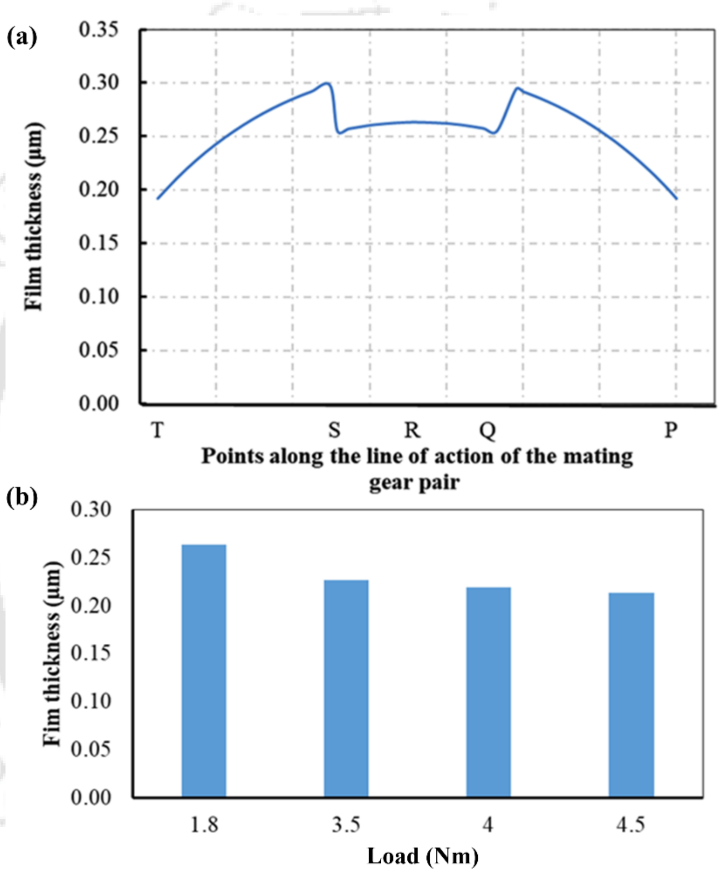

Figure 4.17 (a) Variation in the minimum film thickness along the line of action for the meshing gear pair subjected to a load of 1.8 Nm and (b) The computed central film thickness at the pitch point when the gear pair is subjected to various considered loads.

Figure 4.17 (a) shows the variation in the minimum film thickness along the line of action of the meshing gear pair subjected to a load of 1.8 Nm. In the single tooth contact region, the film thickness is maximum at pitch point (R) owing to the high normal relative radius of curvature (Figure 4.14 (a)). As the contact point progresses from the pitch point on both directions, the decrease in film thickness is very gradual up to Q (LPSTC) and S (HPSTC) due to concurrent decrease in the radius of curvature. During the transition from single tooth contact region to double tooth contact region, the slope of the film thickness curve changes. In the region S to T, initially, the film thickness is high due to the less load at this point, whereas, at P (SAP) and T (EAP), the film thickness is minimum due to the lower normal relative radius of curvature at these points (Figure 4.14 (a)). Similar trend was also observed by Dearn *et al.* (2013). Figure 4.17 (b) shows the minimum film thickness at the pitch point when the gear pair is subjected to various considered loads. The film thickness decreases with an increase in load. To compare with the results of Dearn *et al.* (2013), the ideal load-sharing factor has been considered.

This section presented the failure analysis of the test gear at various loads under lubricated conditions. Failure is determined by visual examination of the gear teeth surfaces. The failure load is the load that caused both scuffing and flank edge damage of the test gear teeth. Unlike in the dry conditions, in the lubricated conditions, pitting is not observed at any of the considered loads. This could be attributed to a reduction in the gear tooth modulus.

4.7.2 Wear and damage morphology of test gears under the lubricated condition

Figure 4.18 (a–e) show the various stages of the life of the test gear subjected to a 1.8 Nm load under lubricated conditions. The test gear that is run up to 5.7×10^5 cycles (Figure 4.18 (b)) shows only uniform wear on the face and flank surfaces. Although no wear marks are observed, gear tooth reduction is observed, and is shown in Figure 4.4. In contrast, under the dry condition, the gear exhibited pitting under the same loading condition. Senthilvelan (2006) noted that the maximum shear stress depth was higher for gear materials having low elastic moduli. Polyamide 66 and steel gear material have elastic moduli of 2.7 and 200 GPa, respectively, corresponding to their maximum shear depths of 0.10 and 0.02 mm. It has already been established that a reduction in the elastic modulus of the material in contact increases the depth from the surface at which maximum sub shear stress appears. The chances of crack growth up to the surface at higher shear stress depth reduce, which results from a lower probability of pitting failure. Baena *et al.* (2018) immersed polyamide 66 tensile specimen in biodiesel (Palm oil, methanol) for 14 weeks at 328 K and observed increased polyamide ductility. It was reported that it could be due to the physical absorption of the solution by polyamide. Hassan *et al.* (2011) carried out a tensile test evaluation of polyamide 66 material under dry and wet (after 24 h immersed in hot water) conditions and found that the tensile moduli of PA 66 under dry and immersed conditions were 0.7 and 0.38 GPa, respectively. Water is the usual/common plasticizer being several polar polymers, including polyamide material. Plasticizers decrease the glass transition temperature and crystallinity along with

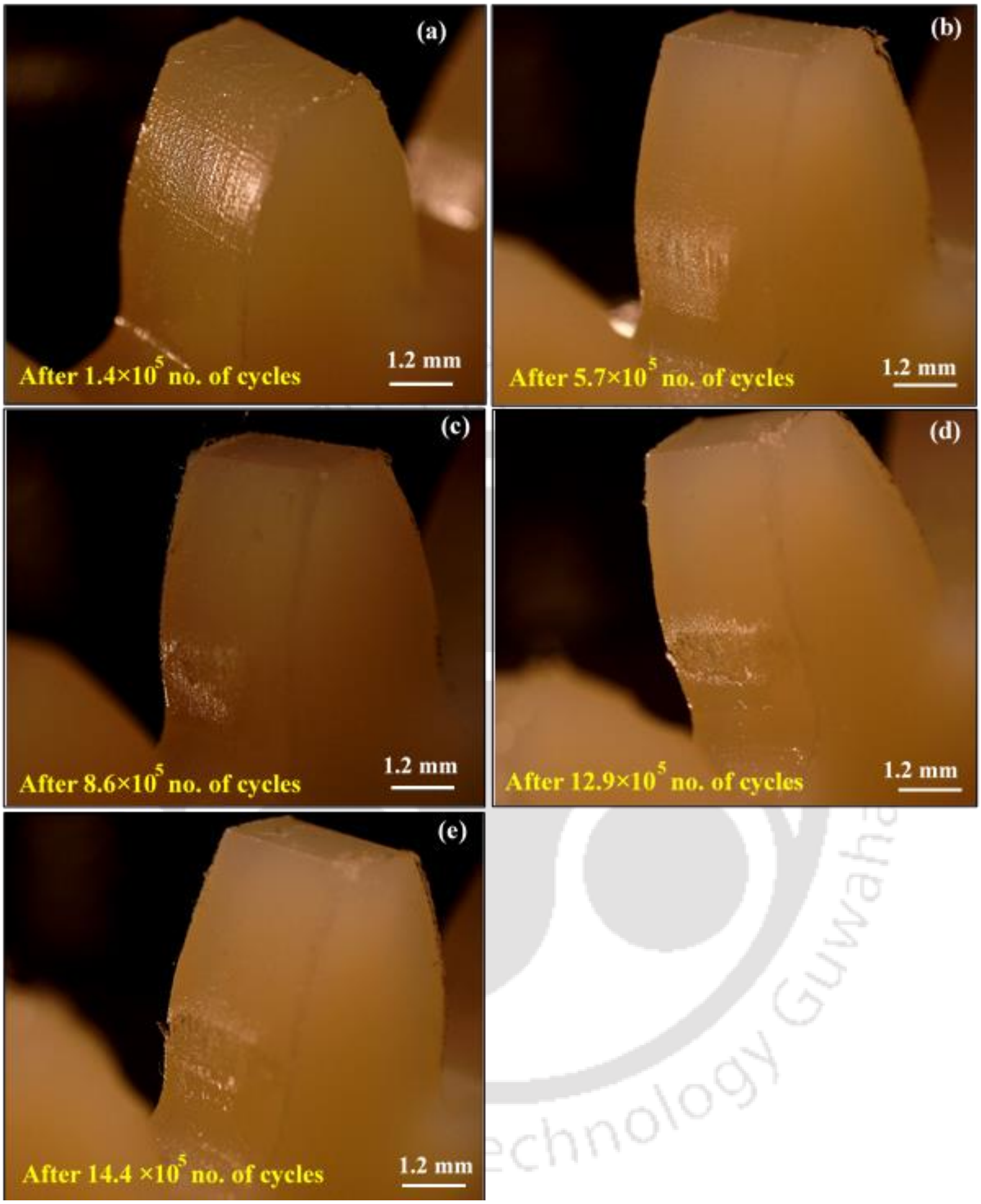

Figure 4.18 (a–e) Digital microscope image of the test gear tooth subjected to the 1.8 Nm load under lubricated condition

diluting the amorphous phase. As a result, the modulus and breaking stress decrease, and elongation to break increases. The measured modulus of the gear material is found to be 0.954 GPa after immersion of 30 hours. Beyond 5.7×10^5 cycles, as shown in Figure 4.18 (c–e), scuffing begins and grows with an increase in the cycles between SAP and the LPSTC region.

The initial wear is caused by the asperities present on the mating gear tooth surfaces. After the initial wear, the wear in severe form (scuffing) occurs due to the contact stress in the presence of a lubricant. In this region, the contact temperature achieves a maximum, as shown in Figure 4.16. The test was terminated at 14.4×10^5 cycles, when the test gear exhibited severe scuffing, as shown in Figure 4.18 (e). Illenberger and Stahl (2019) also reported severe damage on the flank region of the lubricated PEEK gear while paired with metal gear under lubricated conditions. Under the lubricated condition, Hasl *et al.* (2018) observed plastic deformation in the polyacetal gear's dedendum area due to the steel gear's approaching tip edge.

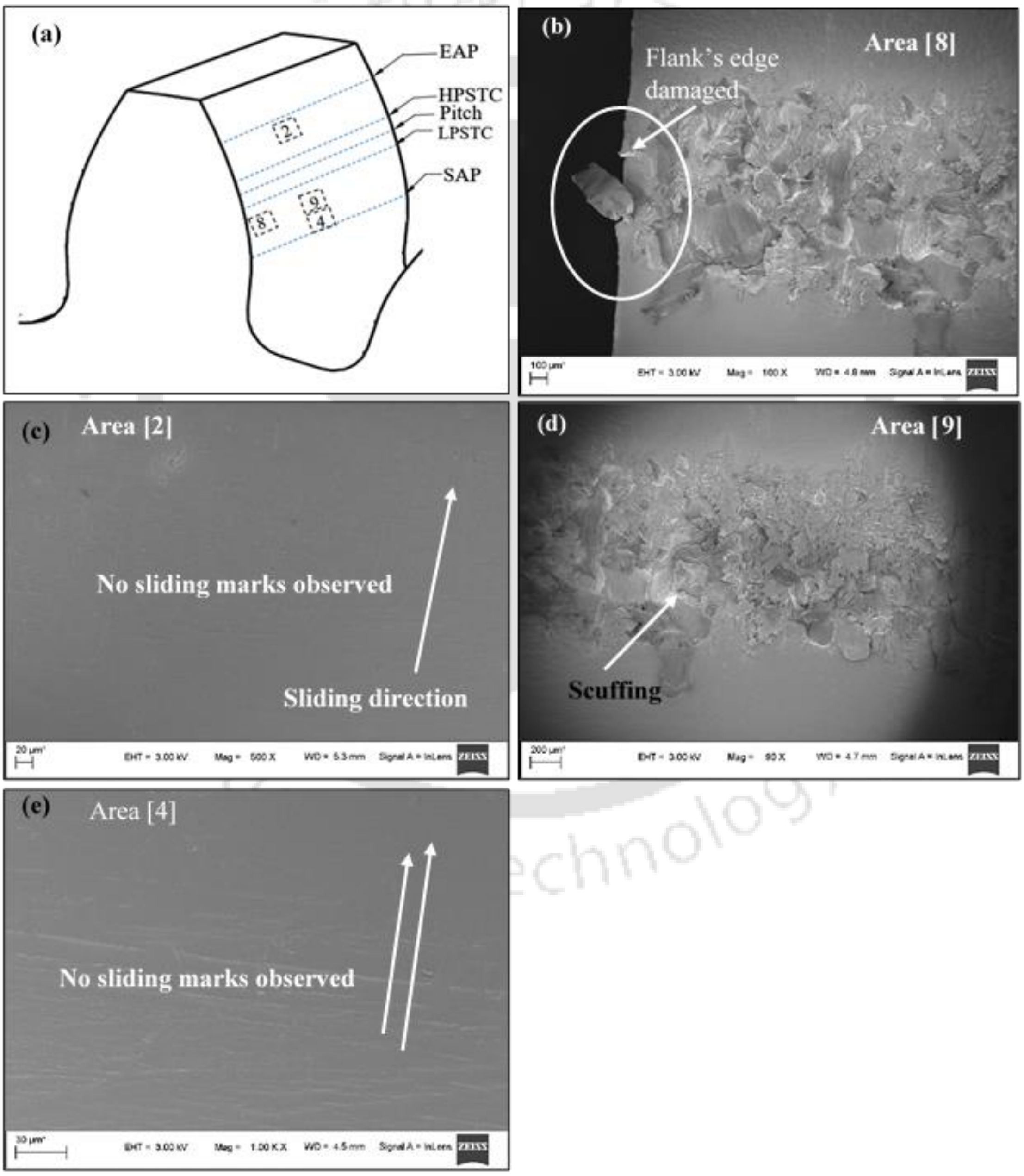

Figure 4.19 (a) Schematic view, and (b–e) FESEM morphology, showing the failure surface of the test gear tooth subjected to a 1.8 Nm load under the lubricated condition

Niemann *et al.* (1961) performed the test on an alloy steel gear with loads in the 2.4–401 Nm range in the presence of three different mineral gear oils under immersed lubricated conditions using FZG apparatus and observed scuffing/scoring on the flank of the test gear tooth. The FZG test can check the safety against scuffing to any gear set run any desired operating conditions. Padmore and Rushton (1964) examined a hardened EN 34 gear in the presence of the SAE 90 lubricant. Scuffing was observed in the flank region of the test gear. Scuffing is caused by the critical flash temperature in the contact region.

To further understand the wear morphology, failed gears (after 14.4×10^5 cycles) were observed with FESEM. A schematic view of tooth surface failure is shown in Figure 4.19 (a). Figure 4.20 (a–d) shows the morphology of the test gear tooth surface. Figure 4.19 (a) shows the portion of the flank where detachment is observed. No plastic flow is observed on the middle of the face of test gear surface (Figure 4.19 (c)) under the lubricant condition. However, the plastic flow is observed with finer subsurface cracks near the edge of the face region (Figures 4.8 (b) and 4.8 (f)) under the dry condition at the same load. It is to be noted this test gear under the dry condition exhibited 10 times lower life compared to the lubricated condition. Scuffing in the middle of the flank is shown in Figure 4.19 (c). No sliding marks on the lower portion of the flank are observed (Figure 4.19 (d)). However, the gears tested at the same load but in dry conditions exhibited sliding marks on the lower flank surface (Figure 4.8 (g)). The damaged surface area on the test gear tooth surface is lower under lubricated conditions compared to dry conditions.

Figure 4.20 (a) shows morphology of failed surface of the test gear subjected to a load of 3.5 Nm under lubricated gear condition. A digital image and schematic view of the test gear tooth surface after failure (3.5 Nm, 5.7×10^5 cycles) are shown in Figure 4.20 (a) and (b), respectively. At this loading condition, owing to the higher load (3.5 Nm), the presence of a lubricant accelerates plastic flow on the middle of the face of the test gear surface (Figure 4.20 (c)). The test gear subjected to the same load but under dry conditions exhibited subsurface cracks in the direction normal to the sliding direction. Under lubricated gear conditions, gears subjected to the load of 1.8 Nm do not show plastic flow. Severe scuffing on the flank surface is depicted in Figure 4.20 (d). Mild sliding marks are observed at this load on the lower portion of the flank region (Figure 4.20 (e)) under the lubricated condition. This could be due to the presence of a lubricant film that reduced friction and wear. However, test gears running under dry conditions show severe sliding marks at this load (Figure 4.9 (h)).

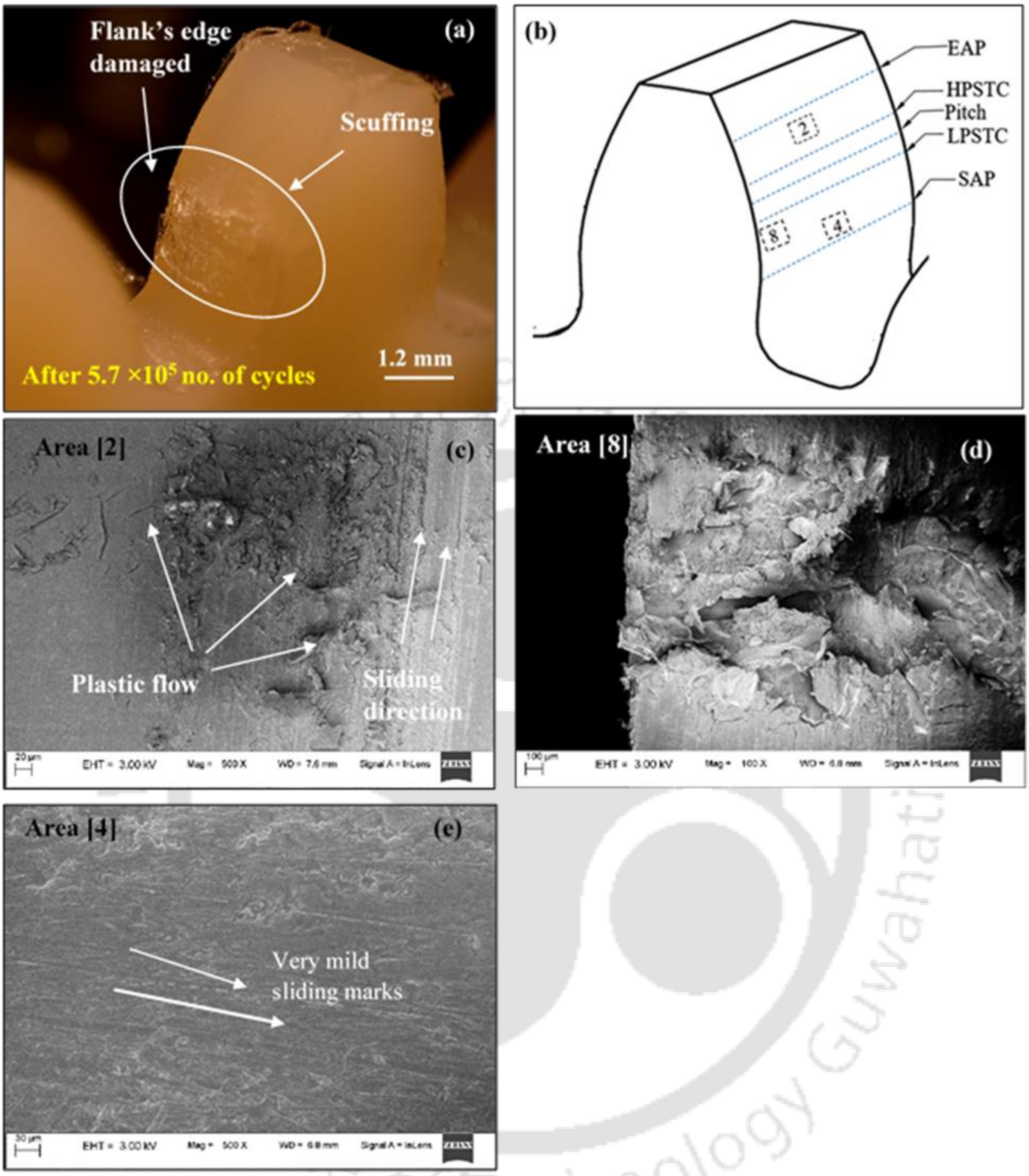

Figure 4.20 (a) Digital microscope image, (b) Schematic view, and (c–e) FESEM morphology, showing the failure surface of the test gear tooth subjected to a load of 3.5 Nm under lubricated gear condition.

The test gears exhibited scuffing failure at 4 Nm after 4.3×10^5 cycles (Figure 4.21 (a)). A schematic view of the test gear tooth surface is depicted in Figure 4.21 (b). To further understand the wear morphology, surface was observed with FESEM and shown in Figure 4.21 (b–f). No initial subsurface cracks are observed on the edge of the face of the test gear tooth under lubricated gear conditions (Figure 4.21 (c)), unlike under dry conditions. Figure 4.21 (d) shows the worn surface at 4 Nm very pronounced large thin polymer flakes are formed at the face surface of the sliding and are almost always associated with the breaking out / transferring at the surface of the slide out. This result reveals that cohesive forces inside the polymer weakened in this condition. As the load increased the scuffed area increased (Figure 4.21 (e)). Under the lubricated condition, lubricant diffuses into the polymer surface could weaken the bonds between polymeric chains (Plasticization), resulting in the reduction of strength and hardness of the polymer.

In contrast, a ripple-like pattern normal to the sliding direction along the smooth surface is observed in the flank region of the test gear as depicted in Figure 4.21 (f), whereas in dry conditions and low loading conditions, this feature is not observed. A ripple (an arrangement of plastic flow) is principally related to the interaction between the lubricant film and surface in the presence of a high temperature (Landen (1968)). The presence of lubrication contributes to this adhesion-dominated fatigue failure. A similar feature was observed by Zhang *et al.* (2015) while investigating the block-on-ring performance of PEEK against steel in the presence of diesel oil and engine oil. The studied sliding speed varied from 0.3 to 1.8 m/s condition; the system lied in boundary friction regime. At higher loading under lubricant conditions, severe sliding marks are observed (Figure 4.21 (f)). On the other hand, at low loading conditions, mild wear marks are observed on the face and in the lower flank regions.

The damaged surface of the test gear tooth surface subjected to a load of 4.5 Nm is depicted in Figure 4.22 (a). A schematic view of the failed tooth surface is shown in Figure 4.22 (b). Figure 4.22 (b–e) are FESEM images of a test gear tooth subjected to a load of 4.5 Nm under lubrication after 2.8×10^5 cycles. Under lubrication, no cracks are observed near the edge on the face region (Figure 4.22 (b)), whereas cracks are observed in the dry conditions (Figure 4.11 (a)). As shown in Figure 4.22 (c), some wear particles are entrapped and compacted onto the face region during the meshing under the lubricated condition. Due to this, the limited amount of lubricant on the interface existent at the mating surfaces. It is clear from the observation that, by increasing the load, the damaged area increased in the gear tooth flank lower region, as shown in Fig. 4.22 (f) owing to an increase in the product of pressure and velocity. On the other hand, at low load condition (3.5 and 4 Nm), only sliding marks are observed, and at the same loads under dry conditions, severe plastic deformation is observed. Table 4.1. Lists the surface failure modes of the test gear tooth at various loads under dry and lubricated conditions.

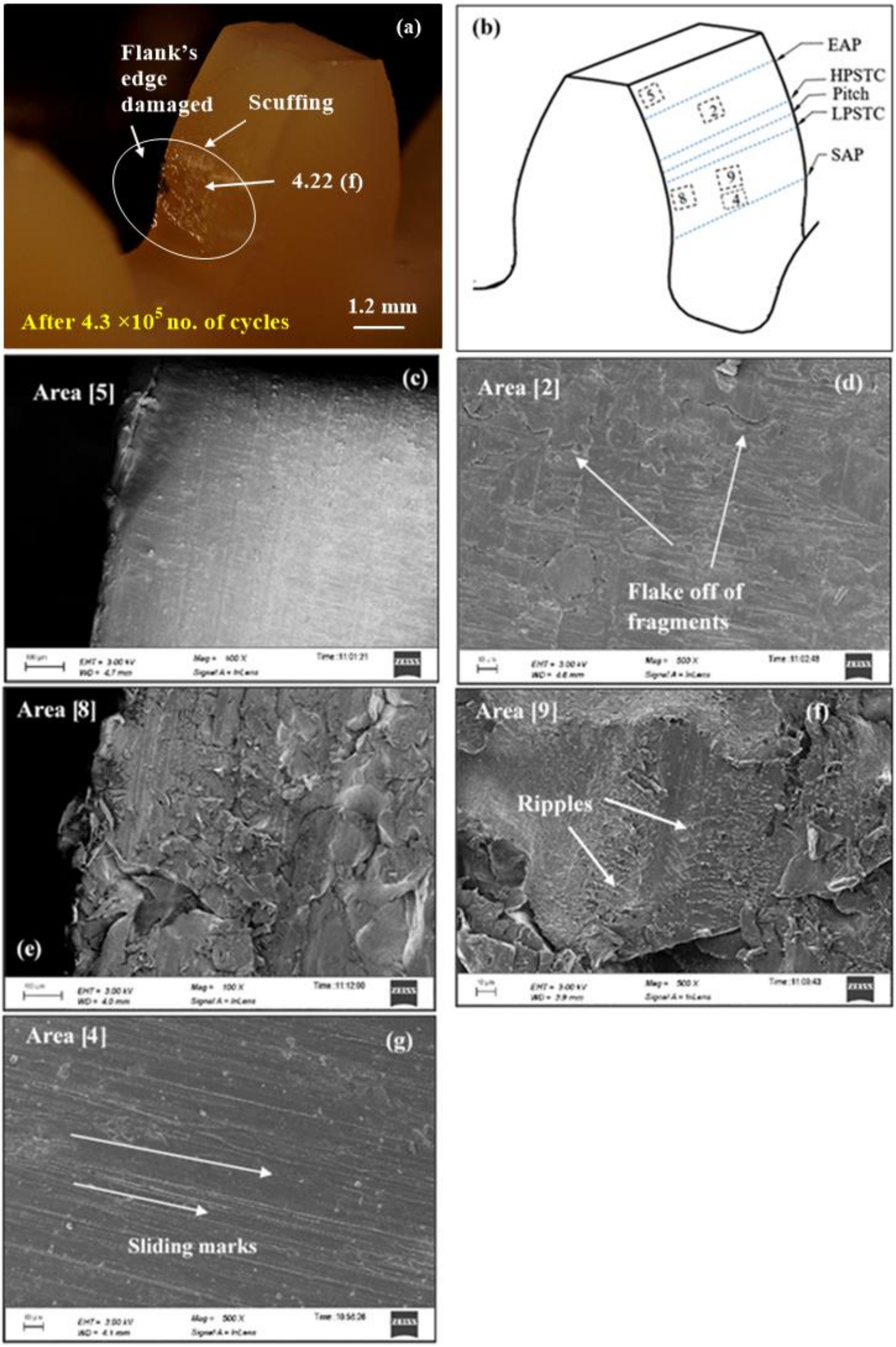

Figure 4.21 (a) Digital microscope image, (b) Schematic view, and (c–g) FESEM morphology, showing the failure surface of the test gear tooth at 4 Nm load under the lubricated condition

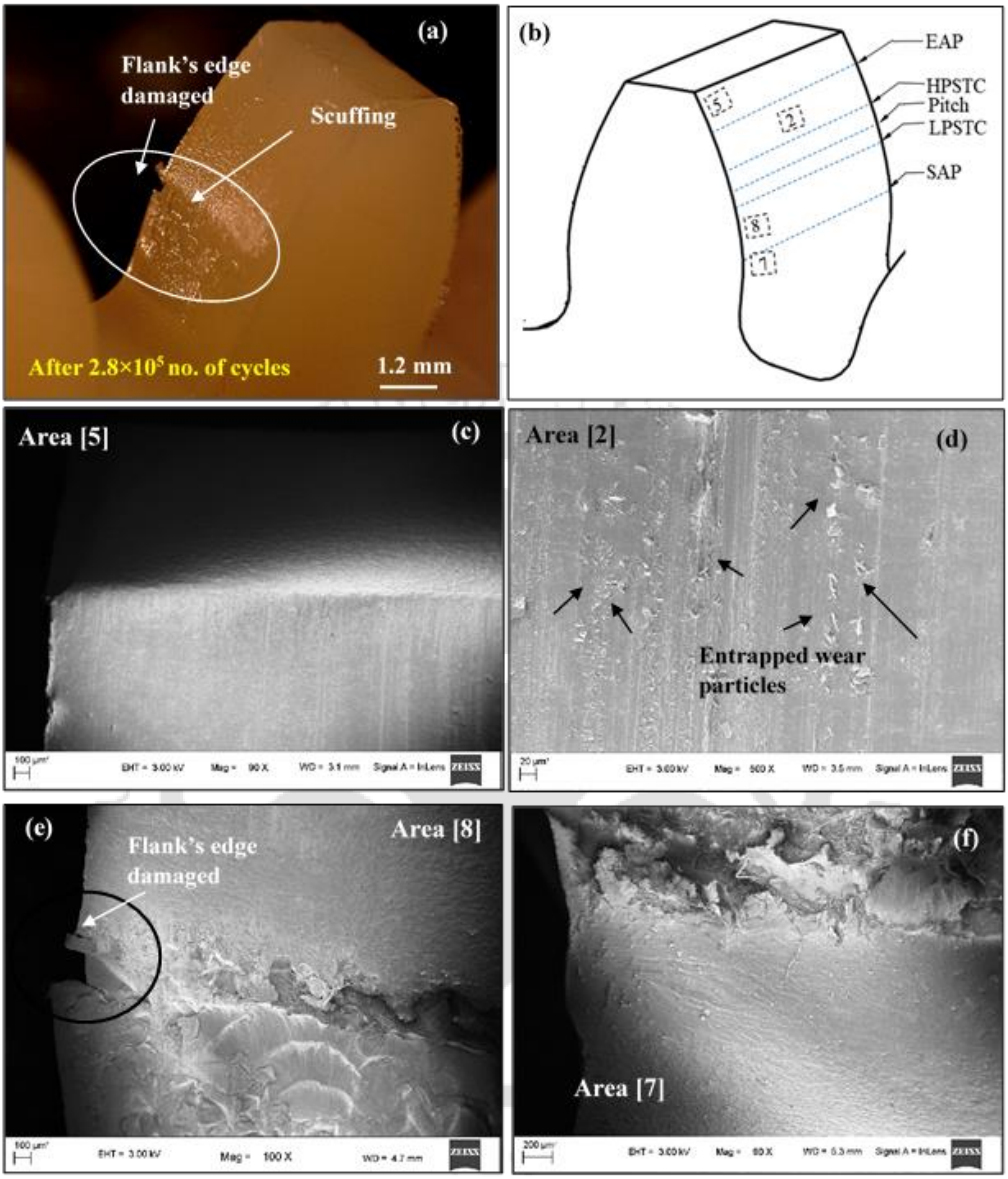

Figure 4.22 (a) Digital microscope image, (b) Schematic view, and (c–f) FESEM morphology, showing the failure surface of the test gear tooth at a load of 4.5 Nm under the lubricated condition

Table 4.1 Summary of failure modes.

Test conditions	Loads (Nm)	Failure mode of test gear	Life (10^5 cycles)
Dry	1.8	Pitting (pitch region), subsurface crack (near edge of the face and front face of the pitch region), plastic flow (middle of the face region), and mild sliding marks (lower flank region)	8.6
Lubricated	1.8	No plastic flow (middle of the face region), scuffing (flank region), and no sliding marks (lower flank region)	14.4
Dry	3.5	Local softening (pitch region), subsurface crack (near the edge of the face and the front face of the pitch region) and abnormal wear/plastic deformation (root region), and severe sliding marks (lower flank region)	2.8
Lubricated	3.5	Plastic flow (face region) and scuffing (flank region), and very mild sliding marks (lower flank region)	5.7
Dry	4	All modes of failure similar to the 3.5 Nm dry condition failure but comparatively severe in nature, subsurface crack (front face of the face region), and accumulated sliding material (pitch region)	1.4
Lubricated	4	Flake off of fragment (middle of the face region), scuffing and ripple (flank region), and sever sliding marks (lower flank region)	4.3
Dry	4.5	Severe plastic flow (middle of the face region), subsurface cracks (near the edge of the face and front face of pitch region), severe thermal damage (pitch region), and abnormal wear/plastic deformation (root region)	1.29
Lubricated	4.5	No subsurface cracks (near the edge of the face region), and severe scuffing (root region)	2.8

4.8 Summary

The durability performance of injection molded polyamide 66 gears under dry and lubricated conditions was investigated. The failure mode of the test gear under lubricated condition was significantly different from that under dry condition. Based on the results obtained from the above study, the following major conclusions were drawn:

- The net gear tooth temperature increased with an increase in applied load. The measured gear tooth temperature at a load of 4.5 Nm was observed to be about 32% higher than that at a load of 1.8 Nm under dry condition.
- Under lubricated condition, only a 3 K rise in lubricant temperature was observed when the load increased from 1.8 to 4.5 Nm. The lubricant between the interacting surfaces of the gear teeth dissipated the generated heat effectively from the gear teeth surfaces. This phenomenon resulted in a reduction in heat accumulation on the gear tooth surface. Gears tested under lubricated gear condition, compared to those tested under dry condition, at various loads (1.8–4.5 Nm) exhibited a 66– 200% enhancement in gear life.
- Surface pitting was observed as a dominant mode on the test gears near the pitch region under dry condition when the test gears were subjected to low load (1.8 Nm). Abnormal wear near the root, change in sliding direction, and heat build-up on the gear tooth surface led to the formation of surface cracks in the gear tooth pitch region at higher loads (3.5–4.5 Nm). However, test gears under lubrication condition did not show any cracks in the pitch region or other regions owing to improved heat dissipation characteristics.
- The contact tooth temperature computed along the line of action using the Block model shows the maximum temperature between SAP and the LPSTC region. This was confirmed by the observation of scuffing failure features on the test gear tooth precisely at this location under lubricated gear condition.
- The minimum film thickness of the gear pair under lubricated gear condition was computed along the line of action. A lower film thickness between the SAP and LPSTC regions compared to the pitch region also contributes to the scuffing failure in this region.

Chapter 5

Effects of mating gear on the surface durability of the polyamide gear

5.1 Introduction

In the previous chapter 4, the effect of lubricant on the performance of injection molded polyamide gear meshed with metallic gear was presented. In this chapter 5, mating gear was also considered as polyamide gear; with this work, the aspect of adhesion due to similar material is being considered. In this chapter, polyamide-polyamide gear pairs under dry and lubricated conditions were studied. In addition to the measurement of test gear surface temperature and lubricant temperature, contact fatigue failure features of both test and mating gear are also investigated for the comprehensive analysis entailing digital microscope and FESEM.

5.2 Methodology

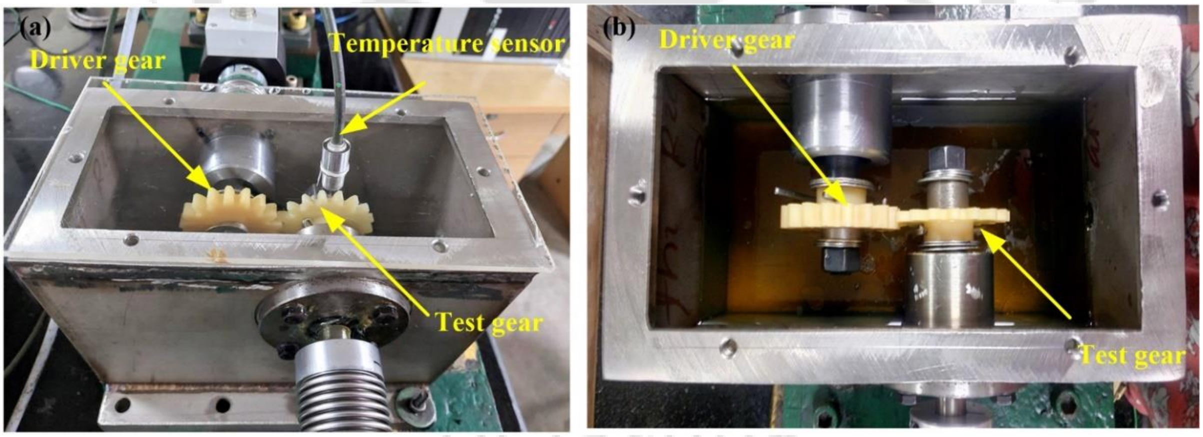

Figure 5.1 Close up view of polyamide-polyamide gear pair (a) Under the dry condition and (B) Under the lubricated condition

In this work, an 8 mm face-width injection-molded polyamide driving gear was connected to a 3HP PMDC motor that can rotate up to a maximum of 1500 rpm. The test (driven) injection molded polyamide gear has a 4 mm face width connected through the 1HP PMDC generator, which was loaded through a rheostat. The 8 mm wide polyamide driving gear is in mesh with a 4 mm wide polyamide driven gear. The experiment was conducted under dry and lubricated conditions at a range of torques 1.8–4.5 Nm and a rotational speed of 800 rpm. The test was terminated if no failure was detected until 2 million cycles. Figure 5.1 shows the close-up view of the polymer-polymer gear mesh.

5.3 Fatigue performance of test gear

The fatigue life of test gears when meshed with similar material at various loads under dry and lubricated conditions is presented in Figure 5.2. Test gear exhibited surface cracks near the pitch region under dry conditions at a lower load (1.8 Nm). Test gear exhibited a sudden rise in temperature and thermal damage at higher loads (2.5 and 3.5 Nm). The sudden temperature rise is due to the combined contact stress along with sliding and rolling motions. However, gears tested under oil-lubricated conditions exhibited improved life due to improved heat dissipation as well as reduced frictional resistance. Lubricated gear at a lower load of 1.8 Nm exhibited initiation of surface fatigue near the tip and face region. Pitting near the gear tooth tip region is observed when the lubricated gear is subjected to 2.5 Nm.

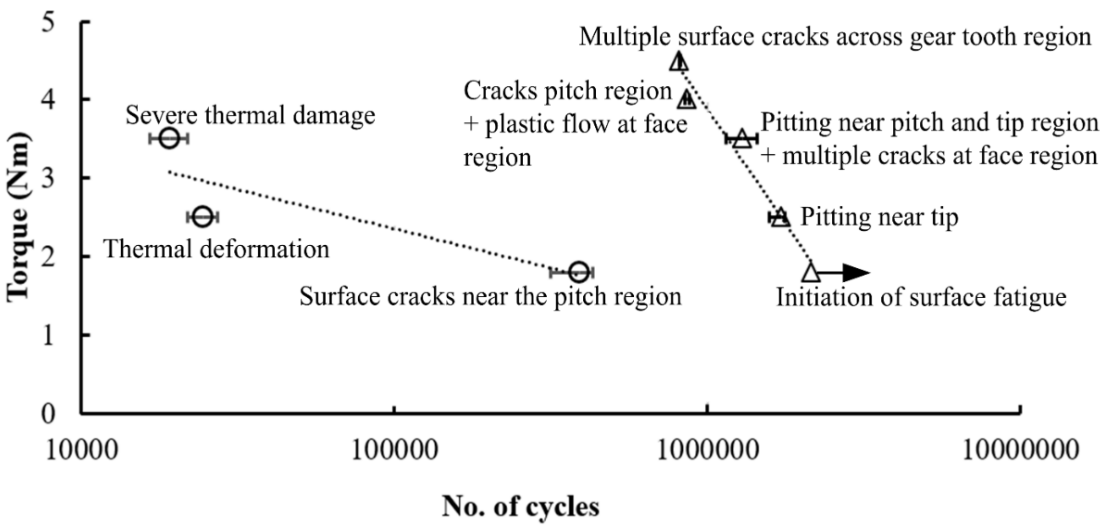

Figure 5.2 Gear life under dry and lubricated conditions

Test gear showed surface contact failure at higher loads (3.5–4.5 Nm), including multiple cracks. Thus, oil lubrication helps to avoid thermal failure, and surface contact fatigue failure features only are observed with enhanced life.

5.4 Temperature measurement

The measured tooth surface temperature of the test gear, while paired with similar material under dry conditions, is shown in Figure 5.3 (a). The gear tooth exhibited a rise in tooth surface temperature for all the considered loads. At 2.5 and 3.5 Nm, the temperature rise is very rapid and reached (350–360 K) which is confirmed by the thermal failure (Figures 5.8 (a, b) and 5.9 (a, b)).

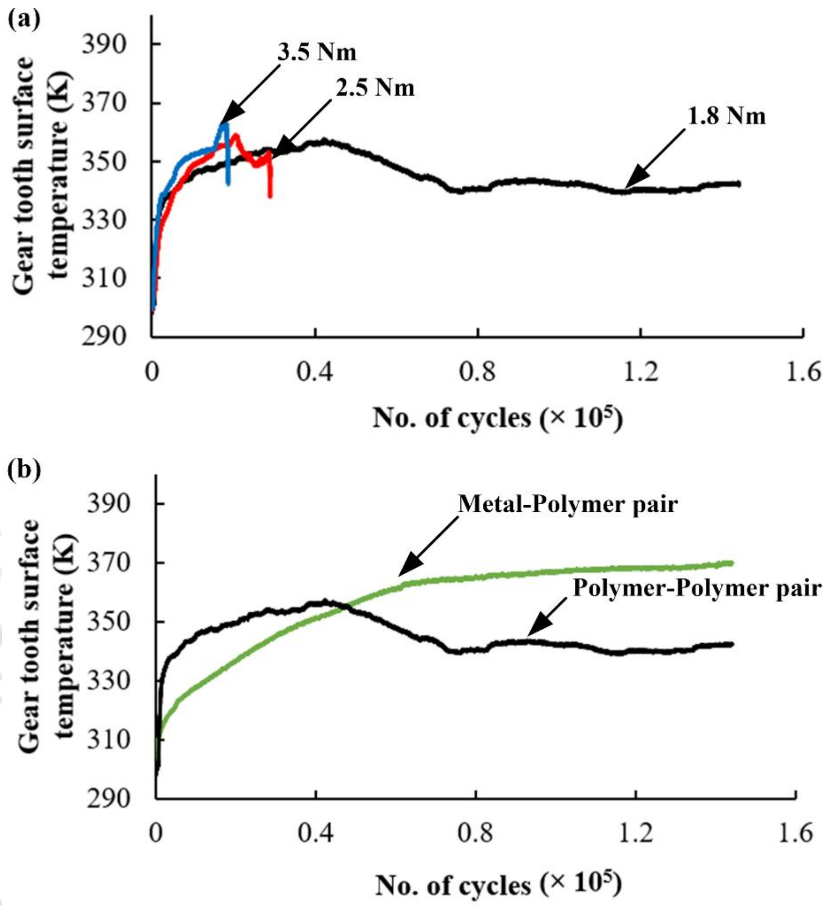

Figure 5.3 (a) Surface temperature of test gear tooth for polyamide-polyamide gear under dry condition at various loads and (b) Surface temperature of test gear tooth for polyamide-polyamide and steel-polyamide gear pair at 1.8 Nm unde dry condition

At 1.8 Nm loading condition, the tooth surface temperature of the test gear initially reaches about 350 K, then drops down and reaches saturation at about 340 K. In the beginning, the test gear exhibited higher temperature due to the increased adhesion between polymer-polymer contacts subsequently mating polyamide gear exhibited surface damage as test gear. Surface damage of the mating gear reduces the surface interaction, and hence the amount of heat generation and the net measured surface temperature is reduced. Yakut and Düzcükoglu (2014) also observed a drop in the surface temperature of polymer gear after the initial raise while in mesh with similar material at higher rotational speed due to adhesion. When the polyamide test gear meshed with the metal gear, the test gear surface temperature (was already reported in chapter 4); this rise and drop behavior of surface temperature was not observed (Figure 5.3 (b)). The adhesion component at the contact interface significantly influences the frictional behavior of polymer-polymer contacts (Erhard (1983)). The adhesive wear is the predominant mechanism when sliding polymers against polymers, whereas abrasive wear is the predominant mechanism when polymer materials slid against steel (Czichos (1983)).

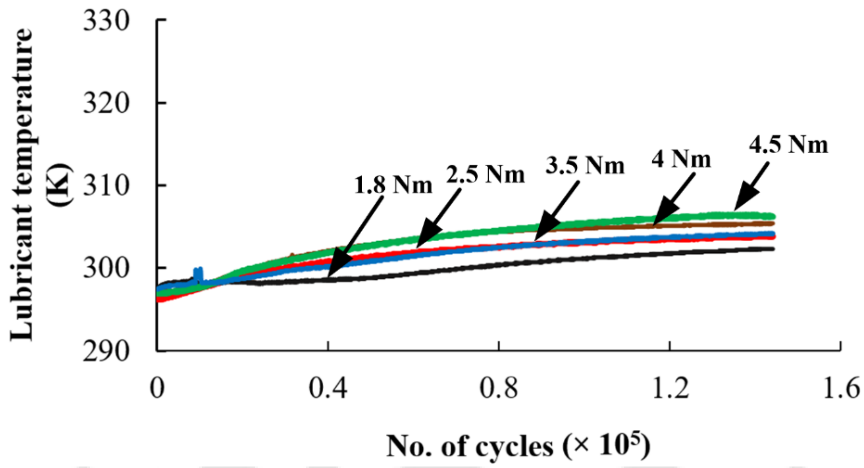

Figure 5.4 Lubricants temperature at various loads

Figure 5.4 shows the measured oil lubricant temperature for the various loads when the polyamide test gear mates with similar material. There is a temperature rise with an increase in the load; however, it is not significant.

5.5 Gear failure modes under dry conditions

Under the dry condition at 1.8 Nm, worn-out surfaces of test gear, as well as mating gear, have been depicted in Figure 5.5. Sliding wear marks are observed on both test and mating gear teeth (Figures 5.5 (a, b)) up to 1.4 $\times 10^5$ cycles. In addition, near the pitch region, an accumulation of wear particles in the form of the hump on the test gear and groove in mating is observed (Figure 5.5 (a, b)). These features are observed as sliding away from the pitch line on the mating gear results in a groove, whereas driving toward the pitch line results in a hump on the test gear.

Similar behavior was also reported by Mao *et al.* (2009) while running the polymer-polymer gear pair under dry conditions. As the running cycle progresses, these 'hump marks on the driven spread over a larger surface and disappear, as shown in Figure 5.5 (c). At the end of 4.3×10^5 cycles, the face region exhibited a smooth surface due to the same direction of gear rolling and sliding (Figure 5.5 (c). Figure 5.5 (c) shows that the torn surface is observed on the flank region due to the opposite direction of gear rolling and sliding. Figure 5.5 (d) reveals the substantial groove formation on the mating gear pitch region after substantial service life.

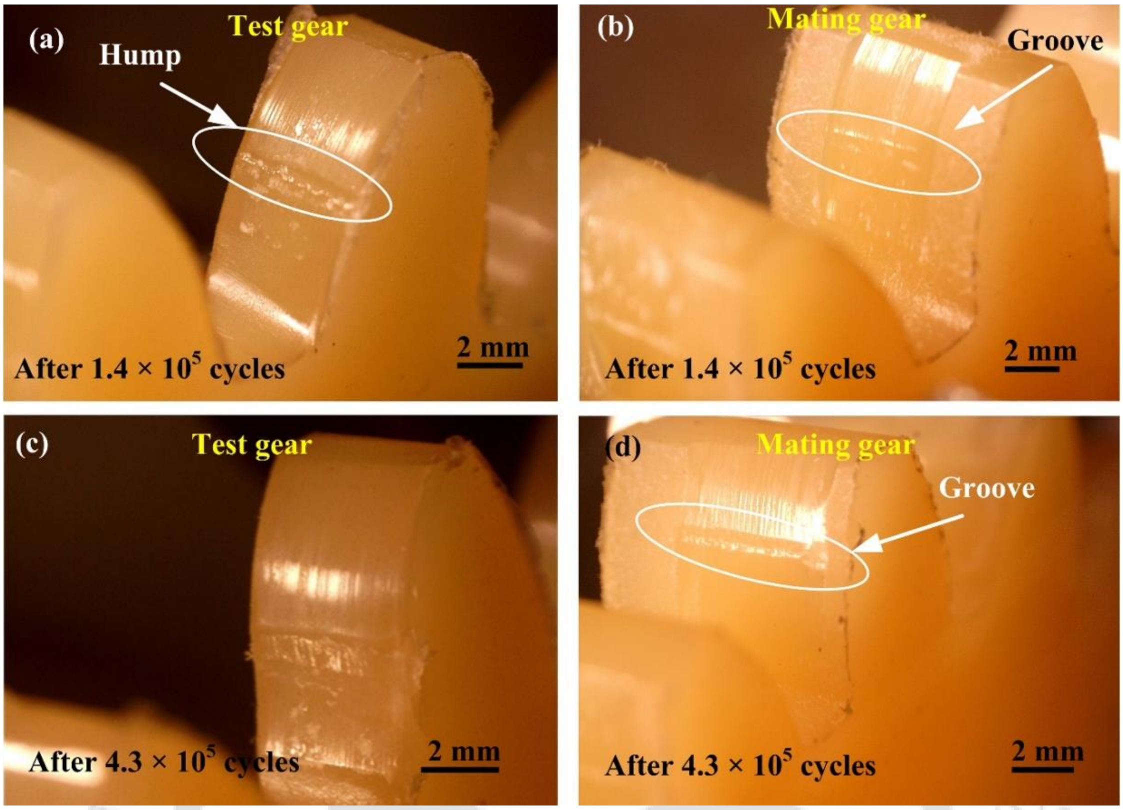

Figure 5.5 Worn-out teeth surface at 1.8 Nm under dry conditions (a, c) Test gear and (b, d) Mating gear

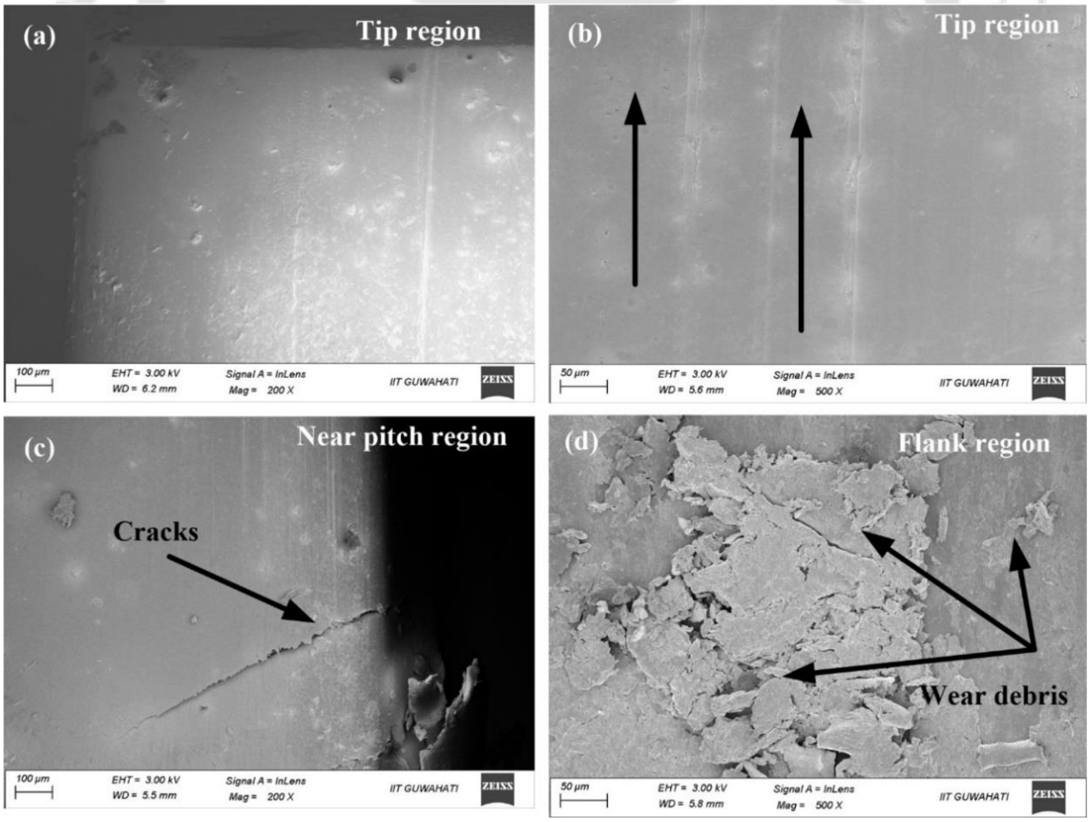

Figure 5.6 FESEM morphology of worn-out test gear surface at 1.8 Nm under the dry condition

The worn-out test gear surface was detected using FESEM to analyze gear failure. On the tip region of the test gear, no multiple subsurface cracks are observed (Figure 5.6 (a)). However, when the test gear meshed with the metal gear, multiple subsurface cracks are observed on the tip region of the gear after 8.6 $\times 10^5$ cycles (Figure 4.8 (f)). This difference in behavior could be due to the hard mating steel gear contact with the polymer test gear, which results in comparatively higher contact stress and friction. Figure 5.6 (b) depicts the face region of the test gear and reveals only mild sliding marks in the sliding region. In contrast, when the test gear was mesh with a steel gear, plastic flow perpendicular to the sliding direction was observed at this load after 8.6 $\times 10^5$ cycles (Figure 4.8 (b)). Figure 5.6 (c) reveals cracks near the pitch region. Figure 5.6 (d) reveals a large amount of flat and plate-like wear material on the flank region of the test gear tooth.

The worn-out surface of the mating gear was also detected in FESEM after completing 4.3 $\times 10^5$ cycles (Figure 5.7). Figure 5.7 (a) revealed the sliding marks on the face, and Figure 5.7 (b) revealed a worn-out surface and an adjacent molded surface, which is not in contact with the test gear.

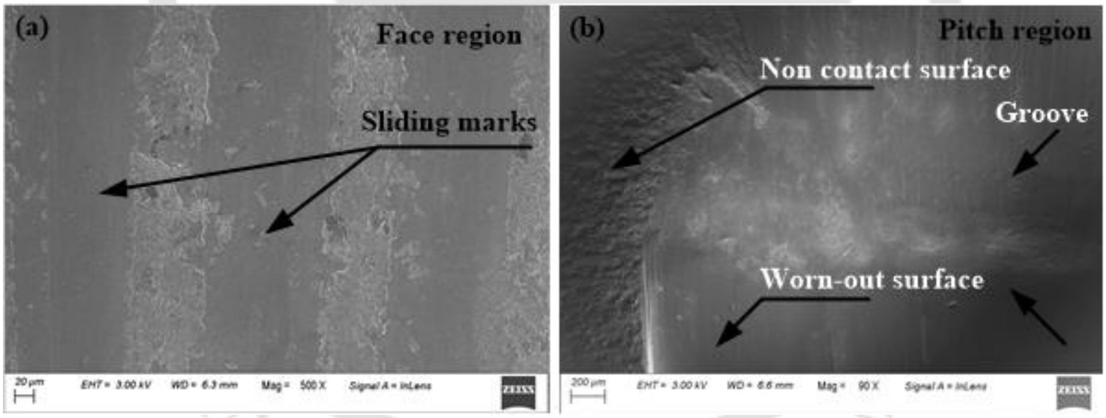

Figure 5.7 FESEM morphology of mating gear at 1.8 Nm under dry condition

At 2.5 Nm and 3.5 Nm, the test gear showed thermal-induced failure, which is confirmed by the plastic deformation (Figures 5.8 (a) and 5.9 (a)). At these higher loads, higher contact stresses combined with frictional sliding generate higher heat generation. In addition, due to repetitive tooth bending and viscoelastic characteristics of gear material, the gear tooth experiences hysteresis heating. The higher temperature sensitivity of polymer gear, heat accumulation due to surface interactions, and material hysteresis during operation accelerate contact fatigue and root cracking (Kukureka *et al.* (1999), Gauvin *et al.* (1983), Liu *et al.* (1987)). PEEK-PEEK discs under rolling-sliding contacts exhibited surface melting and contact fatigue damages under higher load and slip-ratio conditions Hoskins *et al.* (2014). Under polymer-polymer gear pair contacts, the adhesion component of friction will dominate. In addition, due to the poor thermal conductivity of mating polymer gear, the heat dissipation would be less, which results in a higher net measured surface temperature of test gear. However, when the test gear mates with steel gear at 3.5 Nm, the test gear exhibits cracks at the pitch region combined with thermal softening (Figure 4.9 (b, d)). Mating steel gear helped dissipate the generated heat, so the severe thermal failure of the test gear is avoided. The worn-out test gear and mating gear teeth surface at 2.5 Nm under the dry condition are depicted in Figure 5.8. Figure 5.8 (a, b) reveals the severe wear, plastic deformation, and thermal softening on the test and mating gear tooth surface. FESEM morphology of the test gear teeth surface at 2.5 Nm is depicted in Figure 5.8 (c) and (d). A deformed involute profile near the pitch region is depicted in Figure 5.8 (c). Figure 5.8 (d) reveals the thermal softening.

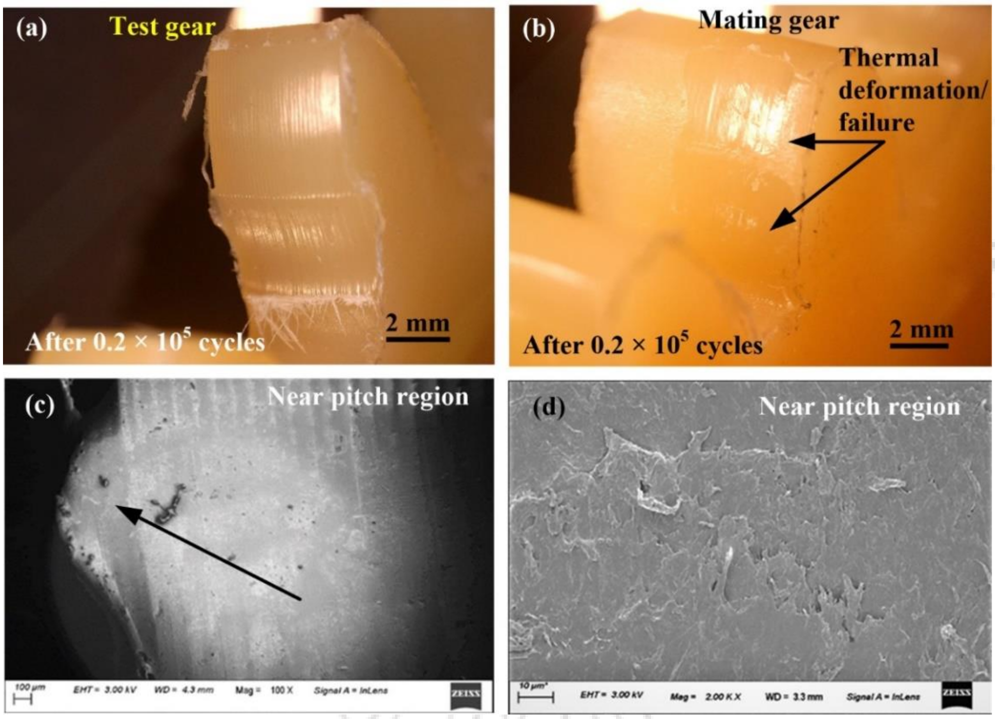

Figure 5.8 Worn-out test gear and mating gear tooth surface at 2.5 Nm under dry conditions

Test gear subjected to the higher load (3.5 Nm), the damage in the test gear is more severe, and a large amount of deformed sliding material accumulated near the pitch and flank region (Figure 5.9 (a)). Also, the failure revealed the softening of the test gear teeth surface. The mating gear tooth surface also reveals severe thermal failure (Figure 5.9 (b). Thermal failure in the POM–POM gear pair above the transition load under dry conditions was also stated by Mao *et al.* (2019). Figures 5.9 (c) and (d) depict the FESEM of the worn-out test gear surface at 3.5 Nm under dry conditions. Test gear tooth regions (face and flank) reveal molten layers (Figure 5.9 (c, d)). In the case of the test gear meshed with a steel gear, the face region reveals multiple cracks perpendicular to the sliding direction, and the flank region reveals severe sliding marks on the flank region at 3.5 Nm after completion of 2.8 ×10^5 (Figure 4.9 (f, h)).

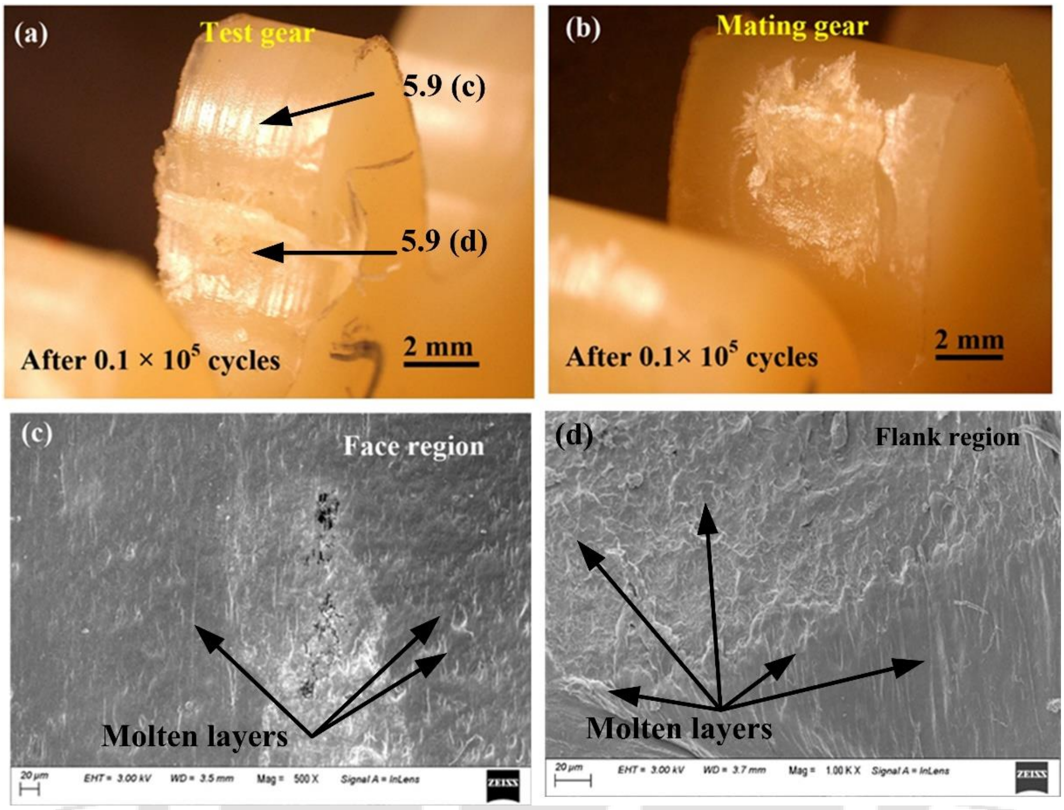

Figure 5.9 Worn-out test gear and mating gear tooth surface at 3.5 Nm under dry conditions

5.6 Gear failure mode under lubricated conditions

The worn-out test gear surface under lubrication at different cycles while testing at 1.8 Nm is depicted in Figure 5.10 (a) and (b). Gear tooth wear is infinitesimally small (Figure 5.10 (a) compared to dry condition (Figure 5.5 (c)) after a similar period (4.3 × 10^5) cycles). Lubrication prevented direct contact between the contact pair due to lubricant film formation between the contacts. This film lowered the friction and temperature between the contacts, dissipated the heat from the gear tooth surface, and resulted in reduced gear tooth wear. Yu *et al.* (2021) also observed significantly less wear (polymer-polymer gear) and less net surface temperature under lubricated conditions compared to dry conditions. Initiation of pitting is observed on the gear tooth near the tip region of the gear (Figure 5.10 (b, c)) after 20 × 10^5 cycles. Figure 5.10 (d) shows the mating gear surface after 20 × 10^5 cycles and reveals very mild wear on the surface.

The surface damage/mild wear near the tip region of the test gear could be due to the higher flash temperature near the tip region.

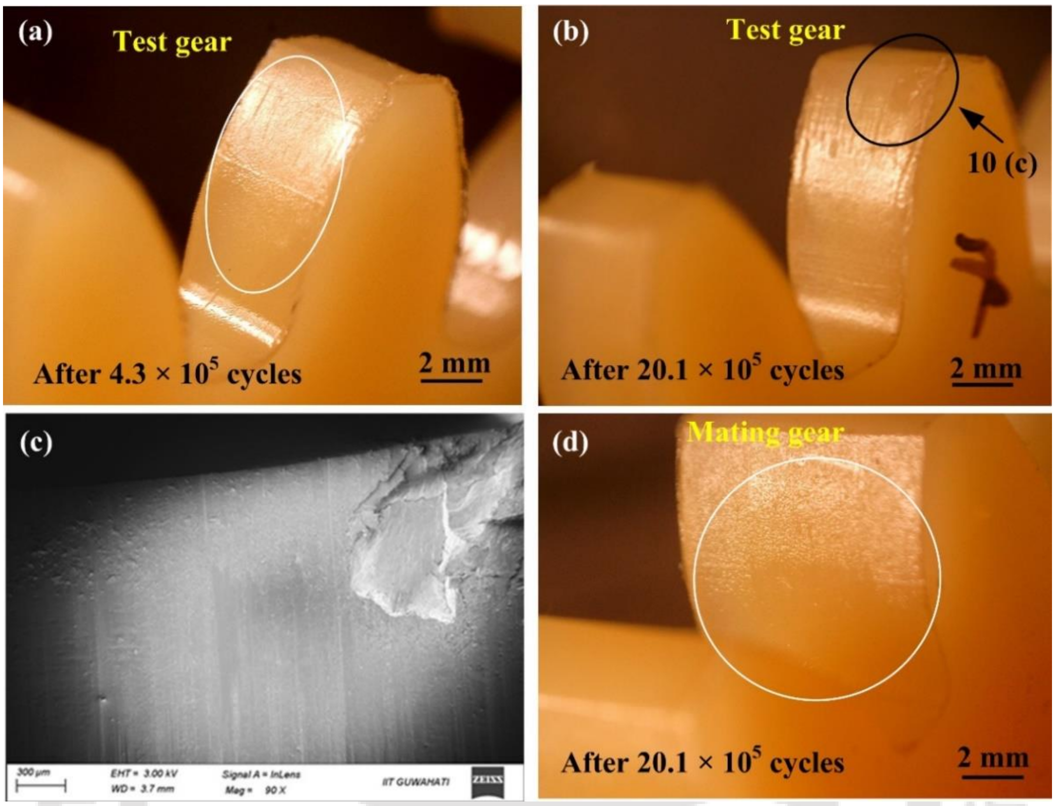

Figure 5.10 Worn-out lubricated gear surface at 1.8 Nm (a–c) Test gear and (d) Mating gear

Hook *et al.* (1993) predicted the flash temperature of polymer-polymer gear contact pair at various locations of the gear tooth, and it is higher at the gear's tip and root regions than at the pitch region. Mao (2007) also predicted the flash temperature of polymer-polymer gear contact pair at various locations of the gear tooth using a Finite different method by considering heat generation and dissipating during the operation, and it is higher at the gear's tip and root regions than the pitch region. When the test gear is in mesh with steel gear under lubrication, the flank region exhibited scuffing and has been reported in the previous chapter 4. Hasl *et al.* (2018) observed plastic deformation in the dedendum area of polymer gear due to the approaching tip edge of the steel gear under lubrication conditions. Severe flank wear was observed on polymer gear meshed with steel gear under lubrication conditions (Illenberger *et al.* (2021)). Thus, it observed that mating gear tip interaction as well as the higher flash temperature at the flank region, was responsible for the wear/failure at the flank region of polymer gear while in pair with a steel gear. In the case of the polymer-polymer gear pair, the polymer gear is not in mesh with the steel gear but with a polymer gear; hence the absence of hard tip interaction avoided damage at the root and but at the tip region.

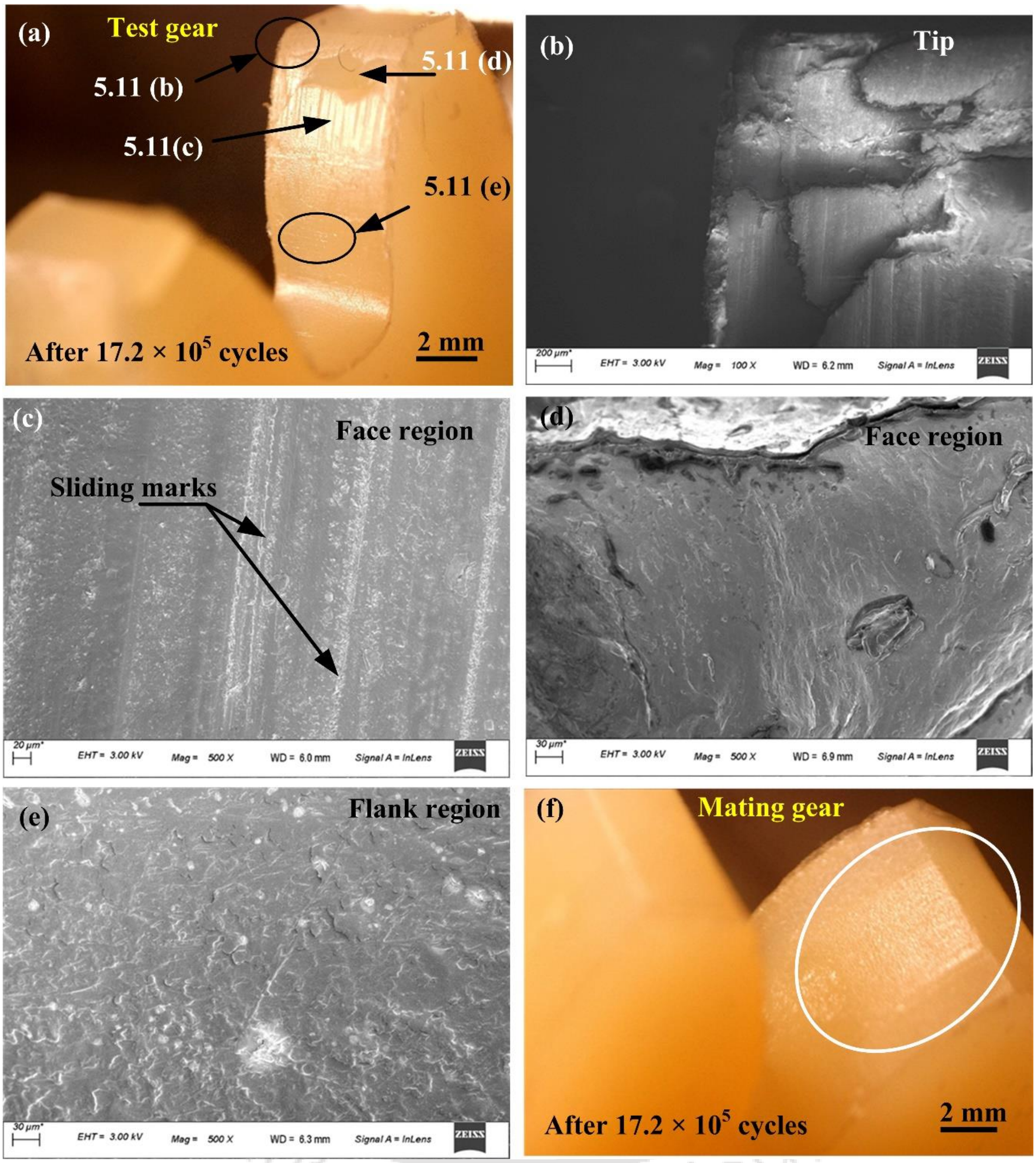

Figure 5.11 Worn-out lubricated gear surface at 2.5 Nm (a-e) Test gear and (f) Mating gear surface

The worn-out test gear and its failure morphology (2.5 Nm, lubricated) observed under FESEM after its life ($17.2{\times}10^5$ cycles) are shown in Figures 5.11 (a-e). The test gear exhibited pitting (Figure (5.11 a)) similar to steel gear. Pitting is observed on the tip region due to surface fatigue, as shown in Figure 5.11 (b). FESEM morphology reveals sliding marks on the face region Figure 5.11 (c). Figure 5.11 (d) shows the magnified view of the pit feature on the tip region of the gear tooth. Figure 5.11 (e) shows wear marks on the flank region of the test gear. In contrast, the gear exhibited severe plastic deformation under dry conditions at similar loading conditions. The mating gear image after 17.2 × 10^5 is depicted in Figure 5.11 (f), revealing an infinitesimal wear track.

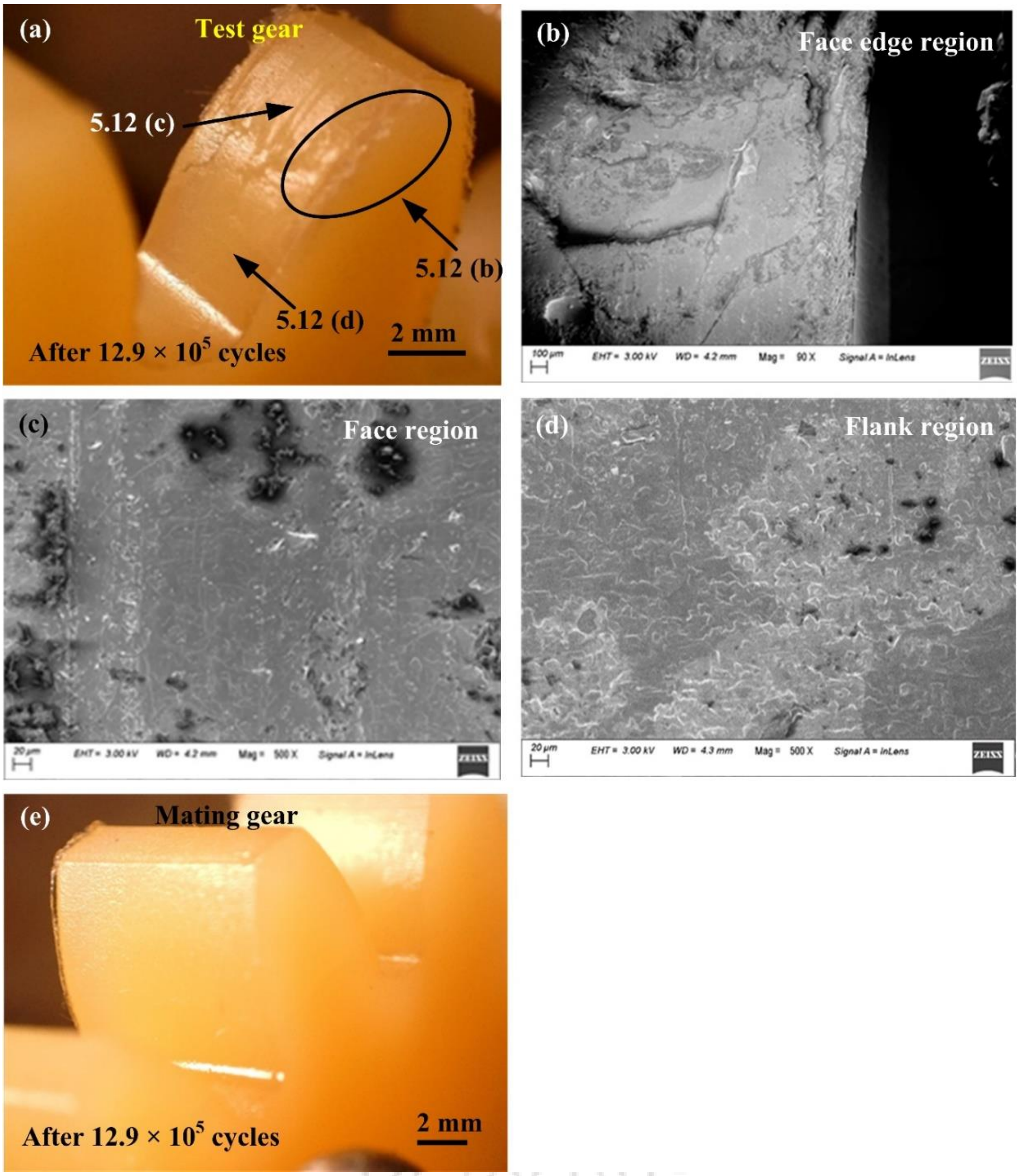

Figure 5.12 Worn-out lubricated gear surface at 3.5 Nm (a–d) Test gear and (e) Mating gear

Worn-out test gear image and FESEM morphology after the completion of 12.9 ×10^5 cycles at 3.5 Nm under lubricated conditions are shown in Figures 5.12 (a–d). Damage on the tooth face and pitch region has been observed. Figure 5.12 (a) reveals pits due to surface fatigue on the tooth surface. Figure 5.12 (b) reveals multiple subsurface cracks on the face region. Sliding marks on the face region are revealed in Figure 5.12 (c). Figure 5.12 (d) revealed separated fragments from the flank region. Figure 5.12 (e) shows the mating gear tooth surface where no significant wear is observed. However, when the test gear is run under dry operating conditions, after 0.1×10^5 cycles, thermal damage is observed, which is confirmed by the molten layers (Figure 5.9 (c, d)).

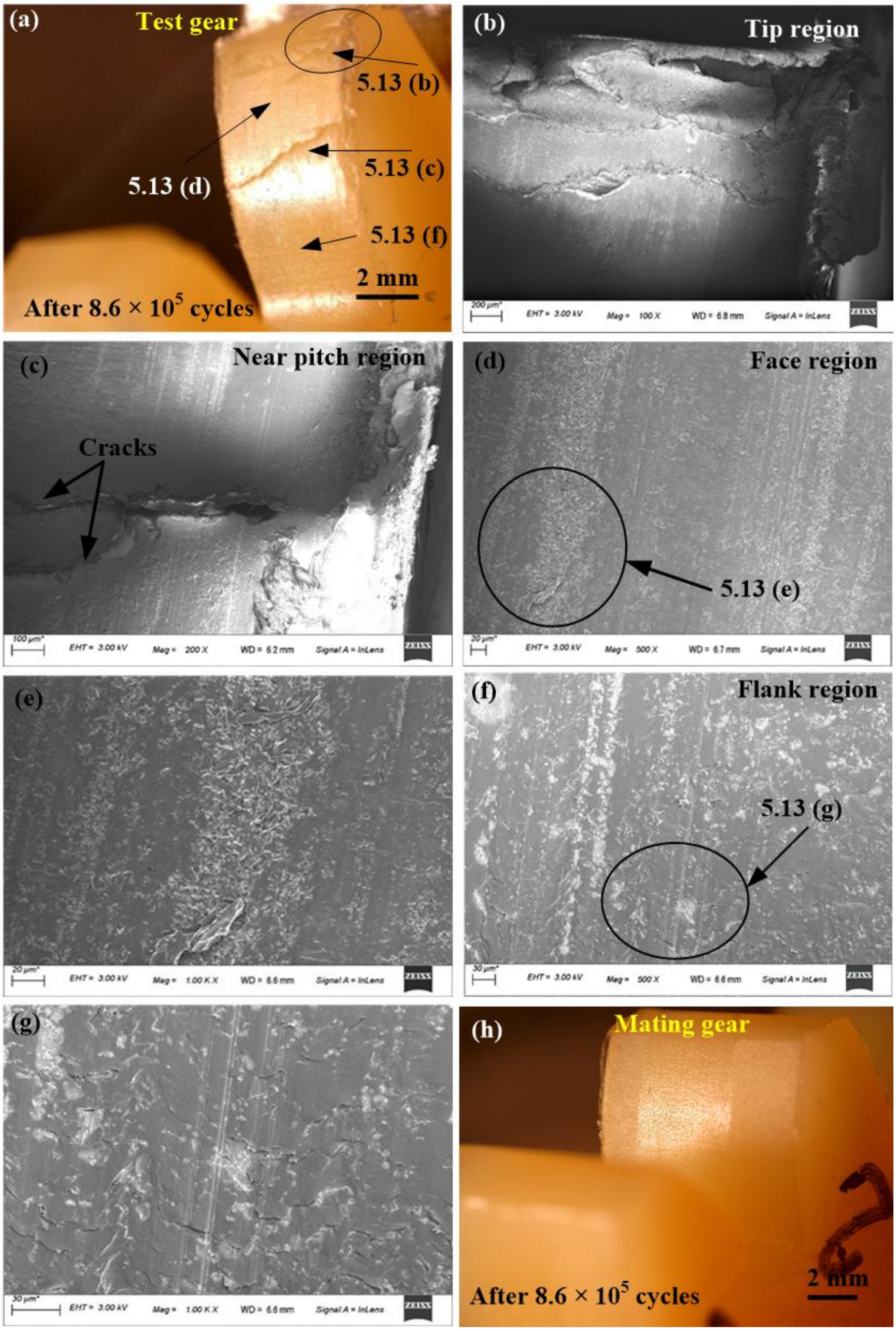

Figure 5.13 Worn-out lubricated gear surface at 4 Nm (a–g) Test gear and (h) Mating gear.

Figure 5.13 (a) depicts the worn-out surface of the lubricated test gear at 4 Nm. The tip region reveals surface crack as well as initiation of plastic deformation (Figure 5.13 (b)). Cracks near the pitch region are depicted in Figure 5.13 (c). The face region evidences the plastic flow in the sliding direction (Figure 5.13 (d, e)). The smeared surface along with sliding marks, also confirmed plastic deformation on the flank region (Figure 5.13 (f, g)). The mating gear tooth surface shown in Figure 5.13 (h) revealed very less wear.

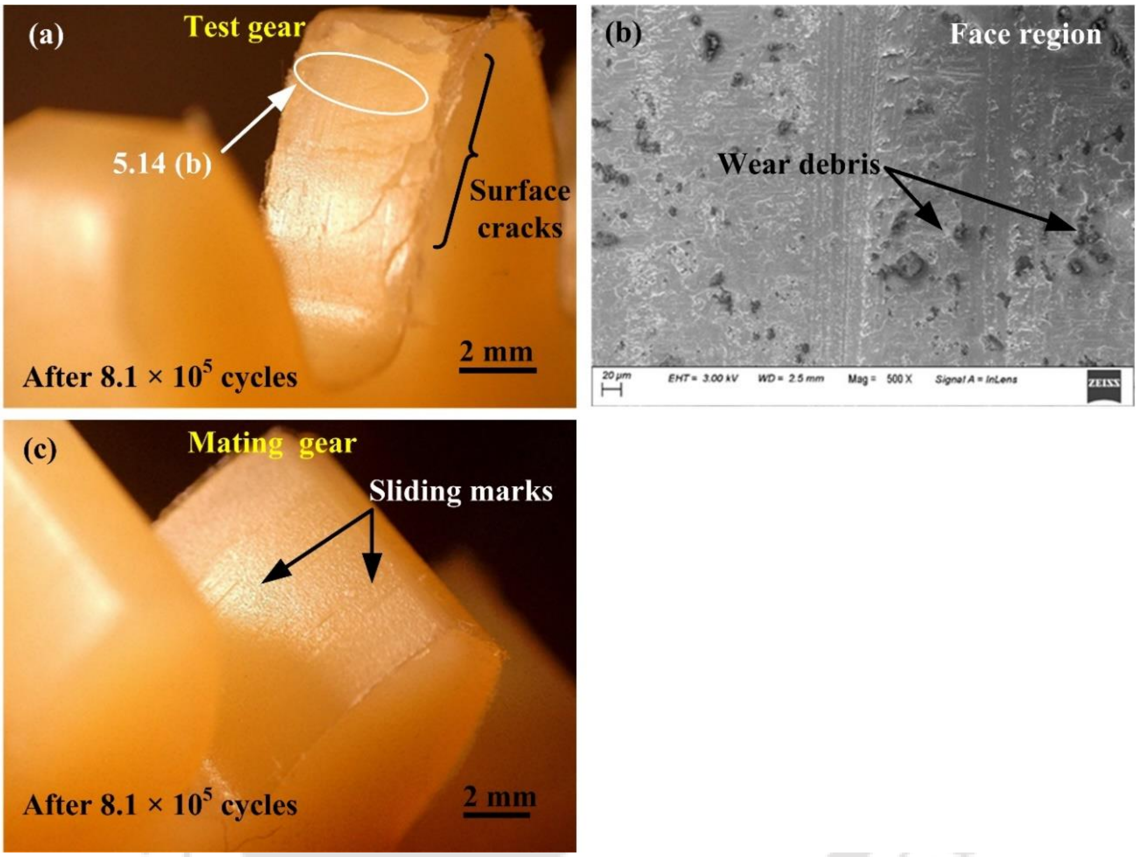

Figure 5.14 Worn-out lubricated gear surface at 4.5 Nm (a–c) Test gear and (d) Mating gear

Under the loading condition of 4.5 Nm, multiple surface cracks across all the regions of the gear tooth are shown in Figure 5.14 (a). The face region reveals sliding marks and entrapped wear debris (Figure 5.14 (b)), whereas the pitch region reveals surface cracks ((Figure 5.14 (c)). Like other considered loading conditions, the mating gear surface reveals insignificant wear marks on the gear tooth (Figure 5.14 (d)).

5.7 Weight loss (%)

At 1.8 Nm, the measured weight loss of test gear and mating gear under dry conditions is $0.254\% \pm^{0.0003}_{0.1366}$ and $0.13\% \pm^{0.0240}_{0.0281}$, respectively, per 10^5 cycles. Under dry conditions, at higher loads, test gear exhibited thermal failure; hence weight loss is not plotted. The weight loss of test gear under lubricated conditions has been reported in Figure 5.15. At 4.5 and 4.0 Nm, the test gear exhibited a significant weight loss; however, in the 1.8–3.5 Nm range, the weight loss is not significant and almost in the same range. In addition to surface contact damage, cracks are also observed in gear under higher loading conditions (Figures 5.13 (a) and 5.14 (a)). Under the lubricated condition, the test gear exhibited less wear than in the dry condition (Figure 5.5). Mating gears under lubricated conditions did not exhibit any failure but exhibited some weight loss (Figure 5.15 (b)).

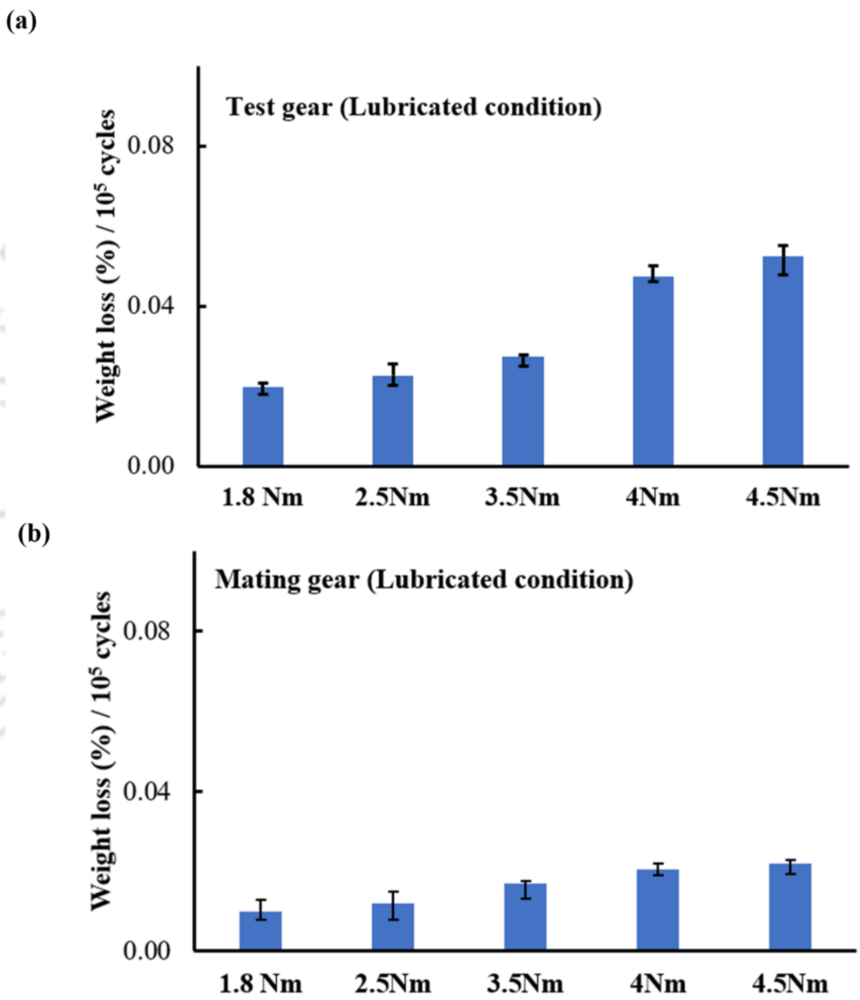

Figure 5.15 (a) Measured weight loss of test gear under lubricated conditions and (b) Measured weight loss of mating gear under lubricated conditions

Figure 5.16 (a) and (b) reveal flakes and fibrils in the wear debris of test gear at 1.8 Nm; similar morphology is observed at other investigated loads. The adhesion between polymer-polymer contact is responsible for the flake form and fibrils due to the repetitive sliding combined with the rolling of entrapped debris between surfaces. Alharbi (2019) also observed the combination of chips and fibers form of debris while evaluating injection-molded polymer-polyamide gear pairs. Under higher loading conditions (2.5 and 3.5 Nm), the presence of high stress and generation of higher temperature results in accelerated severe plastic deformation, causing more accumulation of wear debris between the contact surfaces (Figures 5.16 (c, d)). Hu and Mao (2017) also reported similar debris features while evaluating the performance of acetal-acetal gear pairs under dry conditions.

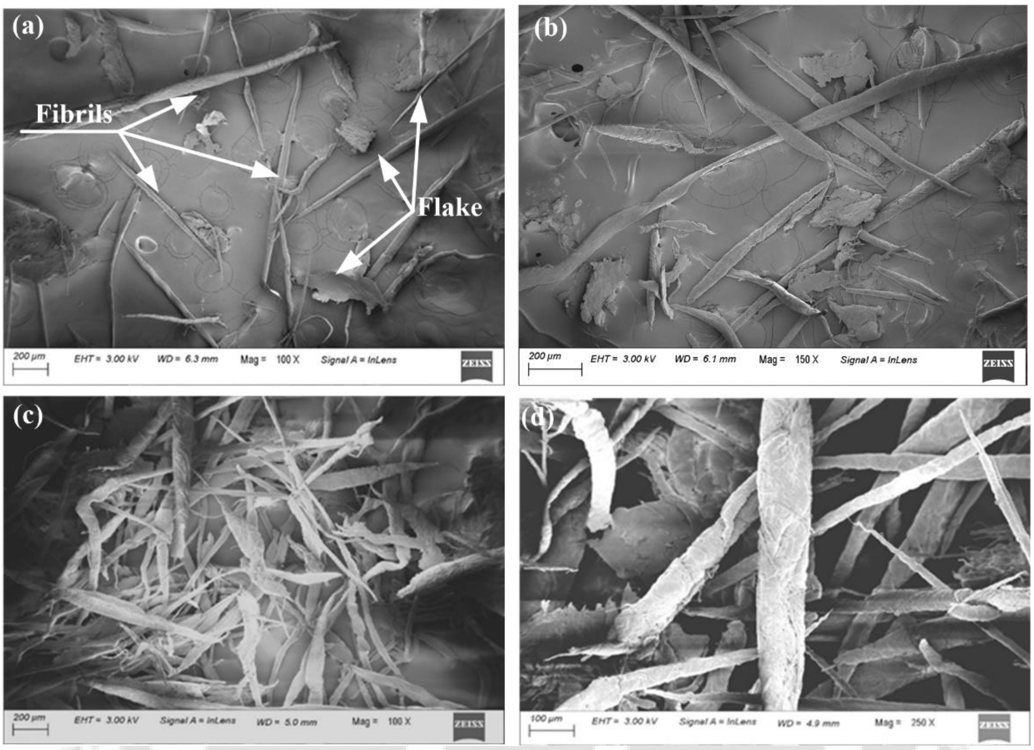

Figure 5.16 Gear wear debris under dry conditions (a, b) 1.8 Nm and (c, d) 3.5 Nm

5.8 Summary

- Polyamide gear exhibited cracks near the pitch region at 1.8 Nm under the dry condition, whereas under the lubricated condition, only failure initiation was observed on the face region when paired with similar material. In the earlier chapter, when the mating gear was metallic gear, surface pitting was observed along with cracks near the pitch region under dry condition when the test gears were subjected to low load (1.8 Nm).
- Polyamide gear exhibited severe plastic deformation at higher loads (2.5 Nm and 3.5 Nm) under dry condition when paired with similar material. Less thermal conductivity and high contact friction of the polyamide material contribute to the heat accumulation of heat, resulting in thermal damage to the gear. In the earlier chapter, when the mating gear was metallic gear, severe wear near the root, along with surface cracks in the gear tooth pitch region, was observed at higher loads (3.5 and 4.5 Nm).

- Under lubrication, polyamide gear exhibited surface fatigue failure at higher loads (2.5 Nm and 3.5 Nm) when paired with similar material. Lubrication prevents heat accumulation, which significantly avoids severe plastic deformation and improved gear life (about two orders of magnitude) compared to dry condition. In the earlier chapter, when the test gear meshed in metal gear, the major mode of failure was scuffing, and no cracks (surface contact fatigue failure feature) in the pitch region or other regions owing to improved heat dissipation characteristics due to metallic mating gear as a lubricant.
- It can be summarized that polymer-polymer gear is not preferred for dry and higher load conditions, and designers need to focus more on heat generation while utilizing polymer-polymer gear pair.

Chapter 6

Selective laser sintered material–Sliding contact and gear performances

6.1 Introduction

In the earlier chapters, test gears were manufactured through injection molding, and their surface durability was evaluated under dry and lubricant conditions. In this chapter, an effort is being attempted to understand the influence of the manufacturing process on gear performance. In recent years, selective laser sintering has been considered for product development for many applications due to its many advantages, including customized design. Initially, the sliding contact performance of injection molding polyamide (IM) and selective laser sintered (SLS) polyamide was evaluated using standard pin-on-disc configuration under dry and lubricant conditions. Frictional coefficient, net surface temperature, and wear were monitored, and worn-out surface morphology was also analyzed, entailing stereomicroscope and FESEM. Subsequently, gears were developed through the selective laser sintered process, and gear performance was evaluated under dry and lubricant conditions.

6.2 Sliding contact performance of injection molded and selective laser sintered material

6.2.1 Methodology

The main objective of this work is to investigate the effect of the manufacturing process on tribological performance; hence only one operating condition (normal load and sliding speed) was considered. Injection molded polyamide and selective laser sintered polyamide were fabricated in cylindrical pin shape, and sliding contact tests were conducted under dry and oil-lubricated conditions under an applied normal load of 60 N and a sliding velocity of 1.13 m/s. The gear oil, the lubricant, was supplied at a rate of 8 ml/s. Before and after testing, the specimens were dried at 353 K for 2 hours to remove moisture. Test specimens were weighed before and after testing to analyze wear. Schematic diagrams of the SLS pin on the print platform are shown in Figure 6.1.

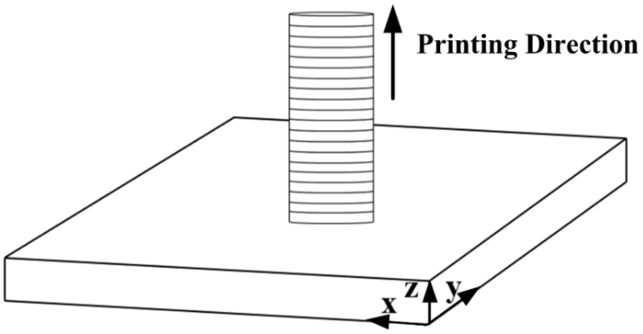

Figure 6.1 Schematic diagram of the SLS pin on the print platform

To understand the ductility characteristics, the tensile test was carried out on IM and SLS specimens. IM and SLS specimens (ASTM D638 type 1) were tested at a strain rate of 1 mm /min using a universal test machine (BISS: MEDIAN 250 KN). The stress-strain curve and the fractured specimen are shown in Figure 6.2.

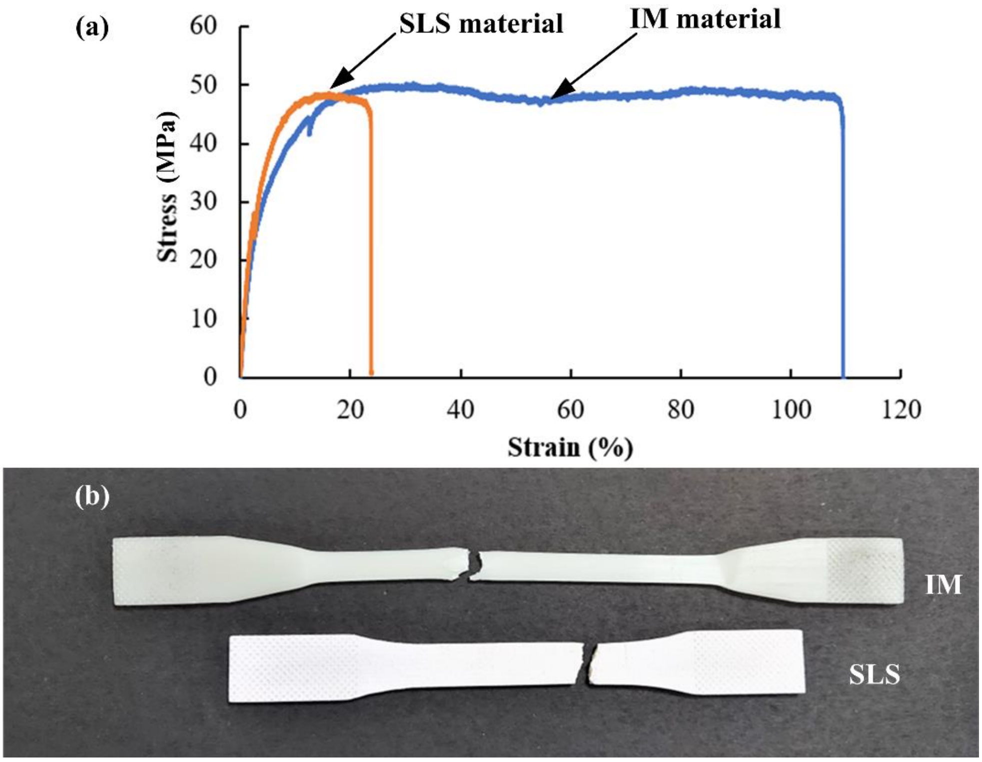

Figure 6.2 (a) Stress-strain curve of SLS and IM materials and (b) Fractured specimens

The modulus, elongation, and yield stress (0.5 % offset) are observed to be 1.071 GPa, 109.6 %, and 23.8 MPa for IM material, and for SLS material, it is 1.406 GPa, 23.8 %, and 26. 5 MPa, respectively. As observed, the ductility of IM material is significantly higher (around four times) than SLS material. Athreya *et al.* (2011) reported that SLS polyamide exhibited higher flexural and tensile moduli than IM polyamide. Zhu *et al.* (2015) observed around four times higher elongation in IM polypropylene compared to SLS polypropylene.

6.2.2 Surface condition characterization before sliding contact testing

Figure 6.3 shows the FESEM micrographs of flattened pin specimen's surface prepared by sliding against the silicon carbide abrasive papers before testing. Figure 6.3 (a) shows only sliding marks on the IM surface, whereas SLS shows powder particles along with sliding marks (Figure 6.3 (b)). Power particles were also observed on the fractured surface of the SLS polyamide tensile specimen by Van Hooreweder *et al.* (2010) due to incomplete fusion.

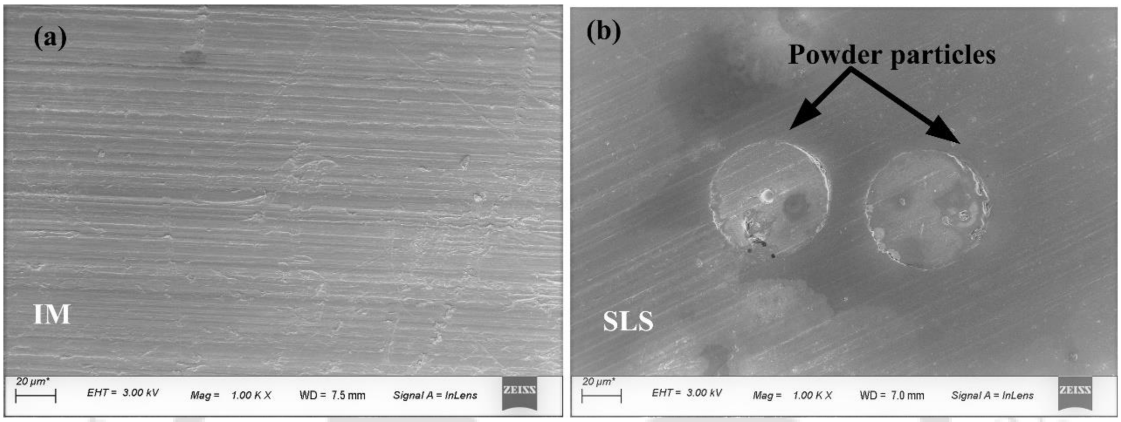

Figure 6.3 FESEM morphologies of the (a) IM and (b) SLS materials

Before testing, the surface roughnesses of the steel disc, IM, and SLS materials were measured. The pin surface roughness was measured in five different regions. The surface roughnesses (R_a) of the steel disc, IM, and SLS materials are 0.27, 0.26, and 0.46 µm, respectively (Figure 6.4). The average shore D hardness of the IM and SLS is 80 and 81D, respectively.

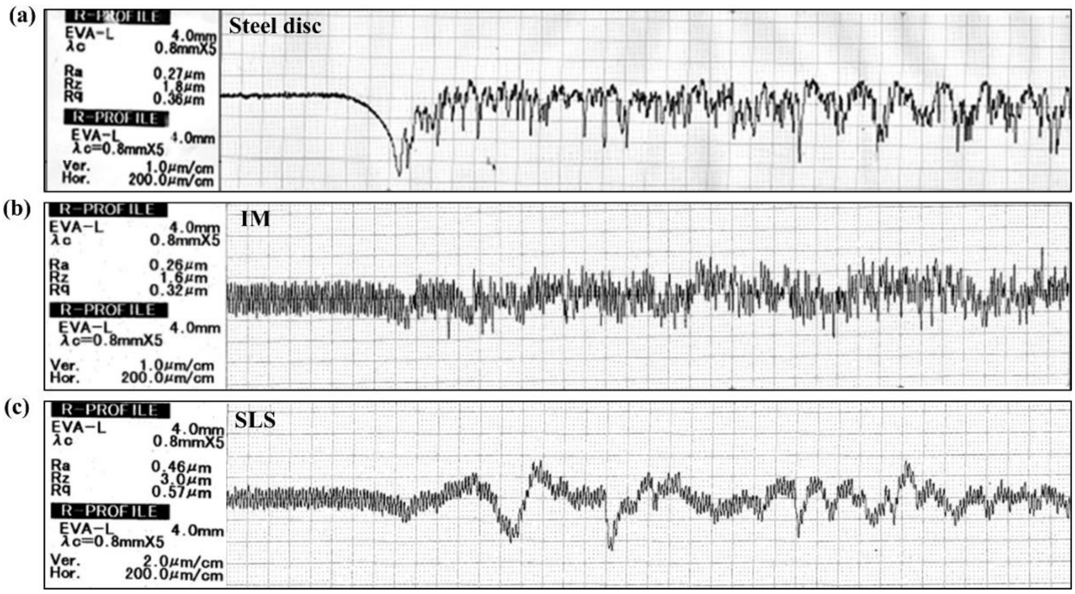

Figure 6.4 Average surface roughnesses of the profiles for the (a) Steel disc, (b) IM, and (c) SLS materials.

6.2.3 Friction and contact temperature measurements

6.2.3.1 Dry condition

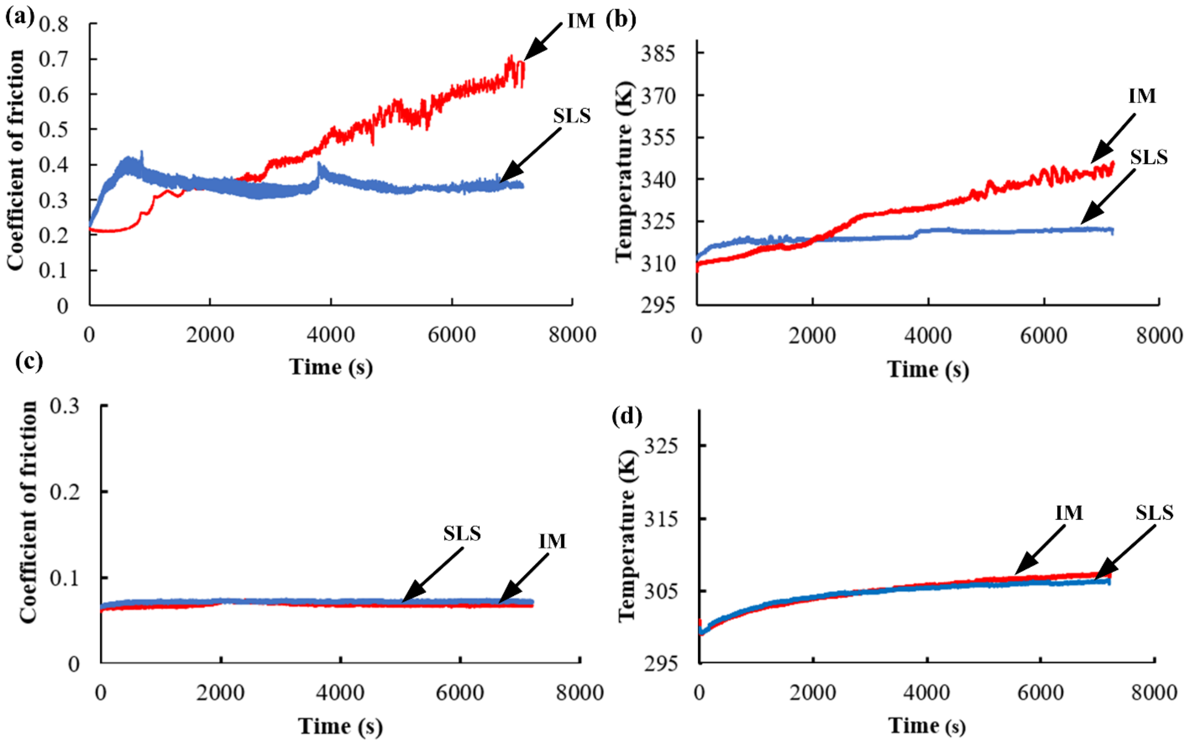

Figure 6.5 Variations in the friction coefficient and temperature as functions of the sliding time (a, b) Under the dry condition and (c, d) Under the lubricated condition

The friction coefficient and temperature variations with respect to the sliding time of IM and SLS materials under the dry condition are shown in Figures 6.5 (a) and (b). The temperature close to the contact interface was measured with the help of an IR camera for the specimen, as shown in Figure 6.6. The friction coefficient increased with the sliding time in the IM material, whereas no such fluctuation is observed in the SLS material. This behavior of IM material is due to the formation of plastic flow during sliding and is confirmed by the morphology of the worn-out surfaces (Figure 6.7).

SLS material exhibited less ductility due to the sintering characteristics; hence, no plastic flow is observed as in IM material. The friction coefficient continues to vary (0.2–0.66) during sliding under this test condition. The SLS material generates less heat while sliding because of the lower friction coefficient, and no plastic flow is observed, unlike IM material. In the SLS material, the friction coefficient initially exhibited a slight increase due to the initial plastic asperities effect and then dropped before saturating (0.33). In the SLS specimen, the friction coefficient is reduced by 50 % compared to the IM material.

The main contributing mechanism of friction in IM is plastic flow, whereas, in SLS, plastic flow is insignificant due to the reduced ductility. Figure 6.5 (b) shows a comparatively smooth initial temperature variation, but after some time (5000 s sliding time), a significant variation is observed in IM material. After a time, the generated heat softens the surface and causes the stick-slip phenomenon, where changes in the friction coefficient (Figure 6.5 (a)) occur because of breaks in the contact between the surfaces. Plastic flow on the worn surface confirmed this behavior. The stable temperature of SLS material under dry conditions is around 322 K, significantly lower than IM material. Meng *et al.* (2009) also observed a rapid increase in adhesive friction of the IM polyamide which caused due to the increase in the apparent area of contact and surface temperature.

6.2.3.2 Lubricated condition

Figure 6.5 (c) and (d) show the friction coefficient and temperatures of the IM and SLS materials under lubricated conditions. Under the lubricated condition, coefficient of friction is observed almost stable along the sliding time. The friction coefficient is significantly smaller under lubricated than under dry conditions. The presence of lubricant reduces the contact between asperities and reduces frictional heating, resulting in lower friction. The friction coefficient and surface temperature are almost the same for the IM and SLS materials under lubricated conditions. The presence of lubricant reduced the friction by 89 % and 78 %, respectively, for the IM and SLS relative to dry conditions. Under lubricated conditions, IM and SLS materials showed a 10 % and 5 % reduction in temperature compared to the dry condition.

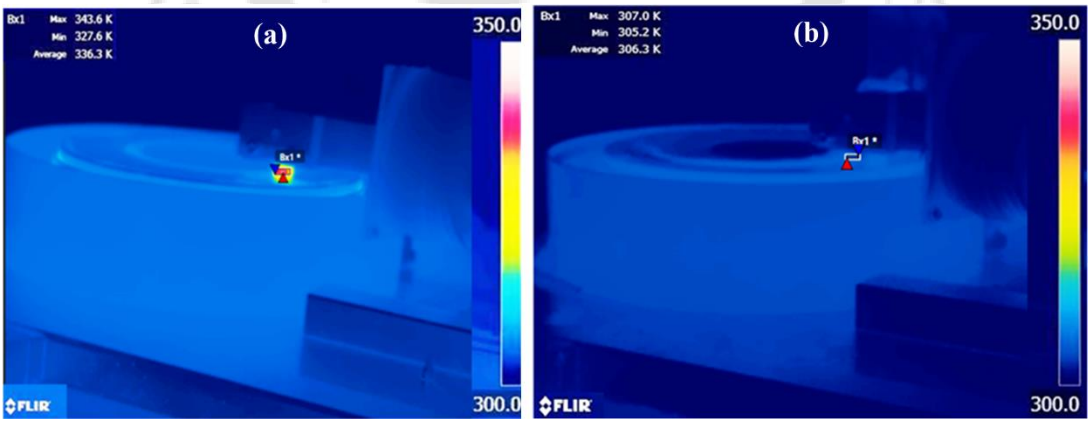

Figure 6.6 Thermographs of IM material under (a) Dry condition and (b) Lubricated condition

6.2.4 Wear morphology

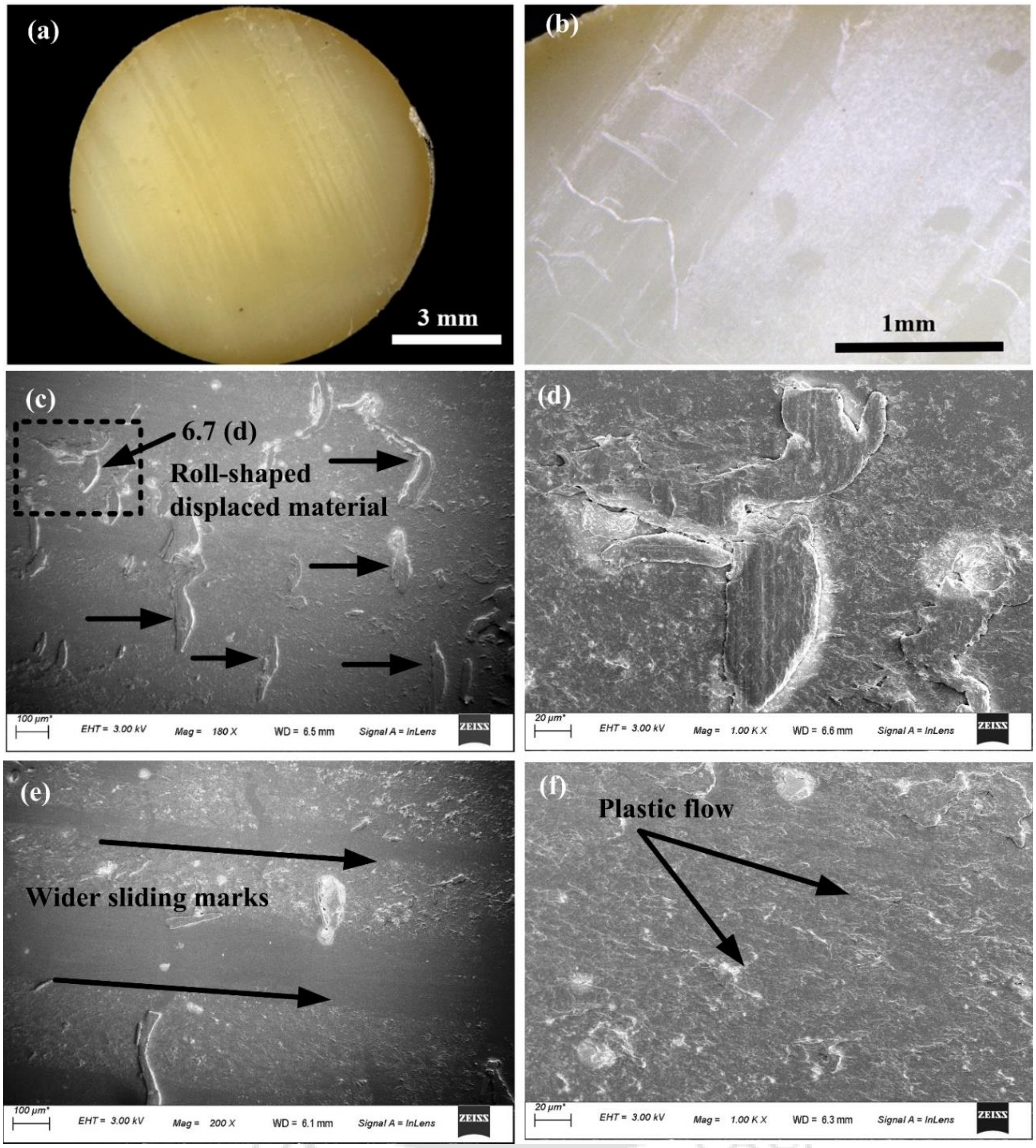

Figure 6.7 (a–f) Worn-out surface morphology of the IM material under the dry condition

The worn-out surface was observed under a stereomicroscope to elucidate the friction mechanism. The stereomicroscope images of the tested IM surfaces under dry conditions are shown in Figure 6.7 (a) and (b), where the multiple deformed sliding materials and severe wear on the worn-out surface are apparent.

To further understand the failure, the worn-out surface was also observed using FESEM. Figure 6.7 (c) reveals that multiple roll-shaped deformed materials adhere to the surface. A magnified view is presented in Figure 6.7 (d). The presence of higher friction and temperature between the contact pair and longer sliding duration, as shown in Figures 6.7 (a) and (b), caused the formation of broader sliding marks on the surface, as shown in Figure 6.7 (e). Figure 6.7 (f) clearly shows the plastic flow to the worn-out surface due to the excessive heat generated on the contact surface. Chen *et al.* (2003) reported similar worn-out morphology on the polyamide disc under rolling-sliding conditions. Shibata *et al.* (2014) also reported similar features over a worn-out surface of polyamide when the polyamide disc surface ran against the metal ball under dry conditions and suggested that plastic flow and roll-shaped material were caused by local surface braking. Unal and Findik (2008) also reported that the thermal softening effect caused high wear in polyamide under dry conditions.

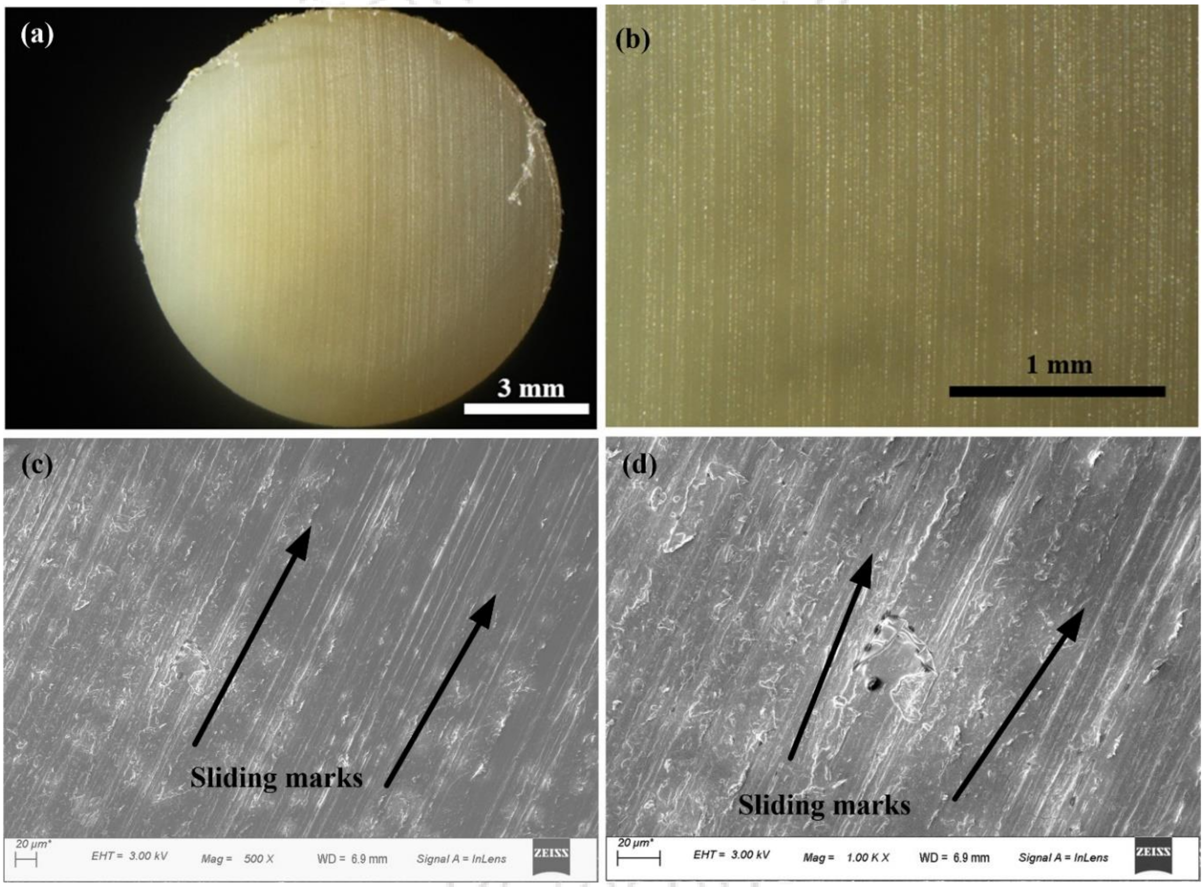

Figure 6.8 (a–d) Worn-out surface of the IM material under the lubricated condition

Stereo (Figure 6.8 (a, b)) and FESEM micrographs (Figure 6.8(c, d)) of the IM material under lubricated conditions are illustrated, which reveal only sliding marks with no plastic flow.

The worn-out SLS surface morphology under dry conditions is shown in Figure 6.9 (a) and (b) as revealed by a stereomicroscope. Figure 6.9 (b) shows the brown spots on the worn-out surface after testing that result from the local degradation of the powder particles. The worn-out surface was observed under FESEM for a detailed understanding which are shown (Figure

6.9 (c) and (d)). No severe deformation pattern is observed in the SLS surface (Figure 6.9 (c, d)), unlike in the IM material, because there is less friction between the contact pairs (Figure 6.5 (a)). Powder particles are observed on the worn-out SLS surface (Figure 6.9 (c)), and sliding marks on the worn-out surface are also observed as the consequence of sliding between the contact pairs. Hence, the examinations of the thermal and worn-out surface morphology of the SLS material indicate a better contact performance of the SLS material than the IM material at particular testing conditions.

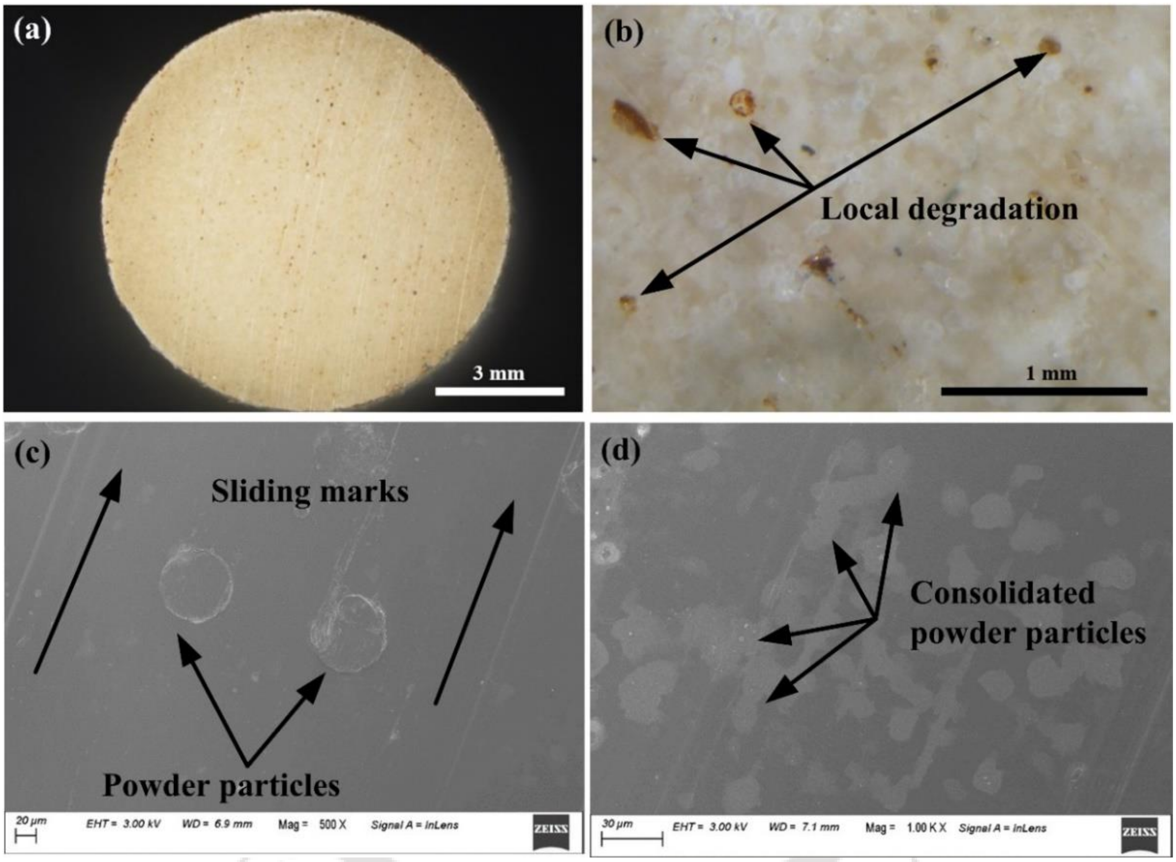

Figure 6.9 (a-d) Worn-out surface of SLS material under the dry condition

Worn-out SLS surface under lubricated conditions is shown in Figure 6.10 (a) and (b) as revealed by stereomicroscope. No color change is observed in contrast to dry conditions. The presence of lubrication lowered the contact surface temperature (as indicated in Figure 6.5 (d)) without local degradation (Figure 6.10 (b)). This blackish track of FESEM images further confirmed the presence of absorption of lubricant oil on the worn-out surface (Figure 6.10 (c, d)). The presence of pores on the surface caused the lubricant to diffuse inside the material.

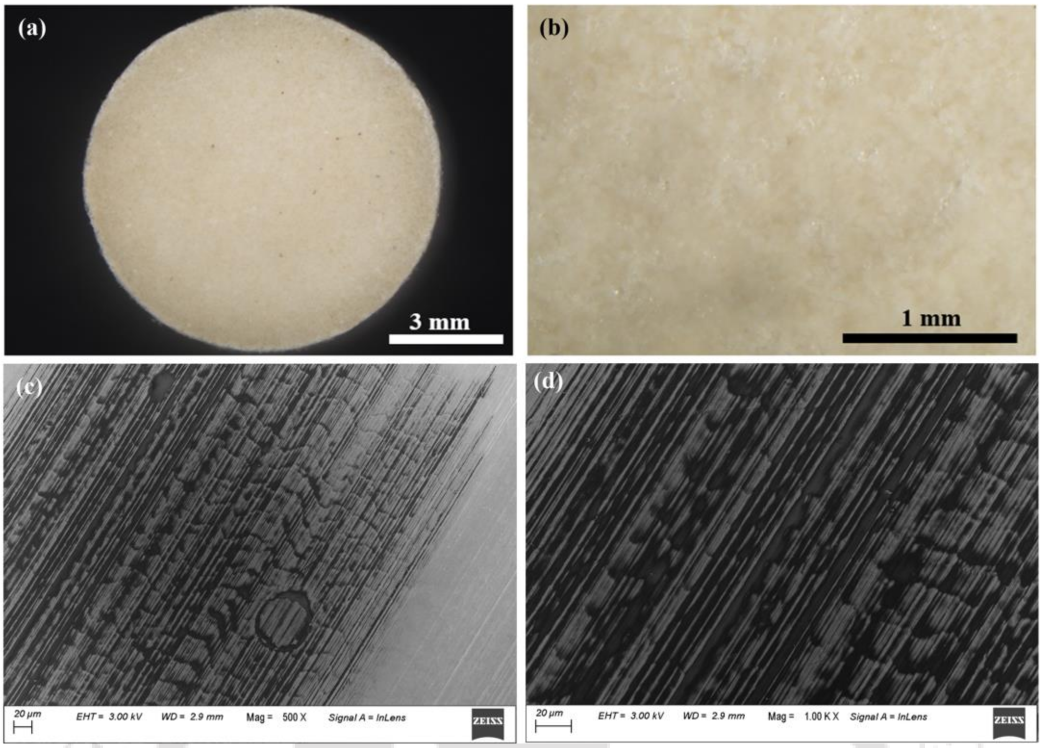

Figure 6.10 (a-d) Worn-out surface of the SLS material under the lubricated condition

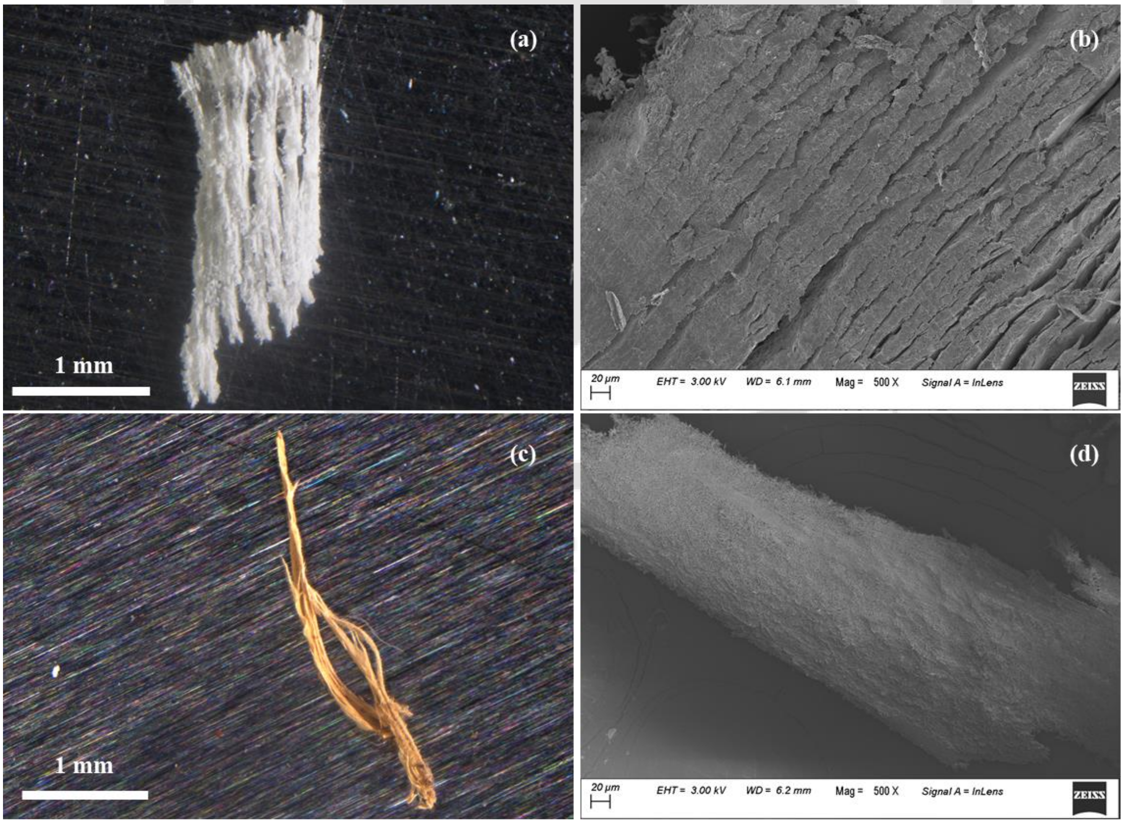

Figure 6.11 Stereo and FESEM micrographs of wear debris for (a, b) IM and (c, d) SLS materials.

The wear debris was collected after the test under dry conditions and observed under a stereomicroscope and FESEM (Figure 6.11). The IM wear debris appears as fibrils and is produced by severe shear deformation resulting from interaction with the counter material, as depicted in Figure 6.11 (a) and (b). Fibrillation due to the strong plastic deformation was reported by Michler (2016). Kim *et al.* (2012) reported similar debris formed in the polyamide 12 composite material while testing against a steel ring. In the SLS material (Figure 6.11 (c, d)), owing to the improved adhesion between the fibrils, the generated debris coagulated to form larger particles.

6.2.5 Weight measurement

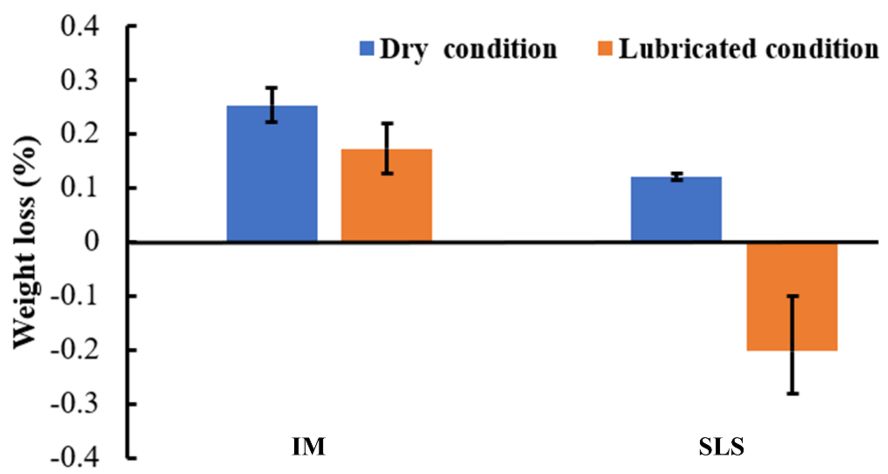

Figure 6.12 Weight loss (%) in IM and SLS materials under dry and lubricated conditions

After performing the test, the weight loss was computed for all the tested specimens, and the average value of the three repeated tests is reported (Figure 6.12). SLS material exhibited less wear (52 %) than IM material because there is less friction. The absence of plastic flow also confirmed this observation. Blattmeier *et al.* (2012) also reported that SLS specimens achieved a longer lifetime but less deformation than IM specimens. Figure 6.12 illustrates that the wear in the specimen under dry conditions is higher than under lubricated conditions, except for SLS material. Lubrication between the contact pair prevents direct contact and reduces wear. The presence of pores in the SLS material absorbs the lubricant, causing a weight increase relative to the specimen before testing. Athreya *et al.* (2011) also reported that the extrusion and IM polyamide had less than 5 % porosity, whereas SLS had 6.5 %. Wang *at al.* (2017) developed polyimide specimens through pressing and sintering at various porosity levels and observed that the maximum amount of lubricant was absorbed by the specimens having higher porosity.

Environmental stress cracking was carried out for IM and SLS materials as mentioned in chapter 3 (strained at 1.2 % and duration 168 hours). The weight gain of IM and SLS materials is found to be 0.2 % and 0.8 %, respectively. This higher weight gain indirectly quantifies the porosity of SLS. Wörz *et al.* (2018) compared the long-term properties of IM and SLS materials where CT scan was utilized to confirm the presence of pores (1.7 %) in the SLS material. Van Hooreweder *et al.* (2013) compared the structural and fatigue performance of IM and SLS materials and observed the porosity of SLS material with the help of optical micrograph and imaging processing. Figure 6.13 shows the surface of the specimen before and after ESC testing. The surface morphology of IM material (Figure 6.13 (b) reveals some surface texture changes due to the diffusion/absorption of the oil after testing. The SLS material exhibited few cracks at the edge of the specimen, as shown in Figure 6.13 (d). The effect of environmental stress cracking of different classes of polyethylene in the presence of biodiesel was examined by Saad *et al.* (2020). The test was performed using bending testing for the duration of a maximum of 1000 h or until the failure of specimens. Their research concludes that the biodiesel plasticized the polyethylene material. The polyamide tube specimen was investigated under different concentrations of Solupan and water solution for various durations (100, 200, and 300 hours) using tension stresses by Polkowski *et al.* (2016). At higher stress and test duration, the Solupan solution degrades rapidly and fails the polyamide material as a result of the reduction in interaction between polymer chains.

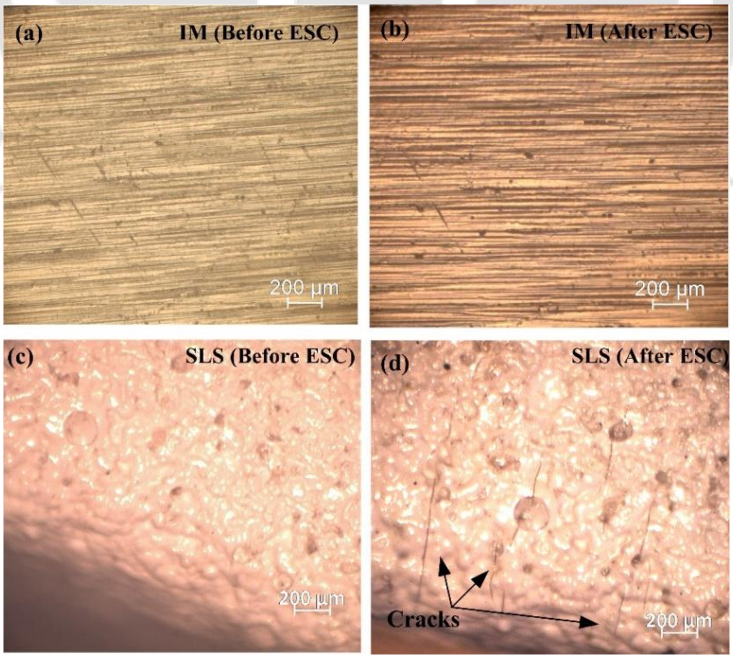

Figure 6.13 Environmental stress cracking specimens' surface (a, b) IM specimen before and after testing and (c, d) SLS before and after testing

6.2.6 Summary of sliding contact performance of selective laser sintered and injection molded polyamide

- Under dry condition, injection molded material exhibited an increase in friction coefficient (0.2–0.66) with the sliding time due to the dominant plastic deformation which is confirmed by the wear morphology.
- Sintering increased the surface undulations of SLS, which caused the initial frictional rise; subsequently, the initial asperities worn out stabilized the friction coefficient (0.33). The absence of plastic deformation in the SLS material helps to reduce friction and heat generation.
- Selective laser sintered material exhibited significantly less wear (52 %) than injection molded due to its less friction under dry condition. Reduced ductility due to the sintering contributes to reduced friction, wear, and heat generation. Under the dry condition, IM material exhibited plastic flow and roll-shaped deformation, whereas SLS material exhibited only local degradation due to its lesser ductility.
- The brown color wear track of the selective laser sintered material confirmed the role of surface porosity and lubricant. Under lubricated condition, injection molded and selective laser sintered material showed less friction.

The following section discusses the selective laser sintered gear performance under dry and lubricated conditions.

6.3 Performance of selective laser sintered polyamide gear

6.3.1 Gear test methodology

The surface durability performance of the SLS polyamide gear was evaluated using an in-house developed gear absorption test rig. The experiment was performed under both dry and splash-lubricated conditions at a speed of 800 rpm, with a torque range of 1.8–3.5 Nm. The thermal behavior of the SLS gear and lubricant temperature was measured. The gear tooth surface was periodically observed under a digital microscope to monitor for failure. The worn-out gear tooth surface and wear debris was observed using FESEM. Figure 6.14 (a) shows that the SLS gear tooth surface reveals the built layers along the tooth profile. Figure 6.14 (b) shows the close-up view of the steel-SLS gear mesh.

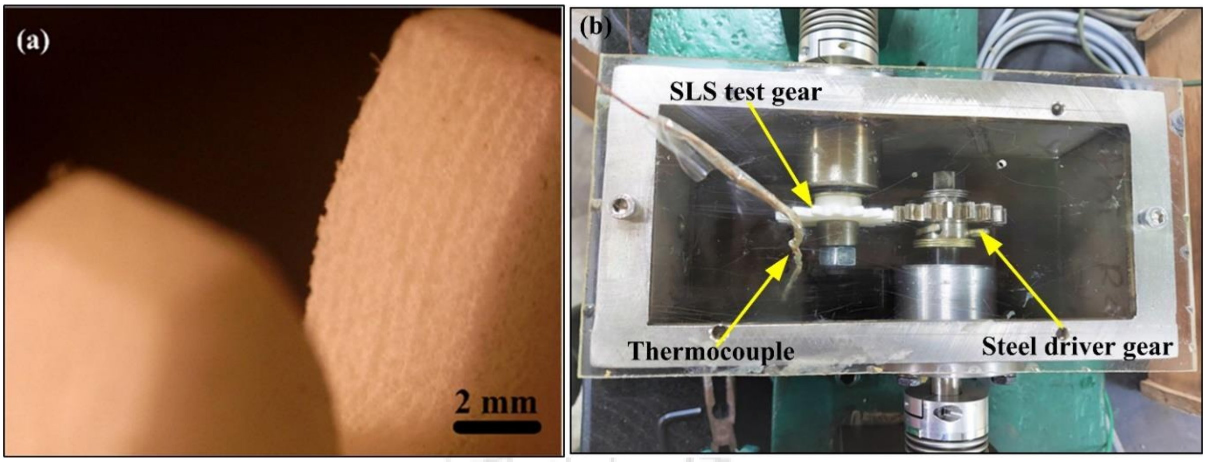

Figure 6.14 (a) SLS gear tooth surface and (b) Close-up view of steel-SLS gear mesh

6.3.2 Surface morphology of the SLS gear tooth

The FESEM micrograph of the SLS gear tooth surface before testing reveals consolidation between the powder particles with clear boundaries and micropores (Figure 6.15 (a)). Figure 6.15 (b) shows the sectioned sub-surface, which is 1 mm below the surface, also revealed micropores owing to its layered manufacturing technique.

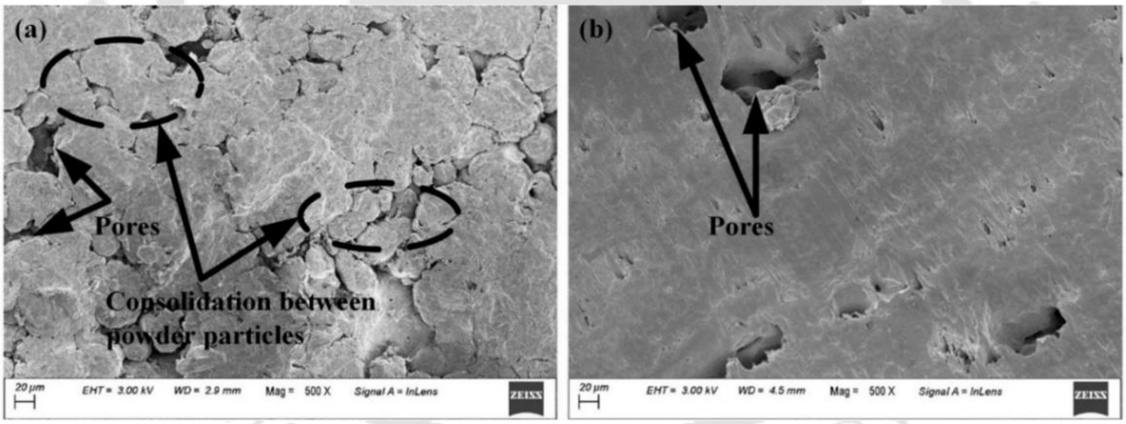

Figure 6.15 FESEM morphology of tooth surface: (a) Contact side and (b) Surface below the 1-mm contact surface

6.3.3 Gear tooth base tangent length measurement

Figure 6.16 shows a reduction in the base tangent length across the three teeth of the gear under the dry condition (1.8 Nm). Typical SLS gears exhibit a rougher surface (Figure 6.15 (a)) owing to the layer manufacturing process. The run-in wear is primarily dependent on the initial surface roughness of the test and mating gear tooth surface. During the initial period (4.3×10^5 cycles), the run-in wear rate increased. After the initial run-in wear period, the layered manufacturing features observed before testing disappeared significantly, and after this run-in wear period, the transfer of the polymeric film to the mating steel gear tooth surface further prevented the polishing of the gear tooth surface. After a certain period, the formed film layer is broken owing to repeated interactions, and a polishing effect is observed on the test gear tooth surface.

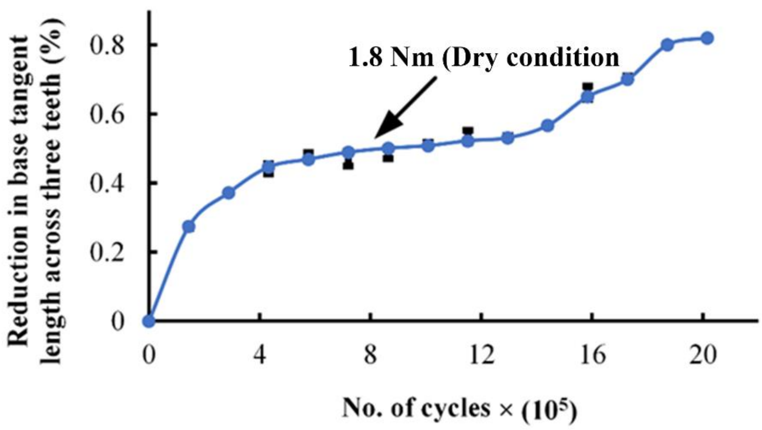

Figure 6.16 Variation of the base tangent length of the gear at 1.8 Nm under the dry condition

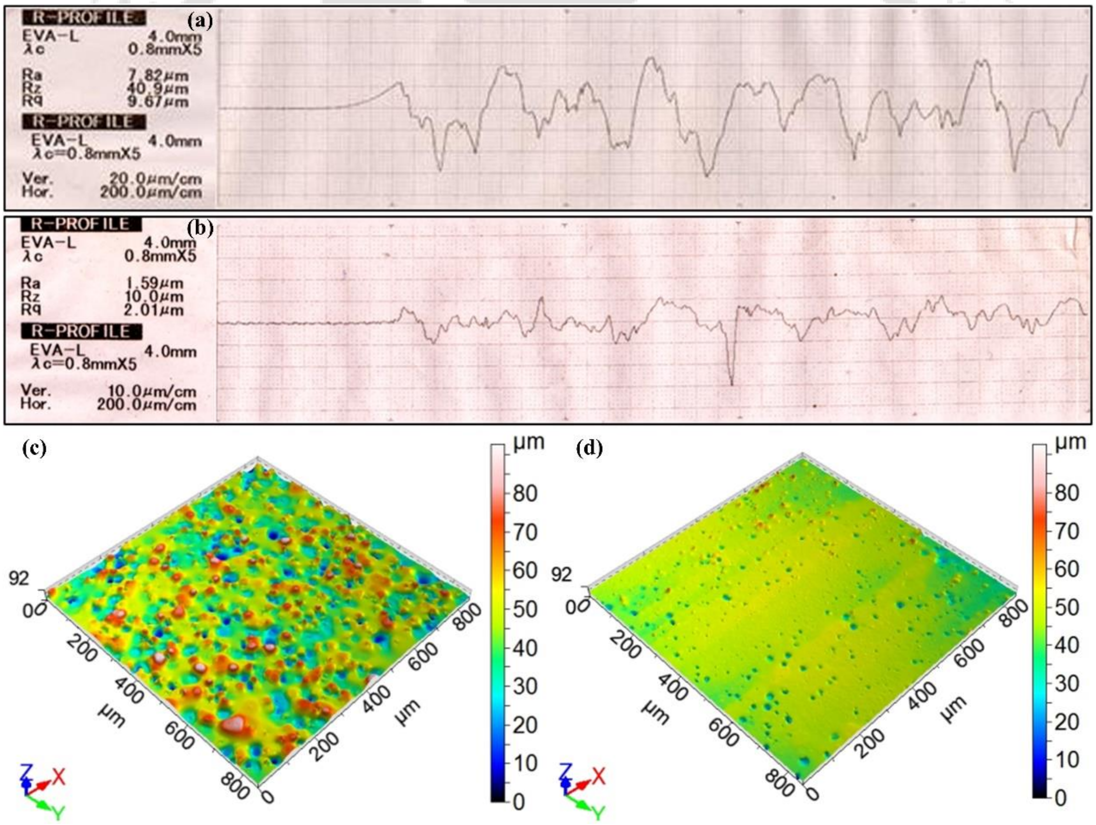

Figure 6.17 Surface roughness of the test gear tooth (a) Before and (b) After testing, and 3D view of the gear tooth surface (c) Before and (d) After testing

Figure 6.17 (a) and (b) shows the roughness of the gear tooth surface before and after testing (2.0×10^6 cycles, 1.8 Nm) under dry conditions. The average roughness of the gear tooth surface reduced from 7.82 to 1.59 µm after testing, which confirmed the polishing effect (Figure 6.17

(a, b)). The gear tooth surface was observed using a non-contact profilometer (Taylor & Hobson−CCI MP) before and after the test. Figure 6.17 (c) and (d) shows the gear tooth surface and confirms the polishing effect after the testing.

6.3.4 Thermal condition of the gear surface and lubricant

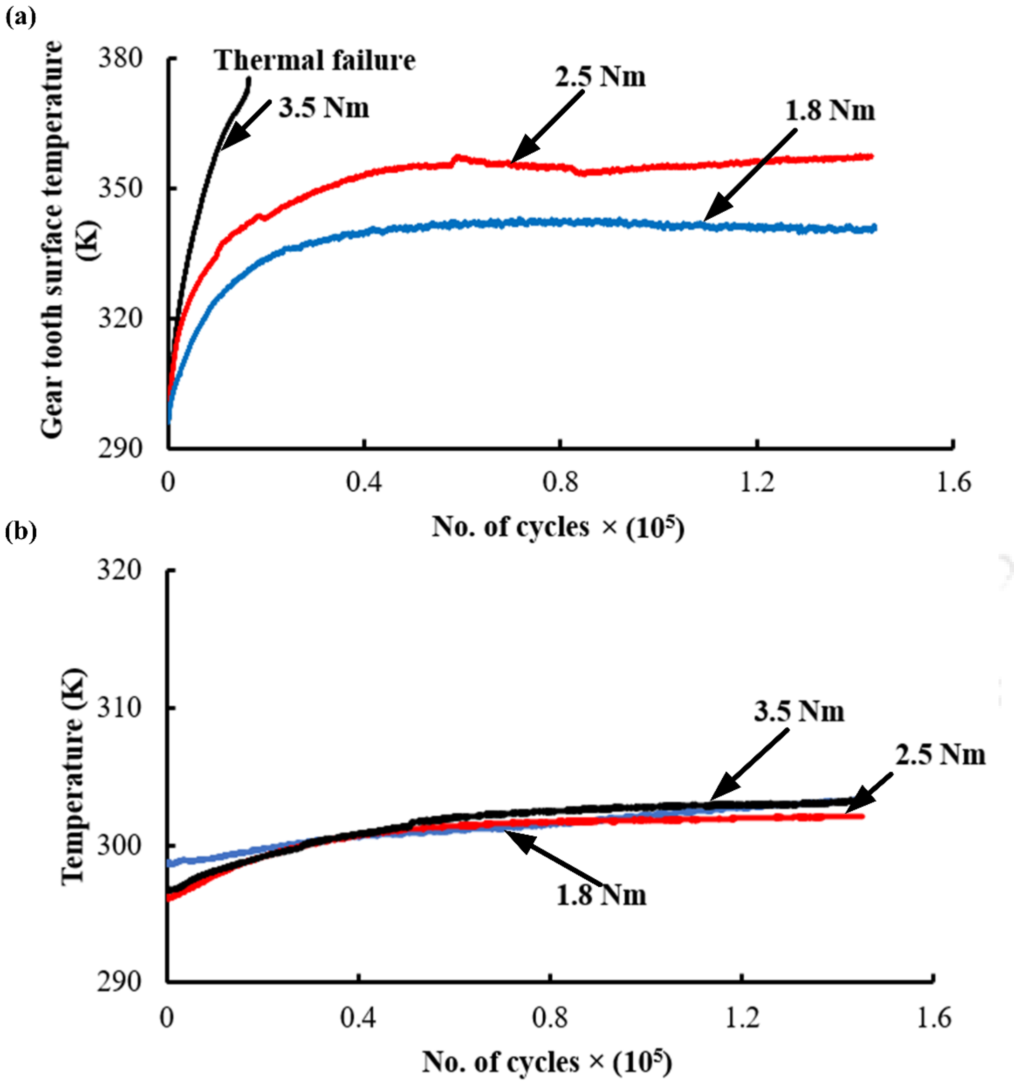

Figure 6.18 Thermal condition (a) Gear tooth surface temperature under the dry condition and (b) Lubricant temperature under the lubricant condition

The gear tooth surface temperature was measured during testing using an IR sensor, and a plot of the measured surface temperature of the gear tooth at various loads under dry conditions is shown in Figure 6.18 (a). At 1.8 and 2.5 Nm, the test gears exhibited an initial gradual increase and then stabilized. The initial rise in surface temperature is due to surface interactions, and the stability is due to the transfer layer formation on the mating metal surface. The formation of a polymer surface on the mating metal surface further reduces the surface interaction. Zhang *et al.* (2020) also observed a steady temperature while evaluating the performance of an FDM-fabricated polyamide gear. A similar trend in temperature variation was observed in the polyamide and polypropylene gears while running against the steel gears (Düzcükoğlu (2009a) and Mertens and Senthilvelan (2016)). The test gear exhibited steady temperatures of 343 K and 357 K when subjected to 1.8 and 2.5 Nm. At 3.5 Nm, the temperature generation at the gear teeth is very high compared with other test conditions. A continuous increase in the temperature is observed until gear failure occurred. A similar trend in temperature and failure was observed at higher loading conditions while testing the FDM-fabricated gear (Zhang *et al.* (2020)). Figure 6.18 (b) shows the lubricant temperature while testing gears at various loads, and the maximum increase in the lubricant temperature is approximately 7 K.

6.3.5 Weight measurement

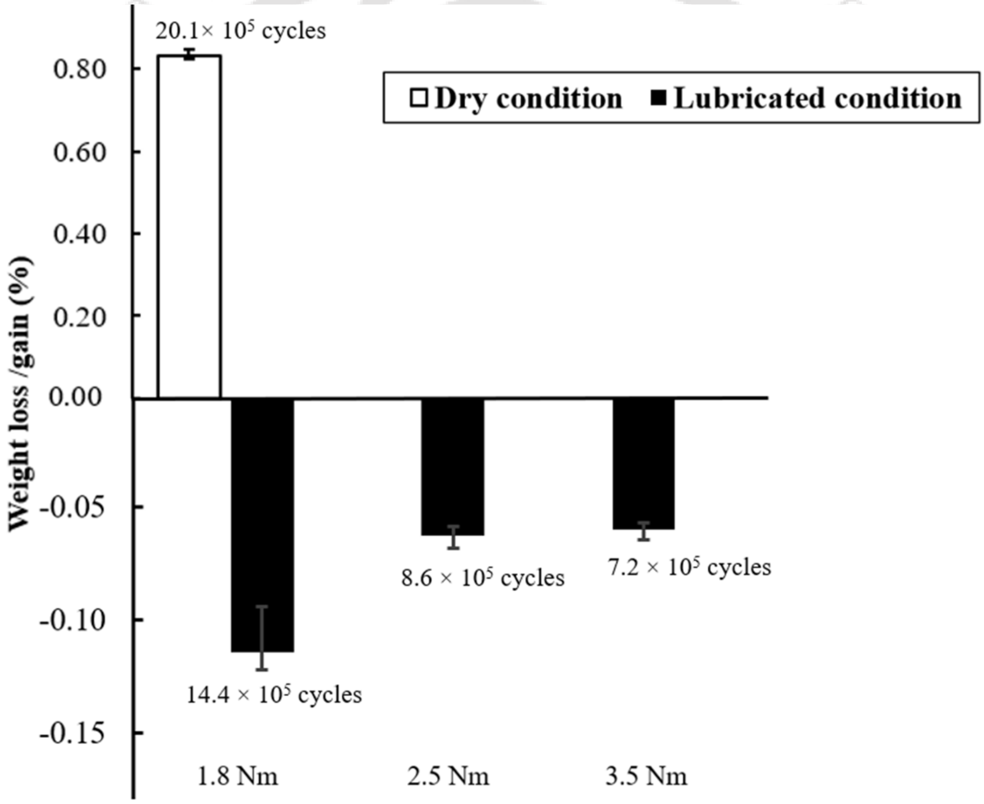

Figure 6.19 Change in gear weight percentage after test

Figure 6.19 shows the changes in the weights of the test gears under dry and oil-lubricated conditions for various loads. Despite wear, the gears tested under the lubricant exhibited weight gain. The sliding motion under contact stresses against the mating metal gear pushes the lubricant oil into the porous structure of the test SLS gear and contributes to the absorption of lubricant by the test gear. The lubricated test gear exhibited weight gain with an increase in test duration. The test gear weight was also measured under dry conditions at 1.8 Nm; however, weights are not reported at other loads of 2.5 and 3.5 Nm owing to the thermal softening along with crack and thermal failure under these conditions. Seltzer *et al.* (2011) also observed this weight gain behavior while investigating the performance of SLS specimens, and the absorption rate was higher in a larger number of pore specimens.

6.3.6 Surface durability of dry and lubricated SLS gears

Figure 6.20 shows the surface durability of the gears under dry and lubricated conditions. The SLS gear tested under dry conditions exhibited different failure modes (thermal failure, surface cracks along with thermal softening, and wear) at different loads; however, the SLS gear tested under lubrication exhibited only pitting failure for all the considered loads. Under dry conditions, the SLS gear subjected to 1.8 Nm showed only wear, and no visible surface damage is observed even after 2.0 $\times 10^6$ cycles. Under FESEM, some initiation of surface fatigue failure features are observed on the gear tooth surfaces. At 2.5 Nm, the gear exhibited micro-surface cracks and thermal softening near the pitch region owing to the exceedance of subsurface shear stresses. At 3.5 Nm, the gear exhibited gear tooth thermal bending owing to higher heat generation because of material hysteresis and sliding friction. The measured surface temperature also confirmed this fact. The fatigue limit of a polymer gear was affected by its temperature (Kodeeswaran *et al.* (2019) and Terashima *et al.* (1986)).

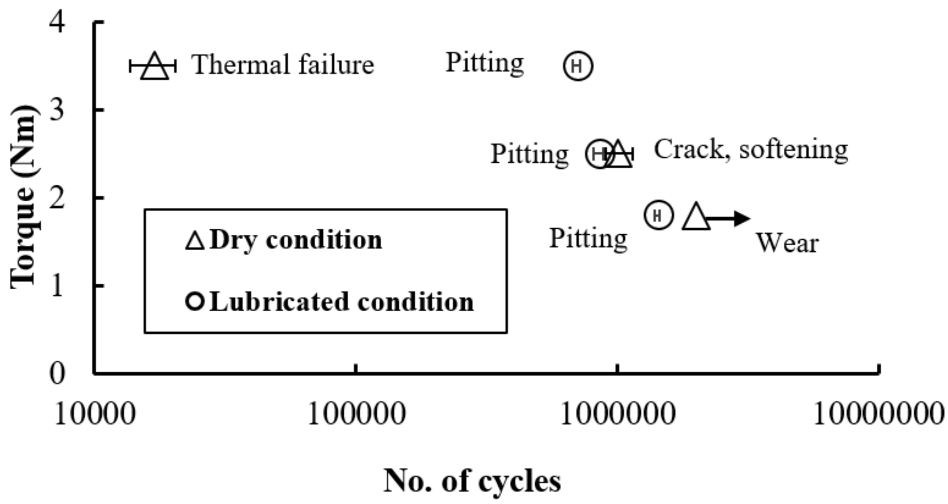

Figure 6.20 Surface durability of the SLS gear with failure mode

Under lubrication, lubricant oil diffused into the porous structure of the SLS gears, and softening of the tooth surface caused this pitting failure. At 1.8 and 2.5 Nm, the SLS gear exhibited inferior surface durability compared with the dry condition. Only at 3.5 Nm, the lubricant significantly improved the surface durability of the SLS gear compared to the dry condition. It is important to note that the SLS gear under dry conditions exhibited thermal failure at this load. Lu *et al.* (2019) also observed pitting around the pitch region of a PEEK gear when paired with a steel gear under lubrication. Zhang *et al.* (2020) investigated the wear and thermal characteristics of 3D printed (FDM) polyamide gear in pair with another polyamide gear under the dry condition. 3D printed gear exhibited wear, root cracking, and thermal failure at 10, 12, and 15 Nm, respectively. SLS gear exhibited only wear at 1.8 Nm, whereas injection-molded gear exhibited surface cracks have been reported in chapter 4. SLS gear exhibited better performance compared to injection-molded gear at the lower load due to the brittle surface and reduced ductility. The higher degree of crystallinity of SLS-processed parts compared to IM parts causes brittleness in SLS parts. The results of Dupin *et al.* (2012) substantiated this; an increase in elongation at break was noticed for polyamide specimens with a decrease in crystallinity. In SLS, a slow cooling rate improves the thermal mobility of molecules during the crystallization process (Zhu *et al.* (2015). At higher load of 3.5 Nm, the SLS gear showed thermal bending, whereas injected molded gear exhibited severe cracks on the tooth surface. Injection-molded gear is better than SLS gear at higher load. This could be due to the higher heat deflection temperature of injection molded polyamide (473 K at 0.45 MPa; Soe *et al.* (2018) and AZO material (2001)) than SLS polyamide (453 K at 0.45 MPa; (3D systems (2007)).

6.3.7 Failure morphology of the SLS gear under the dry condition

Under dry conditions, the worn-out surface of the SLS gear tested at a 1.8 Nm load was periodically examined under a microscope (Figure 6.21 (a–c)), and no significant difference is observed at these stages of life. These surfaces exhibited wear in both the flank and face regions at all stages. The accumulated black-colored wear debris revealed that they separated wear debris owing to the repetitive contact load and temperature under a prolonged test duration. Sliding marks are also visible near the pitch region. The worn tooth surface also revealed a change in the sliding direction (sliding–rolling–sliding) near the pitch region.

As the duration increased, the gear tooth contact region did not significantly differ, and the test was terminated after 20.0×10^5 cycles. The worn gear tooth surface is also examined using FESEM (Figure 6.21 (d)) to understand the wear mechanism in the pitch region of the SLS gear. Although no visible damage is observed under a microscope, very mild and shallow pits are observed near the pitch region under the FESEM.

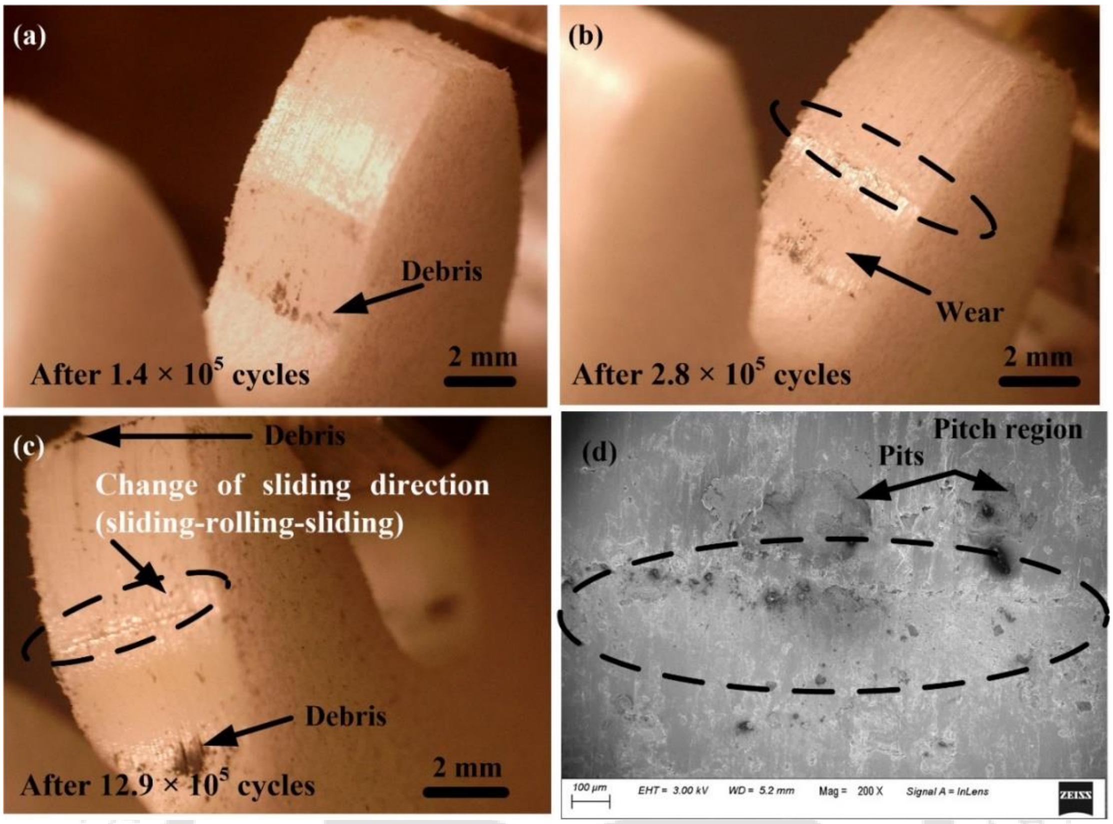

Figure 6.21 (a–d) Worn-out gear teeth surface at 1.8 Nm under dry condition

Under dry conditions, the worn-out teeth surface of the SLS gear at 2.5 Nm loading was periodically detected under a digital microscope, and minor differences are observed at various stages of life. The gear tooth surface damage is similar to that in the 1.8 Nm condition (Figure 6.21 (a, b)), but slightly more severe. In addition to the contact stress, the gear tooth surface experiences sliding friction in conjunction with high heat generation, causing a ridge to form in the pitch region. As seen in Figure 6.18 (a), the higher heat generated on the contact surface compared with the 1.8 Nm condition aided the formation of ridges, resulting from the accumulation of plastically deformed materials near the pitch region, as indicated in Figure 6.22 (a). Figure 6.22 (b, d) shows the FESEM micrographs of the worn-out gear tooth surface. The sliding marks on the face region are observed to be severe. Surface crack normal to the sliding direction is also observed on the face region (Figure 6.22 (b)). The gear teeth experienced repetitive compression and tension loads in conjunction with sliding, resulting in the formation of surface cracks normal to the sliding direction. An accumulated plastically deformed material is observed near the pitch region, as shown in Figure 6.22 (c). Many researchers have mentioned pitch-line cracks on polymer tooth surface under dry conditions (Terashima *et al.* (1986) and Soudmand and Shelesh-Nezhad (2020)). Senthilvelan and Gnanamoorthy (2004) reported that the generation of cracks near the pitch region was due to changes in the sliding direction and heat buildup. Figure 6.22 (d) shows the flank region of the test gear tooth, where sliding marks and plastically deformed material are observed.

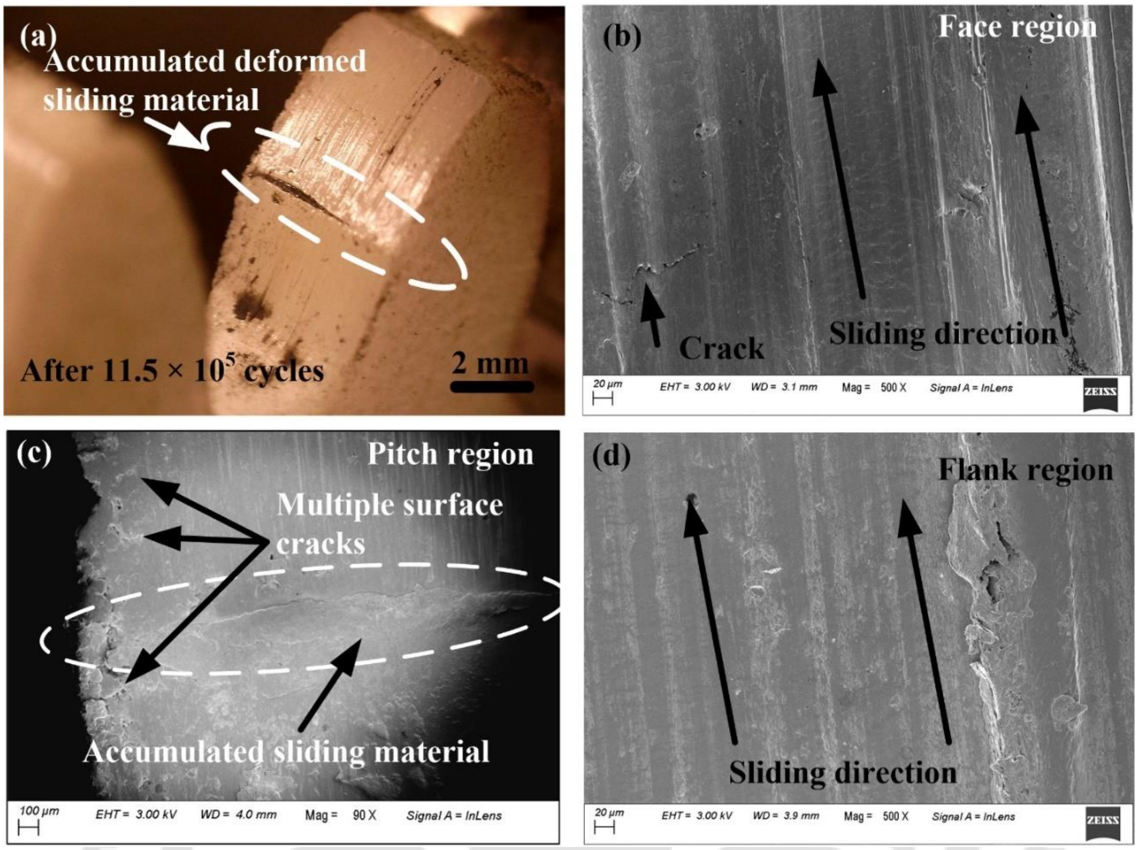

Figure 6.22 (a–d) Worn-out tooth surface at 2.5 Nm under dry condition

Figure 6.23 (a–b) shows the gear teeth surfaces when a load of 3.5 Nm is applied under dry conditions. Thermal failure revealed the onset of melting on the gear tooth surface and the piled-up deformed sliding material near the pitch region. The transparent displaced material confirms the melting of the material. Owing to the viscoelastic nature of the polymer gear material, the gear subjected to a higher load (3.5 Nm) generated significant heating owing to material hysteresis, in addition to surface friction. The measured temperature of the gear at this load confirmed a sudden increase in the temperature (Figure 6.18 (a)). At 3.5 Nm applied loading condition, the contact stress between the test and mating gear pair increased, leading to a higher operational temperature. This low-cycle fatigue (less than 10^4 cycles) is mainly influenced by the load and surface temperature, and only severe deformation, melting, and teeth bending are observed. Zhang *et al.* (2020) evaluated the performance of injection-molded and FDM-fabricated gears and observed a significant influence on the thermal properties of the gear material. Wear (loss of material at the pitch region), root fracture, and tooth bending owing to thermal load were observed under various loading conditions.

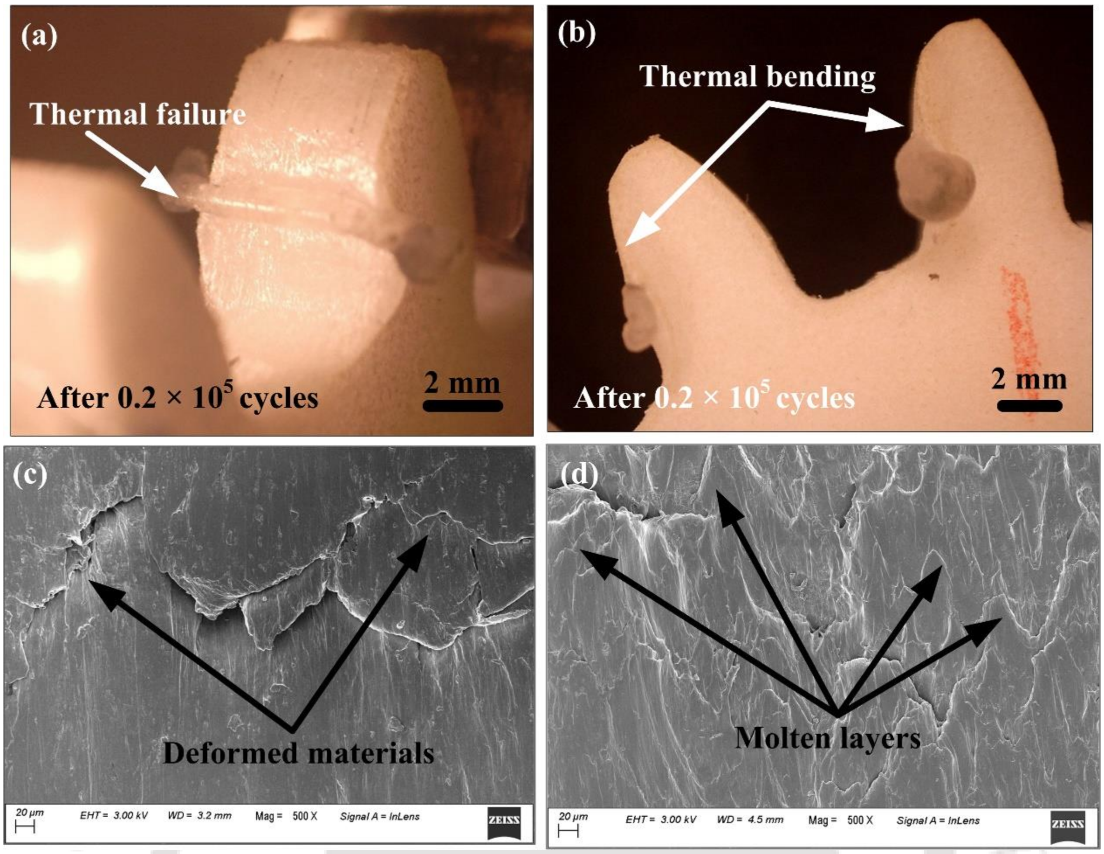

Figure 6.23 (a)–(d) Worn-out tooth surface at 3.5 Nm under dry condition

The gear tested at 3.5 Nm loading was further observed under FESEM (Figure 6.23 (c, d)). Plastically deformed material (Figure 6.23 (c)) on the face region and molten layers (Figure 6.23 (d)) on the flank region of the tooth are observed.

6.3.8 Failure morphology of the SLS gear under the lubricated condition

Figure 6.24 (a–c) reveals significant differences at various stages of life while testing at 1.8 Nm under lubricated conditions. Initially, almost uniform wear is detected on the gear tooth contact surface (Figure 6.24 (a)) owing to the interaction between the asperities of the layered surface of the SLS gear tooth and the mating steel gear surface. Surface fatigue failure pitting began near the pitch region (Figure 6.24 (b)) when the cyclic contact stress exceeded its critical value at this single-tooth contact region. The initial pitting increased with further testing, and multiple small pits formed on the tooth surface combined and culminated into larger pits, which became a severe surface failure feature/scuffing (Figure. 6.24 (c)). The worn-out lubricated tooth surface was detected using FESEM for detailed analysis. A pitting failure is observed near the pitch region of the lubricated gear (Figure 6.24 (d)). FESEM micrographs confirmed that the presence of a lubricant significantly reduced the surface fatigue strength, resulting in severe surface damage compared with the dry condition. Donzella *et al.* (2011) also reported that with an increased number of cycles, the generated micropits turn into macropits and then finally spall under the rolling contact condition. Under lubricated conditions, the lubricant prevents direct contact between the contact pairs, owing to the formation of a lubricant film.

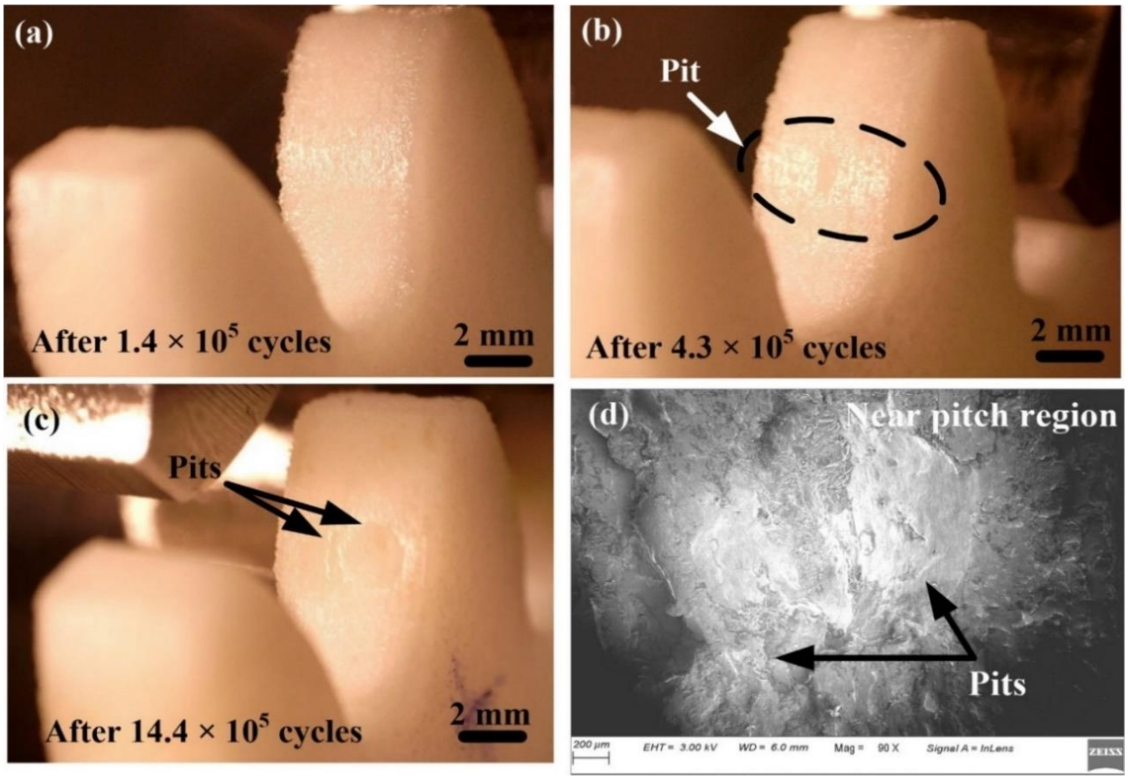

Figure 6.24 (a–d) Worn-out gear tooth surface at 1.8 Nm under lubricated conditions

In addition, the presence of a lubricant dissipates the generated heat owing to material hysteresis and surface interaction through the lubricant, resulting in reduced gear tooth temperature and the absence of severe plastic deformation on the contact surface. Under lubricated conditions, the porous structure of the SLS gear tooth surface is subjected to repetitive contact load and sliding friction. Combined loading and sliding would diffuse more lubricant into the gear tooth subsurface, which would contribute to the inferior contact fatigue strength of the SLS gear under lubrication compared to that under dry conditions. Seltzer *et al.* (2011) evaluated the strength and fracture behavior of SLS polyamide under water conditioning. It has been reported that the presence of water and the porous structure of SLS polyamide deteriorate the yield strength and toughness owing to the hydrolysis of the molecules. Goodridge *et al.* (2010) evaluated the long-term aging of SLS polyamide and observed a reduction in its tensile strength owing to the absorption of water.

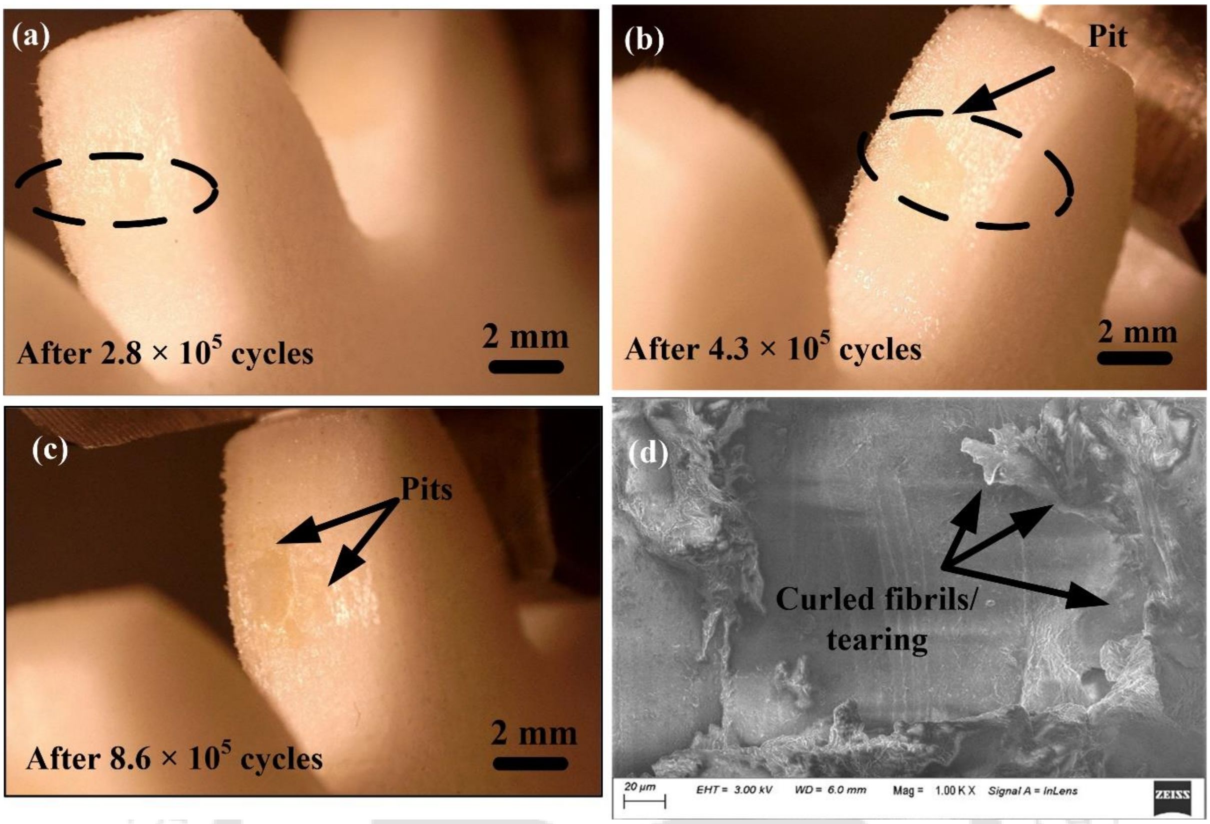

Figure 6.25 (a–d) Worn-out tooth surface at 2.5 Nm under lubricated conditions

Figure 6.25 (a–c) reveals the worn-out lubricated gear teeth surface at 2.5 Nm with a significant difference at various stages of life. The wear characteristics are similar to those under the 1.8 Nm loading condition; however, pitting began earlier owing to the higher contact stress. Furthermore, the worn-out surface was observed under FESEM (Figure 6.25 (d)), which revealed curled drawn-out fibrils at the pit boundaries. Under the same loading condition, the gear exhibited a deformed sliding material near the pitch under dry conditions owing to higher temperatures. However, the test gear exhibited poor performance at the same load compared with that in the dry condition.

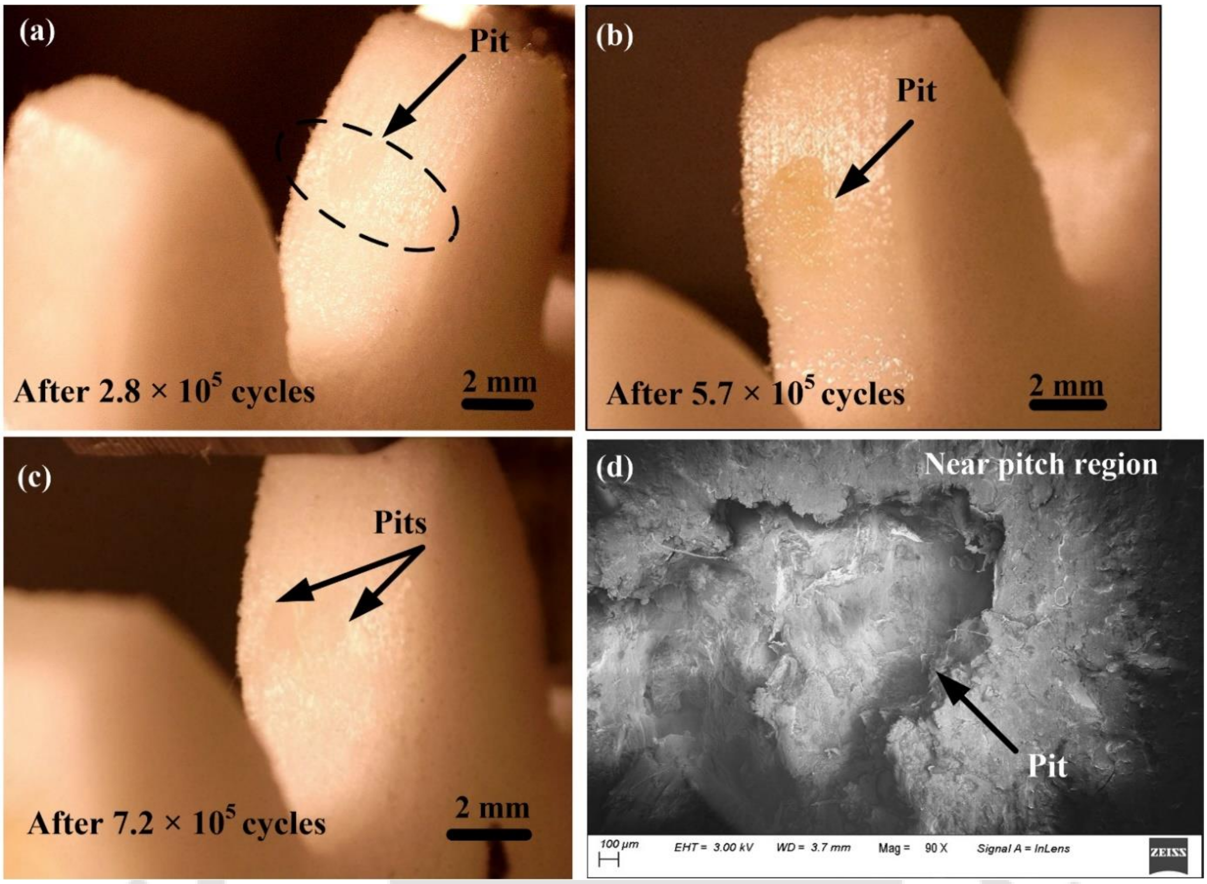

Figure 6.26 (a–d) Worn-out gear tooth surface at 3.5 Nm under lubricated conditions

Figure 6.26 (a–c) shows the worn-out lubricated gear teeth surface at 3.5 Nm. Under lubricated conditions, despite the improved heat dissipation characteristics, the contact fatigue strength of the gear deteriorated for the considered loads, except for a load of 3.5 Nm. At a 3.5 Nm loading, the test gear exhibited severe thermal bending failure/tooth plastic deformation under dry conditions. However, the presence of a lubricant prevents thermal failure and thus enhances the performance of the lubricated test gear.

The presence of lubrication reduced the heat generation, further reducing friction, and the lubricated gear exhibited a longer (41 times) life than the dry gear. Figure 6.26 (d) displays the FESEM morphology of the test gear, revealing pitting features that are severe near the pitch region. Under the same loading condition, the gear exhibited a deformed sliding material near the pitch under dry conditions owing to the higher temperatures.

6.3.9 Gear debris

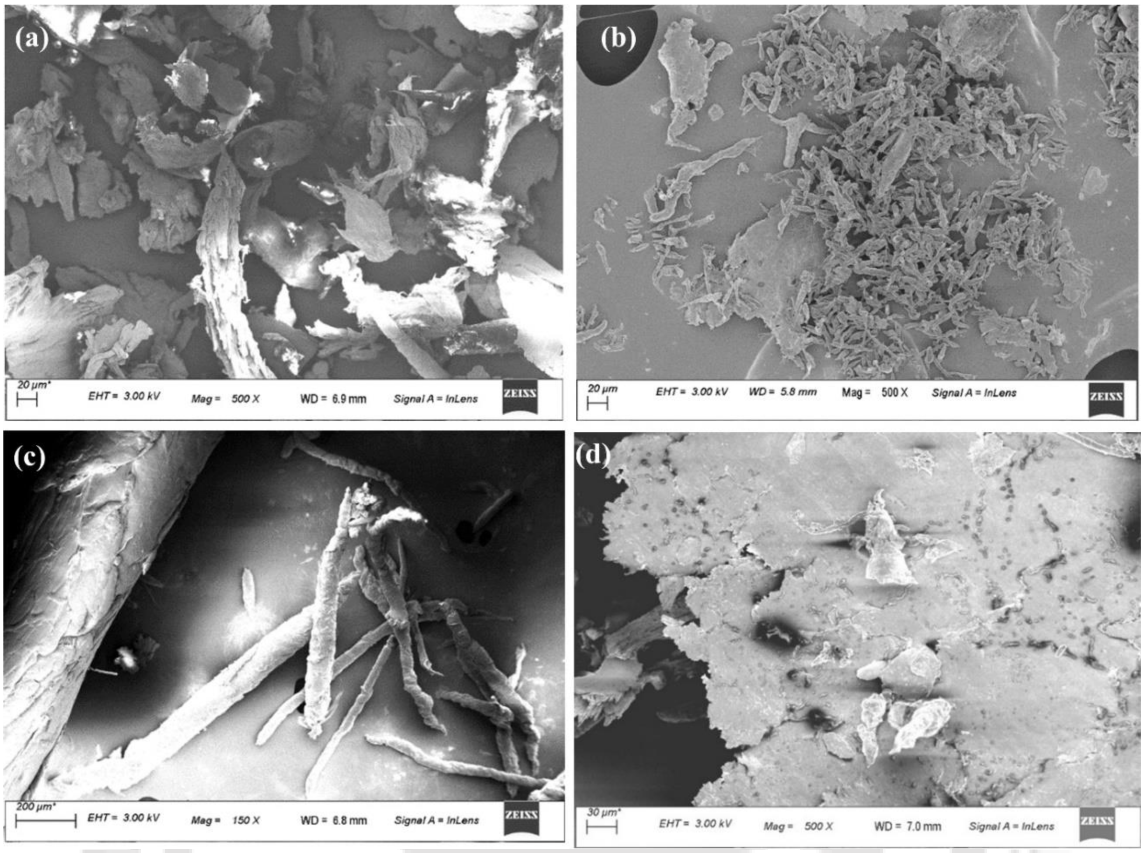

Figure 6.27 Gear wear debris under dry conditions at (a) 1.8, (b) 2.5, (c) 3.5 Nm, and (d) Gear debris under the lubricated condition

Wear debris was collected after the gear test to understand the mechanism. The debris features differed at various loadings under dry conditions; however, this load-sensitive behavior is not observed for the lubricated gear. The flushing action of the lubricant and surface temperature of the test gear contributed to this behavior. Under dry conditions, the gear at 1.8 Nm generated flake-like debris (Figure 6.27 (a)). Initially, the surface asperities of the test gear ruptured owing to the abrasive action of the mating steel gear. The generated debris sticks with the mating steel gear tooth surface, and this adhesive action results in the generation of flake-like debris.

At 2.5 Nm, the initially generated wear debris became entrapped between the test and mating steel gear surface and changed into fibril form owing to the higher contact stresses and higher surface temperature (Figure 6.27 (b)). At 3.5 Nm, the temperature generation is significantly high, resulting in severe plastic deformation, and the generated wear debris is fibrous/needle-like (Figure 6.27 (c)). Figure 6.27 (d) displays the collected wear debris from the lubricated gear at 1.8 Nm loading, and similar debris forms are also observed at 2.5 and 3.5 Nm. The lubricant between the contact surface flushes generates debris and reduces surface interaction and temperature; hence, the generated wear debris is not load-sensitive. The generated wear debris has a larger flake form owing to the consolidation of the wear debris by the lubricant.

In the earlier chapter 4, it was observed that in the case of injected molded gear, surface fatigue failure was not only restricted to the pitch region but also on adjacent to the pitch region, that is, on the flank region of the gear tooth. However, in this chapter, it is observed that surface fatigue failure is predominantly pitting but also restricted to the pitch region for the same condition (load and environment). This behavior could be due to the superior tooth stiffness of SLS gear compared to IM gear as well as due to the brittle characteristics of SLS gear material. Higher modulus of SLS gear material contributes to this superior tooth stiffness and hence lesser single tooth contact area on the pitch region. It is well established that the single tooth contact area on the gear tooth region is inversely proportional to tooth stiffness. Therefore, IM gear exhibited a higher single-tooth contact region on the pitch region compared to SLS gear for the same loading condition. Consequently, surface fatigue failure is only limited to the pitch region in the SLS, whereas it is spread out to the adjacent region also in the case of IM gear.

6.3.10 Summary

The surface durability of the selective laser-sintered polyamide gear was investigated under dry and lubricated conditions, and the following major conclusions were drawn:

- Under the dry condition, SLS gear exhibited superior performance (no failure, only polishing effect) at a lower load (1.8 Nm) enabled by the enhanced surface fatigue strength due to the layer-by-layer manufacturing process compared to the injection molding process. Under lubricant condition, both SLS and IM gear (as observed in an earlier chapter 4) exhibited contact failure features and similar life while subjected to a lower load (1.8 Nm)
- The lubricated SLS gear exhibited inferior contact fatigue performance at lower loads (1.8 Nm and 2.5 Nm) than that under dry condition. Cyclic contact stress coupled with sliding motion diffuses the lubricating oil into the porous subsurface and reduces the contact fatigue strength of the gear tooth.
- Under dry conditions, SLS gear (2.5 and 3.5 Nm) gear exhibited thermal softening along with cracking and thermal bending, respectively. Poor surface roughness of the SLS gear contributes to the rapid rise in surface temperature. In the earlier chapter, it was found

that injected molded gear exhibited severe cracks but not severe thermal damage as observed in SLS gear, and its better life than SLS gear could be due to higher HDT.

- The lubricated SLS gear exhibited superior performance at a higher load (3.5 Nm) compared to the dry gear. The lubricant dissipated the generated heat and delayed the thermal failure.

Chapter 7

Surface durability performance of thordon gear under dry and oil lubricated condition

7.1 Introduction

In the earlier chapters, the surface durability of injection molded polyamide gears under dry and lubricant conditions has been reported. Oil-lubricated polyamide gear was found to exhibit better performance than dry conditions. Thermoplastic polyamide gears are widely used in many applications under dry conditions; this chapter aims to identify any other bearing material that is compatible with oil/lubricant. It is well established that commercial grade elastomeric material, Thordon class, is being used under marine environments with water as a lubricant. In this chapter, thordon SXL material is being considered for gear application. Initially, the sliding contact performance of a thordon material under dry and oil-lubricated conditions was examined. Subsequently, the Thordon gears were subjected to bending and contact loads under dry and oil-lubricated conditions.

7.2 Sliding contact performance of thordon material

7.2.1 Mechanical characteristics

The tensile specimen (ASTM D638 type V) was extracted from the thordon SXL rod with the help of the machining process. Testing was carried out using an Electromechanical universal testing machine (Zwick Roell: Z005TN) at a strain rate of 1 mm/min. The tensile specimen photograph and stress-strain curve obtained are shown in Figure 7.1. Young's modulus, % of elongation, and ultimate tensile strength are found to be 220 MPa, 251%, and 51MPa.

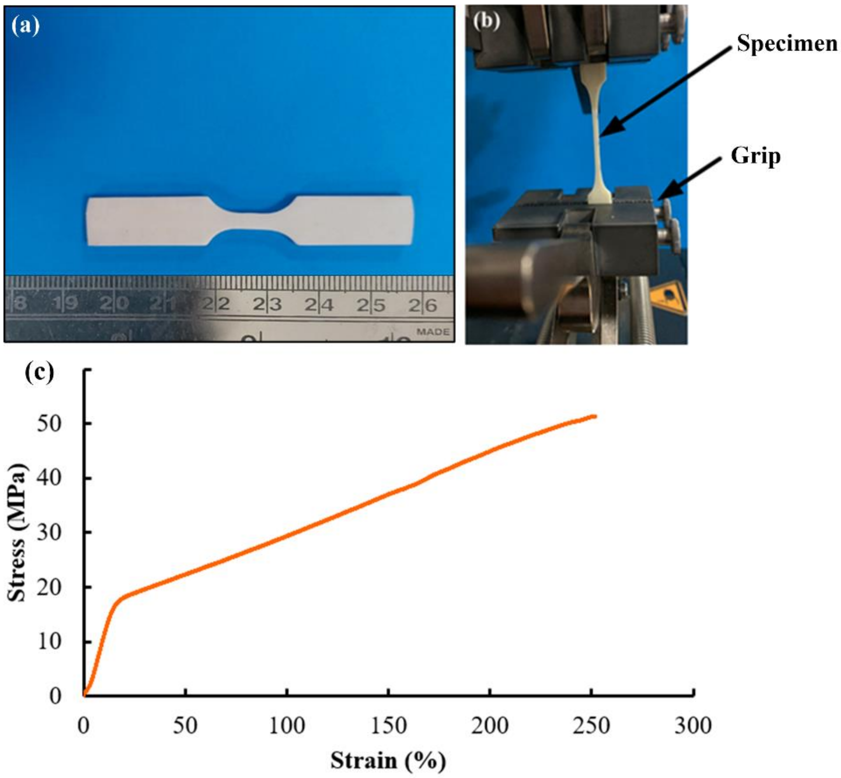

Figure 7.1 (a) Machined tensile specimen (b) Specimen during tensile testing and (c) The stress-strain curve obtained during tensile testing

7.2.2 Environmental stress cracking

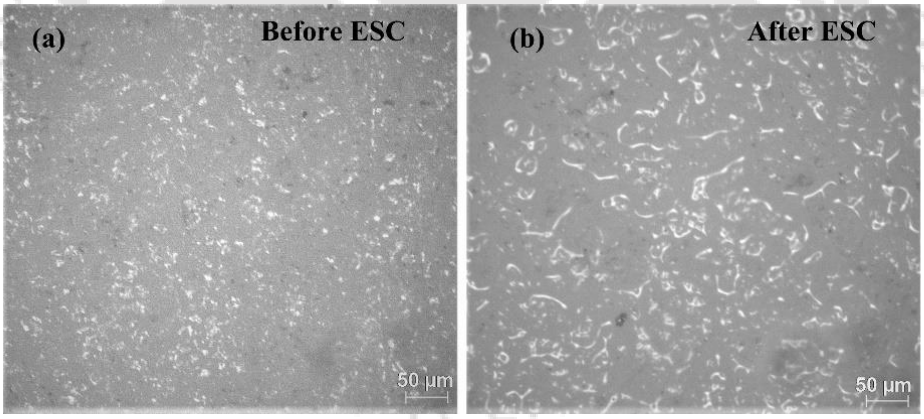

Figure 7.2 Environmental Stress Cracking specimens' surface (a) Before testing and (b) After testing

As mentioned in chapter 3, for the evaluation of oil resistance, the environmental stress cracking (ESC) thordon specimen was strained (1.2 %) using a 3-point bending configuration, and the whole setup was immersed in lubricating oil for seven days at room temperature. After seven days, the measured weight is found to be a 0.5 % gain. The weight gain of thordon material is higher than the injection molded polyamide material. Figure 7.2 (a) and (b) shows the specimen surface before and after ESC testing. The surface morphology (Figure 7.2 (b) reveals some surface texture changes due to the diffusion/absorption of the oil after testing. Hanley *et al.* (2008) found that the presence of oil led to swelling of the material surface.

7.2.3 Sliding contact performance methodology

The thordon rod form was reduced to a pin through the turning process to evaluate the sliding contact performance. The machined pin specimen was studied using a pin-on-disc configuration under dry and oil-lubricated under an applied normal load of 60 N and a sliding velocity of 1.13 m/s.

7.2.4 Pin surface characterization

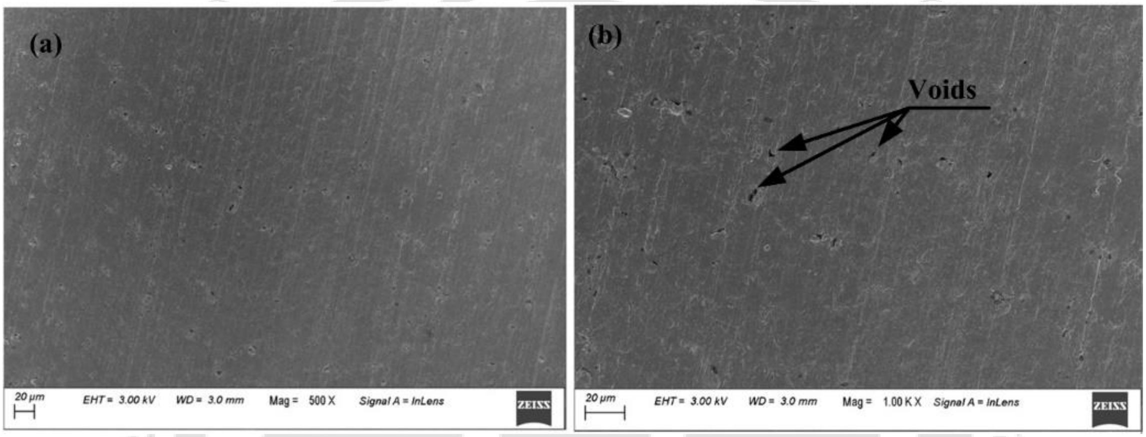

Figure 7.3 Surface of thordon pin specimen before the sliding test

Figure 7.3 shows the FESEM micrographs of the pin surface prepared by sliding against silicon carbide abrasive paper before testing, indicating the presence of multiple voids on the thordon material surface. In polymer blends, the interface between the polymers as well as air entrapped during molding, are responsible for void formation. Hazre (2014) observed voids due to the phase separation of components in the blend material. Hasanpour *et al.* (2020) observed cavitation or debonding owing to the rubbery phase in the blended polymer. The measured average Shore D hardness of pin specimen was 73 ± 1D. The measured average roughness (R_a) of the pin specimen is 0.42 µm.

7.2.5 Sliding friction and surface temperature

The variations in the coefficient of friction with respect to the sliding time of the thordon material under dry and lubricated conditions are shown in Figure 7.4. The coefficient of friction under dry conditions (0.27) is higher than that under lubricated conditions (0.10). The presence of a lubricant reduces the contact between asperities and hence reduces frictional heating, resulting in lower friction. Lubricant reduced friction by 63% relative to the dry condition.

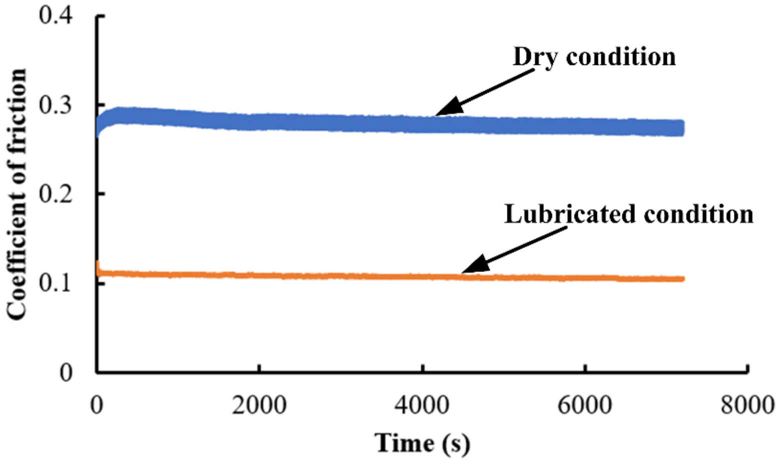

Figure 7.4 Measured coefficient of friction of thordon material under dry and oil-lubricated conditions

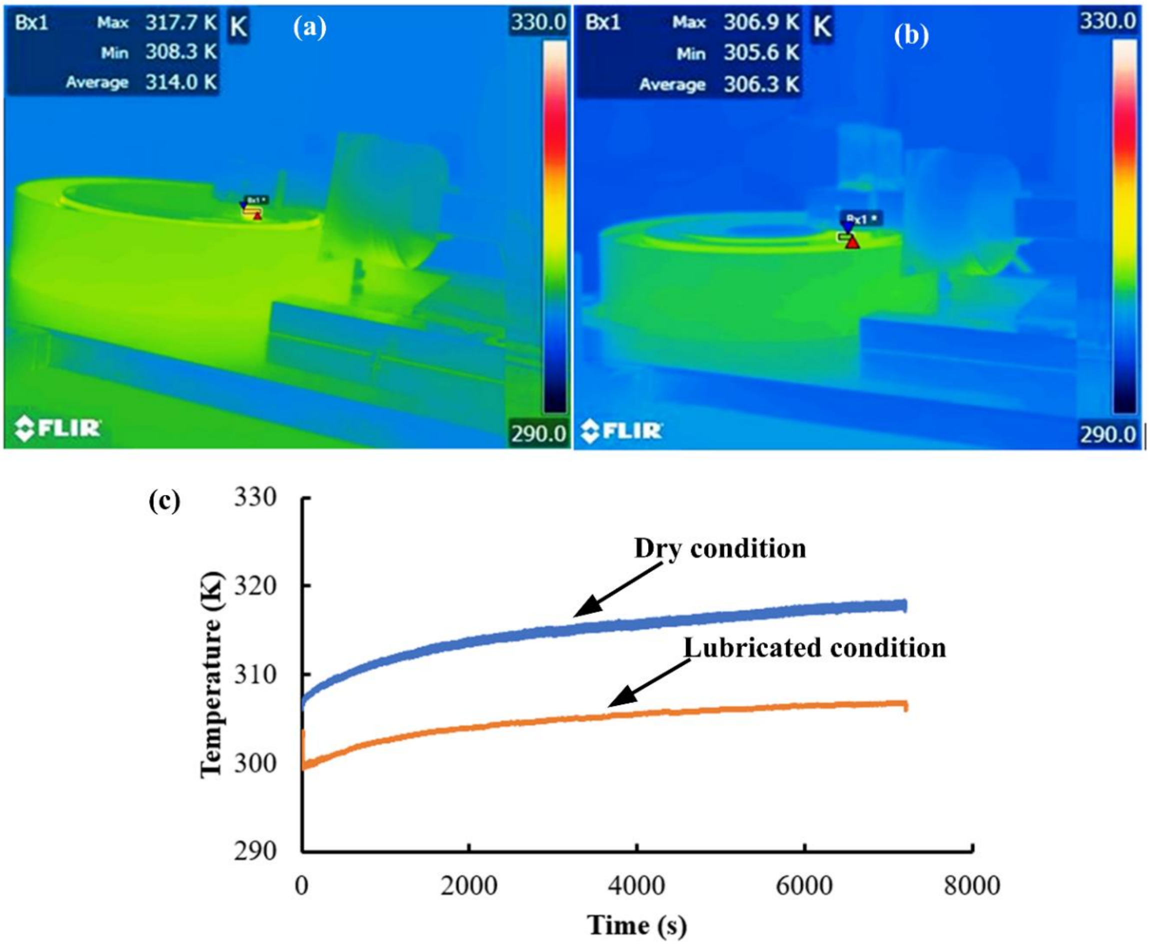

Figure 7.5 (a), (b) Thermographs of thordon material under dry and oil-lubricated conditions, and (c) Surface temperature of thordon material under dry and oil-lubricated conditions

Figure 7.5 (a) and (b) show the IR camera images of the thordon material under dry and oil-lubricated conditions. The rise in the surface temperature is gradual in the beginning and then stabilized after some time, as shown in Figure 7.5 (c). Under dry and lubricated conditions, the steady temperatures are 318 and 306 K, respectively. Berglund and Shi (2017) reported a reduction in sliding friction and wear thordon thorplas bearings under a sustainable Lube lubricant. Three trials were performed under the same condition. The weight losses are almost the same ($0.127\% \pm^{0.033}_{0.019}$ and $0.124\% \pm^{0.048}_{0.041}$ under dry and lubricated conditions, respectively).

7.2.6 Wear morphology of thordon material surfaces

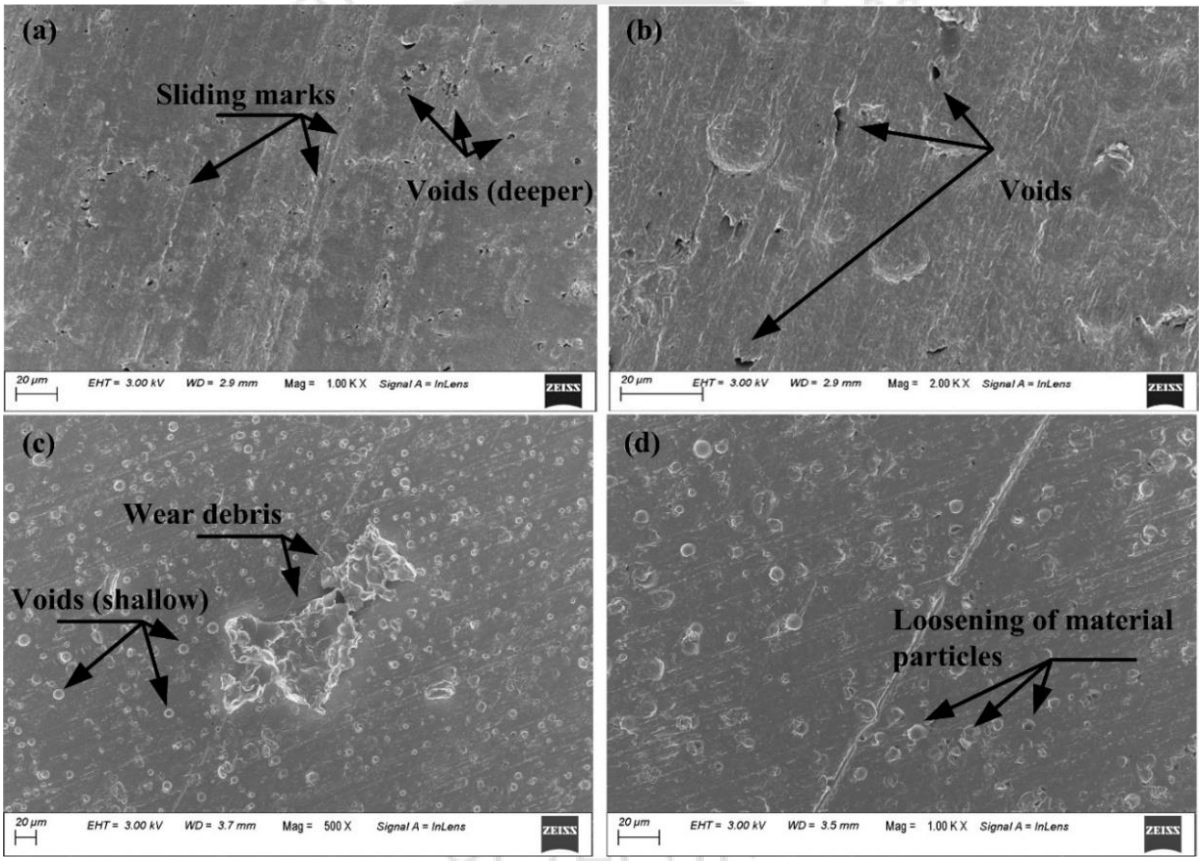

Figure 7.6 Worn-out thordon material surface under (a, b) Dry conditions and (c, d) Oil-lubricated conditions

Figure 7.6 (a) and (b) show FESEM micrographs of the worn thordon material surface under dry conditions; the voids on the surface are deeper. The sliding action of the test material increased and exposed more voids than on the initial test surface (see Figure 7.3). Similar features/voids were observed in carbon black-filled rubber and recycled ethylene propylene diene monomer blend fracture surfaces (Nabil *et al.* (2013)). FESEM micrographs of the worn tooth surface under lubricated conditions are shown in Figure 7.6 (c) and d). Sliding under oil lubrication generated a greater number of voids owing to the flushing effect of the lubricant. Because of the loosening of the material around the voids, the size of these voids increased, and they became shallow. Huang *et al.* (2021) observed similar features/voids on a worn-out surface thordon COMPAC material under water-lubricated conditions. Under dry conditions, the worn-out surface revealed a few deeper voids, whereas, under oil lubrication, more shallow voids are observed.

In this section, an attempt is made to understand the basic sliding behavior of flat thordon material under dry and oil-lubricated conditions. However, this configuration (pin-on-disc) is not equivalent to the gear tooth surface interaction. In the gear pair contact, a nonconformal contact pattern exists along with combined rolling and sliding with varying sliding velocities along the line of contact. It is revealed that oil lubrication significantly reduces the friction and heat generation of thordon material; however, no appreciable wear difference between dry and lubricated conditions is observed for the considered test conditions.

7.3 Thordon gear performance

7.3.1 Gear performance methodology

The thordon material in the cast rod form was hobbed into the spur gear and considered for the test (driven) gears. The gear performance was evaluated using a gear test rig developed in-house at different torque levels of 1.8, 2.5, and 3.5 Nm and a rotational speed of 800 rpm under dry and lubricated conditions. Figure 7.7 shows the steel-thordon gear pair mesh.

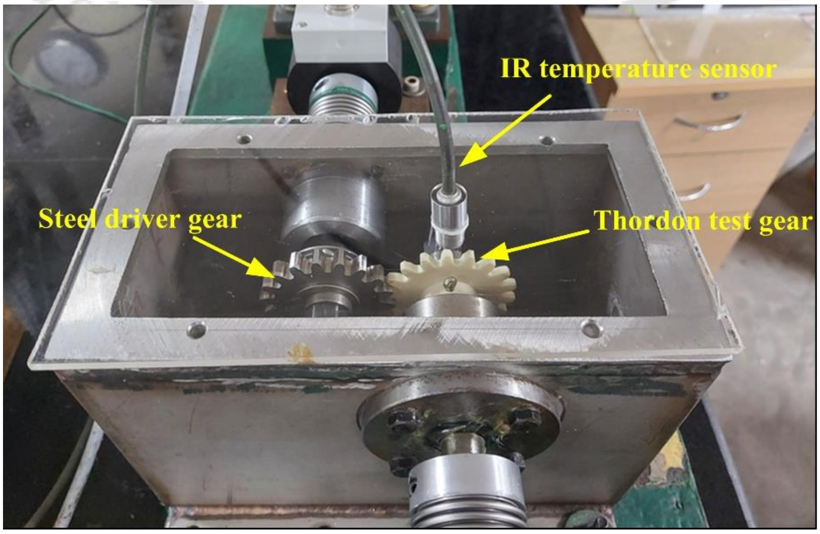

Figure 7.7 Close up view of steel-thordon gear pair mesh

7.3.2 Gear tooth surface

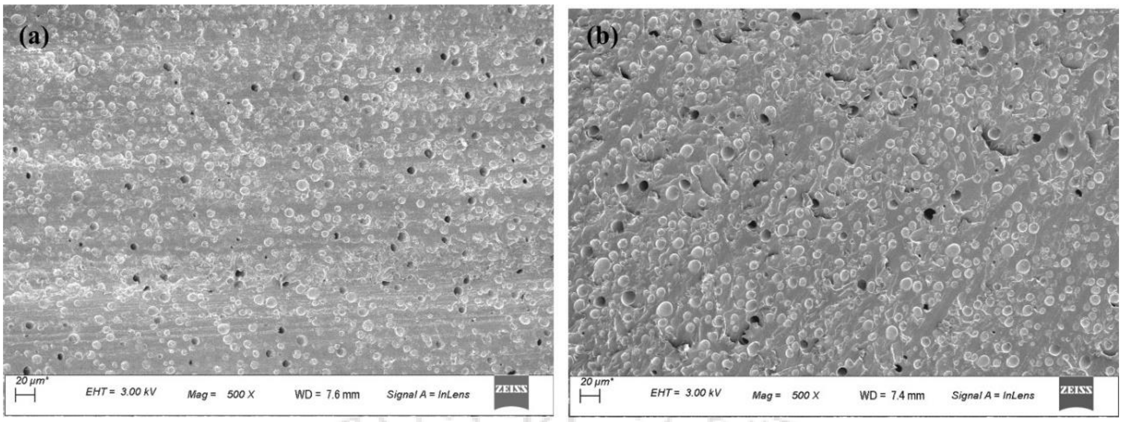

Figure 7.8 (a) Morphology of gear tooth face surface and (b) The sectioned subsurface

The hobbed test gear tooth surface was observed using FESEM (Figure 7.8 (a)), revealing an inhomogeneous surface with a large number of voids due to the hobbing action. An inhomogeneous surface with large numbers of voids is also observed in the sectioned subsurface, 1 mm below the gear tooth surface (Figure 7.8 (b)). Similar types of features/voids were observed in blended polylactic acid and hydroxylated soya bean oil material (Hazre (2014)). However, these surface defects/inhomogeneities are not present on the injection-molded thermoplastic gear surface or subsurface.

7.3.3 Thordon gear tooth surface and lubricant oil temperature

The measured gear-tooth surface temperatures at different loads under dry conditions are shown in Figure 7.9 (a). At 1.8 Nm, the gear tooth temperature gradually increased in the beginning, and it became stable at 326 K. After 5.7×10^5 cycles, a crack is initiated at the gear tooth root owing to the exceedance of the bending fatigue life (Figure 7.12 (c)). However, when testing at 2.5 and 3.5 Nm, the test gear exhibited a progressive increase in surface temperature with the test cycles.

At a lower load, the temperature initially increased, followed by a steady state until failure. The gears tested at 2.5 and 3.5 Nm had surface temperatures of approximately 334 K and exhibited root cracks (Figure 7.13 (b). As the load increased, the temperature generated by the bending and contact stresses further weakened the gear material and reduced the gear life. Under the high-load condition, the heat generation of the thermoplastic gear was significantly higher than that of dissipation, resulting in continuous heat build-up and progressively increasing temperature until failure (Senthilvelan and Gnanamoorthy (2004)). Fernandez *et al.* (1996)

reported a reduction in thordon XL material shear strength with increasing temperature. Under the considered testing conditions (1.8–3.5 Nm), the lubricant temperature increased by approximately 6 K (Figure 7.9 (b)).

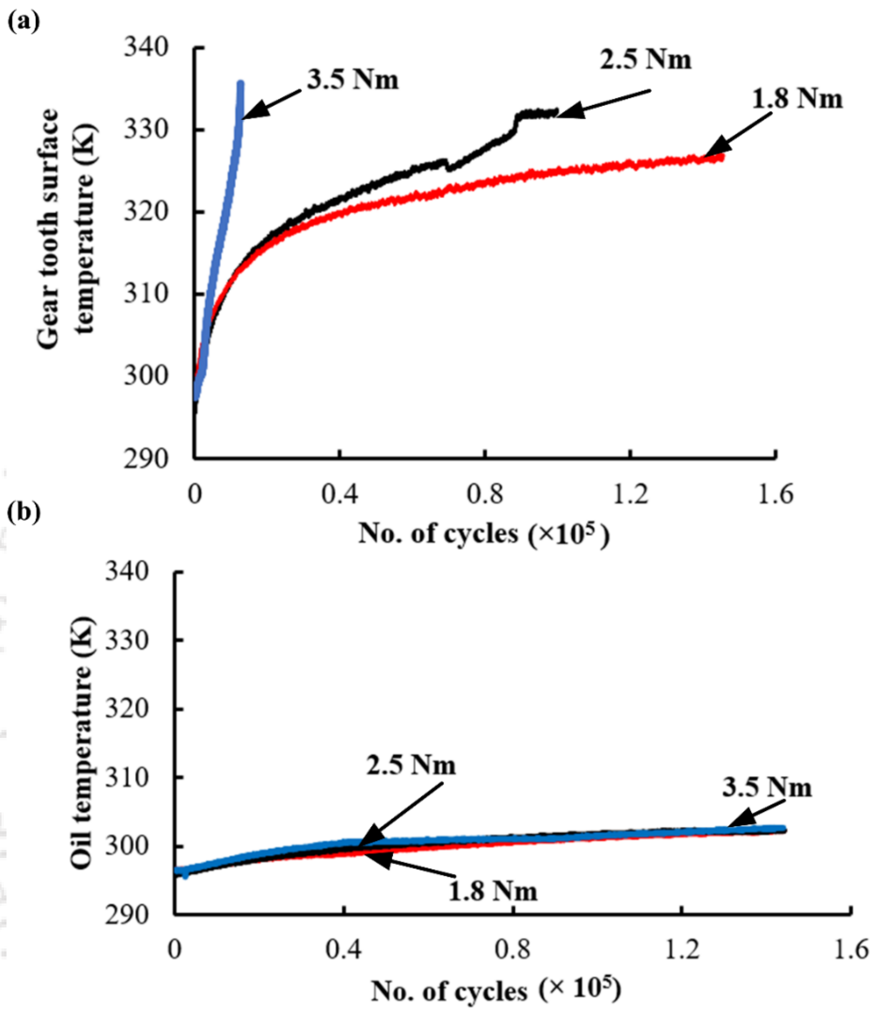

Figure 7.9 (a) Gear tooth surface temperature under dry conditions and (b) Lubricant oil temperature

The gears tested at 1.8 Nm under oil lubrication did not show any root cracks; hence, the base tangent length across the three teeth was measured periodically. A 0.38 % reduction in the base tangent length is found after 20.1 × 10^5 cycles, and the weight loss of the test gear is found to be 0.3 %. Figure 7.10 (a) and (b) shows the surface roughness of test gear (R_a); the initial roughness (2.23 μm) due to the machining marks is reduced (1.55 μm) because of run-in wear. The gear tooth profile is measured using an optical profile projector (PP400 TE), and no significant differences are observed. The test gear exhibited cracks at the gear tooth under all other considered conditions except 1.8 Nm and oil-lubricated; hence, wear data and surface roughness are reported only for this test condition.

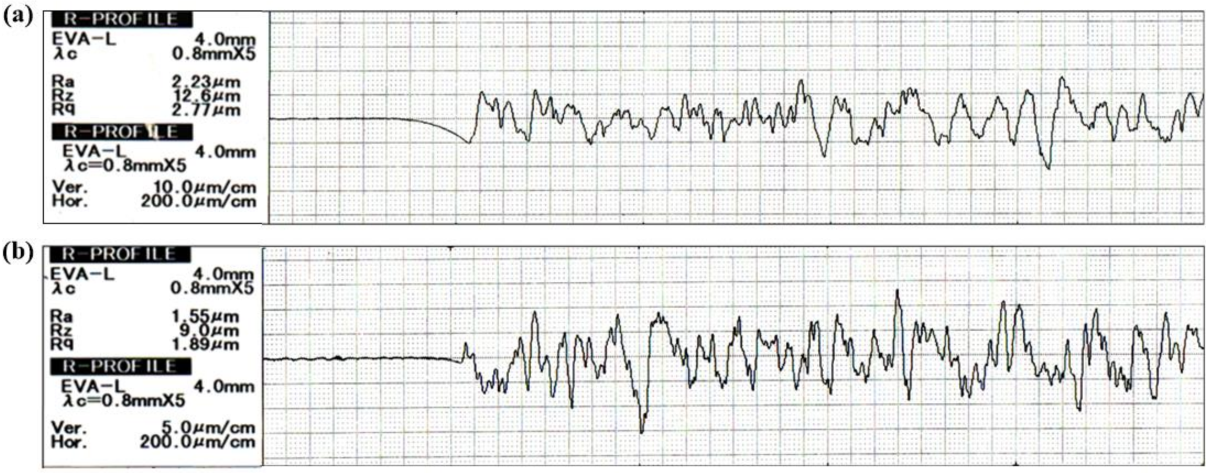

Figure 7.10 (a), (b) Initial and final surface roughness of test gear under oil lubrication condition at 1.8 Nm

7.3.4 Failure modes and fatigue life models

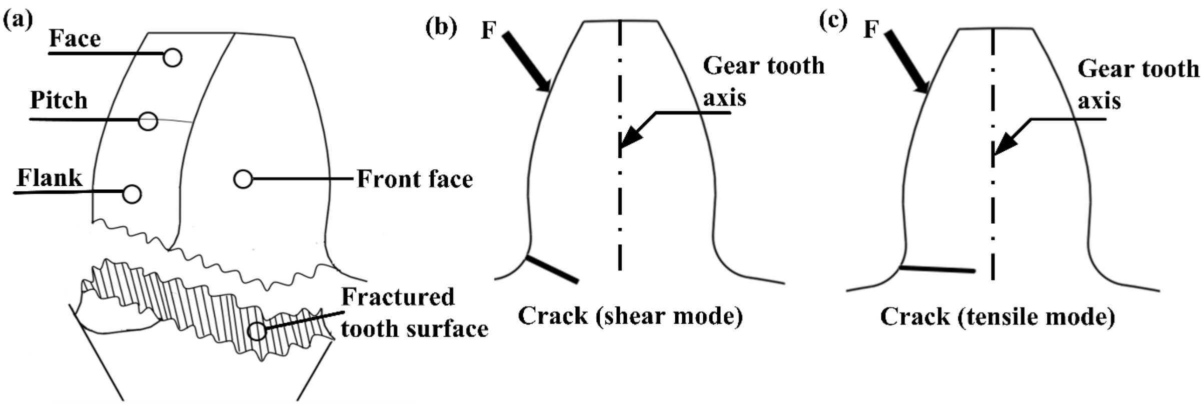

Figure 7.11 (a)–(c) Schematic of various gear tooth regions, fractured surfaces, and root crack modes

Figure 7.11 (a) shows various regions of the gear tooth, including the face, pitch, flank, and fractured surfaces at the root. These gear tooth regions are critical failure regions due to the bending and contact fatigue loads. The gear tooth face, flank, and pitch regions are susceptible to excessive wear, pitting, and surface damage when the gear contact fatigue stress exceeds its contact fatigue strength. The gear-tooth root region is susceptible to root cracks when the gear bending fatigue stress exceeds its bending fatigue strength. In general, these nucleated fatigue cracks grow in the shear plane (at an angle to the free surface) and then in the tensile mode (normal to the free surface) towards the end of life (Stephens *et al.* (2000)). Figure 7.11 (b) and (c) show the schematic of the pure shear and pure tensile modes of the gear tooth root crack when subjected to bending fatigue load. The gear design based on the Lewis bending model considers a gear tooth analogous to a cantilever beam. A cantilever beam subjected to a higher bending load typically exhibits a tensile-mode crack in the root region during a low-fatigue cycle (< 10^4 cycles). On the other hand, a cantilever beam subjected to a lower magnitude of bending load typically exhibits a shear mode crack in the root region during a high fatigue cycle (>10^4 cycles).

7.3.5 Failure morphology of thordon gears under dry conditions

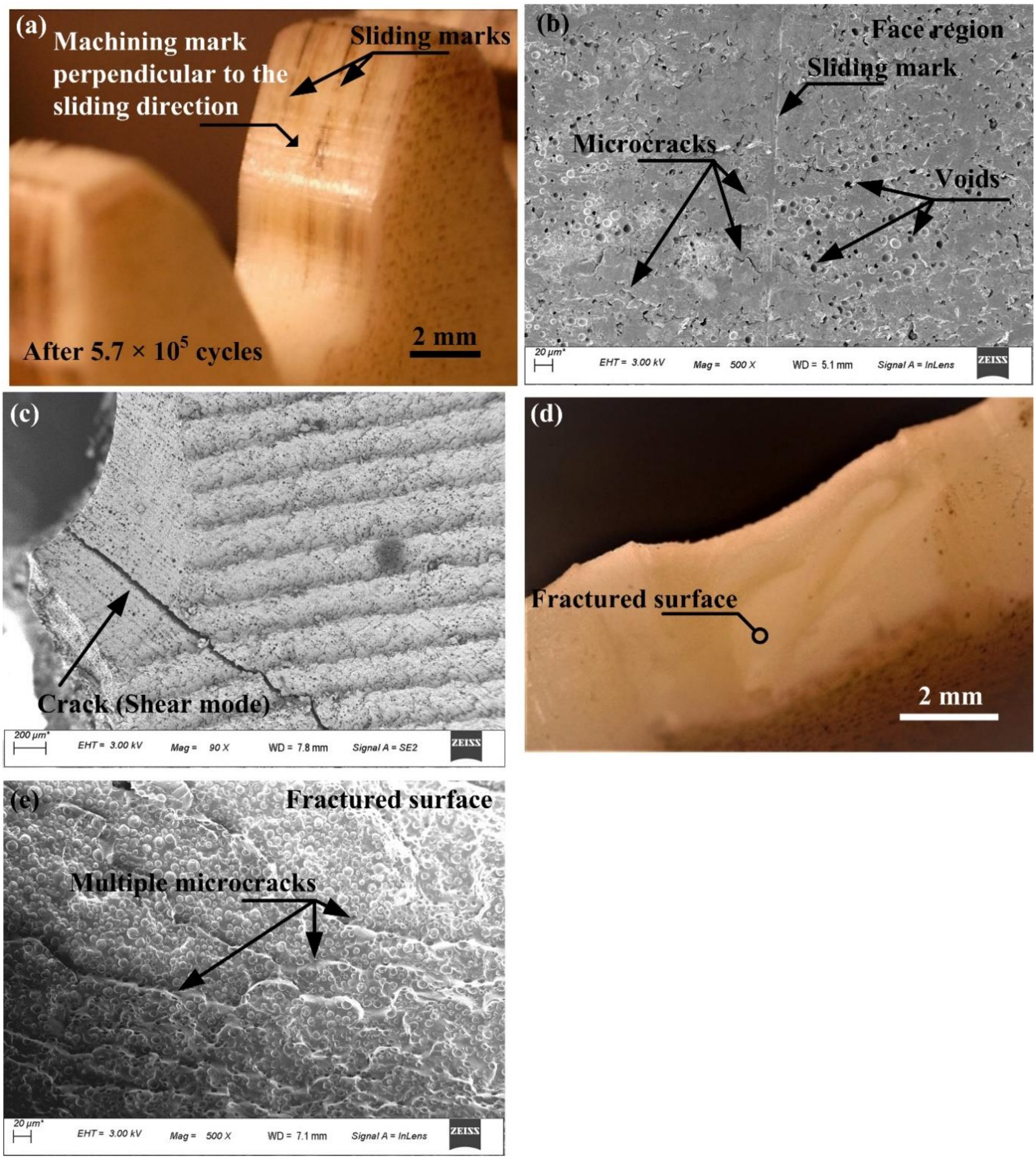

Figure 7.12 (a)–(e) Failure morphology of thordon gear tooth surface at 1.8 Nm under dry conditions

Figure 7.12 (a) shows the sliding marks on the face and flank regions of the gear tooth parallel to the sliding direction. Machining marks normal to the sliding direction are also visible on the gear tooth surface. The face region of the worn gear tooth surface was observed using FESEM (Figure 7.12 (b)) revealed sliding marks, voids, and microcracks. The presence of voids on the thordon material surface initiated microcracks owing to repetitive sliding and rolling. A similar worn-out surface is observed in the pitch and flank regions of the gear tooth surface. Fernandez *et al.* (1996) also reported the generation of microcracks on a thordon XL surface when sliding against a Cr_2O_3-coated metallic surface. Under fatigue, material discontinuities lead to a higher localized inelastic strain, resulting in microcracking (Stephens *et al.* (2000)). Fatigue crack nucleation occurs near discontinuities, such as second-phase particles, microcracks, pores, and voids. However, these microcracks on the face and flank regions of the thordon gear did not generate pitting on the gear tooth surface, which could be owing to the dominance of bending fatigue stress over contact fatigue stress for the considered load condition. Prior investigations on thermoplastic gears under dry conditions demonstrated excessive wear failure at lower load (Zorko *et al.* (2017) and (Mertens and Senthilvelan (2018)). Under a low load, cracks are initiated in the gear root region of the thordon test gear when the bending fatigue stress exceeded the bending fatigue strength of the gear material. Figure 7.12 (c) shows a crack in the gear tooth root region, and the mode of failure is shear, as indicated in Figure 7.12 (b).

The growth of these cracks under cyclic loading reached a critical size, and subsequently, a fracture occurred. Figure 7.12 (d) shows the fractured surface of the gear tooth. The fractured tooth surface was also observed using FESEM (Figure 7.12 (e)), revealing multiple microcracks. The gear tested at 2.5 Nm under dry conditions exhibited a similar failure.

Figure 7.13 (a) shows the face region of the test gear tooth at 3.5 Nm. Only voids and microcracks are observed in the face region, and no machining or sliding marks are observed. A similar surface is observed in the flank region. The test gear exhibited a tensile mode crack at the tooth root at this load, as shown in Figure 7.13 (b). The fractured surface exhibited severe multiple crack formations, as shown in Figure 7.13 (c) and (d). The presence of multiple cracks confirmed uncontrolled crack growth. Prior investigations of thermoplastic gears under dry conditions exhibited thermal failure at higher loads (Düzcükoğlu (2009b) and Mao *et al.* (2019)), in contrast to thordon gears.

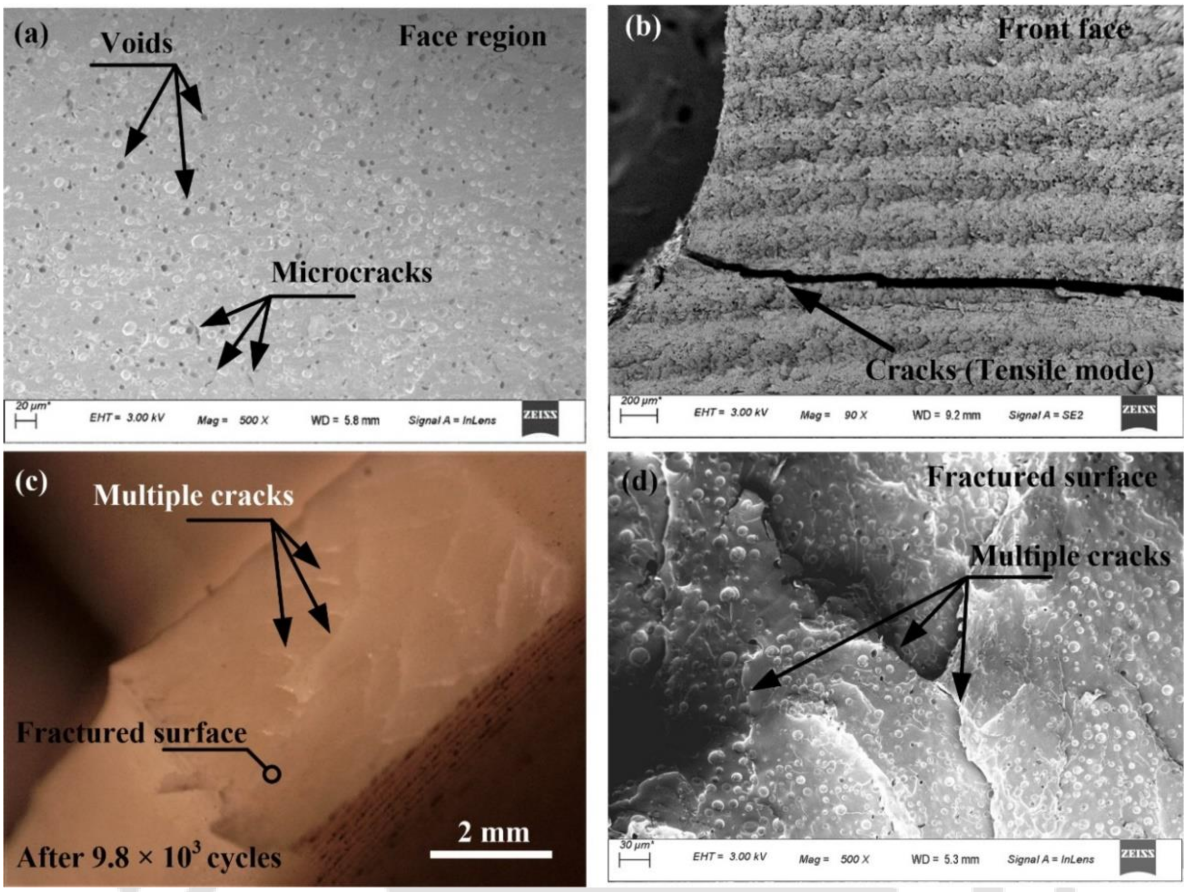

Figure 7.13 Failure modes of thordon gear at 3.5 Nm under dry conditions

7.3.6 Failure morphology of thordon gear under lubricated conditions

Figure 7.14 (a-c) shows the worn tooth surface of the thordon gear at different stages of life when testing at 1.8 Nm under lubricated conditions. The machined marks on the gear tooth face and flank region are reduced with the test duration. The lubricant separated the contact surface and dissipated the heat generated from the tooth surface of the test gear. Additionally, lubricant oil flushed the generated wear debris from the gear tooth surface, resulting in a clean surface. The worn surface of the thordon gear under lubrication is very smooth, with no surface damage. The thordon gear under lubrication did not exhibit any surface failure, and the test was terminated after 20×10^5 cycles. The face surface observed by FESEM (Figure 7.14 (d)) revealed sliding marks parallel to the sliding direction, and machining marks normal to the sliding direction. The morphology also confirmed the absence of microcracks, unlike in dry conditions. A similar feature is observed in the flank region (Figure 7.14 (e)).

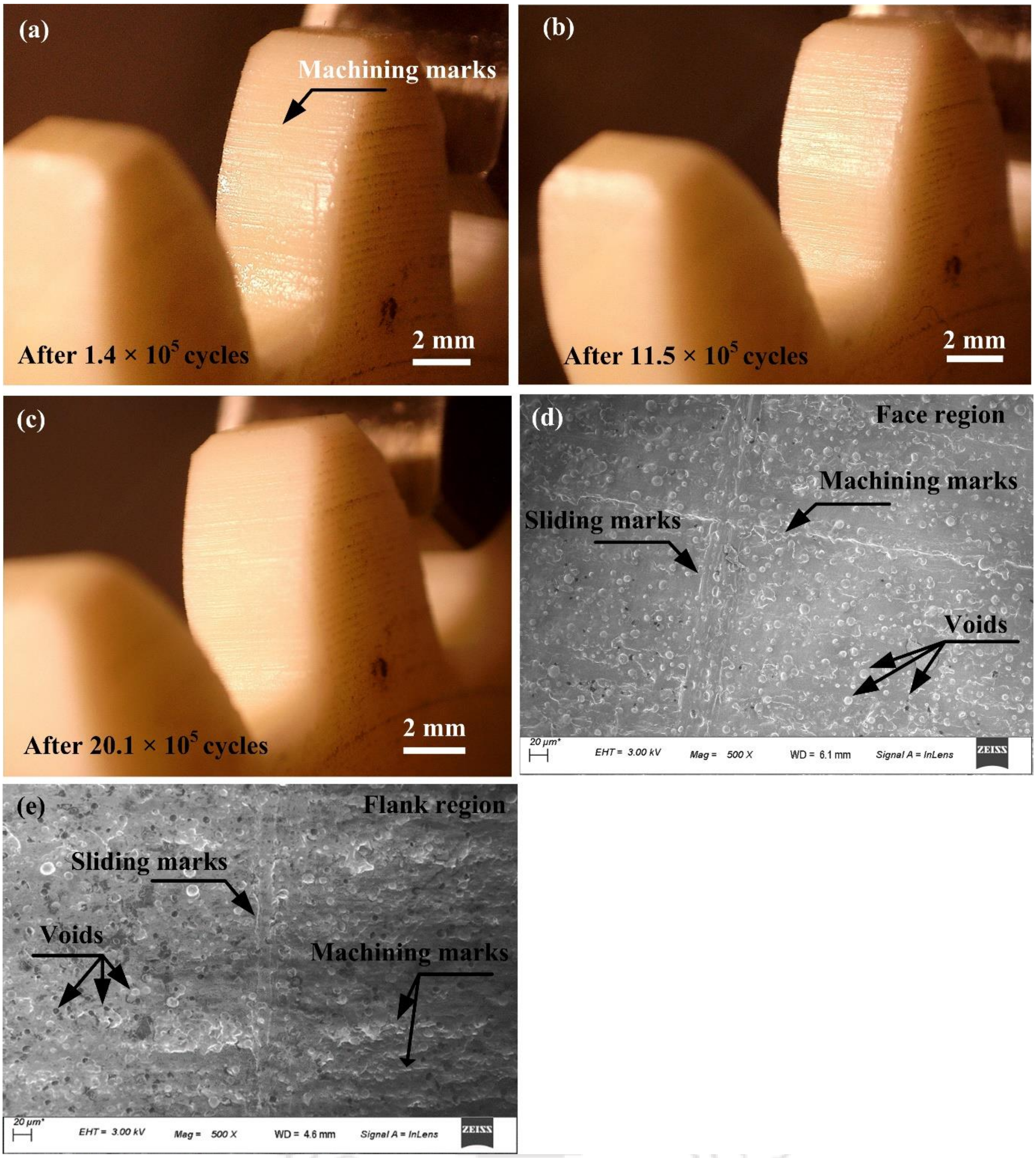

Figure 7.14 Worn-out gear tooth surface at 1.8 Nm under lubricated conditions

Figure 7.15 (a) shows the test gear tooth surface after the fatigue life (7.5×10^5 cycles) when tested at 2.5 Nm. Furthermore, the failed tooth surface was observed using FESEM (Figure 7.15 (b, c)) for detailed surface analysis. A shear-mode tooth crack is observed in the root regions (Figure 7.15 (b)). The face and flank regions of the gear tooth revealed only machined marks and no sliding marks, which confirmed the insignificant surface damage under the lubricated condition, as depicted in Figure 7.15 (a) and (c). Lubrication helped reduce the friction between the thordon gear tooth surfaces, resulting in insignificant surface damage.

However, the thordon gear under dry conditions exhibited surface damage even at a lower load (1.8 Nm) after 5.7×10^5 cycles (Figure 7.12 (a, b)).

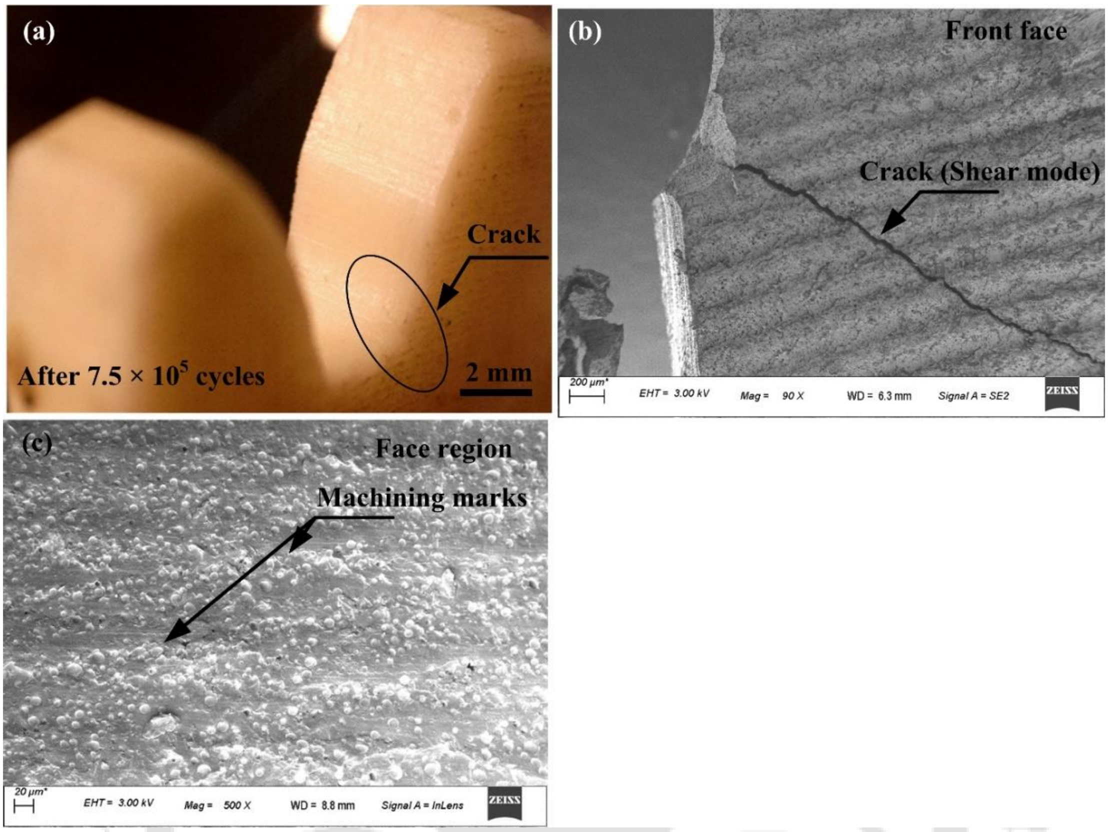

Figure 7.15 Failure morphology of gear tested at 2.5 Nm under the lubricated condition

Figure 7.16 (a) shows the gear tooth surface after 1.4×10^5 cycles when testing at 3.5 Nm under the lubricated condition. Under lubricated conditions, no sliding marks are observed on the face region of the worn tooth surface at 3.5 Nm (Figure 7.16 (b)). Figure 7.16 (c) shows the shear-mode crack of the root crack. The presence of lubrication enhanced the gear life compared to the dry condition and altered the tensile mode crack to a shear mode crack. The presence of oil has plasticized the material; this softening behavior was also reported by other researchers (Balasooriya *et al.* (2018) and Baena *et al.* (2018)) in elastomer and thermoplastic. Neoprene and Buna-N Cork Blend elastomer exhibited increased ductility while exposed to liquid fuel, Durbin *et al.* (2016). Thus, material softening could be the reason behind the change in tensile to the shear mode of tooth crack at this low cycle of fatigue. Figure 7.16 (d) shows the fractured surface, in which multiple cracks are not observed, and lubrication helped control the crack growth, unlike under dry conditions at 1.8 Nm and 3.5 Nm (Figure 7.12 (e) and 7.13 (d)).

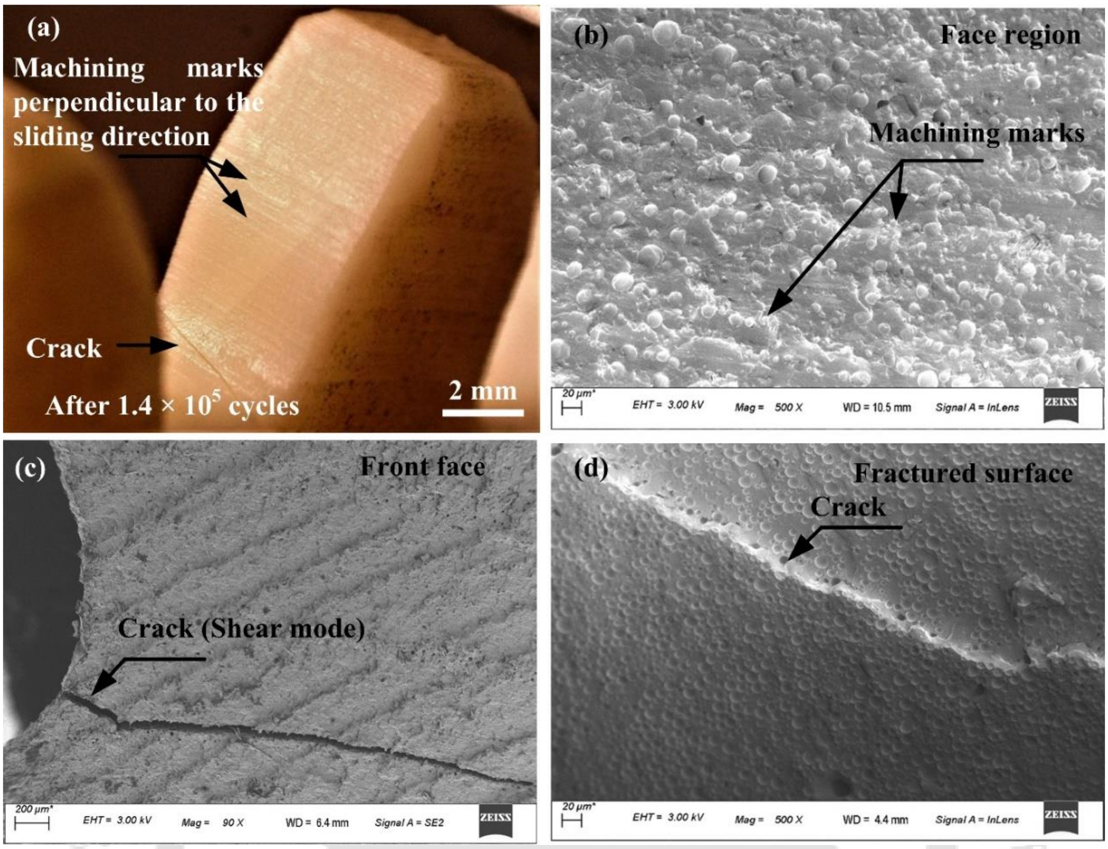

Figure 7.16 Failure morphology of gear at 3.5 Nm under the lubricated condition

7.3.7 Durability of thordon gear

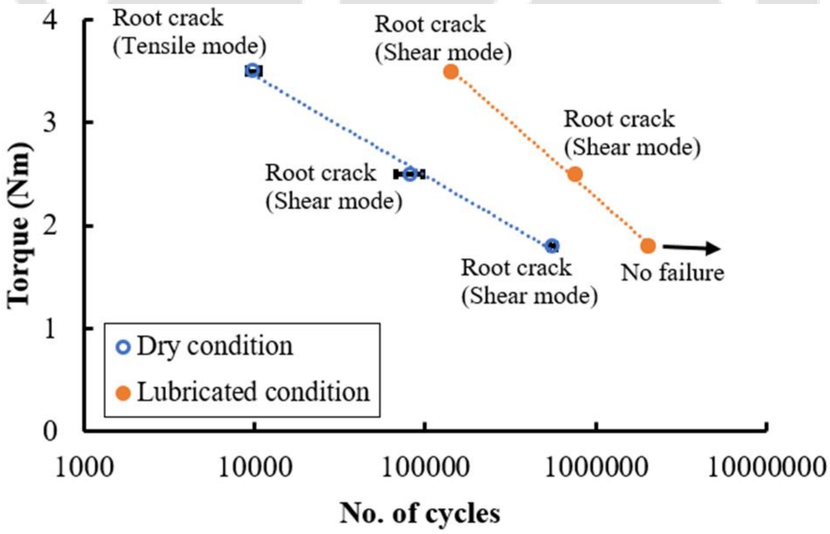

Figure 7.17 Fatigue life of thordon gear

The fatigue lives of thordon gears under dry and oil-lubricated conditions are shown in Figure 7.17. When tested at 1.8 Nm, the thordon gear under dry conditions failed at 5.5×10^5 cycles, but no failure (indicated by arrow marks) is exhibited under the lubricated condition. Oil lubrication helped reduce heat generation and enhanced the life of the thordon gear at all considered loads. The life of the lubricated thordon gear increased by 9 and 14 times for 2.5 and 3.5 Nm, respectively, compared with the dry conditions. Yu *et al.* (2021) reported an improvement in thermoplastic gear performance under lubricated conditions compared with dry conditions.

7.3.8 Summary

The sliding contact performance of the thordon material was initially investigated, followed by an evaluation of the contact and bending fatigue performance of the thordon gears. The major findings of this study are as follows:

- The friction and net surface temperature of the thordon material under oil-lubrication conditions to reduce when sliding against steel. The worn surface of the thordon material revealed an enlargement of voids due to the flushing action of the oil.
- In thordon gears, the presence of voids (owing to the interface between the polymers) caused multiple microcracks.
- The thordon gear exhibited only tooth root cracks owing to bending fatigue under both dry and oil-lubricated conditions. Root cracks were either shear or tensile modes based on the service conditions. Unlike injection-molded polyamide gears and SLS polyamide gears (discussed in an earlier chapter), thordon elastomeric gears do not exhibit thermal deformation or wear failures.
- Thordon gears under lubrication exhibited superior performance compared to dry conditions. Oil-lubricated thordon gear controlled crack growth at the tooth root and changed the cracking mode from tensile to shear under the high load condition.
- Thordon gear under lubrication exhibited no failure even after 20×10^5 cycles, whereas injection molded polyamide exhibited scuffing in the flank region, and SLS polyamide exhibited pitting near the pitch region after 14.4×10^5 cycles.
- At other investigated higher loads, the thordon gear showed inferior life compared to injection molded polyamide as well as SLS polyamide gears both under dry and lubricated conditions. Injection molded gear exhibited surface failure, whereas Thordon gear did not exhibit any surface failure but only root cracking. Thus, we can summarise that thordon gears have better surface fatigue strength under lubricated condition, and the designer needs to concentrate on the bending fatigue strength.

Chapter 8

Conclusion and scope for future work

8.1 Conclusions

In this thesis, surface durability performance evaluation of polymer-based spur gears were carried out using an in-house developed gear test rig. The thermoplastic polyamide gear was manufactured with injection molding and selective laser sintering process. In addition, elastomeric material (thordon) was hobbed into gear and evaluated for its performance. The surface durability performance of the steel-polymer and polymer-polymer gear pair was evaluated under both dry and lubricated conditions at various operating conditions. The frictional and wear performance of injection molded, selective laser sintered, and thordon material against steel discs were also carried out using pin-on-disc configuration under dry and lubricated conditions. The major conclusions from this thesis work are presented below.

- Pitting was observed as a dominant mode near the pitch region when injection molded polyamide gear was in mesh with steel gear under dry condition at low load (1.8 Nm). Abnormal wear near the root, change in sliding direction, and heat build-up on the gear tooth surface led to the formation of surface cracks in the gear tooth pitch region at higher loads (3.5–4.5 Nm).
- The lubricant between the interacting surfaces of the gear teeth dissipated the generated heat effectively. Gears tested under lubricated gear condition (1.8–4.5 Nm) exhibited a 66– 200% life enhancement compared to dry condition while in pair with a steel gear. Gears under lubrication condition did not show any cracks in the pitch region or other regions owing to improved heat dissipation characteristics. Lubricated gear exhibited only scuffing failure at the flank region. Oil lubrication was found to be the effective method for the performance enhancement of injection molded polymer gear while in pair with a steel gear.
- Under dry condition, polyamide gear exhibited inferior life when paired with similar material compared to polyamide–steel gear pair at all the considered loads. At lower loads (1.8 Nm), the test gear exhibited surface failure due to the dominance of the adhesion component of friction. At higher loads (2.5 and 3.5 Nm), test gear exhibited thermal

damage due to less thermal conductivity and high contact friction of mating material resulting in higher heat accumulation. It can be summarized that polymer-polymer gear is not preferred under dry condition.

- Under lubrication, polyamide gear exhibited superior life when paired with another polyamide gear compared to polyamide–steel gear pair at all the considered loads. Lubrication prevented heat accumulation, which significantly avoids severe plastic deformation and improved gear life compared to dry condition.
- Under dry condition, the sliding contact performance of selective laser sintered (SLS) material revealed less wear (52 %) than injection molded (IM) material due to its lesser friction. Reduced ductility due to the sintering contributes to reduced friction, wear, and heat generation, whereas IM material exhibited plastic flow and roll-shaped deformation.
- Under dry condition, SLS gear exhibited superior performance (no failure, only polishing effect) at a lower load (1.8 Nm) due to the enhanced surface fatigue strength due to the layer-by-layer manufacturing process compared to the IM gear.
- Under dry condition, SLS gear exhibited thermal bending at a higher load (3.5 Nm). Poor surface roughness of the SLS gear contributes to the rapid rise in surface temperature. Injected molded gear exhibited severe cracks but no severe thermal bending damage as observed in SLS gear, which could be due to the higher heat deflection temperature of injection molded material. Injection molded gear life was better than SLS gear.
- The lubricated SLS gear exhibited inferior contact fatigue performance at lower loads (1.8 Nm and 2.5 Nm) compared to dry condition. Cyclic contact stress coupled with sliding motion diffuses the lubricating oil into the porous subsurface and reduces the contact fatigue strength of the gear tooth.
- The lubricated SLS gear exhibited superior performance at a higher load (3.5 Nm) compared to the dry condition. The lubricant dissipated the generated heat and delayed the thermal failure.
- Thordon gear under lubrication exhibited no failure even after 20×10^5 cycles, whereas injection molded polyamide exhibited scuffing in the flank region, and SLS polyamide exhibited pitting near the pitch region even after 14.4×10^5 cycles.
- The thordon gear exhibited only tooth root crack owing to bending fatigue under dry as well as oil-lubricated conditions. Root cracks were either shear or tensile modes based on the service conditions. Unlike injection molded polyamide gears and SLS polyamide gear, thordon gears not exhibited thermal deformation or wear failures.

8.2 Scope for future work

This section outlines a few possible directions for extending the current study.

- In this work, only one type of lubricant was considered; however, other types of lubricants can be considered and evaluated. In the dry condition, gear temperature was measured; however, under the lubricant condition, only lubricant temperature was measured; however, with an appropriate sensor, gear temperature also can be measured and correlated with failure.
- In this work, only one type of build orientation was considered for selective laser-sintered polymer gear and compared with injection molding. The selective laser sintered gear can be built on different orientations, and its effect can be investigated and compared with injection molding.

References

1. Ajoku, U., Saleh, N., Hopkinson, N., Hague, R., & Erasenthiran, P. (2006). Investigating mechanical anisotropy and end-of-vector effect in laser-sintered nylon parts. *Proceedings of the Institution of Mechanical Engineers, Part B: Journal of Engineering Manufacture*, *220*(7), 1077-1086.
2. Alharbi, K. A. M. (2019). Wear and mechanical contact behavior of polymer gears. *Journal of Tribology*, *141*(1), 011101.
3. Amel, H., Rongong, J., Moztarzadeh, H., & Hopkinson, N. (2016). Effect of section thickness on fatigue performance of laser sintered nylon 12. *Polymer Testing*, *53*, 204-210.
4. American Gear Manufacturers Association. (1965). AGMA 217.01, Gear scoring design for aerospace spur gear and helical power.
5. American Gear Manufacturers Association. (1989). *Geometry Factors for Determining the Pitting Resistance and Bending Strength of Spur, Helical and Herringbone Gear Teeth*. American Gear Manufacturers Association.
6. American Gear Manufacturers Association. (1995). ANSI/AGMA 1010-E95, Appearance of Gear Teeth Terminology of Wear and Failure. *United States of America*.
7. American Gear Manufacturers Association. (2003). *Effect of Lubrication on Gear Surface Distress*. American Gear Manufacturers Association.
8. Amirruddin, M. S., Ismail, K. I., & Yap, T. C. (2022). Effect of layer thickness and raster angle on the tribological behavior of 3D printed materials. *Materials Today: Proceedings*, *48*, 1821-1825.
9. Arai, S., Tsunoda, S., Kawamura, R., Kuboyama, K., & Ougizawa, T. (2017). Comparison of crystallization characteristics and mechanical properties of poly (butylene terephthalate) processed by laser sintering and injection molding. *Materials & Design*, *113*, 214-222.
10. Athreya, S. R., Kalaitzidou, K., & Das, S. (2011). Mechanical and microstructural properties of Nylon-12/carbon black composites: Selective laser sintering versus melt compounding and injection molding. *Composites science and technology*, *71*(4), 506-510.

11. AZO Material, Data sheet . (2001 May). Polyamide 6/6 - Nylon 6/6 - PA 6/6. May 16, 2001.

12. Baena, L. M., Zuleta, E. C., & Calderón, J. A. (2018). Evaluation of the stability of polymeric materials exposed to palm biodiesel and biodiesel–organic acid blends. *Polymers*, *10*(5), 511.

13. Bai, J., Yuan, S., Chow, W., Chua, C. K., Zhou, K., & Wei, J. (2015). Effect of surface orientation on the tribological properties of laser sintered polyamide 12. *Polymer Testing*, *48*, 111-114.

14. Bai, J., Zhang, B., Song, J., Bi, G., Wang, P., & Wei, J. (2016). The effect of processing conditions on the mechanical properties of polyethylene produced by selective laser sintering. *Polymer Testing*, *52*, 89-93.

15. Balasooriya, W., Schrittesser, B., Pinter, G., & Schwarz, T. (2018). Induced material degradation of elastomers in harsh environments. *Polymer Testing*, *69*, 107-115.

16. Balasubramaniam, R. (2012). Callister's Materials Science and Engineering: *Indian Adaptation (W/Cd)*. *John Wiley & Sons*. ISBN: 978-81-265-2143-2.

17. Bansal, P., Shipway, P. H., & Leen, S. B. (2007). Residual stresses in high-velocity oxy-fuel thermally sprayed coatings–Modelling the effect of particle velocity and temperature during the spraying process. *Acta Materialia*, *55*(15), 5089-5101.

18. Bedaiwi, B. A., & Abdalkadum, H. A. A. (2018, November). The Effect of Temperature on Stress Relaxation Behaviours in Bovine Cortical Bones. In *IOP Conference Series: Materials Science and Engineering*, *433*(1), 012-048.

19. Berglund, K., & Shi, Y. (2017). Friction and wear of self-lubricating materials for hydropower applications under different lubricating conditions. *Lubricants*, *5*(3), 24.

20. Bhandari, V. B. (2017). Design of machine elements. *Tata McGraw-Hill Education.* Fourth edition, ISBN 13:978-93-392-2112-6.

21. Bhushan, B. (2013). Introduction to tribology. *John Wiley & Sons*, ISBN *978-0-471-15893-6.*

22. Blattmeier, M., Witt, G., Wortberg, J., Eggert, J., & Toepker, J. (2012). Influence of surface characteristics on fatigue behaviour of laser sintered plastics. *Rapid Prototyping Journal*, *18*(2), 161-171.

23. Blok, H. (1937, June). Les temperatures de surface dans les conditions de graissage sons pression extreme. In *Second World Petroleum Congress, Paris*.

24. Breeds, A. R., Kukureka, S. N., Mao, K., Walton, D., & Hooke, C. J. (1993). Wear behaviour of acetal gear pairs. *Wear*, *166*(1), 85-91.

25. Bryce, D. M. (1996). Plastic injection molding: manufacturing process fundamentals. *Society of manufacturing engineers*.
26. Budynas, R. G., & Nisbett, J. K. (2016). Shigley's mechanical engineering design. *New York: McGraw-Hill. Tenth edition in SI Units*, ISBN -13: 978-93-392-2163-8.
27. Calabrese, A., Davoli, P., & Quaranta, S. (1995). Noise reduction with plastic gears: a case history for diesel engines. *In imeche conference transactions*, *5*, 133-140. Mechanical engineering publications.
28. Chen, Y. K., Kukureka, S. N., Hooke, C. J., & Rao, M. (2000). Surface topography and wear mechanisms in polyamide 66 and its composites. *Journal of materials science*, *35*, 1269-1281.
29. Chen, Y. K., Modi, O. P., Mhay, A. S., Chrysanthou, A., & O'sullivan, J. M. (2003). The effect of different metallic counterface materials and different surface treatments on the wear and friction of polyamide 66 and its composite in rolling–sliding contact. *Wear*, *255*(1-6), 714-721.
30. Crippa, G., & Davoli, P. (1995). Comparative fatigue resistance of fiber reinforced nylon 6 gears. *Journal of Mechanical. Design*, *117*(1), 193-198.
31. Czichos, H. (1983). Influence of adhesive and abrasive mechanisms on the tribological behaviour of thermoplastic polymers. *Wear*, *88*(1), 27-43.
32. Dearn, K. D., Hoskins, T. J., Andrei, L., & Walton, D. (2013). Lubrication regimes in highperformance polymer spur gears. *Advances in Tribology*, *2013*, ID 987251.
33. Dennig, H. J., Zumofen, L., & Kirchheim, A. (2021). Feasibility investigation of gears manufactured by fused filament fabrication. In *Industrializing Additive Manufacturing: Proceedings of AMPA2020*, 304-320. Springer International Publishing.
34. Dieter, G. E., & Bacon, D. (1976). Mechanical metallurgy. *New York* McGraw-hill, *3*, 43-53.
35. DIN 3962. (1978 August). Tolerances of cylindrical gear teeth-Tolerance for deviations of individual parameters, Tolerances for tooth trace deviations.
36. Donzella, G., Faccoli, M., Mazzù, A., Petrogalli, C., & Desimone, H. (2011). Influence of inclusion content on rolling contact fatigue in a gear steel: experimental analysis and predictive modelling. *Engineering fracture mechanics*, *78*(16), 2761-2774.
37. Dupin, S., Lame, O., Barrès, C., & Charmeau, J. Y. (2012). Microstructural origin of physical and mechanical properties of polyamide 12 processed by laser sintering. *European Polymer Journal*, *48*(9), 1611-1621.

38. Durbin, T. D., Karavalakis, G., Norbeck, J. M., Park, C. S., Castillo, J., Rheem, Y., ... & Hunter, K. (2016). Material compatibility evaluation for elastomers, plastics, and metals exposed to ethanol and butanol blends. *Fuel*, *163*, 248-259.
39. Düzcükoğlu, H. (2009a). PA 66 spur gear durability improvement with tooth width modification. *Materials & Design, 30*(4), 1060-1067.
40. Düzcükoğlu, H. (2009b). Study on development of polyamide gears for improvement of load-carrying capacity. *Tribology International*, *42*(8), 1146-1153.
41. Eiss Jr, N. S., & McCann, B. P. (1993). Frictional instabilities in polymer-polymer sliding. *Tribology transactions*, *36*(4), 686-692.
42. Erhard, G. (1983). Sliding friction behaviour of polymer-polymer material combinations. *Wear, 84*(2), 167-181.
43. Felhös, D., Karger-Kocsis, J., & Xu, D. (2008). Tribological testing of peroxide cured HNBR with different MWCNT and silica contents under dry sliding and rolling conditions against steel. *Journal of applied polymer science, 108*(5), 2840-2851.
44. Fernández, J. E., Wang, Y., Montes, H. J., Cuetos, J. M., Miranda, M., & Rincón, A. (1996). Friction and wear behaviour of Thordon XL and LgSn80 in sliding against plasma-sprayed Cr2O3 coatings. *Tribology international*, *29*(4), 323-331.
45. Gauvin, R., Girard, P., & Yelle, H. (1983). An improved method to establish the heat transfer coefficient on gear tooth surface. In *Sixth World Congress Theory Machines and Mechanisms, New Delhi, India, Dec*, 15-20.
46. Goodridge, R. D., Hague, R. J. M., & Tuck, C. J. (2010). Effect of long-term ageing on the tensile properties of a polyamide 12 laser sintering material. *Polymer Testing*, *29*(4), 483-493.
47. Goodridge, R. D., Tuck, C. J., & Hague, R. J. M. (2012). Laser sintering of polyamides and other polymers. *Progress in Materials science*, *57*(2), 229-267.
48. Hakami, F., Pramanik, A., & Basak, A. K. (2022). *Tribology of Elastomers*. Springer.
49. Hanley, J., Murphy, N., Ali, H., & Jerrams, S. (2008). The effect of oil swelling on the fatigue life of elastomers subjected to cyclic bubble inflation. *Kautschuk und gummi kunststoffe*, *61*(1/2), 49.
50. Harsha, K. M., & Rao, Y. S. (2021, July). Comparison of wear behaviour of polymer spur gears using FDM process. In *IOP Conference Series: Materials Science and Engineering*, *1168*(1), 012-028.

51. Hasanpour, M., Razavi Aghjeh, M. K., Mehrabi Mazidi, M., & Afsari, B. (2020). Effect of morphology alteration on mechanical properties and fracture toughness of polypropylene/polyamide 6/ethylene polypropylene diene monomer graft maleic anhydride (PP/PA6/EPDM-g-MA) reactive ternary blends. *Polymer Bulletin*, *77,* 3767-3794.

52. Hasl, C., Illenberger, C., Oster, P., Tobie, T., & Stahl, K. (2018). Potential of oil-lubricated cylindrical plastic gears. *Journal of Advanced Mechanical Design, Systems, and Manufacturing*, *12*(1), JAMDSM0016

53. Hassan, A., Salleh, N. M., Yahya, R., & Sheikh, M. R. K. (2011). Fiber length, thermal, mechanical, and dynamic mechanical properties of injection-molded glass-fiber/polyamide 6, 6: plasticization effect. *Journal of Reinforced Plastics and Composites*, *30*(6), 488-498.

54. Hazer, B. (2014). The properties of PLA/oxidized soybean oil polymer blends. *Journal of Polymers and the Environment*, *22*, 200-208.

55. Hertz, H. (1896). On the contact of elastic solids, miscellaneous papers of Hertz, *(Translation by D. C. Jones), Macmillan, New York.*

56. Hooke, C. J., Mao, K., Walton, D., Breeds, A. R., & Kukureka, S. N. (1993). Measurement and prediction of the surface temperature in polymer gears and its relationship to gear wear. *Journal of Tribology 115*(1), 119-124.

57. Hoskins, T. J., Dearn, K. D., Chen, Y. K., & Kukureka, S. N. (2014). The wear of PEEK in rolling–sliding contact–Simulation of polymer gear applications. *Wear*, *309*(1-2), 35-42.

58. Hu, Z., & Mao, K. (2017). An investigation of misalignment effects on the performance of acetal gears. *Tribology International*, *116*, 394-402.

59. Huang, Q., Guo, Z., Wu, Z., & Yuan, C. (2021). Insight into the tribological performance of polyurethane composites under high temperature water lubrication. *Tribology International*, *155*, 106784.

60. Hutchings, I., & Shipway, P. (2017). *Tribology: friction and wear of engineering materials*. Butterworth-heinemann.

61. Illenberger, C. M., Tobie, T., & Stahl, K. (2019). Flank load carrying capacity of oil-lubricated high performance plastic gears. *Forschung im Ingenieurwesen*, *83*(3), 545-552.

62. Illenberger, C. M., Tobie, T., & Stahl, K. (2021). Operating behavior and performance of oillubricated plastic gears. *Forsch Ingenieurwes*, *86*, 557–565
63. İmrek, H. (2009). Performance improvement method for Nylon 6 spur gears. *Tribology International*, *42*(3), 503-510.
64. Jia, B. B., Li, T. S., Liu, X. J., & Cong, P. H. (2007). Tribological behaviors of several polymer– polymer sliding combinations under dry friction and oil-lubricated conditions. *Wear*, *262*(11-12), 1353-1359.
65. Kalácska, G., Zsidai, L., Keresztes, R., Tóth, A., Mohai, M., & Szépvölgyi, J. (2012). Effect of nitrogen plasma immersion ion implantation of polyamide-6 on its sliding properties against steel surface. *Wear*, *290*, 66-73
66. Kelley, B. W. (1953). A new look at the scoring phenomena of gears. *SAE transactions*, 175-188.
67. Kim, C. H. (2006). Durability improvement method for plastic spur gears. *Tribology International*, *39*(11), 1454-1461.
68. Kim, S. S., Shin, M. W., & Jang, H. (2012). Tribological properties of short glass fiber reinforced polyamide 12 sliding on medium carbon steel. *Wear*, *274*, 34-42.
69. Kirupasankar, S., Gurunathan, C., & Gnanamoorthy, R. (2012). Transmission efficiency of polyamide nanocomposite spur gears. *Materials & Design*, *39*, 338-343.
70. Kodeeswaran, M., Verma, A., Suresh, R., & Senthilvelan, S. (2016). Bi-directional and unidirectional bending fatigue performance of unreinforced and carbon fiber reinforced polyamide 66 spur gears. *International Journal of Precision Engineering and Manufacturing*, *17*, 1025-1033.
71. Kodeeswaran, M., Verma, A., Suresh, R., & Senthilvelan, S. (2019). Effects of frequency on hysteretic heating and fatigue life of unreinforced injection molded polyamide 66 spur gears. *Proceedings of the Institution of Mechanical Engineers, Part L: Journal of Materials: Design and Applications*, *233*(5), 781-789.
72. Koffi, D., Gauvin, R., & Yelle, H. (1985). Heat generation in thermoplastic spur gears. *Journal of Mechanisms, Transmissions, and Automation in Design*, *107*(1), 31-36.
73. Koide, T., Yukawa, T., Takami, S., Ueda, A., Moriwaki, I., Tamura, A., & Hongu, J. (2017). Tooth surface temperature and power transmission efficiency of plastic sine-curve gear. *Journal of Advanced Mechanical Design, Systems, and Manufacturing*, *11*(6), JAMDSM0082.

74. Kruth, J. P., Levy, G., Schindel, R., Craeghs, T., & Yasa, E. (2008). Consolidation of polymer powders by selective laser sintering. In *Proceedings of the 3rd international conference on polymers and moulds innovations*, 15-30.

75. Kukureka, S. N., Hooke, C. J., Rao, M., Liao, P., & Chen, Y. K. (1999). The effect of fibre reinforcement on the friction and wear of polyamide 66 under dry rolling–sliding contact. *Tribology International*, *32*(2), 107-116.

76. Landen, E. W. (1968). Slow speed wear of steel surfaces lubricated by thin oil films. *Asle Transactions*, *11*(1), 6-18.

77. Lemanski, A. J. (1965). Gear scoring design guide for aerospace spur and helical power gears. In *Information sheet*. American Gear Manufacturers' Association.

78. Letzelter, E., Guingand, M., De Vaujany, J. P., & Schlosser, P. (2010). A new experimental approach for measuring thermal behaviour in the case of nylon 6/6 cylindrical gears. *Polymer testing*, *29*(8), 1041-1051.

79. Liu, R., Burns, D. J., & Yelle, H. (1987, September). Flank Temperature Profile for Thermoplastic Spur Gear. In *Seventh World Congress Theory Machines and Mechanisms, Seville, Spain*, 17-22.

80. Lu, Z., Liu, H., Zhu, C., Song, H., & Yu, G. (2019). Identification of failure modes of a PEEKsteel gear pair under lubrication. *International Journal of Fatigue*, *125*, 342-348.

81. Mao, K. (2007). A new approach for polymer composite gear design. *Wear*, *262*(3-4), 432-441.

82. Mao, K., Greenwood, D., Ramakrishnan, R., Goodship, V., Shrouti, C., Chetwynd, D., & Langlois+, P. (2019). The wear resistance improvement of fibre reinforced polymer composite gears. *Wear*, *426*, 1033-1039.

83. Mao, K., Langlois, P., Hu, Z., Alharbi, K., Xu, X., Milson, M., ... & Chetwynd, D. (2015). The wear and thermal mechanical contact behaviour of machine cut polymer gears. *Wear*, *332*, 822-826.

84. Mao, K., Li, W., Hooke, C. J., & Walton, D. (2009). Friction and wear behaviour of acetal and nylon gears. *wear*, *267*(1-4), 639-645.

85. Marshek, K. M., & Chan, P. K. (1981). Qualitative analysis of plastic worm and worm gear failures. Wear, *66*(3), 261-271.

86. Meng, H., Sui, G. X., Xie, G. Y., & Yang, R. (2009). Friction and wear behavior of carbon nanotubes reinforced polyamide 6 composites under dry sliding and water lubricated condition. *Composites Science and Technology*, *69*(5), 606-611.

87. Mertens, A. J., & Senthilvelan, S. (2016). Durability enhancement of polymer gear using compressed air cooling. *Proceedings of the Institution of Mechanical Engineers, Part L: Journal of Materials: Design and Applications*, *230*(2), 515-525.

88. Mertens, A. J., & Senthilvelan, S. (2016). Durability enhancement of polymer gear using compressed air cooling. *Proceedings of the Institution of Mechanical Engineers, Part L: Journal of Materials: Design and Applications*, *230*(2), 515-525.

89. Mertens, A. J., & Senthilvelan, S. (2018). Surface durability of injection-moulded carbon nanotube–polypropylene spur gears. *Proceedings of the Institution of Mechanical Engineers, Part L: Journal of Materials: Design and Applications*, *232*(11), 909-921.

90. Michler, G. H. (2016). Atlas of polymer structures: Morphology, deformation and fracture structures. Carl Hanser Verlag GmbH Co KG.

91. Muraro, M. A., Koda, F., Reisdorfer Jr, U., & Silva, C. H. D. (2012). The influence of contact stress distribution and specific film thickness on the wear of spur gears during pitting tests. *Journal of the Brazilian Society of Mechanical Sciences and Engineering*, *34*, 135-144.

92. Nabil, H., Ismail, H., & Azura, A. R. (2013). Compounding, mechanical and morphological properties of carbon-black-filled natural rubber/recycled ethylene-propylene-diene-monomer (NR/R-EPDM) blends. *Polymer Testing*, *32*(2), 385-393.

93. Niemann, G., Rettig, H., & Lechner, G. (1961). Scuffing tests on gear oils in the FZG apparatus. Asle Transactions, *4*(1), 71-86.

94. Padhy, B. R., & Reddy, R. G. (2006). Performance of DMFC with SS 316 bipolar/end plates. *Journal of power sources*, *153*(1), 125-129.

95. Padmore, E. L., & Rushton, S. G. (1964, June). Paper 19: Effects of Loading Procedure on Surface Failure in Spur Gears. *In Proceedings of the Institution of Mechanical Engineers, Conference Proceedings*, 179(10), 278-317. Sage UK: London, England: SAGE Publications.

96. Palma, T., Munther, M., Damasus, P., Salari, S., Beheshti, A., & Davami, K. (2019). Multiscale mechanical and tribological characterizations of additively manufactured polyamide 12 parts with different print orientations. *Journal of Manufacturing Processes*, *40*, 76-83.

97. Pogačnik, A., & Tavčar, J. (2015). An accelerated multilevel test and design procedure for polymer gears. *Materials & Design (1980-2015)*, *65*, 961-973.

98. Polkowski, R., Melo, P., & Pisanu, L. (2016). Stress Cracking Analysis on Automotive Tubes Made with Polyamide 12. In *Materials Science Forum*, 869, 320-325. Trans Tech Publications Ltd.

99. Radzevich, S. P. (2012). Dudley's handbook of practical gear design and manufacture. *CRC press, Taylor Francis group . Second Edition*, ISBN-13: 978-1-4398-6602-3.

100. Rangappa, M. S., Parameswaranpillai J., Siengchin, S., & Ozbakkaloglu, T. (2022). *Elastomer Blends and Composites Principles, Characterization, Advances, and Applications*. ISBN: 978-0323-85832-8.

101. Ren, G., & Feng, J. (2011). Friction and wear characteristics of ThorPlas bearings and their application in hydro turbines. *Proceedings of the HydroVision International, Sacramento, CA, USA*, 19-22.

102. Rodiouchkina, M., Berglund, K., Mouzon, J., Forsberg, F., Ullah Shah, F., Rodushkin, I., & Larsson, R. (2018). Material characterization and influence of sliding speed and pressure on friction and wear behavior of self-lubricating bearing materials for hydropower applications. *Lubricants*, *6*(2), 39.

103. Rosato, V. D., Rosato, D. V., & Rosato, M. G. (2005). Plastics design handbook. *Springer International Edition,* ISBN 81-8128-369-4.

104. Saad, A. K., Abdulhussain, H. A., Gomes, F. P. C., Vlachopoulos, J., & Thompson, M. R. (2020). Studying the mechanism of biodiesel acting as an environmental stress cracking agent with polyethylenes. *Polymer*, *191*, 122278.

105. Salazar, A., Rico, A., Rodríguez, J., Escudero, J. S., Seltzer, R., & de la Escalera Cutillas, F. M. (2014). Fatigue crack growth of SLS polyamide 12: Effect of reinforcement and temperature. *Composites Part B: Engineering*, *59*, 285-292.

106. Sanes, J., Carrión, F. J., Jiménez, A. E., & Bermúdez, M. D. (2007). Influence of temperature on PA 6–steel contacts in the presence of an ionic liquid lubricant. *Wear*, *263*(1-6), 658-662.

107. Seltzer, R., de la Escalera, F. M., & Segurado, J. (2011). Effect of water conditioning on the fracture behavior of PA12 composites processed by selective laser sintering. *Materials Science and Engineering: A*, *528*(22-23), 6927-6933.

108. Senthilvelan, S. (2006). Design, development and performance of injection molded polymer composite gear. Thesis, IIT Madras.

109. Senthilvelan, S., & Gnanamoorthy, R. (2004). Damage mechanisms in injection molded unreinforced, glass and carbon reinforced nylon 66 spur gears. *Applied composite materials*, *11*, 377-397.

110. Senthilvelan, S., & Gnanamoorthy, R. (2006). Effect of gear tooth fillet radius on the performance of injection molded Nylon 6/6 gears. *Materials & design*, *27*(8), 632-639.

111. Senthilvelan, S., & Gnanamoorthy, R. (2007). Effect of rotational speed on the performance of unreinforced and glass fiber reinforced Nylon 6 spur gears. *Materials & design*, *28*(3), 765772.

112. Senthilvelan, S., & Gnanamoorthy, R. (2009). Efficiency of injection-moulded polymer composite spur gears. *Proceedings of the Institution of Mechanical Engineers, Part J: Journal of Engineering Tribology*, *223*(6), 925-928.

113. Seo, J., Takahashi, H., Nazari, B., Rhoades, A. M., Schaake, R. P., & Colby, R. H. (2018). Isothermal flow-induced crystallization of polyamide 66 melts. *Macromolecules*, *51*(11), 4269-4279.

114. Shibata, K., Yamaguchi, T., & Hokkirigawa, K. (2014). Tribological behavior of polyamide 66/rice bran ceramics and polyamide 66/glass bead composites. *Wear*, *317*(1-2), 1-7.

115. Sinha, S. K., & Briscoe, B. J. (2009). Polymer tribology. *World Scientific*.

116. Soudmand, B. H., & Shelesh-Nezhad, K. (2020). Study on the gear performance of polymer-clay nanocomposites by applying step and constant loading schemes and image analysis. *Wear*, *458*, 203412.

117. Srinath, G., & Gnanamoorthy, R. (2007). Sliding wear performance of polyamide 6–clay nanocomposites in water. *Composites science and technology*, *67*(3-4), 399-405.

118. Stephens, R. I., Fatemi A., Stephens, R. R., & Fuchs, H. O. (2000). Metal fatigue in engineering. *John Wiley & Sons, ISBN 978-0-471-51059.*

119. Stichel, T., Frick, T., Laumer, T., Tenner, F., Hausotte, T., Merklein, M., & Schmidt, M. (2017). A Round Robin study for Selective Laser Sintering of polyamide 12: Microstructural origin of the mechanical properties. *Optics & Laser Technology*, *89*, 31-40.

120. Sułek, M. W., Ogorzałek, M., Wasilewski, T., & Klimaszewska, E. (2013). Alkyl polyglucosides as components of water based lubricants. *Journal of surfactants and detergents*, *16*(3), 369375.

121. Telenko, C., & Conner Seepersad, C. (2012). A comparison of the energy efficiency of selective laser sintering and injection molding of nylon parts. *Rapid Prototyping Journal*, *18*(6), 472-481.

122. Terashima, K., Tsukamoto, N., & Nishida, N. (1986). Development of plastic gears for power transmission: design on load-carrying capacity. *Bulletin of JSME*, *29*(250), 1326-1329.

123. Thordon elastomeric bearings engineering manual version: (2022.1). Thordon Bearing, Inc.

124. Tsukamaoto, N. (1979). Investigation about the strength of plastic gears: 1st report, the strength of nylon gears which have counter-crowning. *Bulletin of JSME*, *22*(173), 1685-1692.

125. Tsukamoto, N. (1981). Investigation about the Strength of Plastic Gear: 2nd Report; Abrasion of the Nylon Gear for Power Transmission, Meshing with the Steel Gear. *Bulletin of JSME*, *24*(191), 872-881.

126. Tsukamoto, N. (1995). Argument on plastic gears for power transmission. *JSME international journal. Ser. C, Dynamics, control, robotics, design and manufacturing*, *38*(1), 1-8.

127. Tunalioglu, M. S., & Agca, B. V. (2022). Wear and Service Life of 3-D Printed Polymeric Gears. *Polymers*, *14*(10), 2064.

128. Unal, H., & Findik, F. (2008). Friction and wear behaviours of some industrial polyamides against different polymer counterparts under dry conditions. *Industrial Lubrication and Tribology*, *60*(4), 195-200.

129. Van Hooreweder, B., & Kruth, J. P. (2014). High cycle fatigue properties of selective laser sintered parts in polyamide 12. *CIRP Annals*, *63*(1), 241-244.

130. Van Hooreweder, B., De Coninck, F., Moens, D., Boonen, R., & Sas, P. (2010). Microstructural characterization of SLS-PA12 specimens under dynamic tension/compression excitation. *Polymer testing*, *29*(3), 319-326.

131. Van Hooreweder, B., Moens, D., Boonen, R., Kruth, J. P., & Sas, P. (2013). On the difference in material structure and fatigue properties of nylon specimens produced by injection molding and selective laser sintering. *Polymer Testing*, *32*(5), 972-981.

132. Walton, D., Cropper, A. B., Weale, D. J., & Meuleman, P. K. (2002). The efficiency and friction of plastic cylindrical gears Part 1: Influence of materials. *Proceedings of the Institution of Mechanical Engineers, Part J: Journal of Engineering Tribology*, *216*(2), 75-78.

133. Wang, J., Zhao, H., Huang, W., & Wang, X. (2017). Investigation of porous polyimide lubricant retainers to improve the performance of rolling bearings under conditions of starved lubrication. *Wear*, *380*, 52-58.

134. Wee, J. W., Zhao, Y., & Choi, B. H. (2015). Observation and modeling of environmental stress cracking behaviors of high crystalline polypropylene due to scent oils. *Polymer Testing*, *48*, 206-214.

135. World Pumps. (2006). Feature non-metallic bearings. August 2006. doi: 10.1016S0262-1762(06)71054-9.

136. Wörz, A., Wudy, K., Drummer, D., Wegner, A., & Witt, G. (2018). Comparison of long-term properties of laser sintered and injection molded polyamide 12 parts. *Journal of Polymer Engineering*, *38*(6), 573-582.

137. Wu, J., Xu, X., Zhao, Z., Wang, M., & Zhang, J. (2018). Study in performance and morphology of polyamide 12 produced by selective laser sintering technology. *Rapid Prototyping Journal*, *24*(5), 813-820.

138. Wu, Y. P., Zhou, Y., Li, J. L., Zhou, H. D., Chen, J. M., & Zhao, H. C. (2016). A comparative study on wear behavior and mechanism of styrene butadiene rubber under dry and wet conditions. *Wear*, *356*, 1-8.

139. Wyzgoski, M. G., & Jacques, C. H. M. (1977). Stress cracking of plastics by gasoline and gasoline components. *Polymer Engineering & Science*, *17*(12), 854-860.

140. Yakut, R., & Düzcükoglu, H. (2014). Examining the abrasion behaviour of PA 66 gears in different cycles. *Advances in Materials Science and Engineering*, (*2014*), Id: 721731.

141. Yamamoto, Y., & Takashima, T. (2002). Friction and wear of water lubricated PEEK and PPS sliding contacts. *Wear*, *253*(7-8), 820-826.

142. Yelle, H., & Burns, D. J. (1981). Calculation of contact ratios for plastic/plastic or plastic/steel spur gear pairs.

143. Yousef, S. S., Burns, D. J., & McKinlay, W. (1973). Techniques for assessing the running temperature and fatigue strength of thermoplastic gears. *Mechanism and Machine Theory*, *8*(2), 175-185.

144. Yu, G., Liu, H., Mao, K., Zhu, C., & Lu, Z. (2021). Examination on the wear process of polyformaldehyde gears under dry and lubricated conditions. *Friction*, *9*, 538-550.

145. Yu, G., Liu, H., Mao, K., Zhu, C., Wei, P., & Lu, Z. (2020). An experimental investigation on the wear of lubricated steel against PEEK gears. *Journal of Tribology*, *142*(4), 041702.

146. Zarringhalam, H., Hopkinson, N., Kamperman, N. F., & De Vlieger, J. J. (2006). Effects of processing on microstructure and properties of SLS Nylon 12. *Materials Science and Engineering: A*, *435*, 172-180.

147. Zhang, G., Wetzel, B., & Wang, Q. (2015). Tribological behavior of PEEK-based materials under mixed and boundary lubrication conditions. Tribology International, *88*, 153-161.

148. Zhang, H., Yuan, C., & Tan, Z. (2021). A novel approach to investigate temperature field evolution of water lubricated stern bearings (WLSBs) under hydrodynamic lubrication. *Advances in Mechanical Engineering*, *13*(2), 1687814021992961.

149. Zhang, P., Hu, Z., Xie, H., Lee, G. H., & Lee, C. H. (2020). Friction and wear characteristics of polylactic acid (PLA) for 3D printing under reciprocating sliding condition. *Industrial Lubrication and Tribology*, *72*(4), 533-539.

150. Zhang, Y., Purssell, C., Mao, K. and Leigh, S. (2020). A physical investigation of wear and thermal characteristics of 3D printed nylon spur gears. *Tribology International*, 141, 105953, 1-10.

151. Zhu, W., Yan, C., Shi, Y., Wen, S., Liu, J., & Shi, Y. (2015). Investigation into mechanical and microstructural properties of polypropylene manufactured by selective laser sintering in comparison with injection molding counterparts. *Materials & Design*, *82*, 37-45.

152. Zorko, D., Kulovec, S., Tavčar, J., & Duhovnik, J. (2017). Different teeth profile shapes of polymer gears and comparison of their performance. *Journal of Advanced Mechanical Design, Systems, and Manufacturing*, *11*(6), JAMDSM0083.

153. 3D systems, Material Datasheet (2007 December). DuraForm® PA plastic for use with all selective laser sintering (SLS®) systems.

Publications based on the research work

1. **Sarita, B., & Senthilvelan, S.** (2019). Effects of lubricant on the surface durability of an injection molded polyamide 66 spur gear paired with a steel gear. *Tribology International*, *137*, 193-211.
2. **Bharti, S., & Selvaraj, S.** (2023). Performance of selective laser sintered polyamide spur gear under dry and lubricated conditions. *Proceedings of the Institution of Mechanical Engineers, Part J: Journal of Engineering Tribology*, *237*(2), 404-414.
3. **Bharti, S., & Selvaraj, S.** (2023). Sliding contact performance of injection moulded and selective laser sintered polyamide under dry and lubricated conditions. *Industrial Lubrication and Tribology*, *75*(1), 126-132.
4. **Bharti, S., & Senthilvelan, S.** (2023). Performance of elastomeric spur gear under dry and oil-lubricated conditions. *Journal of Elastomers & Plastics*, *55*(1), 134-154.

Curriculum Vitae

Name	:	**Sarita Bharti**
Date of birth	:	March 25, 1992
E-mail	:	sarita.bharti@iitg.ac.in
Educational qualifications		
2008–2012	:	Bachelor of Technology
Institution		JSS Academy of Technical Education, Noida, Uttar Pradesh–201301, India. Mechanical Engineering
2013–2015	:	Master of Technology
Institution		Indian Institute of Technology (BHU) Varanasi, Uttar Pradesh–221005, India. Materials Science
2015-2023*	:	Doctor of Philosophy Indian Institute of Technology Guwahati, Guwahati, Assam-781039, India.
Date of registration	:	July 22, 2015
Date of Thesis submission	:	March 9, 2023

Doctoral Committee

Supervisor	**Dr. S. Senthilvelan** Professor Department of Mechanical Engineering Indian Institute of Technology Guwahati
Chairperson	**Dr. S. Kanagaraj** Professor Department of Mechanical Engineering Indian Institute of Technology Guwahati
Member	**Dr. Sukhomay Pal** Professor Department of Mechanical Engineering Indian Institute of Technology Guwahati
	Dr. Venkatesh R. Prasanna Associate Professor Department of Mechanical Engineering Indian Institute of Technology Guwahati